MAX-PLANCK-INSTITUT FÜR RADIOASTRONOMIE
BONN

Warm Inner Envelopes of Massive Star-Forming Regions

Thanh Dat Hoang

2025

MAX-PLANCK-INSTITUT FÜR RADIOASTRONOMIE
BONN

Warm Inner Envelopes of Massive Star-Forming Regions

Dissertation
zur
Erlangung des Doktorgrades (Dr. rer. nat.)
der
Mathematisch-Naturwissenschaftlichen Fakultät
der
Rheinischen Friedrich-Wilhelms-Universität Bonn

von
Thanh Dat Hoang
aus
Kiengiang, Vietnam

Bonn 2025

Angefertigt mit Genehmigung der Mathematisch-Naturwissenschaftlichen Fakultät der Rheinischen Friedrich-Wilhelms-Universität Bonn

Gutachter/Betreuer:	Prof. Dr. Frank Bigiel
Gutachter:	Prof. Dr. Pavel Kroupa
Tag der Promotion:	14.04.2026
Erscheinungsjahr:	2026

RHEINISCHE FRIEDRICH–WILHELMS–UNIVERSITÄT BONN

Abstract

by Thanh Dat Hoang

for the degree of

Doctor rerum naturalium

High-mass stars play crucial roles in the evolution of galaxies, and this thesis focuses on the formation of these massive objects. In detail, this thesis investigates the properties of warm inner gas envelopes surrounding high-mass (proto) stars in a sample (Top100) selected from the brightest cold dust clouds in the Milky Way, covering a wide range of physical properties and evolutionary stages of star formation. It examines the relationships between the evolution of envelopes and the process of high-mass star formation. Probing these envelopes is possible with the observations of mid- and high-J transitions of CO and its rare isotopologues such as ^{13}CO and C^{18}O. The data cubes of the ^{13}CO (6–5) line were used to investigate the distribution of warm gas and the gas kinematics of envelopes in different evolutionary stages. Furthermore, the spectra of high-J CO (11–10) and CO (16–15) lines were studied to characterise their broad wing emission. Finally, we performed radiative transfer modelling of a combination of various mid- and high-J CO transitions.

In the first project, we took advantage of the fast mapping capability of the CHAMP$^+$ receiver at the APEX telescope to obtain ^{13}CO (6–5) data cubes for close to a hundred Top100 sources. Such a large dataset enables us to systematically correlate the properties of the emission with those of the clumps. The correlations and evolutionary trends of the ^{13}CO (6–5) emission with the sources' properties suggest that the excitation of this molecular line, which probes the physical properties of the warm envelopes, is related to the star formation process. Using the zeroth moment maps as a tool to probe the gas morphology, we discovered a common type of simple gas distribution in many envelopes. We found that power-law functions could characterise their radial intensity gradients. The steeper gradient at the most evolved source group implies an increase in temperature and/or density at the source centres. While the excitation of envelope gas is found to be dependent on star formation, it is unclear whether the gas movement is regulated by star formation feedback. Our examination of the first moment (M_1) maps of ^{13}CO (6–5) emission, in combination with the ^{13}CO (2–1) M_1 maps and outflow information from CO (6–5) emission, shows that the ^{13}CO (6–5) kinematics is highly complex and could be driven by multiple physical processes such as outflow entrainment and envelope rotation. Furthermore, our work discusses the potential heating mechanism for gas in the envelopes, including mechanical and radiative processes.

The unique observing conditions of SOFIA, an airborne observatory, and its powerful GREAT receiver provided us with an opportunity to obtain velocity-resolved spectra of CO (11–10) and CO (16–15) emission. Applying a decomposition method, our line profile analysis identified and isolated high velocity components, likely associated with outflows, for the two high-J CO lines. The availability of the line ratio at each velocity channel provides a probe for the dependence of gas temperature on the offset velocity if the emission is optically thin and thermalised. The excitation analysis under both LTE and non-LTE conditions helps constrain the physical conditions of the gas where the high-J CO emission arises from. Additionally, combining with the data of low- and

intermediate-mass clumps in the literature, we show that the CO (16–15) emission is correlated with the bolometric luminosity of the clumps over a large range of physical scales, hinting at a common excitation process.

Finally, we extend our work to detailed emission modelling for ten mid- and high-J transitions of CO, ^{13}CO, and C^{18}O towards six Top100 clumps, which helps constrain the physical properties of molecular gas in the warm envelopes. Additionally, we intend to test whether one gas component can reproduce all the observed lines. However, we find that multiple gas components are required to account for all the observed lines, aligning with previous suggestions that multiple mechanical and radiative processes could be responsible for the excitation of warm gas in the envelopes.

To my parents and my brothers,
whom I love with everything in me

“Only in the darkness can you see the stars."

- Martin Luther King, Jr.

List of Publications

The following list indicates the relevant first-author publications that are discussed and presented in this thesis.

1. **Hoang T. D.**, Karska A., Lee M-Y., Wyrowski F., Le N. T., Yang A., Menten K. (2023), *Velocity-resolved high-J CO emission from massive star-forming clumps*, Astronomy & Astrophysics, 679, A121. DOI:10.1051/0004-6361/202347163
   Author's Contribution: T.D.H. performed the scientific analysis and wrote the manuscript under the supervision of A.K., M-Y.L., F.W., and K.M.. A.Y. assisted T.D.H. in implementing a decomposition method commonly used in her previous works. All authors contributed to the interpretation of the results and the editing of the final manuscript.

2. **Hoang T. D.**, Lee M-Y., Wyrowski F., Karska A., Navarete F., Menten K. (2025), *ATLASGAL-selected high-mass clumps in the inner Galaxy: XI. Morphology and kinematics of warm inner envelopes*, Astronomy & Astrophysics, 695, A24. DOI:10.1051/0004-6361/202452371
   Author's Contribution: T.D.H. reduced the data, performed the scientific analysis, and wrote the manuscript under the supervision of M-Y.L., F.W., and K.M.. F.N. provided insights and his unpublished results of the CO (6–5) outflows. All authors contributed to the interpretation of the results and editing of the final manuscript.

Contents

CHAPTER 1

Introduction

Overview

The Sun that we see in the sky is one of many stars in the Milky Way. While stars may seem eternal, as countless human generations have witnessed light from the same Sun, these celestial objects do have a beginning and an end. *Then where and how are stars formed? How do these objects come to exist?*

It begins with materials in the space between stars, known as the interstellar medium (ISM). The ISM mainly consists of gas and a small amount of dust grains, which exist in the form of clouds or more diffused material. The gravity of these particles pulls them together, gradually forming dense molecular clouds. Fig. 1.1 illustrates an example of a famous cloud named Pillars of Creation, where many new stars are being formed, hence the cloud's name. Various physical processes dominated by gravity eventually transform molecular gas into stars. The regions where this transformation occurs are called star-forming regions. To understand the star formation process, theorists develop theoretical models based on fundamental physics, while observers study the physical and chemical conditions of star-forming regions via observations; the two approaches often complement each other. This thesis will contribute to observational efforts by characterising the warm gas envelopes around regions where high-mass stars are formed. The formation of massive stars is our focus here because it is far less understood than that of low-mass counterparts. This introductory section provides background information necessary to understand the scientific context of this thesis. We will give an overview of the current knowledge of star formation on both theoretical and observational fronts, encompassing both low-mass and high-mass regimes. Additionally, we will introduce the star-forming regions investigated in this work.

1.1 Star formation

Stars are among the most fundamental objects in the Universe, and understanding how they form is a crucial aspect of modern astrophysics. The process of transforming gas into stars, along with the impacts of feedback from star formation on the nearby ISM, shapes the structure and evolution of galaxies. The formations of many elements we know are related to the life and death of stars. Those lighter than Iron can be created through nuclear fusion within stars, while those heavier are made from supernova explosions of massive stars. The formation of stars is also accompanied by the formation

Figure 1.1: Picture of the Pillars of Creation taken by the JWST Near Infrared Camera (NIRCam) onboard the James Webb Space Telescope (JWST). Figure credits: NASA, ESA, CSA, STScI; Joseph DePasquale (STScI), Anton M. Koekemoer (STScI), Alyssa Pagan (STScI).

of planetary systems, in which biological life, such as ours on Earth, can develop. The study of star formation revolves around several key questions, such as: Do stars of all masses form similarly? How do different physical processes and features, such as gravitational collapse, turbulence, and magnetic fields, interact with each other to form stars? How does gas dissipate its momentum before ending up on a protostar?

In the current research community, star formation is roughly divided into two subfields: the formation of stars heavier than approximately $8\,M_\odot$ (i.e. high-mass stars) and the formation of those lighter than this threshold (i.e. low-mass stars). The division between low- and high-mass stars can be viewed in different ways. From stellar physics, those heavier than $8\,M_\odot$ would end their life with supernova explosions and form neutron stars or black holes. In contrast, low-mass stars would eventually end up as planetary nebulae and white dwarfs. From the star formation perspective, high-mass stars reach the zero-age-main-sequence (ZAMS), which is when the hydrogen fusion at the stars' centre starts dominating the energy production of the stars, while still accreting gas from their natal envelopes. The luminosity of low-mass protostars is, therefore, dominated by accretion,

while that of the high-mass counterparts mostly comes from nuclear burning unless the accretion rate is very high. This section provides a brief overview of the current understanding of star formation, encompassing theories and observational evidence in the two mass regimes.

1.1.1 Low-mass star formation

The theoretical model of low-mass star formation from an isolated core was developed quite early by Shu, Adams and Lizano (1987) (Fig. 1.2). This simple theoretical model begins with the formation of slowly rotating single cores within molecular clouds under gravitational contraction. In subcritical regions, ambipolar diffusion, the relative motion of plasma and neutral particles that helps straighten distorted magnetic field lines and leads to a loss of magnetic flux, helps decay the magnetic and turbulent support against gravity, allowing cores to form. As the cores reach instability, they begin to collapse inside out. At this stage, a central protostar is accompanied by a protoplanetary disk, both of which are embedded within an infalling envelope. The protostar gains mass by accreting material from the disk and the envelope. When the deuterium fusion in the protostar begins, it produces a large amount of energy that requires convection for energy transportation. The convection and differential rotation of the protostar drive stellar winds, which would eventually break through the weakest resistance from infalling material (i.e. the rotational poles) to form collimated jets and bipolar outflows. As time proceeds, the opening angle of the escaping winds would widen towards the equator and eventually stop the accretion completely. From this point, the central stellar object has entered the pre-main-sequence phase, and the star has acquired all of its final mass. Contraction keeps happening at the stellar object until the temperature and density conditions at the core are sufficient to ignite the nuclear fusion that transforms Hydrogen atoms into Helium atoms. As for the protoplanetary disk, it continues to evolve to form planets and/or stellar companions or is entirely dispersed by the stellar winds.

While the steps of the theoretical model above seem straightforward, several underlying physical processes can determine whether a star can be born and/or influence the final star's properties. These processes are, for example, gravitational collapse, rotation of cores, and resistance against collapse by magnetic field and turbulence. The timescale for the collapse of the gravitationally bound cores determines the timescale for star formation and the accretion luminosity (McKee and Ostriker, 2007). Pressure from turbulence support is an opposing force against gravitational collapse, and its decay in molecular clouds allows cores to collapse (Myers and Lazarian, 1998). As for the magnetic field, the material in ISM is strongly magnetised, and the magnetic field exerts a force on gas and dust to support against the gravitational collapse of cores. Star formation can only happen when the cores are in the supercritical state, where the gravitational energy exceeds the magnetic energy.

From observations over the last decades, the research community has identified the following sequence of low-mass star formation:

- Pre-stellar cores: these are gravitationally bound cores, which have a typical size of ~0.1 pc, averaged density at a few 10^4 cm^{-3}, and temperatures around 10 K (Bergin and Tafalla, 2007). They are typically found in dense molecular clumps (size: ~0.3 – 3 pc, density: 10^3 – 10^4 cm^{-3}) embedded inside dark molecular clouds (size: 2 – 15 pc, density: 50 – 500 cm^{-3}). These objects are often not associated with infrared sources (e.g. Ward-Thompson et al., 1994), indicating a lack of central heating sources. Ward-Thompson et al. (1994) showed that the luminosities of these objects are consistent with the predicted luminosity for the isothermal phase of protostellar

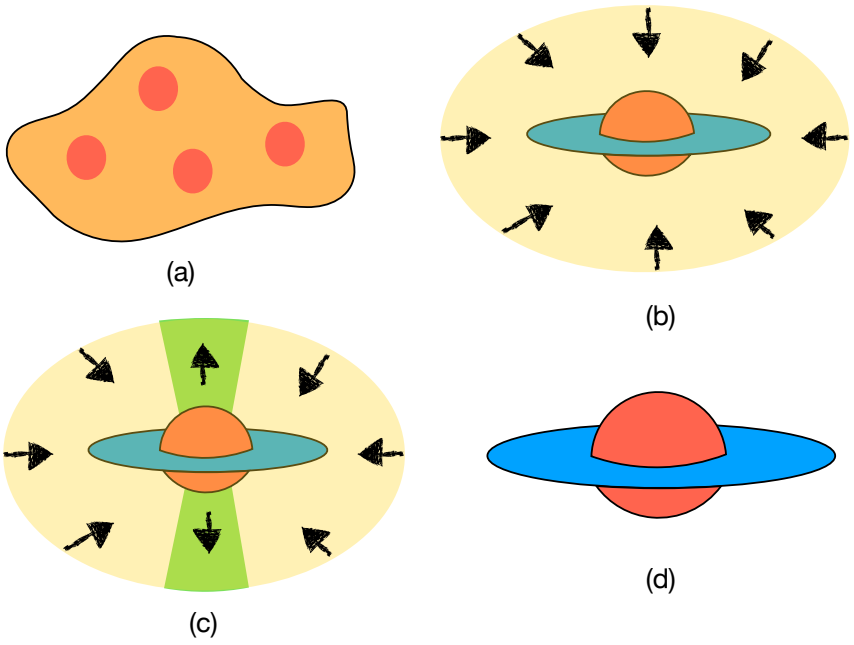

Figure 1.2: Illustration of four stages of the classical star formation model by Shu, Adams and Lizano (1987): (a) the formation of cores within molecular clouds. (b) A core collapses inside out and forms a central protostar; a disk is also formed. The protostar-disk system is embedded within an infalling envelope. (c) The escape of stellar winds at rotational poles leads to the formation of jets and bipolar outflows. (d) The accretion onto the protostar is halted due to stellar winds. Adapted from Shu, Adams and Lizano (1987).

collapse, where luminosity originates from work done by gravitational force rather than accretion. For these reasons, the cores are considered the precursors of protostars. Pre-stellar cores were found to have flat inner radial density profiles (Ward-Thompson et al., 1994), which qualitatively agree with models of magnetically-supported cores (Crutcher et al., 1994) contracting under the effect of ambipolar diffusion.

- Class 0: objects of this class are in the early stage of protostars, where gravitational collapse has formed hydrostatic cores, which then start to accrete matter. These protostellar objects, however, have yet to accumulate the majority of the final stellar mass. Class 0 protostars appear bright at sub-mm wavelengths but faint at the optical and near-IR ranges as they are still deeply embedded in the gas envelopes. To distinguish Class 0 protostars from the pre-stellar cores and the more evolved stages of protostars, Andre, Ward-Thompson and Barsony (2000) summarised three typical observational properties of Class 0 protostars: (i) there are indirect evidence for a central stellar object (ii) sub-mm continuum emission shows the presence of spheroidal circumstellar dust envelopes (iii) high ratio of sub-mm to bolometric luminosity (i.e. $L_{\rm submm}/L_{\rm bol} > 0.5\%$). Additionally, Class 0 protostars are also known for their powerful and collimated outflows (e.g. Bachiller, 1996).

- Class I: these are evolved protostars that continue to accrete mass from the gas envelopes and disks, and the current stellar mass, however, has surpassed the envelope mass. From this point

onwards, the protostars become visible in the near-infrared (IR) wavelengths as their spectral energy distributions are shifted towards higher bolometric temperatures (e.g. Myers and Ladd, 1993). The division of protostars between this and the later stages can be based on the slope of the spectral energy distribution (SED) between 2.2 μm and 10−25 μm: $\alpha_{\rm IR} = \frac{d\log(\lambda F_\lambda)}{d\log(\lambda)}$. For Class I protostars, $\alpha_{\rm IR}$ is typically larger than 0. Compared to Class 0 protostars, the ratio of sub-mm to bolometric luminosity of Class I objects is less than 0.5%. The outflows also become less powerful and less collimated.

- Class II/ Classical T Tauri: the SEDs of these objects show $\alpha_{\rm IR}$ between −1.5 and 0, which is a result of the contribution from the excess IR emission of the disks to the SEDs. The gas envelopes have disappeared, and most of their mass has been transferred to the disks and the central stellar objects, which are now considered pre-main-sequence stars and are visible on the Hertzsprung-Russell diagram.

- Class III: at this final stage, the stellar disks are mostly dispersed, leaving behind planets and stellar companions. The bipolar outflows also cease to exist. The lack of excess IR contribution from the disks to the SEDs results in $\alpha_{\rm IR}$ less than −1.5.

To sum up, the distinction between Class 0, I, II, and III protostars based on their IR and sub-mm emission can be described in Table 1.1.

Table 1.1: Classification of protostar stages based on properties of their IR and sub-mm observations.

Class	SED slope ($\alpha_{\rm IR}$)	Bolometric temperature$^{(*)}$ ($T_{\rm bol}$)	Luminosity ratio ($L_{\rm submm}/L_{\rm bol}$)
0	–	$T_{\rm bol} < 70$ K	$> 0.5\%$
I	$\alpha_{\rm IR} > 0$	70 K $< T_{\rm bol} <$ 650 K	$< 0.5\%$
II	$-1.5 < \alpha_{\rm IR} < 0$	650 K $< T_{\rm bol} <$ 2880 K	–
III	$\alpha_{\rm IR} < -1.5$	$T_{\rm bol} > 2880$ K	–

Note: $^{(*)}$: The values are taken from Andre, Ward-Thompson and Barsony (2000) and references therein.

1.1.2 Envelopes of low-mass protostars

In the previous section, the gas envelopes have been shown to be a vital part of low-mass star formation, as they provide mass for accretion onto the disks and stellar objects. Here we provide in-depth information on the evolution of the envelopes, which were derived from observations of molecular lines towards multiple Class 0, I, and II protostars (Arce and Sargent, 2006). At the early stage, the mass of envelopes dominates the total mass, which has been observed to reduce over time, following:

$$\log(M_{\rm env}/{\rm M}_\odot) = (0.87 \pm 0.5) - (0.45 \pm 0.09)\log(t/{\rm yr}), \tag{1.1}$$

which is equivalent to a mass-loss rate $\dot{M}_{\rm env} \sim -3t^{-1.45}$. This rate, however, is not constant but decreases from $\dot{M}_{\rm env} \sim 10^{-4}\,{\rm M}_\odot yr^{-1}$ for sources as young as 10^3 yr to $2\times10^{-7}\,{\rm M}_\odot yr^{-1}$ for 10^5 yr protostars. Both the infall on the star-disk system and the outflow entrainment are responsible for the

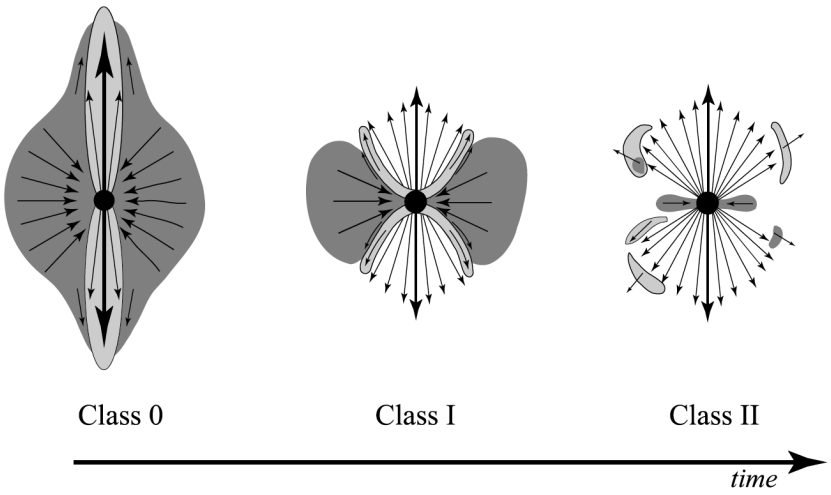

Figure 1.3: Evolution of the outflow-envelope interaction from Class 0 to Class II protostars. Taken from Arce and Sargent (2006).

mass loss of the envelopes. The former dominates the mass loss in Class 0 protostars, while the latter becomes more significant in the Class I stage.

The evolution of the gas envelope's kinematics and morphology is regulated by the outflow-envelope interaction (Arce and Sargent, 2006) (see Fig. 1.3). At Class 0 protostars, the young, powerful, and well-collimated outflows push through the envelopes and entrain the ambient gas in their direction, resulting in an elongated morphology and linear velocity gradients along the outflow axes for the dense gas within the envelopes. At the Class I stage, the opening angles of the outflows widen such that the envelope gas is now distributed in structures outside the outflow cavity walls and perpendicular to the outflow axes (see Fig. 1.3). The velocity structures of the envelopes can now be dominated by either rotation or infall motion, which are demonstrated by linear velocity gradients perpendicular to or parallel with the outflow axes, respectively. When protostars reach the Class II stage, much of the dense circumstellar envelopes has been either swept away by outflows or fallen onto the star-disk system.

1.1.3 High-mass star formation

While the research community has achieved a firm picture about the process that forms low-mass stars, we have yet to reach a consensus about high-mass star formation (HMSF). The fundamental issue that remains under debate is how high-mass stars accumulate all of their final mass despite the strong feedback from star formation activities. For example, Kahn (1974) argued that the formation of stars more massive than 40 $M_\odot$ would be limited by the radiation pressure on dust grains, which halts the accretion. To overcome this intense radiation pressure, it would require peculiar dust properties (Wolfire and Cassinelli, 1987) that have not been observed in high-mass star-forming regions. Alternatively, the non-spherical accretion can also help overcome the pressure barrier by letting thermal radiation, which is converted from stellar radiation by dust, near the dust sublimation zone to escape (Nakano, 1989). Up until now, there have been several competing concepts of HMSF such as collapsing of turbulent cores (McKee and Tan, 2003), competitive accretion in stellar clusters

(Bonnell, Bate et al., 2001; Bonnell and Bate, 2006), global hierarchical collapse (Vázquez-Semadeni et al., 2019), and converging inertial flows (Padoan et al., 2020).

The turbulent core model by McKee and Tan (2003), also known as the monolithic collapse model, is a scale-up version of the standard low-mass star formation model. High-mass stars are proposed to form from massive pre-stellar cores that are supported mainly by turbulent motions, which allow high accretion rates. The massive cores would undergo monolithic collapse. A few characteristics of this model include a strongly peaked density distribution ($n \propto r^{-1.5}$) of the initial cores, and the final stellar mass is pre-assembled within the collapsing cores. While high degrees of turbulence have been observed in high-mass star-forming regions (e.g. Plume et al., 1997), there are still standing questions about this model, such as whether the massive pre-stellar cores actually exist and if the corresponding initial turbulent levels there are actually high (Beuther, Kuiper and Tafalla, 2025). For example, narrow velocity components ($\Delta v \sim 0.3\,\mathrm{km\,s^{-1}}$ at $0.2\,\mathrm{km\,s^{-1}}$ resolution) corresponding to low turbulent levels were seen at the individual cores within a massive starless core candidate, IRDC 18310-4, (Beuther, Henning et al., 2015). The $\Delta v \sim 1.7\,\mathrm{km\,s^{-1}}$ previously obtained for this massive core by a lower spatial resolution observation (Sridharan, Beuther, Saito et al., 2005) was proposed to be a result of the overlap of narrower Δv from the sub-cores within IRDC 18310-4.

The competitive accretion model (Bonnell, Bate et al., 2001; Bonnell and Bate, 2006) suggests that the gravitational potential in cluster environments is key to massive star formation. Stars of all masses in a cluster are proposed to have similar initial masses. The stellar embryos gain mass from the local gas through the Bondi-Hoyle accretion with the accretion rate:

$$\dot{M}_* = \pi \rho v_{\rm rel} R_{\rm acc}^2,$$

where ρ is the local density, $v_{\rm rel}$ is the relative gas-star velocity, and $R_{\rm acc}$ is the accretion radius. The gas density is non-uniform throughout the cluster. It is regulated by the potential well such that densities naturally grow in regions near the centre of the well, allowing protostars there to accrete mass at high rates to form high-mass stars. At the same time, those in poor feeding zones proceed to form lower mass stars. It is noteworthy to mention that the materials that build up the final high-mass stars are initially widely distributed in the cluster (Bonnell, Vine and Bate, 2004). There is no connection between the mass of the initial cores and the final stars. This is in contrast to the initial condition of the turbulent core model, in which all the final mass is pre-assembled in the collapsing core. We note that Bonnell, Bate et al. (2001) treated the accretion radius differently depending on whether gas or stars dominate the gravitational potential. In the former scenario, the tidal radius, $R_{\rm tidal}$, which is analogous to the Roche-lobe radius in accreting binary systems, is preferred. In the other case, the Bondi-Hoyle radius, $R_{\rm BH}$, is more suitable as the accretion radius. The two parameters can be estimated as:

$$R_{\rm tidal} = 0.5 \left(\frac{M_\star}{M_{\rm enc}} \right)^{1/3} r_\star,$$

$$R_{\rm BH} = \frac{2GM_\star}{v_{\rm rel}^2 + c_{\rm s}^2},$$

where $M_\star$ is the stellar mass, $r_\star$ is the distance from the cluster centre to the stellar object, $M_{\rm enc}$ is the mass enclosed within $r_\star$, G is the gravitational constant, and $c_{\rm s}$ is sound speed. The accretion process could be terminated by stellar feedback or by fragmentation-induced starvation (Peters et al., 2010). In this phenomenon, gravitational instability in the dense accretion flows onto a massive protostar

results in the formation of fragments that become secondary protostars, competing with the central protostar for accreting material. In extremely dense cluster potentials, high-mass stars can also form in a rare event of protostars merging (e.g. Bonnell and Bate, 2005). The competitive accretion model predicts a spectrum of stellar masses in a cluster, thereby having the potential to account for the origin of the initial mass function (IMF) as suggested by Bonnell (2005).

In an attempt to illustrate the role of gravity in molecular clouds, Vázquez-Semadeni et al. (2019) present the concept of global hierarchical collapse (GHC). They argue that the formation of stars of all masses, including massive ones, is primarily driven by gravity. The authors adopt the idea of collapses within collapses, in which structures at all scales (e.g. clouds, clumps, cores) collapse and accrete material from their parent structures. The collapse of a structure increases the mean density. It reduces Jeans mass, allowing the structure to fragment into substructures that have a mass of the order of the instantaneous Jeans mass. The substructures then begin to contract while still participating in the collapse of the larger structure. Gravitational collapse also results in filaments, which play a crucial role in tunnelling gas from large-scale structures down to small-scale ones. The GHC model suggests that low-mass stars will first form several megayears after the onset of global contractions, while high-mass stars will form a few megayears later. The global gravitation collapse was suggested for molecular clouds by Goldreich and Kwan (1974) as early as the 1970s. Still, it did not prevail as the corresponding star formation rate would be much higher than the observed value. In the GHC model, collapses occur in a chronological order, such that large and diffuse regions collapse first, while smaller and denser regions begin contracting at a later time but on shorter time scales. This mechanism allows massive stars to form while the collapse of larger-scale structures is ongoing. The stellar feedback would then disperse most of the cloud's mass that has yet to accrete onto stars, maintaining a low star formation efficiency. In general, the GHC scenario shows similarities with the competitive accretion model, especially on small-scale levels. The main difference is that the GHC considers the whole evolution of molecular clouds and giant molecular clouds from formation to dispersal over a few tens of megayears, while the framework of competitive accretion is at local star-forming clumps and on shorter timescales.

A recent extensive numerical simulation by Padoan et al. (2020) has introduced a new scenario for the formation of massive stars, the inertial-inflow model. The authors argue that supersonic turbulence in molecular clouds naturally forms filament structures at the intersections of post-shock sheets, and these filaments subsequently develop dense hubs at their intersections. The inertial-inflow model relies on the converging mass flows in these large-scale filaments to continuously feed material to the hubs, allowing stellar seeds to form and grow to high masses. This is contrary to the GHC model, where gravitation collapse is the primary mass driver and turbulence only contributes partly by making stellar seeds. In the inertial-inflow scenario, the star formation timescale, t_{95}, is found to increase with the final stellar mass, and is much longer than the free-fall time of pre-stellar cores, which contradicts the core-collapse scenario. The simulation by Padoan et al. (2020) show that t_{95} tightly correlates with the size scale of the inflow regions, which further supports the idea that massive stars are formed by the continuous mass supply from the compressive motions occurring in supersonic turbulence. The stellar accretion rate is controlled by the inertial inflow, and it does not increase with time, which is opposite to the increasing accretion rate predicted by the competitive accretion model. The simulation actually shows that the pc-scale regions around pre-stellar cores are gravitationally unbound, and Padoan et al. (2020) argues that competitive accretion would be inefficient under that condition. Even though the GHC and inertial-inflow models assume different mass drivers, both scenarios agree that most of the final stellar mass is not pre-assembled in pre-stellar cores but is transported to the star

formation sites over time.

A comprehensive pathway for HMSF remains largely under debate, with competition between different theoretical and simulation models. It is therefore necessary to conduct observations of massive star-forming regions on various scales to validate the physical and observational properties predicted by each model. This approach does not necessarily disapprove a model when discrepancies are found, but can provide an opportunity for model improvement.

1.1.4 High-mass star formation from the observational perspective

Currently, there is yet a firmly established observational evolutionary sequence for HMSF. The main reasons could be attributed to observational challenges, such as the fact that many massive star-forming sites in the Milky Way are very far away on the kpc scale (e.g. König et al., 2017), and the star-forming regions are deeply embedded in dense molecular clouds, especially those in the early phases. However, new generations of ground-based and space-based observatories over the years with advanced technologies have enabled many surveys that contain high-mass star-forming regions, to name a few the Wood & Churchwell catalogue for HII regions (Wood and Churchwell, 1989), the Galactic Legacy Infrared Midplane Extraordinaire (GLIMPSE, Churchwell et al., 2009) surveys, the *Herschel* infrared Galactic Plane Survey (Hi-GAL, Molinari, Swinyard, Bally, Barlow, Bernard, Martin, T. Moore, Noriega-Crespo, Plume, Testi, Zavagno, Abergel, Ali, Anderson et al., 2010), the *Herschel* imaging survey of OB Young Stellar objects (HOBYS, Motte, Zavagno et al., 2010), and the APEX Telescope Large Area Survey of the Galaxy (ATLASGAL, Schuller, Menten et al., 2009). These surveys have allowed us to observe and categorise several high-mass star-forming phases, such as starless massive dense core (MDC) phase, protostellar MDC phase, IR-quiet high-mass protostar phase, IR-bright high-mass protostar phase, and HII region phase (Motte, Bontemps and Louvet, 2018, and references therein).

High-mass stars enter the ZAMS while their formation process is yet to finish. Therefore, the young stellar objects (YSOs) in late phases of HMSF are expected to be bright in ultra-violet (UV) and IR wavelengths. The radiation from the forming massive stars becomes intense enough that it starts to ionise the nearby hydrogen molecules to form HII regions, which are detectable in radio continuum emission. Given these reasons, the hunt for massive star-forming sites in the Milky Way began with those in the developed phases. In the late 80s, Wood and Churchwell (1989) compiled an HII regions catalogue (1646 objects) by searching for luminous IR sources, which satisfy the $\log(F_{60\mu m}/F_{12\mu m}) > 1.3$ and $\log(F_{25\mu m}/F_{12\mu m}) > 0.57$ colour-colour criteria, in a point source catalogue by *IRAS*, an infrared space telescope. Based on the expansion of the ionised area, an evolution sequence is proposed for HII regions, starting from hyper-compact HII (HCHII) to ultra-compact HII (UCHII), compact HII, and finally developed HII regions (see Churchwell, 2002; Hoare et al., 2007, and references therein). Of these classes, the early phase HCHII and UCHII, which are ~0.1 pc and < 0.05 pc in size and have densities of $\geq 10^4$ cm^{-3} and $\geq 10^6$ cm^{-3}, respectively, are more relevant to the star formation study than the more expanded HII regions (Hoare et al., 2007). It has been suggested that the development of HCHII regions could be delayed by a high accretion rate and the gravitational field of the central stars (Walmsley, 1995; Keto, 2003). The accretion flows are then not only not halted at the ionisation front of the trapped HII regions, but also able to travel through as ionised flows to feed the growing stars (Keto, 2003).

The HMSF phase, preceding the emission of ionising radiation, has been assigned different names; the two common ones are hot molecular core (HMC) (Garay and Lizano, 1999; Kurtz et al., 2000)

and high-mass protostellar object (HMPO) (Beuther, Schilke, Menten et al., 2002). To look for these objects, early works such as the surveys by Molinari, Brand et al. (2000) and Sridharan, Beuther, Schilke et al. (2002) would look into sources in the Wood & Churchwell catalogue, which are associated with high density tracers such as CS lines, with hot cores via emission of complex molecules, and/or with masers. Most importantly, the candidates of HMPO have to show no or weak emission at centimetre wavelengths, which is a sign of HII regions. A common drawback of observational studies towards HMPOs is that the sources are typically distributed over large ranges of distance, leading to a significant variation of the spatial scale between 0.1 and 10 pc (Motte, Bontemps and Louvet, 2018, and references therein). For instance, the distances of 69 HMPOs in Beuther, Schilke, Menten et al. (2002) range from 300 pc up to 14 kpc, and the median HMPO has a size of ∼1 pc. Objects of this size are generally termed as clumps, and they could host several individual high-mass protostars.

Hunting for the precursor of IR-bright protostars is different from searching for HMPO and HII regions, mostly because they emit no or weak IR emission. For this reason, one cannot directly utilise the already conducted IR-bright surveys, such as those with the *IRAS* telescope. Instead, two other methods are commonly used. The first approach is to map high-density tracers, such as sub-mm continuum emission, around massive IR-bright regions to identify dense and massive gas structures that are not detected at mid-IR wavelengths (e.g. Beuther and Steinacker, 2007). In the second method, one commonly sees dark areas on square degrees mid-IR maps by the *ISO*, *MSX*, *Spitzer*, and *Herschel* space observatories. These dark regions, which are called infrared dark cloud (IRDC), are likely representations of cold ($\lesssim$ 20 K, Carey et al., 1998) cloud structures that have absorbed the background mid-IR emission. The existence of these cloud structures is normally checked by the emission of high-density tracers from them (e.g. Sakai et al., 2008). One can then search for the precursor of IR-bright protostars from compact sources within IRDCs (e.g. Rathborne, Jackson and Simon, 2006). Similar to HMPOs, dense cores or fragments within IRDCs have a large size variation (e.g. between 0.1 and 1 pc, Peretto and Fuller, 2010); hence, they could host several individual protostars or pre-stellar cores. Observational studies towards nearby cloud complexes such as Cygnux X (Motte, Bontemps, Schilke et al., 2007) and NGC 6334 (Tigé et al., 2017) have identified large numbers of 0.1 pc structures known as massive dense cores (MDCs), which can form high-mass stars. Many of these MDCs are indeed hosting IR-quiet protostars or even objects in earlier stages of HMSF. One can recognise MDCs with IR-quiet protostars from their weak mid-IR emission ($F_{21\mu m} < 10$ Jy, Motte, Bontemps, Schilke et al., 2007) and clear signs of outflows which are missing at starless MDCs. Interestingly, the SEDs of IR-quiet MDCs can be relatively well described by modified blackbody models (e.g. Gaczkowski et al., 2013). The SEDs of IR-bright MDCs, however, show excessive emission at mid-IR wavelengths (e.g. Tigé et al., 2017).

The existence of high-mass analogues of low-mass pre-stellar cores remains a topic of debate, and finding them is crucial for differentiating various HMSF theories. In detail, the turbulent core model requires massive pre-stellar cores containing all the mass of the final stars. In contrast, the competitive accretion, GHC, and inertial flows models suggest cores with similar initial conditions to those that form low-mass stars. The current strategy to detect pre-stellar cores of HMSF is to observe candidates of starless MDCs at high angular resolutions with interferometer observatories, aiming to find compact sources that contain more than several $M_\odot$ within a region smaller than 0.1 pc. Attempts to detect pre-stellar cores have shown that such objects are elusive. For example, only one candidate (CygXN53-MM2 with 25 $M_\odot$ within ∼0.025 pc, Duarte-Cabral et al., 2013) has been found within the entire Cygnus X region. Recently, the large ALMA-IMF survey towards a dozen nearby protoclusters has provided a large sample of ∼580 cores, from which only 30 have the potential to be pre-stellar

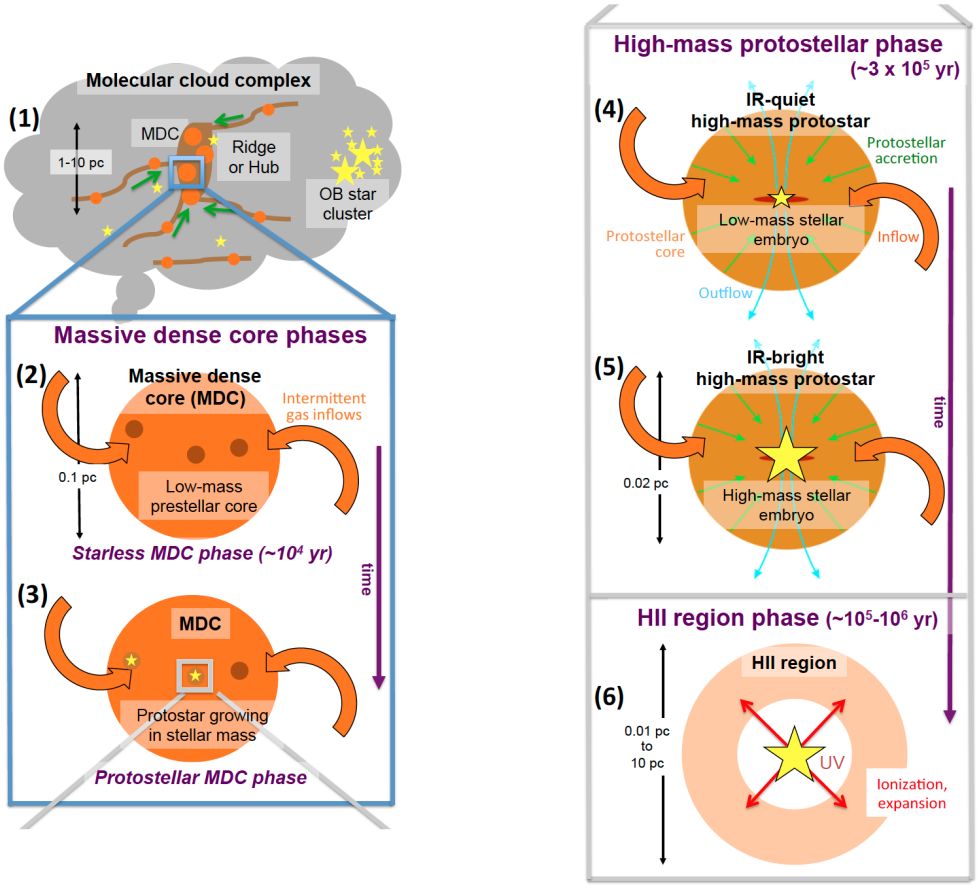

Figure 1.4: Proposed schematic evolution diagram of HMSF from observational constraints. Taken from Tigé et al. (2017).

cores (Valeille-Manet et al., 2025). The authors suggest that the lifetime of these cores can last from ~10 to 30 free-fall times, indicating the existence of non-thermal support (e.g. turbulence or magnetic field) to slow down the core collapse.

From the combination of the observational constraints of massive star-forming regions and an empirical scenario after the GHC model, Tigé et al. (2017) and Motte, Bontemps and Louvet (2018) proposed a schematic evolution diagram of HMSF (see Fig. 1.4). High-mass star-forming sites are 0.1 pc MDCs located at filaments and ridges/hubs of dense gas within molecular clouds. The global collapse of cloud structures (e.g. ridges/hubs) generates inflowing gas streams, feeding mass to the MDCs. The 0.02 pc low-mass pre-stellar cores within the MDCs evolve to protostars and grow in mass simultaneously with the growth of the MDCs. These protostars become IR-quite high-mass protostars when the inflowing gas stream can reach and feed the protostars efficiently. Once the building mass of the stellar objects surpasses 8 $M_{\odot}$, the luminosity spikes and the high-mass protostars enter the IR-bright stage. Soon, the HCHII regions are formed from the intense UV feedback, but the mass accretion onto the stellar embryos continues. Finally, the accretion process is slowed down and eventually stopped by the expansion of the HII regions and other feedback processes such as outflows and winds.

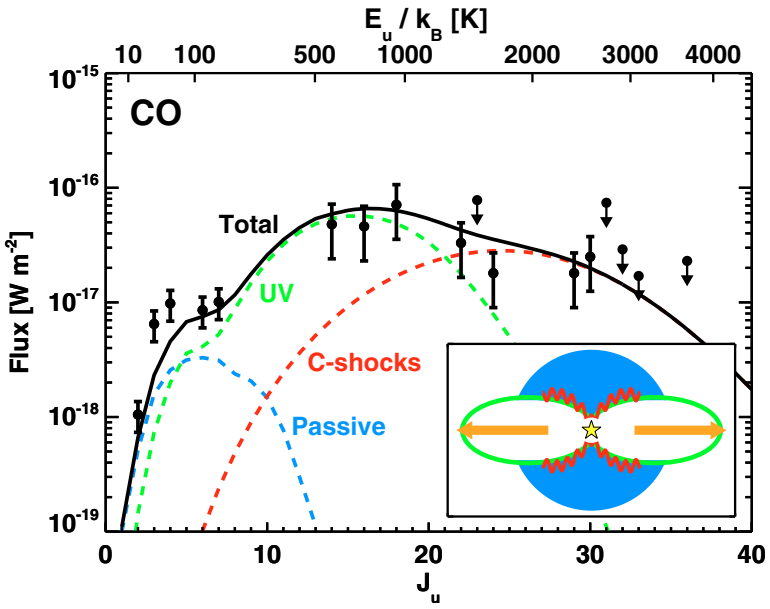

Figure 1.5: CO SED towards the low-mass protostar HH 46. The black circles show the actual observations obtained with the *Herschel*/PACS instrument. The dashed curves demonstrate the modelling of emission from different physical components or processes: UV-heated cavity walls along outflows (in green), small-scale shocks in the cavity walls (in red), and a passively heated envelope (in blue). The black curve presents the total of the three emission types. Taken from van Kempen, Kristensen et al. (2010).

1.2 CO as a gas tracer in star-forming regions

Carbon monoxide (CO) is the second most abundant molecule in the ISM, after the hydrogen molecule (H_2). While cold H_2 is practically invisible in emission in the ISM due to its zero dipole moment, the CO molecule has a weak permanent dipole moment and low excitation energy ($E_u/k_b \approx 5$ K) of the ground rotational transition. These properties allow many CO rotational transitions to be easily excited even in cold molecular clouds. The high abundance and easy excitation conditions let CO become a good tracer of molecular gas in the ISM. A convenient aspect is that the ground state transition of CO at 115 GHz is accessible for many ground-based telescopes. At a few excellent sites, such as the Atacama desert and the Mauna Kea summit, atmospheric windows allow the observations of CO from the ground to mid-J transitions. As for higher-J transitions, they can be observed from airborne and space-based observatories. Since the first detection of CO (1−0) line towards the Orion Nebula over 50 years ago by R. W. Wilson, Jefferts and Penzias (1970), CO emission has been the most commonly used gas tracer in the Milky Way and extragalactic sources. In addition to the main CO isotopologue, there are other rare isotopologues: ^{13}CO, C^{18}O, and C^{17}O, which are also easily excited but probe denser gas than CO due to their lower abundances. For example, Jacob et al. (2020) determined that the relative abundance ratio [^{12}C]/[^{13}C] in the Milky Way, which is an indication of the [CO]/[^{13}CO] ratio, is around 60 at the solar neighbourhood and increases with the distance from the galactic centre.

While CO is very efficient in probing diffuse and cold gas, the molecule is also useful in tracing dense and warm gas in molecular cores where star formation happens. The excitation energy of rotational CO transitions varies broadly from several Kelvins to several thousands Kelvins. Therefore,

the transitions in different J ranges can probe different physical conditions powered by different mechanisms/processes. This is particularly useful for probing different gas components in active star-forming regions, where multiple processes, such as outflow launching and gas accretion, can occur simultaneously, dynamically changing the properties of the gas associated with them. This usage of CO emission is illustrated clearly in a study by van Kempen, Kristensen et al. (2010) towards a low-mass protostar. The authors proposed that CO emission originates from three sources: UV-heated cavity walls along outflows, shocks in the cavity walls, and passively heated envelopes. Modelling shows that each heat sources dominate different ranges of the CO SED (see Fig. 1.5). On the other hand, CO isotopologues can also be used to probe different parts of a star-forming region. The main CO isotopologue is typically used to characterise entrained gas in outflows, primarily through the high-velocity/wing emission (e.g. Lefloch et al., 2015; Navarete et al., 2019), while the rare isotopologues $C^{18}O$ and ^{13}CO are generally used to probe the gas envelopes (e.g. Arce and Sargent, 2006; Yıldız, Kristensen, van Dishoeck, Hogerheijde et al., 2015). Additionally, ^{13}CO emission has also been linked to UV-heated gas in low-mass protostars (e.g. Spaans et al., 1995; Yıldız, Kristensen, van Dishoeck, Hogerheijde et al., 2015).

1.3 The ATLASGAL survey and the Top100 sample

Studying the evolution of high-mass star formation calls for comprehensive surveys of star-forming regions in the Milky Way, which help derive statistically significant results about the characteristics of each evolutionary phase. Among the surveys that have been carried out, many are biased against the early phases or found a very small number of pre-stellar core candidates (see Section 1.1.3). As a result, the advanced stages that emit strong IR emission are well characterised, while little is known about the phases before that. Therefore, the need for an unbiased and complete survey of galactic high-mass star-forming sites emerged, and the APEX Telescope Large Area Survey of the Galaxy (ATLASGAL, Schuller, Menten et al., 2009) was conducted to serve that goal. The ideal high column density tracer chosen for this survey is dust continuum emission at 870 μm (sub-mm wavelength), as it is optically thin and can probe deeply embedded stellar objects. Additionally, the emission is sensitive to both cold and warm dust, allowing it to probe an extensive range of HMSF evolution.

The ATLASGAl survey imaged in total 420 square degrees of the inner Galactic plane (see Fig. 1.6), including two sections: the first one is between Galactic longitude $-60^\circ < l < +60^\circ$ and Galactic latitude $-1.5^\circ < b < +1.5^\circ$, and the second one is between $-80^\circ < l < -60^\circ$ and $-2.0^\circ < b < +1.0^\circ$ (Csengeri, Urquhart et al., 2014). The efficient mapping of such a huge survey was possible thanks to an instrument at the APEX telescope: the Large APEX Bolometer Camera (LABOCA, Siringo et al., 2009), one of the most powerful bolometer cameras at the time. The LABOCA was explicitly designed to operate at 870 μm, and the beam measured at this wavelength had a full width at half maximum of $19.2''$. The instrument consisted of 295 individual bolometers, providing an effective field of view of $11.4'$. The ATLASGAL survey observations were conducted in on-the-fly mode with a scanning speed of $3''$/s. Overall, the whole survey has an average noise of ~70 mJy/beam (Csengeri, Urquhart et al., 2014).

Two source catalogues were compiled from the ATLASGAL maps using different source extraction algorithms: Multi-resolution and Gaussclumps (MRE-GCL, Motte, Zavagno et al., 2010) and SExtractor (Bertin and Arnouts, 1996). The first algorithm was used by Csengeri, Urquhart et al. (2014) to produce the GaussClump Source Catalogue (GCSC) while Contreras et al. (2013) and

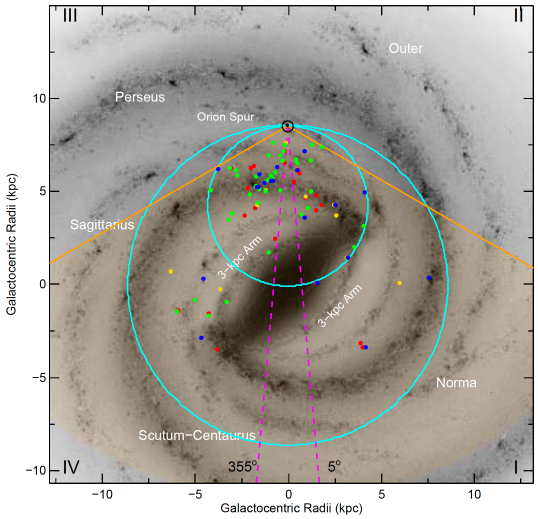

Figure 1.6: Coverage of the ATLASGAL survey and distribution of the Top100 sample in the Milky Way. The orange shaded area showcases the galactic regions observed in the ATLASGAL survey to a distance of 20 kpc. Positions of the Top100 sources are marked by the filled coloured circles. The colours blue, green, red, and yellow represent the evolutionary stages HII region, IR bright, IR weak, and 70 μm weak, respectively. Taken from König et al. (2017).

Urquhart, Csengeri et al. (2014) used the other one to compile the Compact Source Catalogue (CSC). The two catalogues complement each other in the sense that their methods are sensitive to structures on different angular scales. The MRE-GCL is suitable for identifying small and compact sources, while SExtractor is efficient at finding larger condensations. In total, the CSC and GCSC contain ~10000 and ~11000 sources, respectively, with a significant source overlap between the two catalogues.

Following the catalogue compilations, several works have characterised the physical properties and evolution of the sources as well as their associations with HMSF (Urquhart, T. J. T. Moore, Schuller et al., 2013; Urquhart, Thompson et al., 2013; Urquhart, T. J. T. Moore, Csengeri et al., 2014; Urquhart, König, Giannetti et al., 2018; Urquhart, Wells et al., 2022). The majority of the clumps demonstrate their capacity to form massive stars, as indicated by their mass-size relationship and the empirical thresholds established by Kauffmann et al. (2010b). In the latest work, Urquhart, Wells et al. (2022) used the complementary IR and radio emission to classify 5007 clumps into four evolutionary stages of HMSF: quiescent (1218), protostellar (1010), YSO (1543), and HII region (1236). The similarity of the number of sources in each stage suggests that their statistical lifetimes are comparable. It is noteworthy to mention that the clump mass is not correlated with the clump evolution, which raises questions about whether star-forming clumps continuously gain mass from larger-scale environments through global collapse or converging mass flows, as suggested by some HMSF models (see Section 1.1.3). On the other hand, Urquhart, Wells et al. (2022) found clear increasing trends of dust temperature, luminosity, and luminosity-to-mass ratio of the clumps with the evolutionary stages.

The Top100 sample

While the extensive coverage of the ATLASGAL survey provides an edge for statistical analyses, it is costly and time-consuming to perform follow-up spectral line observations for the whole survey. The information from spectral lines is essential for further investigations into the properties and evolution of star-forming clumps, as each molecule can probe different gas conditions associated with various star formation activities. Therefore, a subsample of ~100 bright ATLASGAL sources, named as the Top100 sample (Giannetti, Wyrowski et al., 2014; König et al., 2017), was selected as targets for follow-up spectral line studies.

The sources in the Top100 sample have varying physical parameters. König et al. (2017) analysed the Top100 sources using dust continuum emission from 8 μm to 870 μm and found the dust temperatures of 11 K to 41 K. They also found clump mass, $M_{\rm clump}$, and bolometric luminosity, $L_{\rm bol}$, in the ranges from 17 $M_\odot$ to 4.3×10^4 $M_\odot$ and from 57 $L_\odot$ to 3.7×10^6 $L_\odot$, respectively. The sources are located at different distances in a large range between ~1 and 13 kpc, and the distribution of the sources in the Galactic plane can be viewed in Fig. 1.6. König et al. (2017) used a similar classification scheme (see Fig. 1.7) as the one by Urquhart, Wells et al. (2022) to classify the Top100 sources to four evolutionary stages:

- Starless/pre-stellar stage (far-IR 70 μm weak or 70w, 14 clumps): these sources are likely in a quiescent phase. They are not associated with any compact IR emission, indicating the lack of protostellar objects.
- Protostellar (near/mid-IR weak or IRw, 30 clumps): this group includes sources that are associated with compact 21/24 μm emission below the 2.6 Jy threshold and those that only associate with the compact 70 μm emission. The protostellar objects here are still in the early phase, and their feedback has yet to warm up the gas in the majority parts of the clumps.
- High-mass protostellar (mid-IR bright or IRb, 35 clumps): sources that emit strong compact 21 or 24 μm emission above 2.6 Jy, which corresponds to a mass of 4, 8, or 15 $M_\odot$ at 1, 4, and 20 kpc, respectively (Heyer et al., 2016). The protostellar objects at this phase are already evolved, and the clumps are likely dominated by warm gas.
- Compact HII region (HII, 20 clumps): clumps that are associated with radio continuum emission at either 4 or 8 GHz are put into this most evolved group, where ionised gas from intense radiative feedback started to emerge.

There are currently a dozen published works in the series "ATLASGAL-selected massive clumps in the inner Galaxy", which is dedicated to the Top100 sample studies. Each study observes a different kind of molecular/atomic emission, aiming to shed light on various characteristics of massive star-forming regions and their evolutions. For example, the first work by Giannetti, Wyrowski et al. (2014) investigated CO depletion and found a significant degree of CO depletion in the early phases of HMSF. Csengeri, Leurini et al. (2016) used SiO emission to study shocked gas likely associated with jets and outflows. Tang et al. (2018) attempted to determine the kinetic temperatures and volume densities of the clumps using formaldehyde, H_2CO, emission. Navarete et al. (2019) determined the characteristics of mid-J CO emission, which shows strong and broad wing emission, suitable for outflow investigations. Finally, Hoang, M.-Y. Lee et al. (2025) attempted to characterise the warm inner envelopes of the clumps using maps of ^{13}CO (6–5) emission.

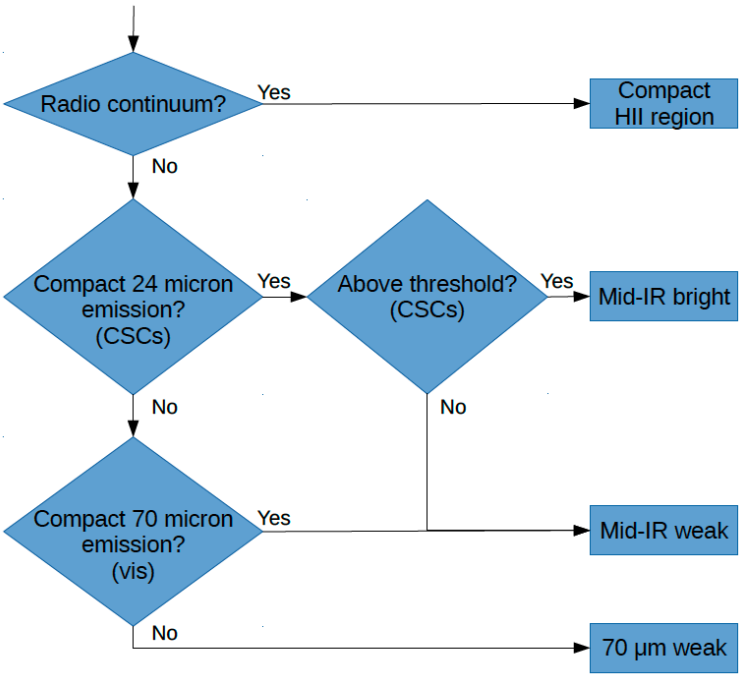

Figure 1.7: Classification diagram for the Top100 sample. Taken from König et al. (2017).

1.4 Scientific goals and outline of this thesis

The previous sections of this chapter have shown that a detailed picture of the process of HMSF is still incomplete. The exact mechanism that supplies mass for the accretion process and the mechanism that helps mass go through feedback barriers are still largely debated from both theoretical and observational aspects. Regardless of the mass transferring mechanism, it would be reasonable to assume that a significant amount of gas is assembled in the envelopes of star-forming regions before going down to the individual stars. The gas envelopes are also under the influence of HMSF feedback and could serve as an indicator of this. Therefore, having a better understanding of the properties and evolution of these envelopes would be essential to improve our knowledge about HMSF. For this reason, this thesis attempts to characterise the warm inner envelopes of the sources in the Top100 sample (see Section 1.3) using mid- and higher-J transitions of CO and CO isotopologues. The scientific contents are divided into three parts as follows:

Part I: Morphology and kinematics of the warm inner envelopes

- As mentioned in Section 1.1.2, the gas envelopes around individual low-mass protostars have changing morphologies and gas kinematics in different protostar stages due to the stellar feedback. The question is whether the envelopes of high-mass star-forming regions undergo a similar evolution or behave differently. In Chapter 3, we address this question by mapping ^{13}CO (6–5) emission towards the Top100 clumps and investigating the gas distribution and kinematics using zeroth and first moment maps.

Part II: Probing gas in massive star-forming regions with high-*J* CO lines

- Navarete et al. (2019) showed that CO (6–5) emission (E_u/k_b ~116 K) is suitable to study outflows in the Top100 clumps due to its extensive high-velocity emission. However, the information about the envelopes is missing in the CO (6–5) emission as the line is heavily affected by self-absorption at low-velocity ranges. How about emission of high-J ($J_{up} \geq 10$) CO lines which have E_u/k_b beyond ~300 K? In Chapter 4, we obtained velocity-resolved line profiles of CO (11–10), CO (13–12), and CO (16–15) towards a subsample of the Top100 sample and characterised these emission lines and their excitation conditions, especially the broad wing components associated with outflows. We found that the low-velocity emission, which is likely associated with the warm envelopes, is not affected by self-absorption in most cases and is further investigated in the next part.

Part III: Radiative transfer modelling with multiple CO lines

- Previous studies have suggested that several physical processes can take part in the excitation of CO and its isotopologue emission in star-forming regions (e.g. van Kempen, van Dishoeck, Güsten, Kristensen, Schilke, Hogerheijde, Boland, Nefs et al., 2009; Yıldız, Kristensen, van Dishoeck, Belloche et al., 2012; Leurini, Wyrowski, Herpin et al., 2013). In Hoang, M.-Y. Lee et al. (2025), the authors suggested a similar nature for the excitation of the ^{13}CO (6–5) emission from the warm envelopes of the Top100 clumps. Given an inventory of ten CO, ^{13}CO, and C^{18}O emission lines towards six Top100 clumps, we aim to test the suggestions above by performing radiative transfer modelling with the RADEX code (F. F. S. van der Tak, Black et al., 2007) and constraining the models with the observations in Chapter 5. Additionally, constraining RADEX models helps determine the physical conditions at our target envelopes.

In addition to the three scientific chapters mentioned above, we present an overview of the observation and data analysis for radio and sub-mm astronomy in Chapter 2. Finally, we summarise the main findings of this thesis and discuss prospects of future projects in Chapter 6.

CHAPTER 2

Observations and data analysis

2.1 Radio and mm/sub-mm astronomy

For thousands of years, humans have been awestruck by the night sky and its shining celestial objects. We have recorded the movements of those celestial objects and attempted to explain them, which constituted traditional astronomy. Little did we know that our vision limited our understanding of the night sky. Light, as electromagnetic waves, can have different wavelengths, and human eyes are only capable of seeing light in a small wavelength spectrum spanning from ~0.38 μm to ~0.75 μm. It was only until 1800 that Sir Frederick William Herschel made a discovery that set one of the foundations for modern astronomy and astrophysics. By that time, we already knew that sunlight could split into different colours when it goes through a glass prism. Herschel discovered that sunlight has another invisible component just beyond the red colour, which heated his thermometer better than any other visible components. That invisible light is known today as infrared (IR) radiation. Later in 1931, at a time when radio waves had already been discovered and used in telecommunication, Karl Guthe Jansky detected an unknown periodic radio signal at $\lambda \sim 14.6$ m from the sky while conducting an experiment for the Bell Telephone Laboratories. That turned out to be the first measurement of the radio signal from the centre of the Milky Way. Inspired by the work of Jansky, Grote Reber later conducted a sky survey of radio emission with a radio telescope he built in his backyard (Reber, 1944). The pioneering works of Jansky and Reber opened the door for radio astronomy to thrive, and this field finally took off in the 60s with the advancement of radar technology during and post World War II.

Why is radio astronomy important? As we mentioned in Chapter 1, the ISM contains mostly dust and gas particles, hence it is best to study ISM properties through radiation emitted/absorbed by these particles. It happens that the thermal continuum emission of cosmic dust and emission of numerous molecular/atomic transitions lie in the ranges of IR, mm/sub-mm, and radio wavelengths (e.g. Wolstencroft and Burton, 1988). Therefore, having access to these frequencies is crucial for various sub-fields of astronomy, from studying the atmospheres of the planets in the solar system to investigating star formation and galaxy evolution.

Not every light from space can reach the Earth's surface. For example, the radio waves that have λ greater than ~30 m are reflected back into space by the charged particles in the Earth's ionosphere. In addition, IR light is heavily affected by the absorption by molecules such as O_2, O_3, and H_2O in the Earth's atmosphere. The combined spectrum of radio and mm/sub-mm wavelengths spans from ~10 m to 0.1 mm (ν = 30 MHz − 3 THz). Fig. 2.1 shows that part of this wide range is observable with

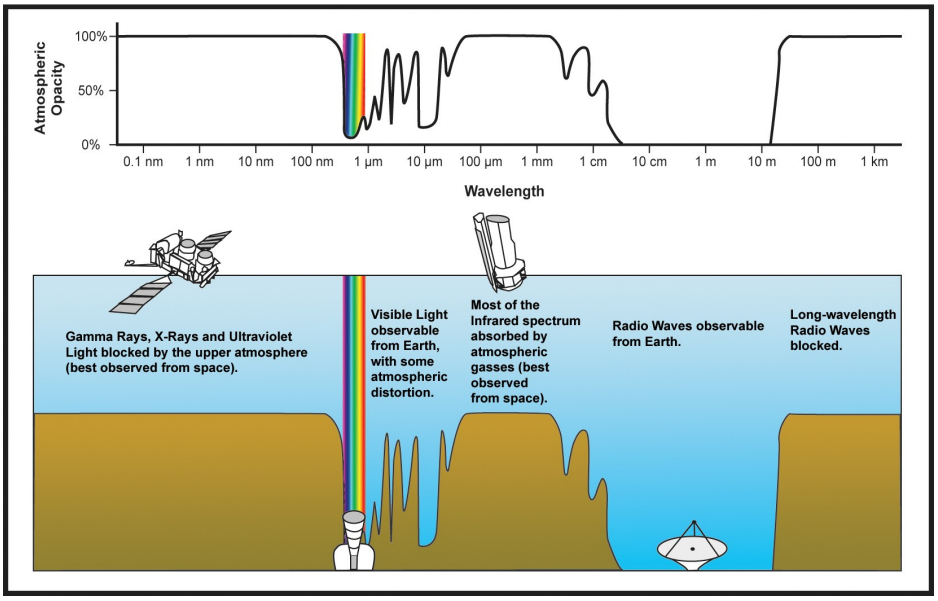

Figure 2.1: Dependence of atmospheric opacity on wavelengths of light from space. At each frequency regime, the feasible observing method is presented. Figure credit: NASA.

ground-based telescopes. In contrast, observations of shorter-wavelength signals in the mm/sub-mm ranges are better carried out with space telescopes. Alternatively, observations in certain mm/sub-mm ranges could be conducted with airborne observatories or telescopes at dry and high-altitude locations, such as the Atacama Desert in Chile, where the atmospheric water content is low. However, observing conditions there would be unstable or not reachable for the signal at THz frequencies.

2.2 Observation with single-dish telescopes

Single-dish telescopes are simple and common observing instruments used in radio astronomy. Most telescopes comprise a primary parabolic mirror or antenna that reflects and converges incoming radio waves towards a secondary reflector, where the waves are converged again towards a receiver that records the signal (see Fig. 2.2). In another variation, the receiver can be placed directly at the position of the sub-reflector. To serve different scientific purposes, each telescope is often equipped with multiple receivers that allow observations over a wide range of wavelengths and support different observing modes.

The measurement by a radio telescope is characterised by the power pattern, $P(\theta, \phi)$, which describes the response of the telescope to the incoming signal as a function of the angular distance (i.e. θ and ϕ) from the pointing direction of the telescope (see Fig. 2.3). As a pointing instrument, the majority of the power measured comes from a main lobe, while a small fraction of the power is from side lobes. A good antenna is supposed to have a high concentration of power in the main lobe. Otherwise, it would be difficult to determine the direction of the measured power.

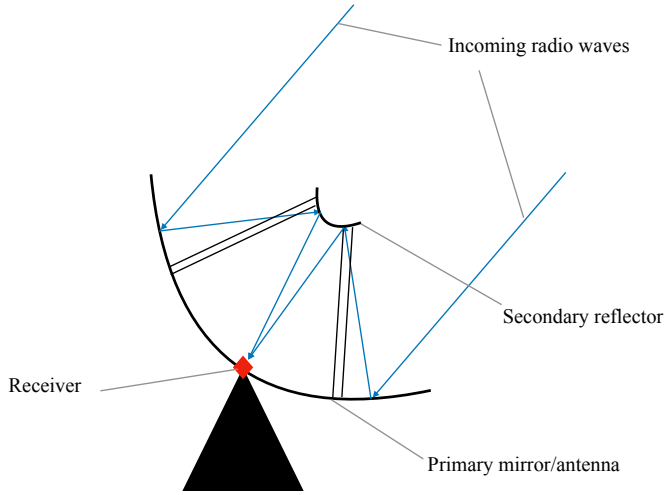

Figure 2.2: Schematic of the main components of a single-dish radio telescope.

The solid angle of an antenna is defined as:

$$\Omega_{\rm A} = \iint_{4\pi} P_{\rm n}(\theta, \phi) d\Omega, \tag{2.1}$$

where $P_{\rm n}(\theta, \phi)$ is the normalisation of $P(\theta, \phi)$ over its peak value. $\Omega_{\rm A}$ is the integration of $P_{\rm n}(\theta, \phi)$ over the full sphere. When the integration is limited to the main lobe only, we obtain the main beam solid angle:

$$\Omega_{\rm MB} = \iint_{\text{main lobe}} P_{\rm n}(\theta, \phi) d\Omega. \tag{2.2}$$

The ratio of $\Omega_{\rm MB}$ and $\Omega_{\rm A}$, known as the main beam efficiency $\eta_{\rm b} = \frac{\Omega_{\rm MB}}{\Omega_{\rm A}}$, indicates the fraction of power concentrated in the main beam. In theory, a wide main beam would allow high $\eta_{\rm b}$. However, a wide beam is undesirable, as it would be equivalent to low degrees of spatial resolution, which is the telescope's capability to distinguish two point sources. Assuming a Gaussian main beam, the spatial resolution is typically characterised by the full width at half maximum, $\theta_{\rm fwhm}$, which is related to the size of the telescope dish, D, and the signal wavelength, λ, as follows:

$$\theta_{\rm fwhm} \propto \frac{\lambda}{D}. \tag{2.3}$$

Therefore, a common practice to achieve high spatial resolution is to build telescopes with large dishes. Currently, the Five-hundred-meter Aperture Spherical Telescope (FAST) is the largest single-dish telescope with a 500 m antenna.

2.3 Telescopes used in this thesis

In this section, we will provide a brief introduction about the observatories used to obtain the data for this thesis. The observatories are either ground-based, airborne, or space-based, thereby providing

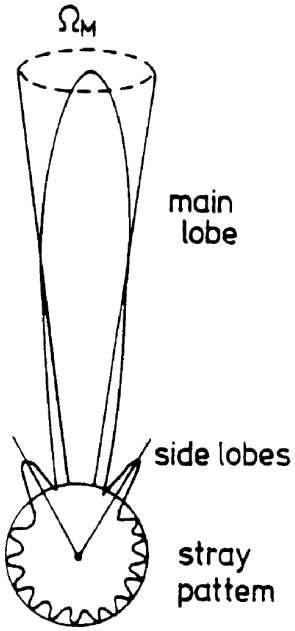

Figure 2.3: Polar power pattern of an antenna. Taken from T. L. Wilson, Rohlfs and Huttemeister (2012).

us with unique observing conditions and access to many spectral windows in the GHz and THz frequencies. Details of the obtained data sets and data reduction are presented in the corresponding chapters.

2.3.1 The Atacama Pathfinder EXperiment (APEX) 12m telescope

Figure 2.4: APEX telescope and me on the Chajnantor Plateau in northern Chile.

APEX (Güsten, Nyman et al., 2006) is a ground-based single-dish telescope developed in a collaboration between the Max Planck Institute for Radio Astronomy (MPIfR), the European Southern Observatory (ESO), and the Onsala Space Observatory. APEX is located at 5100 m above sea level on a plateau close to the Chajnantor summit in the Atacama desert in Chile. The combination of the dry desert atmosphere and the high altitude makes the Atacama Desert an ideal place for sub-millimetre telescopes. The precipitable water vapour (PWV) index at the APEX location can often get below 1.0 mm. In addition to APEX, this area of the Atacama Desert is also home to the Atacama Large Millimetre Array (ALMA), which is an interferometer observatory consisting of 66 antennas.

The APEX telescope is equipped with one Cassegrain and two Nasmyth cabins, providing ample space to host several instruments. The past and current receivers cover a wide range of frequencies between ~157 and ~850 GHz. Arrays such as CHAMP$^+$ (Kasemann et al., 2006) and LASMA (Güsten, Baryshev et al., 2008) have the ability to observe with multiple beams simultaneously, allowing for fast mapping. Complementary, instruments with

wide IF ranges, such as the PI230, are suitable for line surveys towards chemically rich ISM. The mid-J CO maps studied in this thesis were obtained with the CHAMP$^+$ receiver at the APEX telescope.

2.3.2 The Stratospheric Observatory for Infrared Astronomy (SOFIA) telescope

SOFIA (Young et al., 2012) was an airborne observatory, which hosted a 2.7 m mirror onboard the modified Boeing 747SP aircraft. The project was developed and operated by a collaboration between the National Aeronautics and Space Administration (NASA) and the German Aerospace Centre (DLR). SOFIA saw its first light in 2010 and had completed nearly 1000 scientific flights before the program was shut down in 2022. During its operation, SOFIA typically flew into the stratosphere at altitudes of 38000−45000 feet (11600−13700 m), putting it above 99% of the Earth's infrared-blocking atmosphere. Therefore, SOFIA provided an essential access to the IR wavelength windows for astronomers.

Figure 2.5: Picture of me in front of SOFIA in Stuttgart in 2019. Credit: Arshia Maria Jacob.

SOFIA was equipped with multiple receivers such as High-resolution Airborne Wideband Camera Plus (HAWC+, Harper et al., 2018), Field Imaging Far-Infrared Line Spectrometer (FIFI-LS, Fischer et al., 2018), and Faint Object InfraRed CAmera for the SOFIA Telescope (FORCAST, Herter et al., 2018). The data presented in this thesis were collected with the German REceiver for Astronomy at Terahertz Frequencies (GREAT, Risacher, Gusten et al., 2016; Risacher, Güsten et al., 2018; Duran et al., 2021), which was a high-resolution spectrometer with resolving powers beyond 10^7. GREAT was developed in several generations: early science, upGREAT, and 4GREAT. Altogether, it offered access to a wide frequency window between 480 GHz and 2.7 THz and a small window around 4.7 THz.

2.3.3 The *Herschel* Space Observatory

Figure 2.6: Prototype of the *Herschel* telescope at MPIfR. Credit: Anahat Cheema.

Herschel (Pilbratt et al., 2010) was a space telescope developed and run by the European Space Agency (ESA). The telescope operated in the far-infrared and sub-millimetre wavelengths between 55−671 μm. *Herschel* was launched into space by the Ariane 5 ECA rocket on May 14, 2009, and operated until April 29, 2013. Instead of orbiting the low Earth orbit like the Hubble space telescope, *Herschel* went a great distance to orbit around the stable second Lagrangian point (L2) of the Sun-Earth system, keeping it always at the far side of the Earth from the Sun. At the time of the launch, the 3.5 m mirror of *Herschel* was the largest mirror ever flown in space.

On board of *Herschel* were three scientific instruments: Heterodyne Instrument for the Far Infrared (HIFI, de Graauw et al., 2010), Photoconductor Array Camera and Spectrometer (PACS, Poglitsch et al., 2010), and Spectral and Photometric Imaging Receiver (SPIRE, Griffin et al., 2010). The *Herschel* data sets used in this thesis are molecular spectra obtained by HIFI and continuum maps captured by PACS.

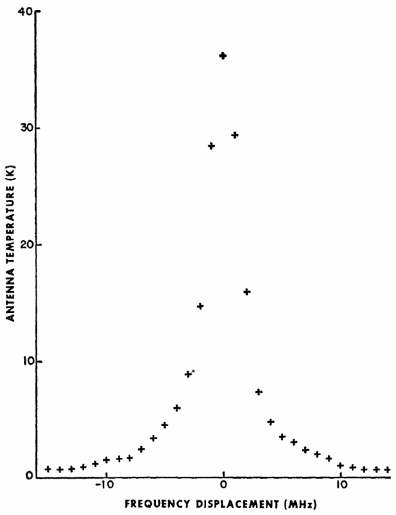

Figure 2.7: Example of an observed spectral line of the interstellar medium. The figure presents a spectrum of CO molecules towards the Orion Nebula. Taken from R. W. Wilson, Jefferts and Penzias (1970).

2.4 Interpretation of molecular line observations

Observations from a single-dish telescope often reveal the source of the signal in the sky, its frequency, and its brightness. This section provides a brief introduction to the data types that comprise that information and the basics of radiative transfer.

2.4.1 Spectroscopy

Spectroscopy is the study of the decomposition/splitting of radiation into different frequencies. Photons emitted or absorbed by molecules/atoms have characteristic frequencies that correspond to specific transitions between upper and lower quantum states of electrons, the vibration and rotation of molecules/atoms, and/or fine- and hyperfine-structure. As the physical conditions of the local ISM influence the population of molecules/atoms at each quantum level and, hence, the amount of emitted/absorbed photons, the observed spectra can help determine the density, temperature, and ionisation states of the regions where the emission originates. Assigning an observed emission/absorption line to a transition of a species requires prior knowledge of its frequency. Therefore, spectroscopists perform sophisticated laboratory measurements of hundreds of molecules/atoms which could exist in the ISM and compile them into accessible databases. The two most commonly used ones are the Cologne Database for Molecular Spectroscopy (CDMS, Müller, Schlöder et al., 2005) and the Jet Propulsion Laboratory catalogue (JPL, Pickett et al., 1998).

The Doppler effect adds an additional layer of information for spectroscopic studies. The frequencies of photons are of stationary particles with respect to the observer along the line-of-sight (LOS). Shifts in such frequencies occur at particles that either move away from or towards us. This frequency shift results in observed line profiles (see an example in Fig. 2.7) which contain valuable information about the emitting/absorbing medium. Usually characterised by a Gaussian profile, the centroid of a line profile provides the mean velocity of the medium. In contrast, the line width indicates velocity dispersion, and the line peak indicates the line intensity. The width of the line, which is typically

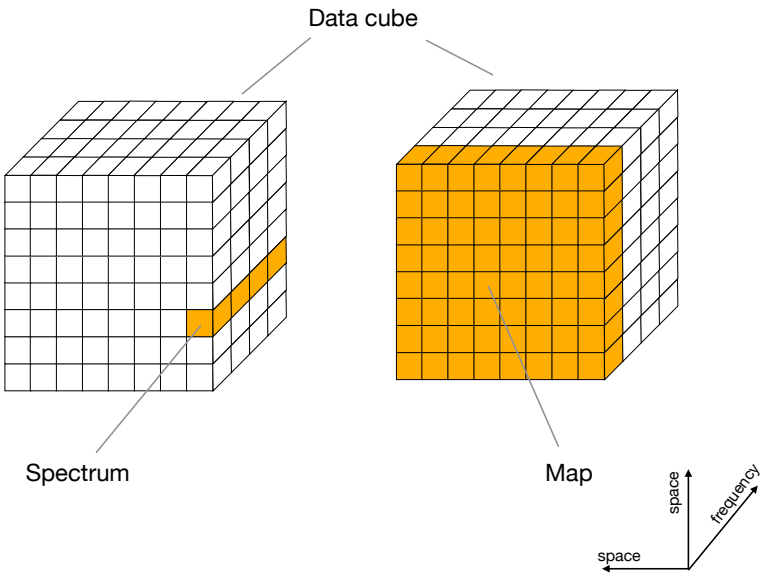

Figure 2.8: Demonstration of the data cube structure.

characterised by the full width at half maximum (FWHM), would be broadened by both thermal motions associated with random motions of particles and/or non-thermal motions. The non-thermal broadening is often linked with the turbulence associated with fluid dynamics in the observed region. Other non-thermal effects that could widen the line width include large-scale motions such as rotation and outflows.

2.4.2 Data cubes and moment maps

In the previous section, we showed that a spectrum provides information along the frequency axis at a position in the sky. Combining the spectra from multiple positions within a region of the sky yields a data cube, a three-dimensional data type comprising two spatial axes and a frequency axis. Fig. 2.8 demonstrates that one can extract either a spectrum at a specific spatial position of a data cube or an intensity map at a particular frequency.

The information along the frequency axis at a spatial position of a data cube can be integrated to estimate moment values. The zeroth and first order moments (M_0 and M_1, respectively) are two commonly used parameters in astrophysics and were used in this thesis. They can be estimated as follows:

$$M_0 = \int T_i \, dv, \tag{2.4}$$

$$M_1 = \frac{\int T_i v_i \, dv}{\int T_i \, dv}, \tag{2.5}$$

where T_i and v_i are the intensity and velocity of each cell along the frequency axis. The M_0 is a representation of the integrated intensity at a spatial position, while M_1 is the intensity-weighted

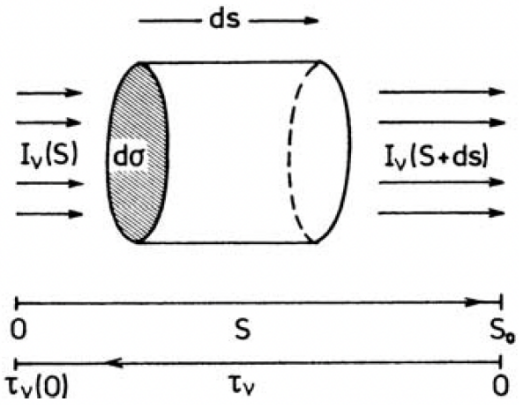

Figure 2.9: Presentation of the parameters in the concept of radiative transfer. Taken from T. L. Wilson, Rohlfs and Huttemeister (2012).

velocity along the line-of-sight at the same position. M_1 is also commonly known as the velocity centroid. A map of M_0 values thus showcases the distribution of the integrated intensity over the probed region and can be used to study the morphology of the emission. A M_1 map, on the other hand, displays the trends in velocity and helps study gas kinematics.

2.4.3 Radiative transfer

Radiative transfer refers to the process by which photons travel through space and interact with matter along their paths. In principle, radiation would travel freely without losing energy in empty space. In the event of interacting with matter, the energy of the incoming radiation can be modified via the emission, absorption, and scattering of photons. Neglecting the effect of scattering, the change of the specific intensity, I_ν, of a radiation beam at frequency ν along a path length, ds, can be described as follows:

$$\frac{\mathrm{d}I_\nu}{\mathrm{d}s} = \varepsilon_\nu - I_\nu \kappa_\nu, \tag{2.6}$$

which is known as the equation of radiative transfer. The sketch in Fig. 2.9 presents the ideas and parameters used in radiative transfer.

The first part of Eq. (2.6) presents the emission of photons from material along the path, which is characterised by the emissivity ε_ν (also known as the emission coefficient). The subtraction term describes the absorption effect, where parts of the I_ν are attenuated by the absorption coefficient κ_ν. Additionally, the term optical depth, τ_ν, which is given by $\mathrm{d}\tau_\nu = -\kappa_\nu \mathrm{d}s$, is often used to described how much light at a particular frequency can go through a medium (e.g. a molecular clump). If $\tau_\nu \gg 1$, the medium is optically thick to the incoming radiation and not much light can go through. As one is often interested in the emission of the medium itself, one needs to be cautious when interpreting the incoming radiation in these high-opacity cases, as such emission likely originates from regions close to the surface of the medium rather than the entire medium. In extreme cases, a large number of photons emitted by particles at the back of a medium can be reabsorbed by materials in the front, resulting in the phenomenon of self-absorption in spectroscopy. On the other hand, the medium is said to be optically thin to the radiation if $\tau_\nu \ll 1$.

Kirchhoff's law, which is applicable regardless of the material in the medium, states that the ratio of the emission and absorption coefficients of a body provides the source function:

$$\frac{\varepsilon_\nu}{\kappa_\nu} = S_\nu. \tag{2.7}$$

Assuming that the radiation goes through a uniform medium under the local thermodynamic equilibrium (LTE) condition, in which small regions of the medium are in thermal equilibrium and properties such as temperature, pressure, and density are uniform throughout these regions, S_ν can be further approximated by the blackbody radiation at a temperature that describes the distributions of molecules/atoms among the possible energy levels, typically known as excitation temperature, $T_{\rm ex}$:

$$S_\nu = B_\nu(T_{\rm ex}) = \frac{2h\nu^3}{c^2}\frac{1}{e^{h\nu/kT_{\rm ex}} - 1}. \tag{2.8}$$

We note that under the LTE condition, $T_{\rm ex}$ is equal to the local kinematic temperature.

From the definition of optical depth and Kirchhoff's law, Eq. (2.6) can be rewritten as:

$$-\frac{1}{\kappa_\nu}\frac{{\rm d}I_\nu}{{\rm d}s} = \frac{{\rm d}I_\nu}{{\rm d}\tau_\nu} = I_\nu - B_\nu(T_{\rm ex}). \tag{2.9}$$

The solution of this equation is given as:

$$I_\nu(s) = I_\nu(0)e^{-\tau_\nu(s)} + \int_0^{\tau_\nu(s)} B_\nu(T_{\rm ex}(\tau))e^{-\tau}{\rm d}\tau. \tag{2.10}$$

In case the excitation temperature is constant across the medium, the solution in Eq. (2.10) becomes:

$$I_\nu(s) = I_\nu(0)e^{-\tau_\nu(s)} + B_\nu(T_{\rm ex})(1 - e^{-\tau_\nu(s)}). \tag{2.11}$$

Practically, the radiation that enters the medium (i.e. $I_\nu(0)$ is normally characterised by blackbody radiation at a background temperature, $T_{\rm bg}$. Hence, Eq. (2.11) can be re-written as:

$$I_\nu(s) = B_\nu(T_{\rm bg})e^{-\tau_\nu(s)} + B_\nu(T_{\rm ex})(1 - e^{-\tau_\nu(s)}). \tag{2.12}$$

In the case of an optically thick medium (i.e. $\tau \gg 0$), I_ν approaches the value of $B_\nu(T_{\rm ex})$, and the observed emission can be solely characterised by the excitation temperature of the medium.

2.4.4 Non-LTE radiative transfer with RADEX

The analytical approach in the above section helps solve the radiative transfer equation, connecting the fluxes from observations to the characteristics of the involved ISM under the LTE assumption. This condition, however, is not always held in various phases and regions of the ISM, especially in low-density areas. Inferring the characteristics of a gas from observed molecular lines under non-LTE conditions is often done using radiative transfer modelling codes. This section provides a brief introduction to RADEX, which is a commonly used one-dimensional statistical equilibrium radiative transfer code developed by F. F. S. van der Tak, Black et al. (2007).

The emission/absorption of molecular/atomic lines occurs as the molecules/atoms transit between

different quantum levels. Therefore, knowing the populations of molecules/atoms at various levels is essential to solving the radiative transfer equation. Considering a system of two levels l and u with popular densities n_l and n_u and collision dominates the de-excitation of molecules/atoms, the ratio of the level population follows the Boltzmann distribution:

$$\frac{n_u}{n_l} = \frac{g_u}{g_l} e^{-h\nu/k_b T_{ex}}, \tag{2.13}$$

where g_u and g_l are statistical weights of the two levels. Under the LTE conditions, T_{ex} can be approximated by the local kinetic temperature, T_{kin}, and it can characterise the relative population across all levels in the system with three or more levels. The problem becomes more complex in the non-LTE conditions as the use of T_{kin} does not apply, and it would require a different T_{ex} for each pair of levels. Solving the radiative transfer equations under the non-LTE conditions is a non-linear problem, which requires a numerical treatment.

RADEX offers a simple approach for those whose main interests lie in the global properties of an interstellar cloud. Instead of solving the complex radiative transfer equations, the programme uses a geometrically averaged escape probability, β, which estimates the chance for a photon to escape from the medium where it was created, to approximate the line intensity as follows:

$$\overline{J}_{\nu_{ul}} = S_{\nu_{ul}}(1-\beta), \tag{2.14}$$

where $\overline{J}_{\nu_{ul}}$ is the specific intensity integrated over all directions and over the line profile. The simplicity of this method comes from the fact that β relies only on the opacity of the medium. Assuming different geometries for the medium, several works have formulated three relations between β and τ, which RADEX users can choose based on their needs. The first β expression is of an expanding spherical shell, which is also known as a large velocity gradient (LVG) environment, developed by Mihalas (1978) and de Jong, Boland and Dalgarno (1980) as follows:

$$\beta_{LVG} = \frac{1}{\tau}\int_0^\tau e^{-\tau'} d\tau' = \frac{1-e^{-\tau}}{\tau}. \tag{2.15}$$

In the case of a static, spherically symmetric, and homogenous medium, Osterbrock and Ferland (2006) provided an expression for β as:

$$\beta_{sphere} = \frac{1.5}{\tau}\left[1 - \frac{2}{\tau^2} + \left(\frac{2}{\tau} + \frac{2}{\tau^2}\right)e^{-\tau}\right]. \tag{2.16}$$

Finally, in the case of instance shocks, a plane-parallel slab geometry is normally assumed and β can be estimated from the work of de Jong, Chu and Dalgarno (1975) as:

$$\beta_{slab} = \frac{1-e^{-3\tau}}{3\tau}. \tag{2.17}$$

CHAPTER 3

Morphology and kinematics of warm inner envelopes

This chapter summarises the content of the article titled **"ATLASGAL-selected high-mass clumps in the inner Galaxy: XI. Morphology and kinematics of warm inner envelopes"** published in the Astronomy and Astrophysics journal by the following authors:

Thanh Dat Hoang, Min-Young Lee, Friedrich Wyrowski, Agata Karska, Felipe Navarete, and Karl M. Menten

The full version of the article can be found in Appendix A or from the following link: https://doi.org/10.1051/0004-6361/202452371.

3.1 Context

High-mass star formation occurs in the densest parts of molecular clouds, in which the envelopes of dense gas cocoon massive stellar embryos. These envelopes are essential for the star formation process as they provide mass for the accretion onto final stars (Shu, Adams and Lizano, 1987; Wyrowski et al., 2016; Beltrán and de Wit, 2016; Pillai et al., 2023). Star formation activities, in return, launch feedback such as outflows and radiation into the vicinity, thereby altering the properties of the gas envelopes. For these reasons, the envelope evolution is likely associated with the star formation sequence and can be used to track and investigate the star-forming process. For example, at low-mass protostars, the distribution and kinematics of gas in the envelopes change systematically from early to later stages (see Section 1.1.2). While the evolution of envelopes around low-mass protostars has been extensively examined, a similar study for high-mass counterparts is lacking. Massive YSOs often stay in clusters, and those in the same star-forming clump may share from an envelope that provides mass and receive feedback from all the YSOs within.

Investigating the envelope evolution requires a statistically significant sample of high-mass star-forming regions covering various evolutionary stages. Such a sample is provided by the Top100 sample of the ATLASGAL survey (see Section 1.3). The sample comprises around 100 bright, massive star-forming clumps that have been categorised into four evolutionary stages starting from the starless phase (i.e. 70w), to the formation of protostars (i.e. IRw), the advanced stage of protostars (i.e. IRb), and finally, the appearance of HII regions as a result of intense stellar radiation (i.e. HII).

3.2 Aims

The primary objectives of this thesis are to characterise the warm envelopes surrounding massive star-forming regions and investigate their evolution in relation to the star formation process (see Section 1.4). In this first project, we aim to investigate the morphology and kinematics of the warm envelopes in different evolutionary stages. Our interest is whether the gas distribution within the envelopes exhibits a high degree of complexity, whether the morphological properties change over time, and, if so, how they are connected to star formation. We also aim to answer questions about the gas motion within the envelopes, whether they exhibit any coherent trends, and the causes of those trends. It is also in our interest to understand the excitation mechanisms of warm gas in the envelopes, as they play a crucial role in helping us connect the properties of the envelopes to the star formation process.

3.3 Methods

The mid-J ($5 < J < 10$) rotational transitions of isotopologues of CO can be used to probe the warm ($T \gtrsim 50$ K) inner parts of gas envelopes at massive star-forming regions. We used the CHAMP$^+$ receiver equipped at the APEX telescope (see Section 2.3.1) to map ^{13}CO (6–5) emission towards 99 clumps in the Top100 sample. Each map has an angular size of $80'' \times 80''$, which is equivalent to physical sizes of 0.3 pc × 0.3 pc to 4.9 pc × 4.9 pc, given that the distances to the clumps from the Earth range from ~1 to 13 kpc. The final data cubes were obtained using the `XY_MAP` gridding routine in CLASS, and they have a final angular resolution of $10''$. We extracted an averaged spectrum towards the central position of each clump to examine the detection of the ^{13}CO (6–5) line and the general line shape at each phase of high-mass star formation. The line luminosity was also derived and compared with the bolometric luminosity and mass. Zeroth and first moment maps were then generated from the data cubes.

The zeroth moment (M_0) maps display the integrated intensity at each map pixel and reveal the morphology of the envelopes. By applying a few criteria to the M_0 maps (see Fig. 3.1), we categorised our sample into four morphology groups, each representing a different degree of complexity. To better understand the distribution of warm gas in the envelopes, we produced the radial intensity profiles for sources with simple morphologies. We attempted to fit them with a power-law function similar to the one used in Beuther, Schilke, Menten et al. (2002). Additionally, to compare the distribution of warm gas with that of colder material, we compared the radial profiles of ^{13}CO (6–5) emission with the radial profiles of Hi-GAL 160 μm dust continuum emission (Molinari, Swinyard, Bally, Barlow, Bernard, Martin, T. Moore, Noriega-Crespo, Plume, Testi, Zavagno, Abergel, Ali, André et al., 2010).

The first moment (M_1) maps present the velocity centroid at each map pixel and reveal the movement of gas within the envelopes. To quantify the velocity fields, we fitted the M_1 maps using the mean velocity gradient (MVG) function introduced in (Goodman et al., 1993). The fitting result would indicate whether a M_1 map shows a trend of linear velocity gradient and what the strength and direction of that gradient are. This information was then put into perspective with kinematics signatures from other lines, such as CO (6–5), which is an outflow tracer, and ^{13}CO (2–1), which probes cooler gas that likely retains the kinematics of the clumps hosting YSOs, to investigate the origin of the gas kinematics in the warm envelopes.

3.4 Results and discussion

With a detection limit of three times the spectral noise, ^{13}CO (6–5) emission is detected towards 81 clumps, equivalent to 83% of our sample. The detection rate, however, varies among the source groups, increasing from 31% for the youngest phase (i.e. 70w) to 81%, 100%, and 100% for the IRw, IRb, and HII groups, respectively. At the same time, we found that the peak intensity of the line increases from below 10 K up to tens of Kelvins as the envelopes evolve. Both trends in the detection rate and peak intensity indicate temperature and/or density enhancements at the gas envelopes. The ^{13}CO (6–5) line luminosity shows positive correlations with the bolometric luminosity and mass of the clumps, implying that the mid-J ^{13}CO transition is a decent tracer for the evolution of the clumps as well as star formation happening within them. Examining the ^{13}CO (6–5) line profiles, we found that the line width is generally wider at more evolved sources, suggesting stronger non-thermal motions there. Interestingly, the representative line profiles of the IRw, IRb, and HII group exhibit minor line wings at high velocities. This non-Gaussian feature possibly suggests that there are at least two heating components responsible for the excitation of the ^{13}CO (6–5) line.

Figure. 3.1 demonstrate the classification of the 81 ^{13}CO (6–5) M_0 maps into four morphology types. While the maps of most 70w and IRw sources are the poorly-resolved type, the majority of the IRb and HII maps are well-resolved, implying the more evolved sources generally appear larger in the sky. When distances to the sources are accounted for, HII sources still show larger sizes compared to the others, indicating the expansion of warm envelopes at the most evolved clumps.

Among 59 well-resolved sources, we found that the majority (52) have the simplest morphology type, single-core, and attempted to fit their intensity radial profiles with a power-law function (see Fig. 3.2). The fit parameters include the radius of a flux-flat region at the centre, $r_{\rm b}$, and the power-law index of a curve beyond that radius, m. The constrained best-fit parameters are statistically significant for 36 sources (one IRw, four IRw, 17 IRb, and 14 HII) and can be used to interpret the structures of the warm envelopes. Firstly, the power-index m ranges from 0.5 to 2.7 across the sub-sample, which is not too far from the power-index of density profiles (i.e. 1 to 2) predicted by theoretical studies (Shu, Adams and Lizano, 1987; Osorio, Lizano and D'Alessio, 1999) and shown by observational studies (Zhang and Li, 2017; Csengeri, Bontemps et al., 2017) for star-forming regions and molecular structures. We discovered that the ^{13}CO (6–5) radial profiles of HII sources are statistically steeper than those of IRb ones, implying the changes in density and/or temperature distributions between the two groups. Secondly, the break radius $r_{\rm b}$ was found to vary between 0.02 pc and 0.44 pc, and tends to increase with evolution similar to m. While the physical nature of the flux-flat region associated with $r_{\rm b}$ is unclear, a plausible scenario is fragmentation on small scales.

To compare the distribution of warm envelopes with that of colder materials, we performed power-law fitting for the radial profiles of Hi-GAL 160 μm maps. At the radii where both the ^{13}CO (6–5) and 160 μm continuum emissions were probed, we found that the power-law indices from the radial profiles of both tracers correlate with each other, and the 160 μm profiles are generally steeper. The offsets between the power-law indices of the two tracers suggest that they probe different physical conditions or processes. Alternatively, it could be that they have different dependencies on temperature and density.

The M_1 maps of the warm envelopes reveal several forms of velocity gradient, such as linear, radial, hour-glass, and outflow-like. This diversity of gradient types suggests that different processes could be driving the warm gas in the envelopes. The warm gas kinematics at each envelope was quantified by an MVG fit (see Fig. 3.3). We found that the velocity fields at 41 envelopes (one 70w, 5 IRw, 21 IRb,

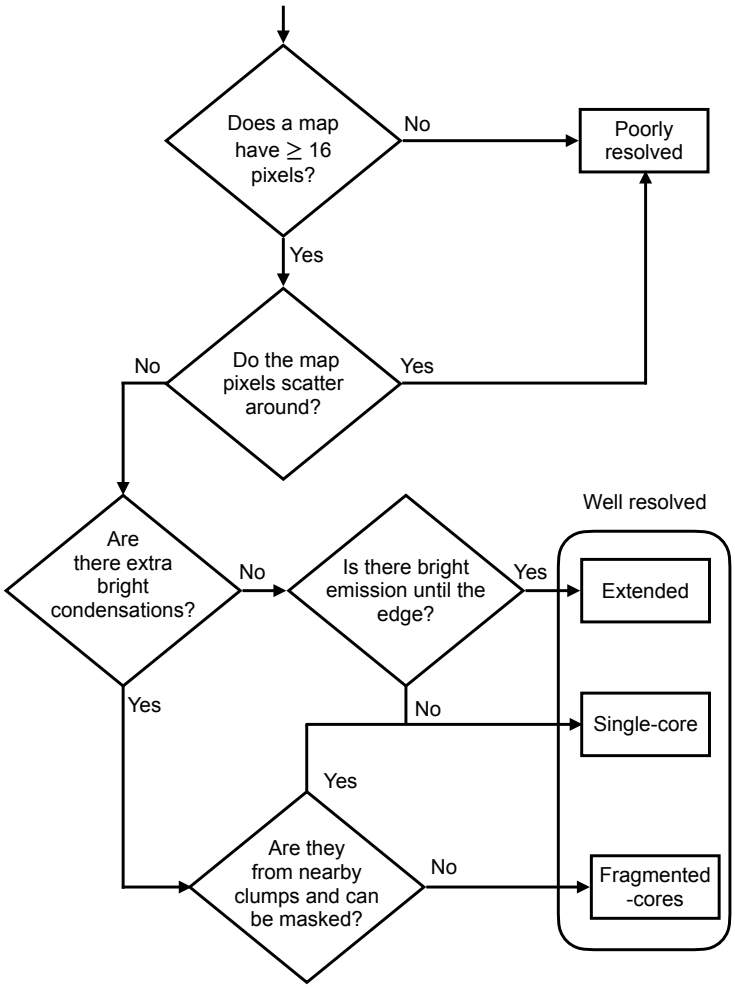

Figure 3.1: Classification diagram of our ^{13}CO (6–5) M_0 maps. Maps that have less than 16 pixels, which show line detection in each, are considered 'poorly resolved'. The combined area of 16 pixels, as defined by this threshold, is equivalent to the coverage of four telescope beams. If there are more than 16 pixels on a map, but they are scattered over the mapping area instead of clustering in a region, the map is also said to be poorly resolved. Those that satisfy those two criteria are considered well resolved and are further classified. The well-resolved sources that show only one bright condensation, but the regions of bright emission continue until the edges of the maps, are categorised as 'extended'. Otherwise, the maps are considered 'single-core'. If there is more than one bright condensation on a map, but the extra ones are likely from nearby clumps and could be masked out, the map is also classified as single-core. If all the bright condensations appear to be part of a clump and masking is not possible, the map is classified as 'fragmented-cores'. Taken from Hoang, M.-Y. Lee et al. (2025).

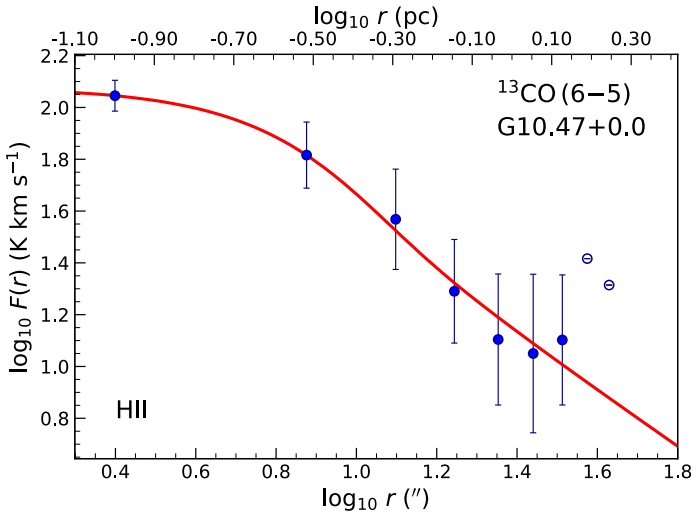

Figure 3.2: Radial profile derived from the ^{13}CO (6–5) M_0 map of an example source G10.47+0.0. The radial points of the profile are shown with the filled blue circles, while the empty circles mark large radii with insufficient numbers of pixels. The red solid line is the best fit with a power-law function.

and 14 HII) have significant gradients, meaning that the fitted velocity gradient is less likely by chance. The values of MVG magnitudes, $\mathcal{G}$, ranges from 1 km s^{-1} pc^{-1} to 8 km s^{-1} pc^{-1}. It is noteworthy that the distribution of $\mathcal{G}$ is similar between the IRw, IRb, and HII groups, implying that the strength of the velocity gradients is independent of the evolutionary stages of the envelopes.

The ^{13}CO (6–5) MVG direction alone could not provide much information and was first put in comparison with the directions of outflows launched from YSOs from small scales. The outflows are probed by high-velocity CO (6–5) emission (Navarete et al., 2019). In principle, if the the velocity gradient across the envelope is perpendicular to the outflow, one may conclude that the envelope is rotating about the outflow axis. If the velocity gradient is parallel to the outflow, it is likely that the gradient is driven by outflow entrainment. In total, we were able to compare the observed velocity gradients with the outflows for 22 sources (one 70w, three IRw, twelve IRb, and six HII) where ^{13}CO (6–5) MVG is significant and CO (6–5)-traced outflows is simple and clear (Navarete et al., in preparation). The angular offset, however, is tilted towards neither perpendicular nor parallel scenario in all evolutionary stages.

In another attempt to investigate the warm envelope kinematics, we derived MVG from ^{13}CO (2–1) data obtained from the SEDIGISM survey (Schuller, Urquhart et al., 2021). The low-J transition of ^{13}CO molecules probes gas which is cooler than the gas in the warm envelopes. These layers of cool gas are likely less affected by stellar feedback, thereby possibly retaining the kinematics of the original clumps. In a sub-sample of 23 clumps (two IRw, twelve IRb, and nine HII) that show significant MVGs in both ^{13}CO (2–1) and ^{13}CO (6–5) maps, 13 clumps show comparable MVG directions (i.e. angular offset less than 45 degrees), while the remaining 10 clumps do not. This behaviour was observed across the evolutionary groups. We found that the ^{13}CO (2–1) MVGs typically have lower magnitudes than the ^{13}CO (6–5) MVGs, which is likely due to the different beam sizes between the two data sets. Finally, we closely examined 15 sources that possess kinematic information from all three CO and ^{13}CO transitions, and were able to determine the origins of the envelope kinematics

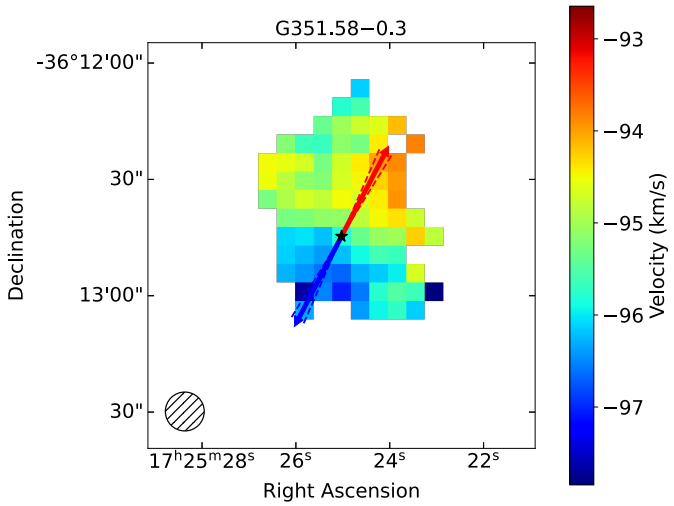

Figure 3.3: M_1 map of an example source G351.58−0.3. The red and blue arrows indicate the direction of the fitted MVG, and the dashed lines showcase the directional uncertainty from the fit. The black star marks the location where the integrated intensity reaches its peak. The hatched circle at the bottom left shows the size of the telescope beam.

for only seven clumps. Even in this small subset of seven cases, the origins show a high degree of diversity. Four clumps show a decouple between the kinematics of the envelopes and the gas on clump scales. Three of them show the signs of envelope entrainment, while one seems to have envelope rotation about the outflow axis. Additionally, the gas in the envelopes and the gas on clump scales are likely rotating together about the outflow axes for two sources. The kinematics of the envelope at the last star-forming region is influenced only by the surrounding clump with no obvious indication of outflow impact.

Understanding the excitation of the ^{13}CO (6–5) transition at warm envelopes around massive YSOs is essential to connect star formation activities to the observed properties of the envelopes. Several radiative and mechanical feedback processes have been discussed in the literature about their ability to excite mid-J CO and ^{13}CO emission around low-mass protostars. This includes passively heated envelopes, UV-heated cavity outflow walls, and outflows (van Kempen, van Dishoeck, Güsten, Kristensen, Schilke, Hogerheijde, Boland, Menten et al., 2009; van Kempen, van Dishoeck, Güsten, Kristensen, Schilke, Hogerheijde, Boland, Nefs et al., 2009; Yıldız, Kristensen, van Dishoeck, Belloche et al., 2012). To explore the efficiency of passive heating at the dense gas envelopes around massive YSOs, one needs to perform dedicated modelling of both gas and dust emission, similar to those performed at the low-mass regime (e.g. Jørgensen, Schöier and van Dishoeck, 2002; Kristensen, van Dishoeck, Bergin et al., 2012; Yıldız, Kristensen, van Dishoeck, Belloche et al., 2012). As for UV-heated gas, PDRs have been observed towards several massive YSOs and have been shown to be able to excite mid-J CO and ^{13}CO lines (Leurini, Wyrowski, Herpin et al., 2013). Finally, as for the roles of outflows, while dedicated modelling to reproduce mid-J ^{13}CO emission from shocked gas in outflows is lacking, the observed line profiles of low- (A. Y. Yang, Thompson et al., 2018) and mid-J ^{13}CO (this work) transitions show the signs of wing emission, suggesting that outflows could entrain and excite ^{13}CO-traced dense gas at massive star-forming regions.

3.5 Conclusions and summary

In summary, our work demonstrated that ^{13}CO (6–5) is ubiquitous in high-mass star-forming regions, and the properties of the emission are correlated with the stages of the star-forming process, indicating a link between the excitation of the line and star formation. The morphology of the warm gas envelopes traced by ^{13}CO (6–5) emission is simple at the majority of our sources, and single power-law functions can reasonably well describe the gas radial distributions. It is noteworthy that the power-law index increases at the most evolved group (HII) compared to the less evolved one (IRb), which could be because of the enhancement of temperature and/or density at the central parts of the envelopes. The kinematics of the warm gas envelopes shows several forms, suggesting that different processes may be responsible for driving the gas. The majority of the observed envelopes exhibit significant linear velocity gradients; however, the origins of these gradients remain unclear for many sources. Further investigations are needed to fully understand the excitation and kinematics of warm gas envelopes at high-mass star-forming regions.

In the next chapter, we extend our research to characterising other tracers of the warm envelopes, high-J CO lines. These lines often contain outflow information in their high-velocity emission, so properties of outflows are also studied.

CHAPTER 4

Velocity-resolved high-J CO emission from massive star-forming clumps

This chapter summarises the content of the article titled **"Velocity-resolved high-J CO emission from massive star-forming clumps"** published in the Astronomy and Astrophysics journal by the following authors:

Thanh Dat Hoang, Agata Karska, Min-Young Lee, Friedrich Wyrowski, Le Ngoc Tram, Aiyuan Yang, and Karl M. Menten
2023, A&A, 679, A121

The full version of the article can be found in Appendix B or from the following link: https://doi.org/10.1051/0004-6361/202347163.

4.1 Context

High-mass stars provide a substantial energy budget for galaxy evolution throughout their entire life (e.g. Kennicutt, 2005). From the very beginning, star formation activities would start to release a significant amount of energy and momentum to the surrounding environment through outflows, which results in substantial gas cooling via far-infrared emission, especially CO rotational transitions (Pilbratt et al., 2010). Outflows also play an essential role in regulating star formation across multiple spatial scales, in both low- and high-mass star-forming regions. For example, at core scales, the envelope dissipation due to outflow entrainment and the mass loss through outflows reduce core-to-star formation efficiency (Krumholz et al., 2014). On clump scales, the momentum carried by outflows induces turbulence, which provides support against gravitational collapse (Frank et al., 2014). Therefore, it is essential to understand the characteristics of emission from outflows and the physical conditions that give rise to them.

Velocity-resolved line profiles of CO transitions are valuable tools for probing different processes and components at massive star-forming regions, especially outflows due to the emission from their high-velocity gas, which results in wing features on CO line profiles. In previous studies, low-J CO ($J_{\rm up} \lesssim 5$) transitions have been used to probe outflows at many star-forming regions (A. Y. Yang, Thompson et al., 2018; A. Y. Yang, Urquhart et al., 2022). As high-J CO ($J_{\rm up} \gtrsim 10$) transitions

have higher upper energy levels, using their observations help probe denser and warmer gas regions and the outflows that arise in them. This approach has been done towards many low-mass protostars by San José-García, Mottram, Kristensen et al., 2013; Yıldız, Kristensen, van Dishoeck, San José-García et al., 2013 and a few high-mass objects such as W3 IRS5 (San José-García, Mottram, Kristensen et al., 2013), AFGL 2591 (Kaźmierczak-Barthel et al., 2014), Orion KL, Orion S, Sgr B*, and W49N (Indriolo et al., 2017). However, it is necessary to extend the approach to a larger number of massive YSOs so that we can examine the outflow evolution along the star formation sequence and assess the outflow's impacts on the surrounding environments.

4.2 Aims

High-J CO lines are one of the vital tracers for the warm envelopes studies in this thesis. Our aim in this project is to characterise high-J CO emission towards a sample of high-mass star-forming regions with high spectral resolution observations. From the velocity-resolved line profiles, we expect to be able to isolate outflow emission from that of gas envelopes, which enables us to constrain the physical conditions required to give rise to the observed lines. In particular, this project aims to constrain conditions in outflow gas while conditions in the envelopes will be probed in Chapter 5 with the help of other CO transitions.

4.3 Methods

Observing high-J CO lines with rest frequencies above 1000 GHz is challenging for ground observatories due to high degrees of interference from the absorption of the Earth's atmosphere. Thanks to the unique conditions provided by SOFIA and the GREAT/upGREAT receivers onboard (see Section 2.3.2), we obtained the spectra of CO (11–10) and CO (16–15) lines towards a sample of 13 high-mass star-forming clumps in the Top100 sample. Additionally, CO (13–12) spectra were collected for two clumps using the 4GREAT receiver. The angular resolutions of our data vary from $14''$ to $20''$ depending on the line frequencies, and these beam sizes correspond to spatial scales of ~0.1 to 0.8 pc for our sources.

In order to decompose the observed line profiles into different physical components, such as gas envelopes and outflows, we employed the method by A. Y. Yang, Thompson et al. (2018). In this method, the line profile of a rare CO isotopologue transition is considered as a proxy for the envelope emission, and it is used to mimic the contribution of the envelope to the high-J CO emission. The residual remaining after subtracting the envelope contribution from the high-J CO line profiles is considered outflow emission if it has a peak intensity greater than three times the spectral noise. In this work, the models of envelope emission were obtained from the $C^{18}O$ (9–8) line for eight sources, the ^{13}CO (10–9) line for three sources, and the $C^{18}O$ (6–5) and ^{13}CO (6–5) lines for one source each. After the decomposition, the wing emission associated with outflows was examined to explore their contribution to total emission. Furthermore, the ratio of the CO (16–15) wing to the CO (11–10) wing emission, an indication of temperature under the assumption that line wing is optically thin and thermalised, was examined at different velocity channels.

Since the ISM regions where outflows propagate have relatively low densities, it is unclear whether an assumption of LTE could apply or not. Therefore, we investigated the excitation of high-J CO wing emission under both assumptions: LTE and non-LTE. In the first approach, the excitation temperatures

were derived separately for the emission of the whole line profiles and the emission of the wings only, using rotational diagrams. In the second approach, we used the radiative transfer model RADEX (F. F. S. van der Tak, Black et al., 2007) with varying kinetic temperatures and densities to find the conditions that match the observed properties of wing emission in CO (6–5), (11–10), and (16–15). In our models, the line widths of all lines were set at 19 km s^{-1}, which is based on the widths of the observed CO (6–5) lines (Navarete et al., 2019) towards clumps in the Top100 sample .

4.4 Results

The CO (11–10) line was detected above three times the spectral noise (σ) levels towards all sources in our sample. In contrast, the CO (16–15) line was detected towards twelve, two of which are only above 2σ levels. Detection of CO (13–12) emission was confirmed towards two observed sources. The profiles of the detected transitions generally exhibit broad wings (see Fig. 4.1), hinting at the contribution from outflows to high-J CO emission. The median of the full width at zero power is 45 km s^{-1} for the CO (11–10) line and 33 km s^{-1} for the CO (16–15) line. The luminosities of the CO (11–10) and CO (16–15) lines show weak correlations with the clump masses (i.e. Pearson correlation coefficients of 0.63 and 0.66, respectively). On the other hand, they show stronger correlations with the bolometric luminosities (i.e. Pearson correlation coefficients of 0.85 and 0.95, respectively). While the line luminosities show correlations with the clump properties, no evolutionary trend was observed, suggesting that similar physical mechanisms are responsible for high-J CO excitation across the different stages of high-mass star formation. It is noteworthy that the correlation between the CO (16–15) line luminosity and the bolometric luminosity extends to the low-mass protostars in literature, suggesting that similar processes may be responsible for the excitation of high-J CO emission across a wide range of physical scales.

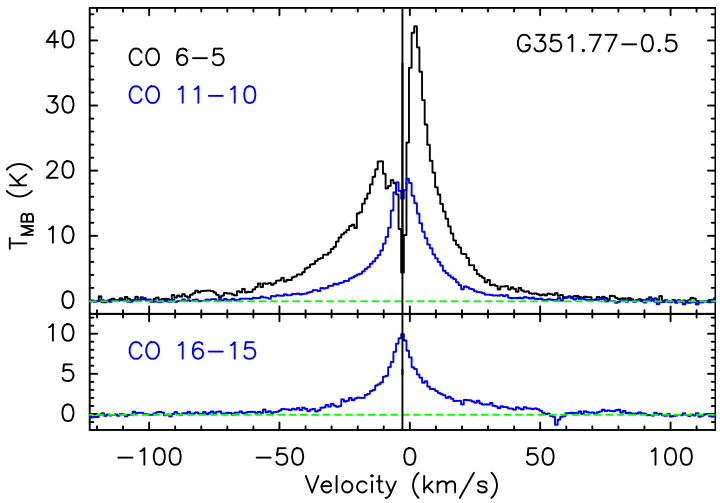

Figure 4.1: Line profiles of CO (11–10) and CO (16–15) transitions towards a source in our sample, G351.77−0.5. In addition, the CO (6–5) line profile is overlaid for a comparison. The source velocity is indicated as a black vertical line. Taken from Hoang, Karska et al. (2023).

The decomposition of the line profiles revealed wing emission that is likely associated with outflows from our sources. Specifically, we were able to extract wing emission in CO (11–10) towards twelve

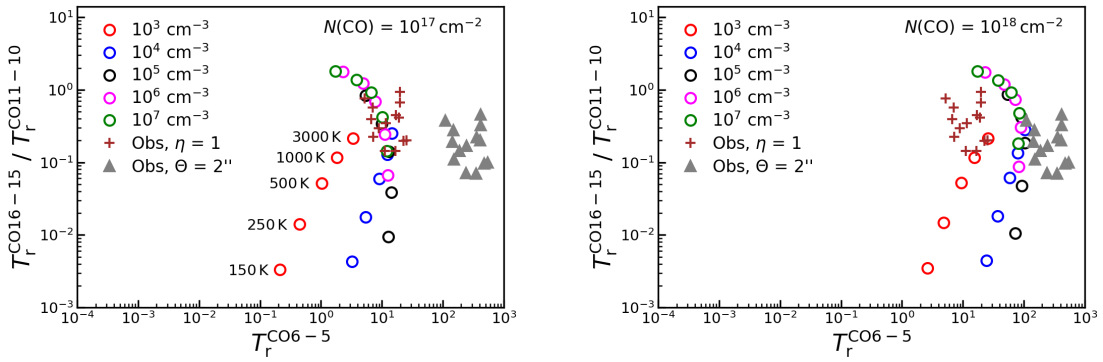

Figure 4.2: Comparison of CO excitation conditions from RADEX models with observations. The models are at two different CO column densities, N(CO), of 10^{17} (left panel) and 10^{18} cm^{-2} (right panel). On each panel, values from RADEX models are shown by empty circles, and their colours correspond to different hydrogen volume densities, n_{H_2}, between 10^3 and 10^7 cm^{-3}. For each volume density level, five temperatures: 150, 250, 500, 1000, and 3000 K were sampled. The crossed symbols show values obtained from observations with an assumed beam filling factor of 1. Observations assuming a tiny source of 2″ are shown with triangles, corresponding to an extreme case of small beam filling factors. Taken from Hoang, Karska et al. (2023).

sources and in CO (16–15) towards eight sources. It is noteworthy to mention that Urquhart, Figura et al. (2019) and Csengeri, Leurini et al. (2016) detected line wing in SiO (2−1) emission towards around half of our sources. Those that show SiO non-detection actually exhibit high-J CO wings, suggesting that the excitation of wing emission in SiO and high-J CO lines might be partly different. The relative contribution from the wings to the total integrated intensities ranges from 28% to 76% for both CO (11–10) and CO (16–15) line. No trend was found between the evolutionary groups in terms of this wing fraction. However, it was predicted that the wing fraction may increase with the rotational level of the CO lines, as indicated by a result from Karska, Herpin et al. (2014). We observed this trend at four out of eight sources in our sample. The ratio CO (16–15)/CO (11–10) is an indicator for the kinematic temperature for outflowing gas. With velocity-resolved line profiles, one can estimate this line ratio at different velocity offsets from the source velocity. Our examination reveals an increase in the line ratio with velocity at a few sources, suggesting a rise in temperature at the regions where gas is escaping at high speeds.

Assuming the LTE condition, we produced rotational diagrams from CO (11–10) and CO (16–15) emission to estimate the rotational temperature T_{rot}. The CO (13–12) flux was also used for the rotational diagrams of two sources that show detection of the line. In total, T_{rot} ranges from 100 K to 220 K for both the total integrated emission and the wing emission. Logarithm of the total number of emitting molecules, $\log_{10}\mathcal{N}_{tot}$, varies between 51.7 and 53.6, which is consistent with an average value for high-mass protostars (i.e. 52.4(0.1)±0.5) measured by Karska, Herpin et al. (2014) using *Herschel*/PACS data. We note that at the source G34.26+0.15, T_{rot} is ~150 K which is much lower than the value obtained using CO lines with J_u from 14 to 30 (~365 K, Karska, Herpin et al., 2014). The discrepancy between the two calculations may arise from the use of the CO (11–10) line in our work, which traces cooler gas than the higher-J CO lines.

The LTE assumption may not hold in the low-density regions of outflows, so non-LTE modelling with RADEX is needed to constrain the physical conditions of outflowing gas giving rise to the observed high-J CO wing emission. Our RADEX models sample the kinematic temperature T_{kin} in

the range of 150–3000 K, hydrogen volume density $n_{\mathrm{H_2}}$ in the range of 10^3–10^7 cm^{-3}, and CO column density N(CO) of 10^{17} and 10^{18} cm^{-2} (see Fig. 4.2). For the comparison between the observations and the RADEX models, the peak of the observed wing emission and the peak intensity from RADEX were used. In Fig. 4.2, one can see that the area, where observations and models match each other, can be described by two scenarios of temperature and density: (i) low density (i.e. 10^3–10^4 cm^{-3}) and high temperature (i.e. above 1000 K) and (ii) high density (i.e. 10^5–10^7 cm^{-3}) and moderate temperature between 150 K and 500 K. In closer inspections, the scenario (ii) matches the observations better as it can reproduce the data points of all sources. In contrast, the scenario (i) would require unreasonably high temperatures (above 3000 K).

4.5 Conclusions

In summary, the high spectral resolution data from SOFIA/GREAT provide an opportunity to investigate the components of high-J CO lines and the excitation mechanisms behind them. Our study showed the detection of the CO (11–10) and CO (16–15) lines towards several high-mass star-forming clumps across different evolutionary stages. We found that the line profiles exhibit broad wing features, which are typically associated with outflows. Using a decomposition method, we were able to extract wing emission for the majority of our sample. Interestingly, we found no dependence of the properties of the wing emission on evolution, suggesting that the mass accretion and ejection are active throughout the entire lifetime of massive star-forming clumps. Under the LTE assumption, the excitation temperature for wing emission is determined to be in the range of ~100–220 K. This range of temperature is in agreement with high-density and moderate-temperature solutions from non-LTE RADEX modelling, which can reproduce all of our observations.

In the next chapter, we proceed to constrain physical conditions in the warm envelopes using non-LTE modelling with several CO transitions, including those studied in Chapter 3 and this chapter.

CHAPTER 5

Non-LTE modelling of CO transitions with RADEX

5.1 Introduction

High-mass stars are crucial to the evolution of galaxies as they are one of the main drivers of their energy budget and chemical inventory. Understanding the formation of these objects thus becomes relevant and is at the centre of many observational studies in the last decade. A major campaign was the ATLASGAL survey, which mapped the entire inner part of the Milky Way to identify thousands of potential high-mass star-forming regions (see Section 1.3). Follow-up studies towards the Top100 sample that includes ∼100 brightest ATLASGAL sources in four different evolutionary stages were done to characterise different aspects of the massive YSOs, such as dust continuum emission (König et al., 2017), gas traced by neutral carbon ([C I]) M. .-. Lee et al. 2022, temperature structure and evolution (Giannetti, Leurini et al., 2017), and warm inner envelopes (Hoang, M.-Y. Lee et al., 2025).

Carbon Monoxide (CO) is a valuable tracer to probe different ISM regions, especially massive star-forming sites, thanks to its high abundance in the ISM, only second to the Hydrogen molecule (H_2) (see Section 1.2). Combinations of multiple CO rotational transitions are often used to determine excitation temperatures, T_{ex}, under LTE conditions. For example, Karska, Herczeg et al. (2013) and Karska, Herpin et al. (2014) used a series of CO transitions from $J_{up} = 14$ to $J_{up} = 49$ to determine T_{ex} for 18 low-mass and 10 high-mass star-forming regions, respectively. When the LTE condition may not hold and non-LTE radiative transfer modellings are needed, emission of multiple CO lines is also often used to constrain physical parameters of the emitting gas. Peng, Wyrowski, L. A. Zapata et al. (2012) used peak intensity of the CO (6–5) line and ratio of the ^{13}CO (8–7) and the C^{18}O (6–5) line peaks to constrain kinetic temperature, T_{kin}, and Hydrogen density, $n(H_2)$, for different regions in the star-forming complex Orion Molecular Cloud 1 (OMC-1).

We aim to characterise the physical conditions of the warm envelopes around Top100 sources and investigate the heating mechanisms in these envelopes. To perform non-LTE modelling, we used multiple CO line observations towards a small part of the Top100 sample, which are taken from Navarete et al. (2019), Hoang, Karska et al. (2023) and Hoang, M.-Y. Lee et al. (2025). This work is organised as follows: in Section 5.2, we describe the six studied sources and their observations. Section 5.3 and Section 5.4 present the procedure of our RADEX modelling and our results, respectively, while Section 5.5 discusses the results. Finally, a summary and conclusions are

given in Section 5.6.

5.2 Observations

5.2.1 Source sample

For this study, six high-mass star-forming clumps were selected from the Top100 sample. The sources were chosen based on the availability of CO molecular line observations (see Section 5.2.2), which facilitates our modelling. The sources have the bolometric luminosities spanning over two orders of magnitude between $3.2 \times 10^3\ L_\odot$ to $4.6 \times 10^5\ L_\odot$ and total masses ranging from $3.7 \times 10^2\ M_\odot$ to $2.3 \times 10^3\ M_\odot$. Most of the sources are located within ~1.3 kpc to ~2.9 kpc from the Earth, except for G351.58−0.4, which is 8 kpc away. All of the clumps are in advanced stages of high-mass star formation. Four are at the high-mass protostellar stage (i.e. IRb) in which active star-formation gives rise to strong IR emission at 8 μm and 24 μm. Two are at the most evolved stage (i.e. HII) where intense radiation from YSOs ionises materials in the close vicinity to form HII regions. The properties of the target clumps are presented in detail in Table 5.1.

Table 5.1: Summary of source properties

No.	Source	$V_{\rm lsr}$ (km s^{-1})	D (kpc)	$L_{\rm bol}$ ($L_\odot$)	$M_{\rm clump}$ ($M_\odot$)	$D_{\rm GC}$ (kpc)	Type$^{(*)}$
1	G12.81−0.2	34.6	2.6	2.5×10^5	1.9×10^3	6.2	HII
2	G34.40−0.2	57.1	2.9	3.2×10^3	7.9×10^2	7.2	HII
3	G35.20−0.7	33.5	2.2	2.4×10^4	4.6×10^2	6.8	IRb
4	G351.16+0.7	-6.0	1.3	8.8×10^3	1.2×10^3	6.7	IRb
5	G351.25+0.7	-2.8	1.3	4.9×10^4	3.7×10^2	6.7	IRb
6	G351.58−0.4	-95.6	8.0	4.6×10^5	2.3×10^3	2.0	IRb

Note: $^{(*)}$: Source classification from König et al. (2017), which refers to the IR-bright (IRb) and HII regions (HII) class.

5.2.2 Molecular lines

For this study, a collection of emission lines of CO and its isotopologues is used. The data include observations from previously published works and those conducted newly. A summary of the employed molecular lines is presented in Table 5.2.

The observations of several low- and mid-J CO lines were conducted using the APEX telescope. Navarete et al. (2019) obtained $80'' \times 80''$ maps of CO (6–5) emission towards most of the sources in the Top100 sample using the CHAMP$^+$ receiver. Hoang, M.-Y. Lee et al. (2025) mapped of ^{13}CO (6–5), ^{13}CO (8–7), and C^{18}O (6–5) emission in areas of $80'' \times 80''$ towards the same sources with CHAMP$^+$ also. Additionally, we obtained $80'' \times 80''$ maps of C^{18}O (3–2) emission towards six sources in our sample using the LASMA receiver in the Summer of 2019. Similar to CHAMP$^+$, LASMA is an array of seven pixels arranged in a hexagonal shape, allowing fast mapping. The spectra were obtained by subtracting a third-order baseline or less, converted to the main-beam temperature,

$T_{\rm MB}$ scale, using a forward efficiency of 0.95 and a main-beam efficiency of 0.73. Afterwards, data cubes were produced using the `XY_MAP` gridding routine in CLASS, a package to process spectral data. The final $C^{18}O$ (3–2) data cubes have angular resolution of 20″. The data of the low- and mid-J CO lines obtained with APEX have various angular resolutions between 7″ and 18″ (see Table 5.2). To remove the influence of this variation in beam size, we smoothed all the cubes to a similar resolution of 20″. Single spectra from the central positions of the maps are then extracted for our usage. The peak main-beam brightness temperatures of those spectra are summarised in Table 5.3.

The spectra of higher-J CO lines were obtained by either the airborne observatory, SOFIA, or the space telescope, *Herschel*. We used the CO (11–10), CO (13–12), and CO (16–15) data from Hoang, Karska et al. (2023), in which CO (11–10) and CO (16–15) spectra are available for all the sources in our sample. In contrast, CO (13–12) spectra are only available for two (see Table 5.3). The observations of ^{13}CO (10–9) and $C^{18}O$ (9–8) emission lines were conducted with the HIFI receiver onboard *Herschel* under the project 'A Water survey of massive star-forming clumps in the inner Galaxy' (project ID OT2_fwyrowsk_3, PI: F. Wyrowski). The reduced spectra of the two transitions are available for all sources in our sample and were collected from Hoang, Karska et al. (2023). The CO data observed with the SOFIA and *Herschel* telescopes here are single-pointing spectra, with beam sizes varying between 16″ and 23″.

In summary, we extracted a collection of single spectra of different mid- and high-J CO lines from the central positions of our sources. The spectra have spectral resolutions ranging from 0.32 km s^{-1} to 1.0 km s^{-1} and represents emission within different beams between 16″ and 23″ (see Table 5.2). The small difference in beam sizes ensures that the extracted spectra mostly probe a similar area of the sky and can therefore be used together to constrain the physical properties of sources in our sample.

Table 5.2: Parameters of the observational data

Line	Frequency$^{(a)}$ (GHz)	$E_{\rm u}/k_{\rm B}{}^{(a)}$ (K)	$A_{\rm u}{}^{(a)}$ (10^{-5} s^{-1})	$g_{\rm u}{}^{(a)}$	Beam$^{(b)}$ (″)	$\Delta V^{(b)}$ (km s^{-1})	Observatory$^{(c)}$
CO (6–5)	691.473076	116.16	2.1	13	9	0.32	APEX/CHAMP$^+$
CO (11–10)	1267.014486	364.97	13.4	23	23	1.00	SOFIA/GREAT
CO (13–12)	1496.922909	503.13	22.0	27	19	1.00	SOFIA/GREAT
CO (16–15)	1841.345506	751.72	40.5	33	16	1.00	SOFIA/GREAT
^{13}CO (6–5)	661.067277	111.05	1.9	13	9	0.35	APEX/CHAMP$^+$
^{13}CO (8–7)	881.272809	190.36	4.5	17	7	0.35	APEX/CHAMP$^+$
^{13}CO (10–9)	1101.349597	290.79	8.8	21	19	0.35	*Herschel*/HIFI
$C^{18}O$ (3–2)	329.330553	31.61	0.2	7	18	0.35	APEX/LASMA
$C^{18}O$ (6–5)	658.553278	110.63	1.9	13	9	0.35	APEX/CHAMP$^+$
$C^{18}O$ (9–8)	987.560382	237.03	6.4	19	22	0.35	*Herschel*/HIFI

Note: $^{(a)}$Molecular data adopted from the Leiden Atomic and Molecular Database (LAMDA; Schöier et al. 2005). $E_{\rm u}$ is the energy of the upper level, $k_{\rm B}$ is the Boltzmann constant, $A_{\rm u}$ is the Einstein A coefficient, and $g_{\rm u}$ is the statistical weight of the upper level. $^{(b)}$Beam is the original angular resolution (FWHM beam width) and ΔV is the smoothed spectral resolution. $^{(c)}$The observatory and receiver used to carry out the observations.

Table 5.3: Summary of peak main-beam temperatures (in Kelvin) of the CO transitions towards our sample.

No.	Source	^{12}CO				^{13}CO			C^{18}O		
		J = 6–5	11–10	13–12	16–15	J = 6–5	8–7	10–9	J = 3–2	6–5	9–8
1	G12.81−0.2	58.3	21.5	12.6	13.4	27.3	21.8	14.1	12.6	15.7	3.32
		(0.2)	(0.1)	(0.2)	(0.2)	(0.3)	(0.8)	(0.1)	(0.1)	(0.2)	(0.05)
2	G34.40+0.2	27.8	5.1	–	0.8	8.7	4.1	0.86	3.9	1.6	0.18
		(0.2)	(0.2)	–	(0.2)	(0.2)	(0.6)	(0.08)	(0.1)	(0.1)	(0.05)
3	G35.20−0.7	38.0	12.3	–	3.8	14.0	5.5	2.57	4.5	2.9	0.39
		(0.1)	(0.2)	–	(0.2)	(0.3)	(0.8)	(0.08)	(0.1)	(0.2)	(0.04)
4	G351.16+0.7	58.5	4.93	–	2.41	30.4	17	5.51	10.9	9.5	1.63
		(0.2)	(0.05)	–	(0.08)	(0.4)	(1)	(0.07)	(0.1)	(0.2)	(0.06)
5	G351.25+0.6	80.1	34.1	14.4	15.4	42.9	28	12.73	18.5	18.3	2.79
		(0.2)	(0.1)	(0.1)	(0.2)	(0.4)	(1)	(0.08)	(0.1)	(0.2)	(0.06)
6	G351.58−0.3	20.8	5.6	–	1.7	13.5	6	2.81	10.2	7.1	1.16
		(0.3)	(0.2)	–	(0.2)	(0.4)	(1)	(0.07)	0.1	0.2	(0.05)

Note: The numbers in the round brackets represent peak main-beam temperature uncertainties, derived from the baseline noise.

Table 5.4: Line width for our RADEX models

No.	Source	FWHM ($km\,s^{-1}$)
1	G12.81−0.2	5.6
2	G34.40+0.2	3.7
3	G35.20−0.7	5.6
4	G351.16+0.7	4.5
5	G351.25+0.6	3.9
6	G351.58−0.3	6.1
	median	5.1

5.3 RADEX modelling

The physical conditions of molecular gas, such as $T_{\rm kin}$, $n(H_2)$, and molecular column density, have a profound influence on the intensities of emission lines. In an attempt to constrain the physical conditions of the warm envelopes around massive YSOs, we performed non-LTE modelling with RADEX (F. F. S. van der Tak, Black et al., 2007). For the modelling, we uniformly sampled $T_{\rm kin}$ in logarithm space from 10^1 K to 10^3 K in 50 steps. Similarly, 50 values of $n(H_2)$, ^{13}CO column density, $N(^{13}CO)$, C^{18}O column density, $N(C^{18}O)$, each were sampled between 10^3 and 10^6 cm^{-3}, 10^{16} and 10^{19} cm^{-2}, and 10^{15} and 10^{18} cm^{-2}, respectively. While the observations of high-J transitions from the main CO isotopologue are available for RADEX modelling, we took a conservative approach to exclude them, as it is uncertain whether the contribution from cooler gas envelopes to high-J CO emission is significant. However, observations of high-J CO lines may still be compared to predictions from the best-fit models to explore the excitation of the high-J CO lines. To run the RADEX models, we assumed all CO lines towards a clump share the same intrinsic line width. We adopted the value from Hoang, Karska et al. (2023), who measure the width from an envelope model obtained with an optically thin emission line, which is C^{18}O (9–8) in the cases of sources in our sample. A summary of the line widths used is presented in Table 5.4.

To look for the models that have physical conditions close to those of our envelopes, we compared the ratios of the observed line peaks, $R_{\rm obs}$, with the line ratios from RADEX models, $R_{\rm model}$. The line peaks were used instead of the integrated intensities to avoid the contributions from wing emission to mid- and high-J CO emission, which have been discovered by Hoang, Karska et al. (2023) and Navarete et al. (2019). The RADEX models produce line peaks as emitted from the gas (i.e. in $T_{\rm R}$ scale) while the observed line peaks are in $T_{\rm MB} = T_{\rm R} f(\theta_{\rm s}, \theta_{\rm beam}) = T_{\rm R}\eta$ scale, where $\theta_{\rm s}$ and $\theta_{\rm beam}$ are the source size and the beam size, respectively, and η is beam filling factor. Assuming that the CO lines trace the same envelopes, we can directly compare ratios of the observed line peaks with the line ratios from RADEX as η of different lines would cancel each other out. To constrain the physical properties of the CO-emitting envelopes, we applied the minimum χ^2 method that selects "good" models which have χ^2 less than or equal to $\chi^2_{\rm min} + \Delta\chi^2$, where $\chi^2_{\rm min}$ is the lowest χ^2 from all models. The values of $\Delta\chi^2$ vary depending on the number of parameters in our models and the level of significance. For the estimation of $\Delta\chi^2$, we used the `chi2.ppf()` function from the *scipy.stats* package in Python. With a significant level of 1 σ and four model parameters (i.e. $T_{\rm kin}$, $n(H_2)$, and column densities of ^{13}CO and C^{18}O molecules), the value of $\Delta\chi^2$ is 4.7. We note that from the

selected models, one can calculate η from each transition by dividing the observation by the RADEX prediction. This parameter can be further used to estimate θ_s as following:

$$\theta_s = \theta_{beam}\sqrt{\frac{\eta}{1-\eta}}. \tag{5.1}$$

Initially, we attempted to constrain our RADEX models with five mid- and high-J transitions of rare CO isotopologues: ^{13}CO (6–5), ^{13}CO (8–7), ^{13}CO (10–9), C^{18}O (6–5), and C^{18}O (9–8) (hereafter referred to as the model I setup). In the model I setup, we took a conservative approach not to include the low-J C^{18}O (3–2) transition, as this line has a low excitation energy level (see Table 5.2), and it could be excited by gas not probed by the other mid- and high-J transitions. With five molecular lines, the model I setup gives four independent line ratios, which is equal to the number of the constraining parameters. Therefore, it is inevitable that our collection of constrained models will exhibit degeneracy between the parameters. For this reason, we proceeded to constrain our RADEX models by including the C^{18}O (3–2) line (hereafter referred to as the model II setup), as it could potentially mitigate the effects of parameter degeneracy. As a precautionary step, we assessed whether the C^{18}O (3–2) line probes similar envelope gas as the other constraining lines by comparing its line profiles with that of the C^{18}O (6–5) transition (see Section 5.7.1). At four sources, the line shapes are similar within the low- and mid-J CO lines. At the two other sources, G12.81−0.2 and G351.58−0.3, similarities were observed only in some velocity ranges of the line profiles, while discrepancies appeared in other parts (see Fig. 5.5).

5.4 Results

In this section, we present the results of the model constraining in the two model setups. Spectral line energy distributions (SLEDs) were constructed to examine how well the RADEX models resemble our observations (see Fig. 5.1). For this purpose, at each source, we constructed representative model SLEDs, which use T_{kin}, $n(H_2)$, $N(^{13}CO)$, and $N(C^{18}O)$ from the medians of the constrained physical parameter distributions, derived from the selected models from each setup. Each modelled SLED was scaled to the observation by η estimated from the ratio between an observed line peak and its RADEX prediction. As our RADEX models produce several emission lines which would result in multiple η, the median value was used for the SLED scaling.

Solutions from the model I setup showcase an ability to reproduce our observations relatively well for most sources (see SLEDs in Fig. 5.1 and Section 5.7.2). Fig. 5.2 presents the selected models on the $T_{kin} - n(H_2)$ and $N(^{13}CO) - N(C^{18}O)$ parameter planes, along with the constrained parameter distributions. The parameters are relatively well constrained for G12.81−0.2, G351.16+0.7, and G351.25+0.6, whereas three other sources show lower constraining degrees as their selected models spread over large areas on the parameter planes. As described in Section 5.3, results from the model I setup are expected to suffer from degeneracies due to the limited number of input line ratios, e.g., the degenerate $T_{kin} - n(H_2)$ curves for G34.40+0.2 and G351.58−0.3. For each source, we derived the parameters and their respective variations as the medians and the 68% confidence intervals of the distributions, respectively. The results are presented in Table 5.5. The values of T_{kin} vary between around 100 K to a few hundreds K while the values of $n(H_2)$ are around 10^5 cm^{-3} or lower. The variations of $N(^{13}CO)$ and $N(C^{18}O)$ are around one order of magnitude around 10^{17} and 10^{18} cm^{-2} and around 10^{16} and 10^{17} cm^{-2}, respectively.

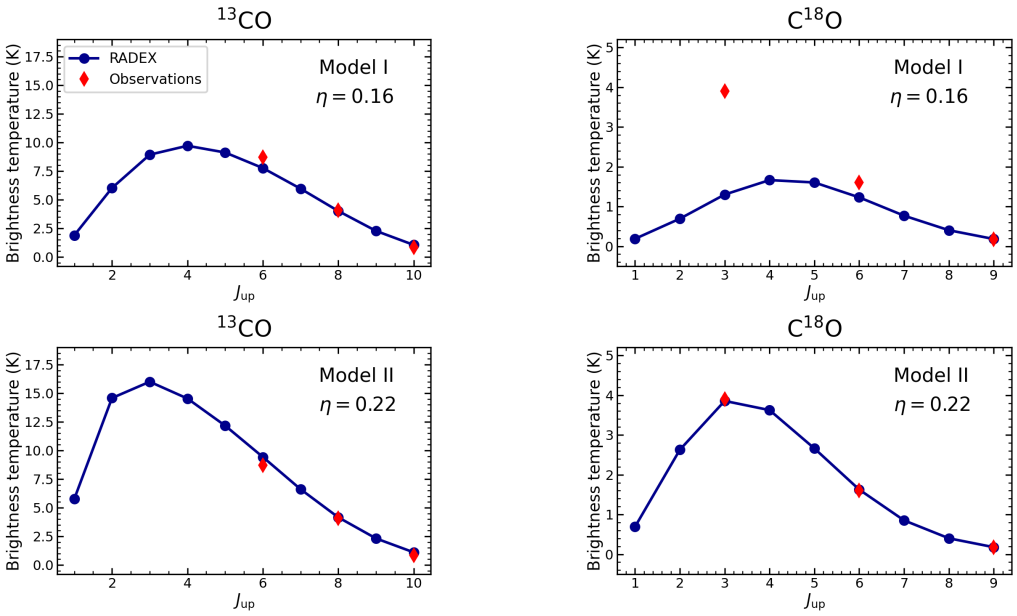

Figure 5.1: The observed and RADEX SLEDs of ^{13}CO and C^{18}O emission for an example source G34.40+0.2. The RADEX models have the physical properties from the medians of the constrained parameter distributions, and their SLEDs were scaled to the T_{MB} unit by the beam filling factor, η, shown on each plot. The scaled RADEX SLEDs are presented by the blue circles, while those from the observations are shown with the red diamonds.

The model II setup uses an additional line ratio and constrains the physical properties more tightly than the model I setup. Fig. 5.1 illustrates a good match between the observations and the predictions from the RADEX models, including the new transition used for the model constraint, C^{18}O (3–2). Similar to the model I setup, we present the parameter distributions and the parameter planes in Fig. 5.3. The improvement in constraining the physical properties can be seen clearly in all sources. For G34.40+0.2 and G35.20−0.7, while the model parameters converge to smaller areas of the parameter spaces, we can still see the effect of degeneracy. The medians of the parameter distributions from the model II setup are within the same ranges as those from the model I setup. The variations, on the other hand, are reduced for most sources, which is likely the result of adding an additional line ratio to the model constraint.

In a previous work by Tang et al. (2018), the authors attempted to measure T_{kin} and $n(H_2)$ in similar regions of our sources using RADEX modelling of formaldehyde (H_2CO), a reliable thermometer and densitometer. Their averaged T_{kin} and $n(H_2)$ for the HII group are 110 K and 1.8×10^6 cm^{-3}, respectively, while the same quantities for the IRb group are 81 K and 1.2×10^6 cm^{-3}. Comparing these numbers with our results from the model II setup in Table 5.5, we found our T_{kin} are significantly higher at three sources, in a similar range at two, and slightly lower at one. As for the constrained $n(H_2)$, our densities are from one to two orders of magnitude lower than the results from Tang et al. (2018). This comparison suggests that our CO lines are likely more sensitive to a warmer but less dense gas than the gas probed by the H_2CO emission.

The estimated beam filling factors are less than 1 in most cases (see Table 5.5 and Section 5.7.3), which is reasonable and further assures the plausibility of our models. Among the sources, the variation

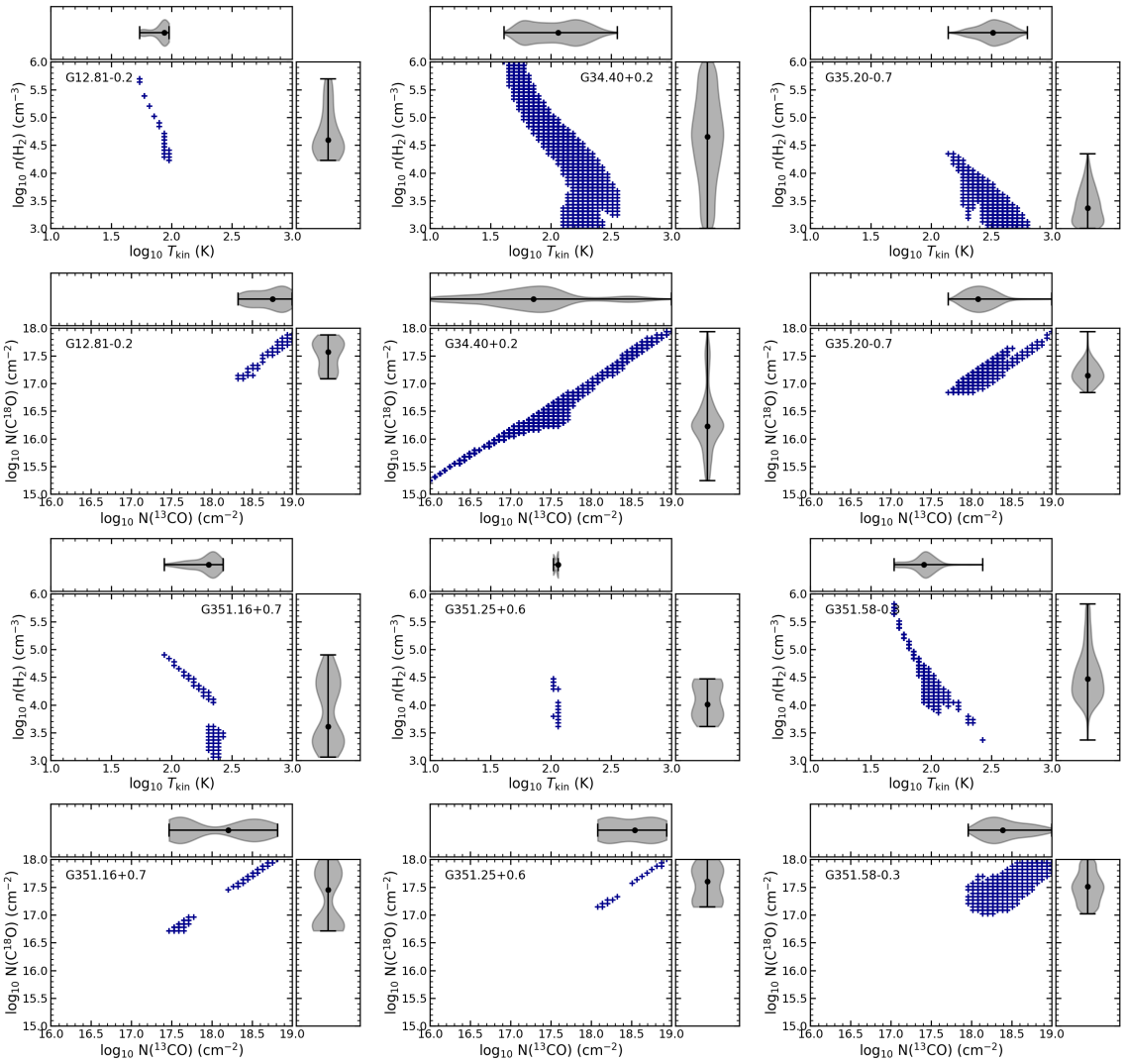

Figure 5.2: The presentation of RADEX models (in blue crosses), selected from the minimum χ^2 method, on the $T_{\rm kin} - n(\rm H_2)$ and $N(^{13}\rm CO) - N(\rm C^{18}O)$ parameter planes. The grey shades in the side panels of each plot present the respective parameter distributions. The median of each distribution is marked with a black circle. The source names are displayed directly on the plots. The results are obtained from the model I setup.

of η is also not significant between the lines. Given a representative beam of 20″, a sample-median η of 0.32 from the model II setup, a representative envelope would have a size of ∼13.7″, which is equivalent to ∼0.16 pc at a median distance of 2.4 kpc. This envelope is on a similar scale to the observed pre-stellar core candidates or the theoretical envelope feeding material to the stellar objects (Padoan et al., 2020, and references therein).

In summary, our RADEX modelling has shown that a single temperature component is capable of producing emission of rare CO isotopologues from warm inner envelopes around massive YSOs. The model II setup, which uses an additional line ratio than the model I setup, shows better constrained results and reduces degeneracy for a few sources.

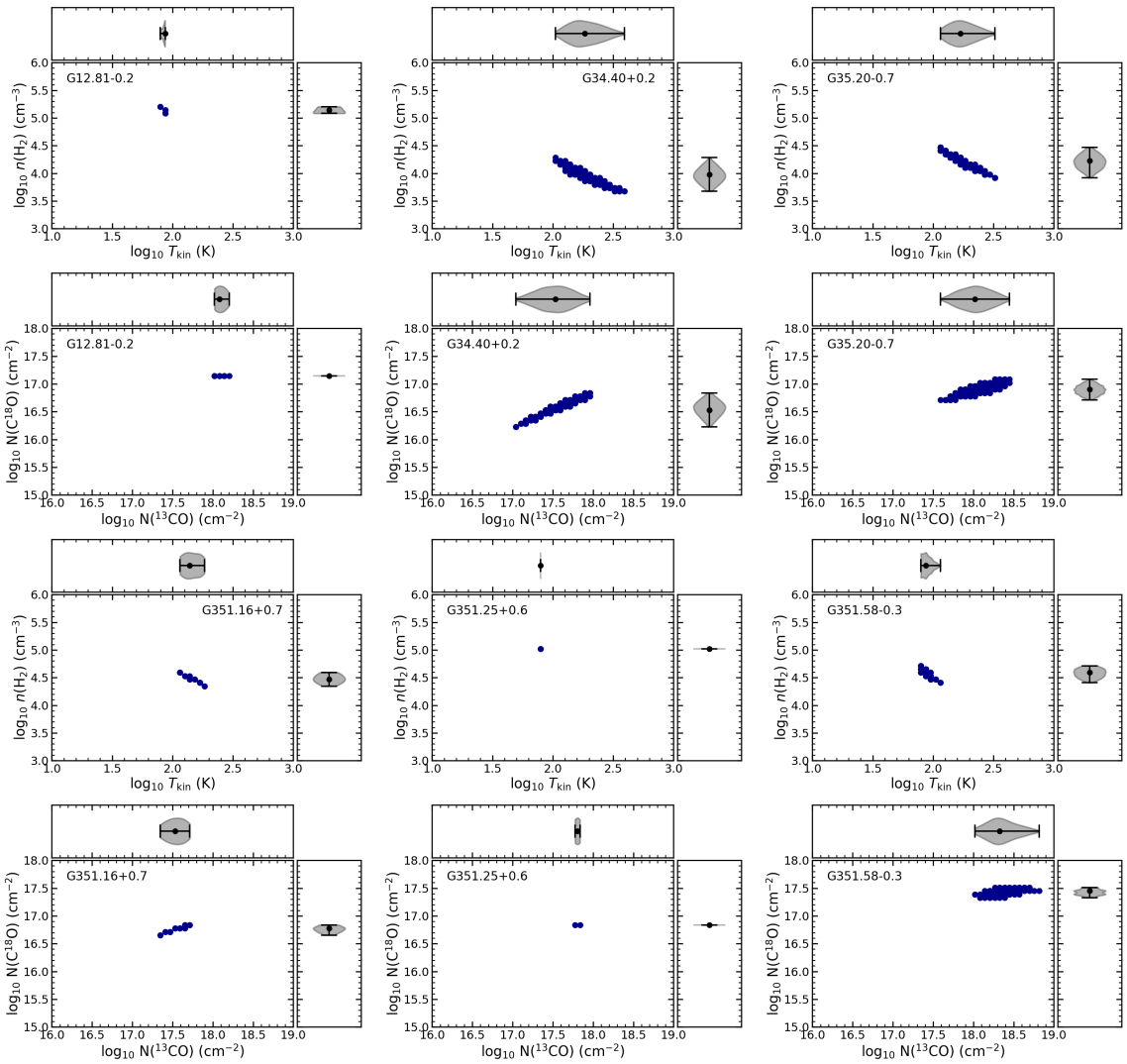

Figure 5.3: The presentation of RADEX models (in blue circle), selected from the minimum χ^2 method, on the $T_{\rm kin} - n(\rm H_2)$ and $N(^{13}\rm CO) - N(\rm C^{18}O)$ parameter planes. The grey shades in the side panels of each plot present the respective parameter distributions. The median of each distribution is marked with a black circle. The source names are displayed directly on the plots. The results are obtained from the model II setup.

Table 5.5: Constrained parameters from the RADEX modelling.

Source	$T_{\rm kin}^{(a)}$ (K)	$\log_{10}[n(\rm H_2)]^{(a)}$ ($\rm cm^{-3}$)	$\log_{10}[N(^{13}\rm CO)]^{(a)}$ ($\rm cm^{-2}$)	$\log_{10}[N(\rm C^{18}O)]^{(a)}$ ($\rm cm^{-2}$)	$\eta^{(a,b)}$	$s^{(c)}$ (pc)	$\chi^2_{\rm min}$	Count$^{(d)}$
Model I setup								
G12.81−0.2	87^{+7}_{-26}	$4.6^{+0.8}_{-0.2}$	$18.8^{+0.2}_{-0.3}$	$17.6^{+0.2}_{-0.4}$	$0.39^{+0.16}_{-0.02}$	$0.20^{+0.08}_{-0.01}$	4.38	40
G34.40+0.2	115^{+69}_{-56}	$4.7^{+0.8}_{-1.0}$	$17.3^{+0.4}_{-0.6}$	$16.2^{+0.5}_{-0.4}$	$0.25^{+0.21}_{-0.08}$	$0.16^{+0.10}_{-0.03}$	0.1	4297
G35.20−0.7	324^{+105}_{-80}	$3.4^{+0.4}_{-0.3}$	$18.1^{+0.2}_{-0.1}$	$17.1^{+0.2}_{-0.1}$	$0.27^{+0.12}_{-0.09}$	$0.13^{+0.04}_{-0.03}$	3.6	1185
G351.16+0.7	202^{+42}_{-64}	$3.6^{+0.9}_{-0.4}$	$18.2^{+0.4}_{-0.6}$	$17.4^{+0.4}_{-0.7}$	$0.48^{+0.06}_{-0.05}$	$0.12^{+0.02}_{-0.01}$	0.5	89
G351.25+0.6	115^{+0}_{-10}	$4.0^{+0.4}_{-0.3}$	$18.5^{+0.3}_{-0.4}$	$17.6^{+0.3}_{-0.4}$	$0.56^{+0.03}_{-0.03}$	$0.14^{+0.01}_{-0.01}$	6.5	16
G351.58−0.3	87^{+18}_{-21}	$4.5^{+0.6}_{-0.4}$	$18.4^{+0.3}_{-0.2}$	$17.5^{+0.3}_{-0.3}$	$0.21^{+0.04}_{-0.07}$	$0.40^{+0.05}_{-0.09}$	5.7	489
Model II setup								
G12.81−0.2	87^{+0}_{-8}	$5.1^{+0.1}_{-0.1}$	$18.1^{+0.1}_{-0.1}$	$17.1^{+0.0}_{-0.0}$	$0.41^{+0.05}_{-0.04}$	$0.21^{+0.02}_{-0.02}$	397.8	7
G34.40+0.2	184^{+84}_{-45}	$4.0^{+0.1}_{-0.2}$	$17.5^{+0.2}_{-0.2}$	$16.5^{+0.2}_{-0.1}$	$0.22^{+0.07}_{-0.05}$	$0.15^{+0.03}_{-0.02}$	1.5	338
G35.20−0.7	168^{+55}_{-29}	$4.2^{+0.1}_{-0.2}$	$18.0^{+0.2}_{-0.2}$	$16.9^{+0.1}_{-0.1}$	$0.17^{+0.04}_{-0.05}$	$0.10^{+0.01}_{-0.02}$	7.5	308
G351.16+0.7	139^{+29}_{-16}	$4.5^{+0.1}_{-0.1}$	$17.5^{+0.1}_{-0.1}$	$16.8^{+0.1}_{-0.1}$	$0.52^{+0.06}_{-0.05}$	$0.13^{+0.02}_{-0.01}$	4.0	18
G351.25+0.6	79^{+0}_{-0}	$5.0^{+0.0}_{-0.0}$	$17.8^{+0.0}_{-0.0}$	$16.8^{+0.0}_{-0.0}$	$0.74^{+0.02}_{-0.10}$	$0.21^{+0.01}_{-0.04}$	117.1	2
G351.58−0.3	87^{+9}_{-8}	$4.6^{+0.1}_{-0.1}$	$18.3^{+0.2}_{-0.1}$	$17.4^{+0.1}_{-0.1}$	$0.21^{+0.02}_{-0.07}$	$0.40^{+0.02}_{-0.09}$	6.4	80

Note: $^{(a)}$The medians of the parameter distributions from the selected models are presented, along with the amounts to the 16th and 84th percentiles of the distributions. $^{(b)}$The beam filling factor distributions include values obtained from all the constraining lines. $^{(c)}$The corresponding physical sizes of the envelopes, estimated from a beam of 20″, η, and the distances from Table 5.1. $^{(d)}$The number of models selected from a collection of 10^4 models using the minimum χ^2 method.

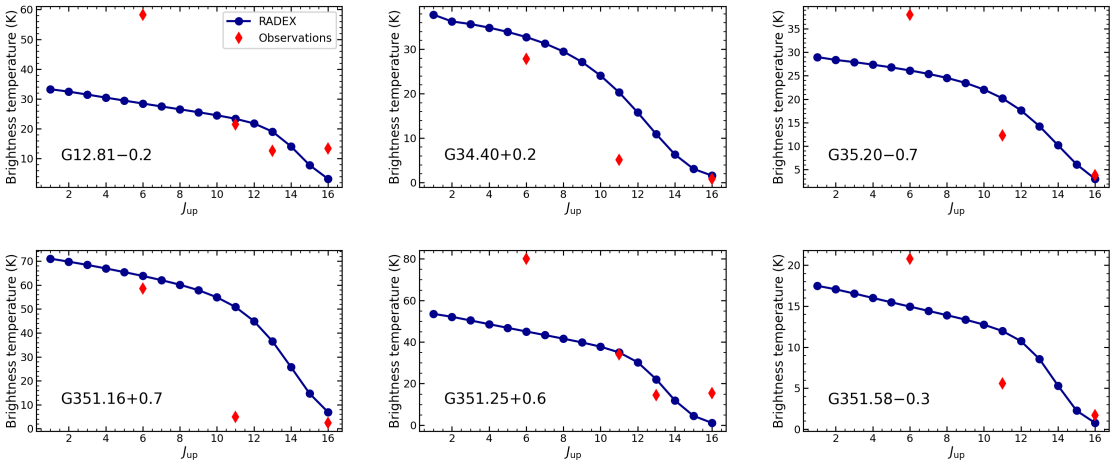

Figure 5.4: SLEDs of main CO isotopologue emission in T_{MB} scale. The red diamonds represent the observations, while the blue circles indicate the data points from the RADEX models. The RADEX models are obtained with the parameter constraints in the model II setup.

5.5 Discussion

Our RADEX modelling of multiple rare CO isotopologue lines has allowed us to constrain the physical parameters of the warm inner envelopes. Here, we further discuss RADEX predictions for the emission of the main CO isotopologue, as well as a comparison of our results with those of another high-mass star-forming region.

5.5.1 Predictions for CO lines

While we did not include any observed main CO isotopologue lines in our RADEX modelling process, we can produce RADEX predictions for them and compare with the observations, providing insights into the excitation of the main CO isotopologue transitions. The CO predictions were generated in RADEX with the medians of the constrained physical parameter distributions from the model II setup. As for the column density of the main CO isotopologue, we assumed that [CO]/[$C^{18}O$] ~ 500. SLEDs for the observed and predicted CO emission were generated in a similar manner as in Section 5.4.

Figure 5.4 shows the comparison of the predicted CO SLEDs with the observations of the CO (6–5), CO (11–10), CO (13–12), and CO (16–15) line. We found CO (6–5) being underestimated at four sources, suggesting a contribution of additional temperature components to this line, which are not accounted by our models. At two sources, G34.40+0.2 and G351.16+0.7, the models slightly overestimate the CO (6–5) emission. The clear overestimation also happens to the CO (11–10) line of G34.40+0.2, G35.20−0.7, G351.16+0.7, and G351.58−0.3 and the CO (13–12) line of G12.81−0.2 and G351.25+0.6. The overestimation of the CO (6–5) line can be explained by the fact that their observations are heavily affected by self-absorption (Navarete et al., 2019). Signs of self-absorption were also seen at the CO (11–10) line of a few Top100 sources (Hoang, Karska et al., 2023), although they are not as severe as in the case of the CO (6–5) emission. For this reason, the overestimation at the high-J CO lines could also be due to the high opacity effect. This suggestion is supported by the fact that the opacities of the CO (11–10) and the CO (13–12) line in a RADEX model, which

has parameters from the medians between the sources, are as high as 73 and 26, respectively. Our finding here, where the observations of a main isotopologue are lower than the predictions derived from the observations of other rare isotopologues, is similar to another case in Gong et al. (2018). The authors found a clear detection of $H^{13}CO^+$ (1–0) while the main isotopologue HCO^+ (1–0) is not detected. Similar to our suggestion here, Gong et al. (2018) claims high opacity as the cause for the missing HCO^+ (1–0) emission. At G12.81−0.2 and G351.25+0.6, the observations of the CO (16–15) line are much higher than their RADEX predictions. This result suggests that additional temperature components are needed to account for the total emission of this high-J CO line.

In summary, our one-component RADEX models seem to be too simple to reproduce all the observed main and isotopologue lines of the CO molecule. This is, however, understandable, as Hoang, M.-Y. Lee et al. (2025) has already suggested that the heating of the warm envelopes around massive YSOs may result from multiple complex physical processes. Our results indicate that the emission of the high-J CO lines from the envelopes around massive star-forming regions may still be optically thick.

5.5.2 Comparisons with another massive star-forming region

Determining physical conditions at massive star-forming regions is essential to understanding the star-formation processes and the emission generated by them. Our RADEX modelling, from the model II setup, was able to constrain $T_{\rm kin}$ in a range between ∼50 and ∼200 K, $n(H_2)$ between $\sim10^4$ and $\sim10^5$ cm^{-3}, $N(^{13}CO)$ between $\sim10^{17}$ and $\sim10^{18}$ cm^{-2}, and $N(C^{18}O)$ between $\sim10^{16}$ and $\sim10^{17}$ cm^{-2} for the warm envelopes of six massive star-forming regions. In a previous simpler RADEX modelling, Peng, Wyrowski, L. A. Zapata et al. (2012) used CO (6–5) emission and the ratio of ^{13}CO (8–7) and $C^{18}O$ (6–5) to constrain temperature and density in various regions of the OMC-1 cloud, a prominent star-forming region. At a fixed ^{12}CO column density of 5×10^{18} cm^{-2}, which translates to $N(C^{18}O) \sim 10^{16}$ cm^{-2} (assuming [CO]/[$C^{18}O$] ∼ 500), close to the $N(C^{18}O)$ from our modelling, many of their observations are in agreements with gas that has temperature between 150 and 250 K and H_2 density between 10^4 and 10^6 cm^{-3}. These numbers are close to the temperature and H_2 density from our work. Peng, Wyrowski, L. A. Zapata et al. (2012) also found matches of $T_{\rm kin} \sim 450$ K for their observations. The column density of these high-temperature models is, however, lower than the column densities constrained by our work. We note that a one-to-one comparison here cannot provide strong implications, as the sources may be in different phases of star formation and thus have different physical conditions. Additionally, the spatial resolution difference, due to the much closer distance from the OMC-1 to us, could also be a source of the discrepancy in our results, as the gas content within the beams could be different. This effect was suggested by Indriolo et al. (2017) when they compared their galactic observations with the extragalactic ones.

5.6 Summary and conclusions

In this work, we performed non-LTE radiative transfer modelling for several transitions of rare CO isotopologues, attempting to determine physical conditions of the warm envelopes around six massive YSOs selected from the Top100 sample. The number of lines allowed us to constrained multiple parameters such as $T_{\rm kin}$, $n(H_2)$, $N(^{13}CO)$ and $N(C^{18}O)$ at the same time. In an attempt to use four line ratios for the model constraining, we observed degeneracies between pairs of parameters, and this

effect was reduced after another line ratio had been added. While our models can reproduce the lines used for the model constraint well, they show limitations in predicting emissions from the main CO isotopologue lines. To account for emissions from all these CO lines, we suggest that future works employ more sophisticated models that include several heating components from different physical processes, such as UV heating and shocks, as suggested in Hoang, M.-Y. Lee et al. (2025).

5.7 Appendices

5.7.1 Line profiles of $C^{18}O$ lines

In Fig. 5.5, we show the overlay between line profiles of the $C^{18}O$ (3–2) and $C^{18}O$ (6–5) transitions at each source. The $C^{18}O$ (6–5) line is scaled at two sources, G34.40+0.2 and G35.20−0.7, for better visualisations.

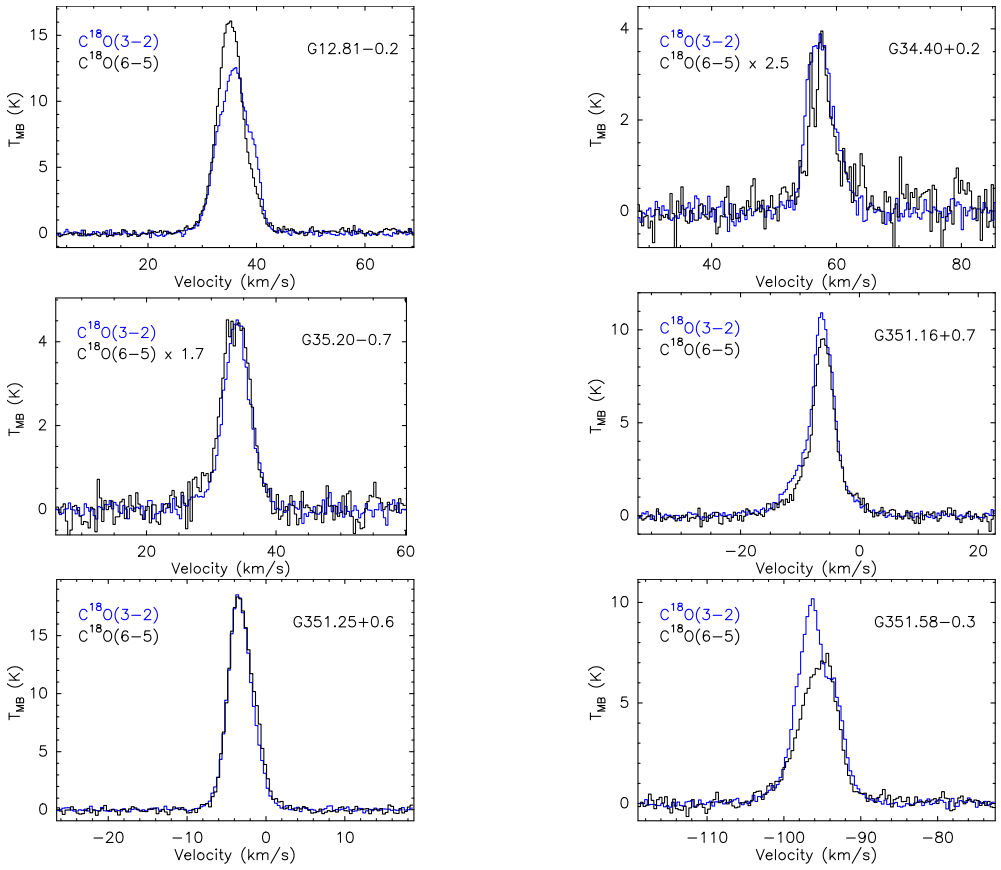

Figure 5.5: Line profiles of the $C^{18}O$ (3–2) (in blue) and $C^{18}O$ (6–5) (in black) emission at our sources.

5.7.2 Spectral line energy distributions

We present in Fig. 5.6 and Fig. 5.7 all the ^{13}CO and $C^{18}O$ SLEDs obtained with the model I and the model II setup.

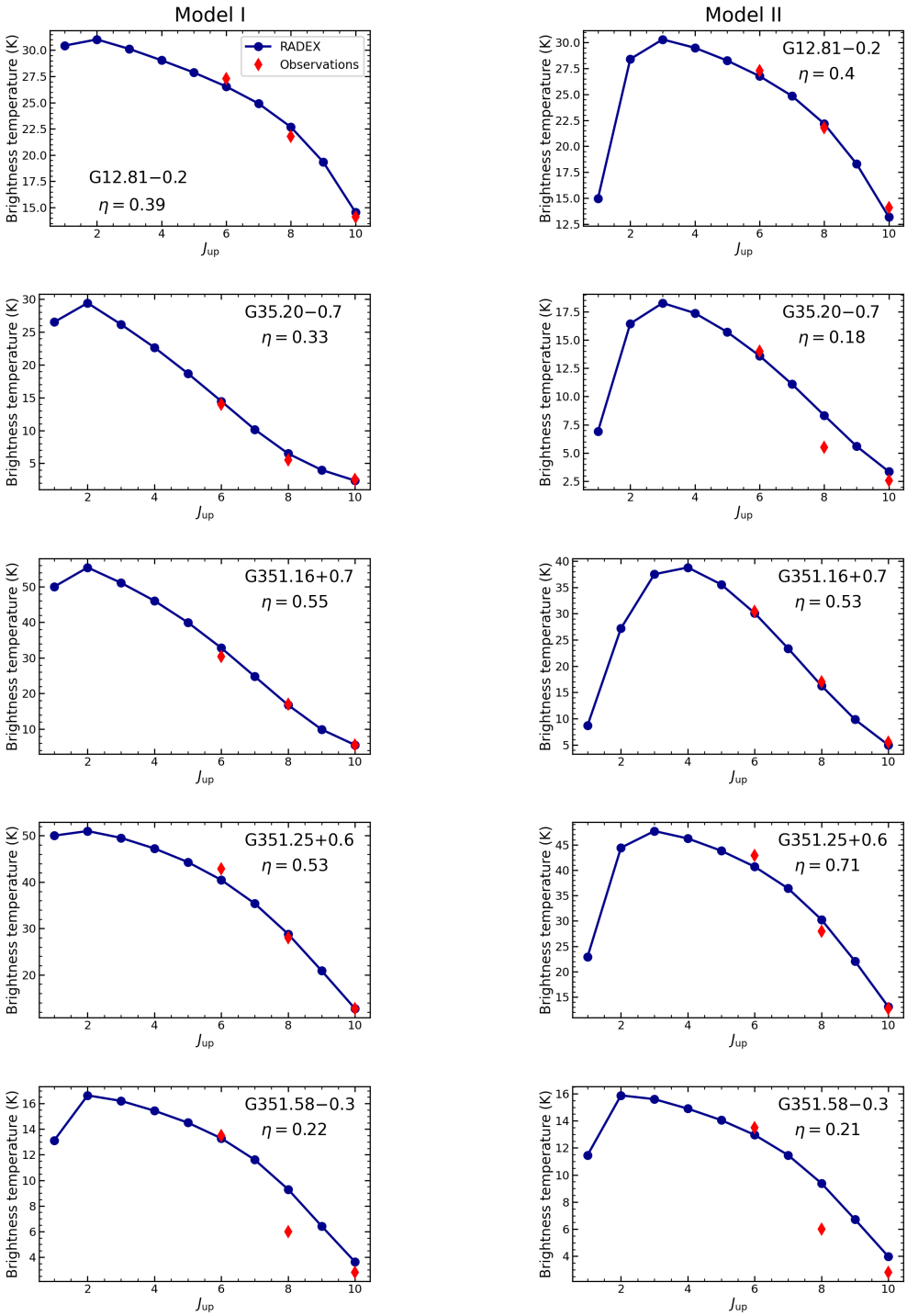

Figure 5.6: SLEDs of ^{13}CO emission in the $T_{\rm MB}$ scale for our sources. The values from the observations and the representative RADEX models are shown by the red diamonds and the blue circles, respectively. The representative RADEX models have physical properties from the medians of the parameter distributions. The RADEX SLEDs from the Model I setup are shown on the left column, while those from the Model II setup are on the right column. The beam filling factors, η, used to scale the RADEX SLEDs and the source names are presented directly on each plot.

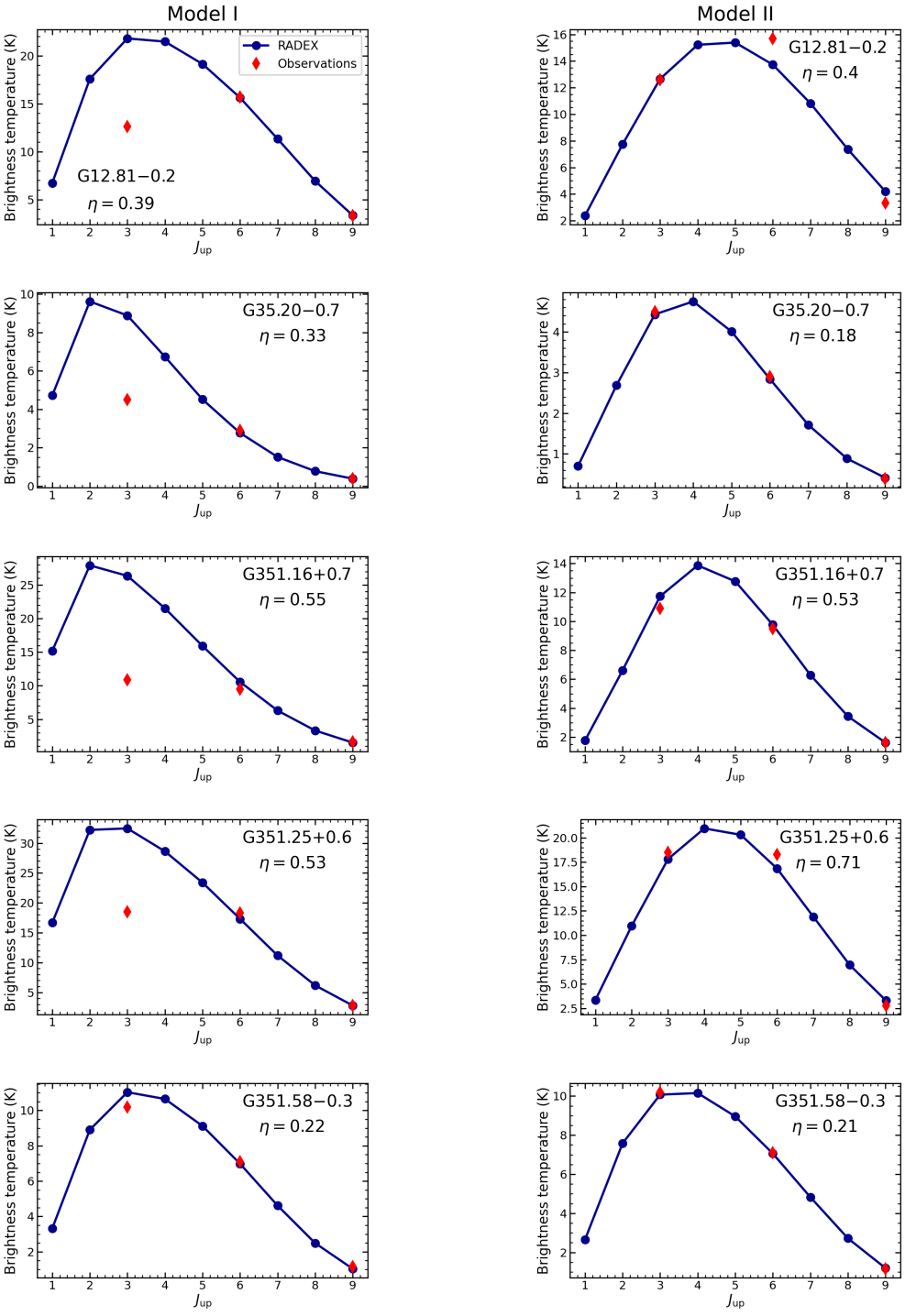

Figure 5.7: SLEDs of $C^{18}O$ emission in the T_{MB} scale. The colours and symbol schemes are the same as in Fig. 5.6.

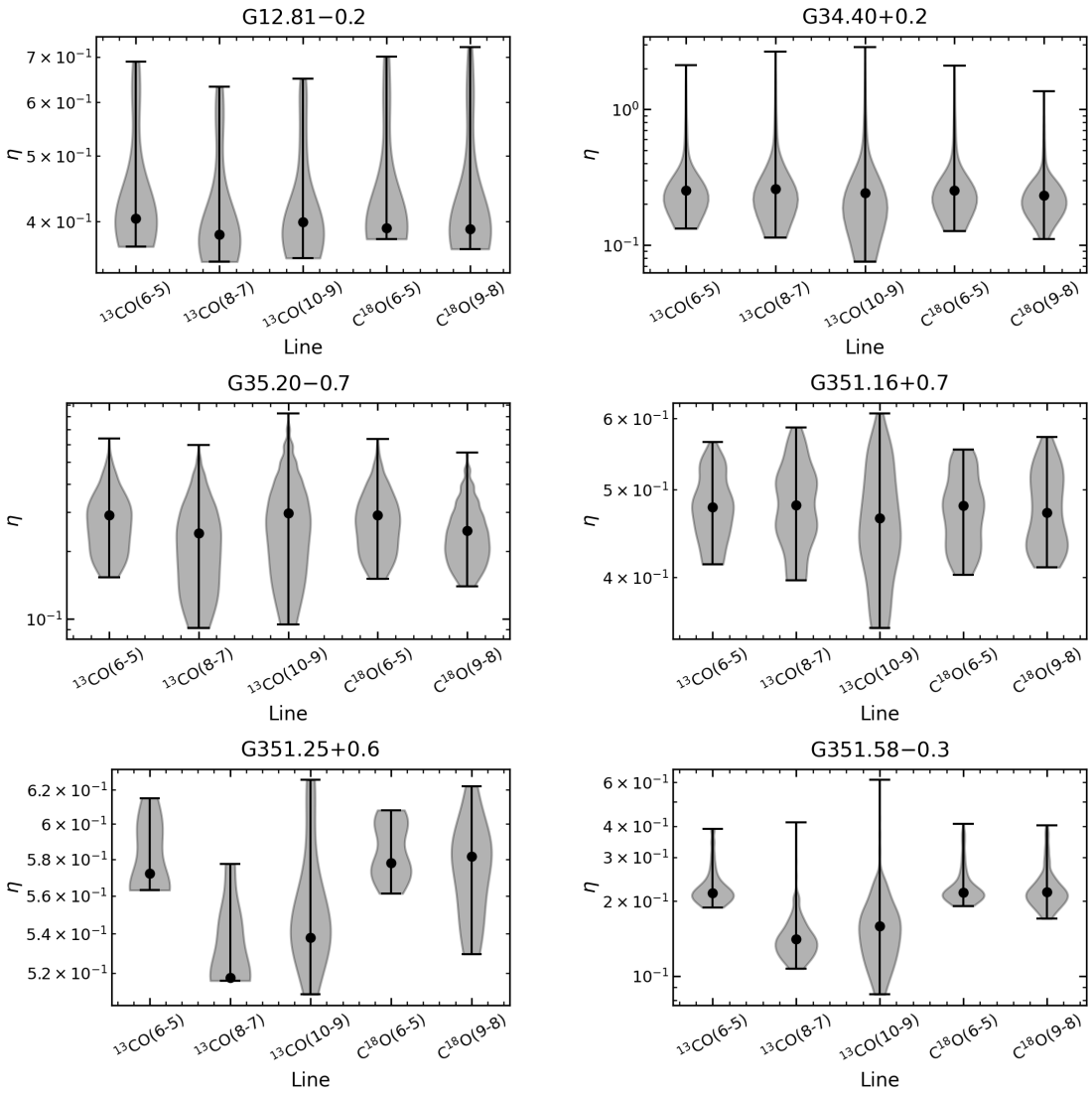

Figure 5.8: Distributions of the beam filling factor estimated from each constraining line at each source in the model I setup. The black circles mark the distribution medians.

5.7.3 Beam filling factors

In Figs. 5.8 and 5.9, we present the distributions of the beam filling factors estimated from the selected models in both the model I and model II setups.

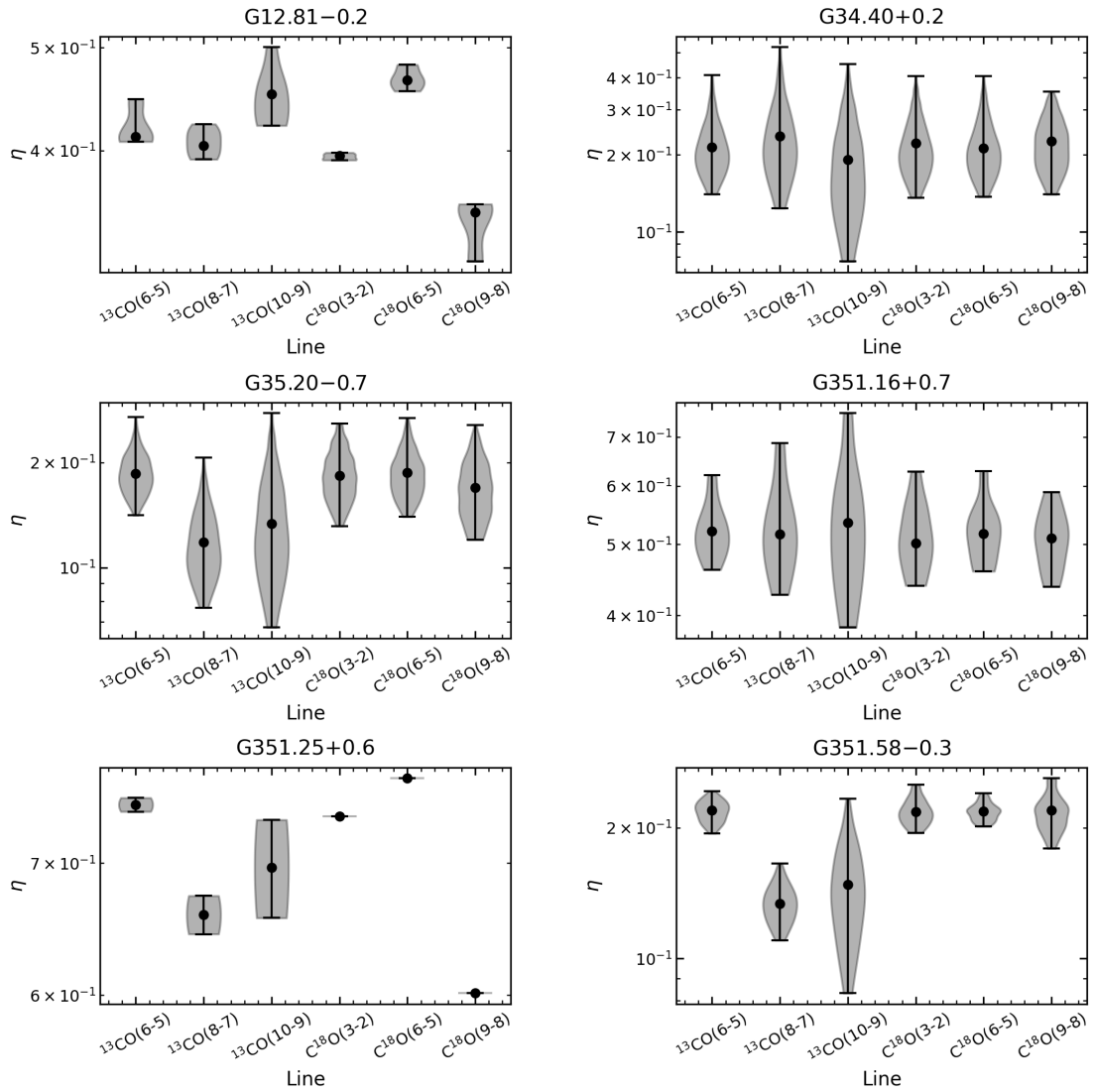

Figure 5.9: Distributions of the beam filling factor estimated from each constraining line at each source in the model II setup. The black circles mark the distribution medians.

CHAPTER 6

Concluding remarks

6.1 Summary

This PhD thesis contributes to the high-mass star formation field with studies of the properties of warm gas envelopes around high-mass (proto) stars. From an observational perspective, we study the warm gas envelopes of sources in the Top100, a well-studied sample of around 100 massive star-forming regions, which are at four different evolutionary stages: starless (70 μm weak, 70w), protostellar (near/mid IR weak, IRw), high-mass protostellar (mid IR bright, IRb), and compact HII region (HII). Using the results from a large sample, this thesis establishes a systematic change in the emission of the envelopes, which follows the process of star formation. The thesis also explores the mechanisms that may be responsible for heating the gas in the envelopes. At the same time, the thesis demonstrates the use of mid- and high-J lines of CO, which are observable with sub-mm telescopes, as tracers of warm gas in the envelopes.

In the following, we summarise the results of each scientific chapter and revisit the questions introduced in Chapter 1 to review their status. Additionally, ideas for further work are also presented.

Part I: Morphology and kinematics of the warm inner envelopes

- In Chapter 3, we show that the ^{13}CO (6–5) emission is ubiquitous in massive star-forming clumps, with detections confirmed in 81 out of 98 sources (i.e. 83% detection rate). The detection rate across evolutionary groups, however, shows a large variation, ranging from 31% at the youngest source group to 100% at the most evolved. This variation is likely related to the change in temperature and/or density of the envelopes, as warmer and denser gas means more ^{13}CO gas is excited to mid-J levels, and warmer environments allow more frozen ^{13}CO molecules to sublimate. Other properties of the ^{13}CO (6–5) line, such as the line width and peak brightness temperature increase in more evolved sources, and the line luminosity correlates positively with $L_{\rm bol}$ and the mass of the clumps. All evidence points to a conclusion that the physical conditions in the warm gas envelopes show higher temperatures and/or densities as the clumps evolve from early stages of HMSF. The non-thermal motions also appear to become stronger with evolution. The likely scenario is that star formation activities and feedback alter the properties of the warm gas envelopes, which is manifested as the changes in ^{13}CO (6–5) emission. Hence, this emission line is a reliable tracer of the progress of HMSF.

- In Chapter 1, we summarise a systematic transformation in both the shapes and kinematics of the envelopes around low-mass protostars, driven by the interaction between outflows and the envelopes. From there, we launch an investigation in Chapter 3 to determine if our massive warm envelopes undergo a similar transformation to that seen in low-mass envelopes. In terms of morphology, we find that the ^{13}CO (6–5) intensity maps of 59 clumps are large enough to study the shape of the envelopes. It shows that the majority of these clumps (i.e. 52/59) share the same morphology type, which is characterised by a nearly circular shape with a single central intensity peak. The envelopes at the current angular resolution appear not to undergo a significant morphological transformation, as seen in low-mass counterparts. A trend we observe is the enlargement of the envelopes in the last phase (i.e. HII). In the 52 clumps that share the same simple morphology, we are able to characterise their radial intensity profiles using power-law functions and indeed find a change between the profiles of sources in different groups. While the power-law indexes, m, of all sources vary between 0.5 and 2.7, IRb sources generally have lower values of m than HII sources; the mean values of m in the two groups are 1.1 and 1.5, respectively. The higher m in HII sources indicates a substantial enhancement of temperature and/or density at the centre of the envelopes compared to the outer parts at large radii, which could relate to how efficiently the influence of feedback propagates through the envelopes. Our power-law function fit to the radial profiles suggests the existence of intensity plateaus at the centres of the envelopes, which can have a radius as large as 0.5 pc. We suggest that these intensity-flat regions are a manifestation of the small-scale fragmentation at the centres of the envelopes, rather than an opacity effect, as we find the ^{13}CO (6–5) emission there to be generally optically thin.
- We characterise the kinematics in the envelopes of the 52 clumps described above by fitting their ^{13}CO (6–5) first moment maps using the mean velocity gradient (MVG) method. Most of the clumps (i.e. 41) show a significant linear MVG with the gradient strength, $\mathcal{G}$, generally varying between 1 km s^{-1} pc^{-1} and 8 km s^{-1} pc^{-1}. Interestingly, the distribution of $\mathcal{G}$ shows no evolutionary trend. Our investigation into the origins of the velocity gradients shows that the angular offsets between the orientations of the ^{13}CO (6–5) MVGs and the CO (6–5) outflows vary widely in all the evolutionary groups except for 70w, supporting neither outflow entrainment nor the envelope-disc co-rotation scenarios, which are systematically seen in Class 0 and Class I low-mass protostars, respectively. We further investigate the influence of large-scale kinematics on the ^{13}CO (6–5) MVGs by comparing the directions of ^{13}CO (2–1) MVGs derived from the maps that are ~1.5 times larger than our ^{13}CO (6–5) maps with the directions of the ^{13}CO (6–5) MVGs. Interestingly, half of the sources exhibit an alignment between the two velocity gradients, while the other half display varying angular offsets. These statistical results show that the origins of the ^{13}CO (6–5) velocity gradients are unclear. In a different approach, our detailed investigations of a few individual sources, in conjunction with information from the literature, suggest several drivers of the ^{13}CO (6–5) kinematics, including outflow entrainment, envelope rotation, shell expansion, and gas flows along filaments. Overall, we find no clear systematic origin for the ^{13}CO (6–5) velocity gradients, and conclude that the envelope kinematics traced by the ^{13}CO (6–5) emission is highly complex.

Part II: Probing gas in massive star-forming regions with high-*J* CO lines

- Our work towards a small sample of 13 Top100 sources in Chapter 4 confirms that the high-J

CO (11–10), CO (13–12), and CO (16–15) lines exhibit broad wing emission, which is generally associated with high-velocity gas in outflows. Emission from the envelopes, contained in low-velocity channels of the line profiles, is generally not attenuated by the self-absorption, which heavily affects lower-J lines such as CO (6–5). Our decomposition method successfully extracts the wing component from the CO (11–10) line for 12 out of 13 sources and from the CO (16–15) line for 8 out of 10 sources. In addition, wing components are also extracted from the CO (13–12) line for the two sources that were observed. Our results show that the relative contributions of the wings to the total emission vary widely between ~30% to over 70%. However, the variation of this fraction shows no clear correlation with the evolution of the sources. In several sources, we notice an increase in the wing contribution with rotational J level. In eight sources, where the wing component is available for both the CO (11–10) and CO (16–15) line, we can examine the variation of the wing ratio at different velocity channels. It reveals that the wing ratio increases at high-velocity channels for a few sources, indicating an increase in temperature of high-velocity gas, assuming the emission is optically thin and thermalised.

- We find that the luminosities of the CO (11–10) and CO (16–15) lines correlate weakly with the mass of the clumps and show stronger correlations with $L_{\rm bol}$. Interestingly, the data from previous studies help us confirm that the correlation of the CO (16–15) line with $L_{\rm bol}$ also holds for low- and intermediate-mass clumps. This result suggests the excitation mechanism of this line could be similar for objects spanning a wide range of physical scales and masses.

- The rotational diagram analysis for emission from the full line profiles and from only the wing components reveal $T_{\rm rot}$ in the ranges 110−200 K and 120−220 K, respectively. These ranges are consistent with $T_{\rm rot}$ obtained with high-J CO lines in other high-mass star-forming regions in the Milky Way, such as W49N, Orion S, Orion KL, and Sgr B2(M). We note that the $T_{\rm rot}$ we derive for the source G34.26+0.15 is significantly lower than the value estimated by Karska, Herpin et al. (2014), who used CO lines with $J_{\rm up}$ ranging from 14 to 30. This result demonstrates that including different CO lines, which are sensitive to different temperatures, in the rotational diagram analysis can lead to different results. In a different approach, our non-LTE modelling with RADEX to constrain the physical conditions of the gas that emits wing emission results in two solutions. One is at low densities with $n_{\rm H_2} \sim 10^3 - 10^4$ cm^{-3} and high temperatures of several thousands Kelvin. Such high temperatures are unrealistic even for outflows of high-mass stars. Therefore, this scenario is not considered further. The second solution is at moderate temperatures between 150 K and 500 K and high densities between 10^5 cm^{-3} and 10^7 cm^{-3}. The CO column densities of all solutions are of order $10^{17} - 10^{18}$ cm^{-2}.

Part III: Radiative transfer modelling with multiple CO lines

- In Chapter 5, our RADEX models are used to constrain the physical conditions in the inner warm envelopes of six Top100 clumps. For most sources, the models successfully reproduce emission of six ^{13}CO and C^{18}O transitions. Kinematic temperatures are found from several dozens to several hundreds of Kelvin, and the constrained densities are from ~10^4 cm^{-3} to ~10^5 cm^{-3}. The ^{13}CO and C^{18}O column densities are determined to be around 10^{18} cm^{-2} and 10^{17} cm^{-2}, respectively. Our models, however, fail to predict the emission of several mid- and high-J CO lines. The models underestimate the CO (6–5) and CO (16–15) transitions of several

sources, suggesting the existence of additional heating mechanisms affecting the CO lines. This suggestion aligns with our discussion and suggestion in Chapter 3 regarding the participation of multiple heating mechanisms in the excitation of gas in the warm envelopes. Interestingly, the CO (11–10) and CO (13–12) intensities are overestimated by our RADEX models in some cases, which may be due to the effect of high opacity.

- As a part of our results, we find that constraining four physical parameters (i.e. temperature, density, and two column densities) using line ratios from at least six transitions would greatly reduce the degeneracies between the parameters, which helps us constrain better the physical conditions of the targeted regions.

6.2 Outlook

This thesis examines the properties of warm envelopes on scales resolvable by single-dish telescopes. One of the main results we find is the dominance of the single-core morphology type among the investigated clumps, while the kinematics of warm gas in the envelopes seems to be complex. Naturally, one would question whether this result is partly because of the limited angular resolution of the data. To answer this question, we suggest probing the morphology of the envelopes on smaller scales using interferometers such as the Atacama Large Millimetre/sub-millimetre Array (ALMA) or the Northern Extended Millimetre Array (NOEMA). While NOEMA will be restricted to studying low-J CO transitions, ALMA is more suitable for this task as the array is located near the APEX telescope; hence, the weather conditions should allow observations at the frequency of the ^{13}CO (6–5) lines (i.e. ~661 GHz), which is covered by the Band 9 receiver of ALMA. In addition to the ^{13}CO (6–5) transition, one can also use ALMA to map CO (6–5) emission ($\nu \sim 691$ GHz) to probe outflow gas. With the most compact 12-m array (i.e. 160 m), ALMA observations at the 661 GHz frequency would yield an angular resolution around $0.7''$, which is equivalent to 0.003 pc and 0.04 pc at the distances of the closest and furthest Top100 sources, respectively. These high-resolution observations will provide an opportunity to investigate the warm gas surrounding individual high-mass protostars and potentially probe the direct interaction between star formation feedback (e.g. outflows) and the ambient gas.

In Chapter 3, we discuss the potential sources of the energy that heat the gas in the envelopes. These include energetic UV photons from photon-dominated regions (PDRs), shocks in outflows, and heat transferred from warm dust. Future work with sophisticated modelling of each process is needed to assess their relative contributions to the emission from warm gas. For instance, one could model the self-consistent temperature structure of the envelopes with the 1-dimensional spherically symmetric dust radiative transfer code DUSTY (Ivezic and Elitzur, 1997), which is then used as the input for the non-LTE excitation line radiative transfer code RATRAN (Hogerheijde and F. F. S. van der Tak, 2000) to produce the ^{13}CO (6–5) emission. As for shock modelling, current shock models in the literature focus mainly on reproducing the emission of the main CO isotopologue. New studies, which assess the amount of ^{13}CO and C^{18}O emission excited by shocks in outflows, are therefore needed.

The RADEX modelling in Chapter 5 has reinforced the suggestion of multiple heating sources of gas in the warm envelopes. The underestimation of the RADEX models for the CO (16–15) line implies that at least one of the heating mechanisms is efficient in exciting high-J CO transitions. Therefore, one would need data points of more high-J CO lines to characterise this heating component. In fact, we carried out this idea by attempting to observe the CO (22–21) line towards two Top100 sources using the SOFIA/GREAT instrument in 2019. Unfortunately, the issue with instrumental

standing waves prevented us from making any assessment about the line detection. The opportunity to observe such high-J CO line is currently not possible after the decommissioning of SOFIA. Therefore, we look forward to new generations of proposed infrared space telescopes such as *PRIMA*, *ORIGIN*, and *SALTUS*, which will provide us again access to THz wavelength windows that contain many essential transitions for star formation studies, such as high-J CO and water lines.

One of the questions in the ISM study is whether environmental factors such as metallicity, density, and location influence the formation and evolution of molecular clouds and star formation within them. This question is essential to the study of galaxy evolution, as different galaxy types can have different environmental conditions. Conveniently, conditions in regions of the Milky Way, from the galactic centre to the inner disc and outer Galaxy, happen to resemble conditions in starburst, spiral, and dwarf galaxies, respectively (Urquhart, König, Colombo et al., 2024, and references therein). Therefore, observational studies are generally conducted in different regions of the Milky Way to investigate the environment question. For example, the large survey SEDIGISM was designed to probe gas in the inner parts of the Milky Way. At the same time, the Outer Galaxy High Resolution Survey (OGHReS, Koenig et al., in preparation) specifically targets gas in the outer Galaxy, where the density and metallicity are low. The studies of warm envelopes in this thesis can be extended further in this direction, as the current studied envelopes are located in inner galactic regions. Therefore, we suggest new observations of mid-J CO lines with the APEX telescopes towards envelopes of star-forming clumps found within OGHReS. The information on the morphology and kinematics of gas envelopes surrounding massive star-forming clumps in the outer Galaxy, compared to those in the inner regions, may shed new light on the influence of environmental factors on the star formation process.

APPENDIX A

Mid-J ^{13}CO emission from the Top100 sample

A&A, 695, A24 (2025)
https://doi.org/10.1051/0004-6361/202452371

Astronomy & Astrophysics

ATLASGAL-selected high-mass clumps in the inner Galaxy

XI. Morphology and kinematics of warm inner envelopes

Thanh Dat Hoang[1,⋆,⋆⋆], Min-Young Lee[2,3], Friedrich Wyrowski[1], Agata Karska[1,4,5], Felipe Navarete[6], and Karl M. Menten[1]

[1] Max-Planck-Institut für Radioastronomie, Auf dem Hügel 69, 53121 Bonn, Germany
[2] Korea Astronomy and Space Science Institute, 776 Daedeok-daero, Yuseong-gu, Daejeon 34055, Republic of Korea
[3] Department of Astronomy and Space Science, University of Science and Technology, 217 Gajeong-ro, Daejeon 34113, Republic of Korea
[4] Argelander-Institut für Astronomie, Universität Bonn, Auf dem Hügel 71, 53121 Bonn, Germany
[5] Institute of Astronomy, Faculty of Physics, Astronomy and Informatics, Nicolaus Copernicus University, ul. Grudziądzka 5, 87-100 Toruń, Poland
[6] SOAR Telescope/NSF's NOIRLab, Avda Juan Cisternas 1500, 1700000 La Serena, Chile

Received 26 September 2024 / Accepted 22 January 2025

ABSTRACT

Context. High-mass stellar embryos are embedded in warm envelopes that provide mass reservoirs for the accretion process onto final stars. Feedback from star formation activities in return impacts the properties of the envelopes, offering us a unique opportunity to investigate star formation processes.

Aims. Our goals are to characterise the properties of warm envelopes of proto- or young stellar objects at different evolutionary stages based on the morphology and kinematics of submillimetre emission from the ^{13}CO (6–5) line and to examine their relations with star formation processes.

Methods. Using the Atacama Pathfinder EXperiment (APEX) telescope, we obtained maps of ^{13}CO (6–5) emission with an angular size of 80″ × 80″ (ranging from 0.3 pc × 0.3 pc to 4.9 pc × 4.9 pc in physical size) of 99 massive clumps from the ATLASGAL survey of submillimetre dust continuum emission. Our maps are classified based on morphological complexities, and the radial structure of ^{13}CO (6–5) emission is characterised for simple single-core sources. In addition, the velocity centroids of ^{13}CO (6–5) emission are compared to small- and large-scale gas kinematics (traced by ^{12}CO (6–5) and ^{13}CO (2–1) emission, respectively), aiming to shed light on the origin of envelope kinematics.

Results. ^{13}CO (6–5) emission is detected towards sources in all stages of high-mass star formation, with a detection rate of 83% for the whole sample. The detection rate, line width, and peak brightness temperature increase with evolutionary stage, and the line luminosity is strongly correlated with the bolometric luminosity and the clump mass. These results indicate that the excitation of ^{13}CO (6–5) emission is closely related to star formation processes. In addition, the radial distributions of ^{13}CO (6–5) emission for single-core sources can be well fitted by power-law functions, suggesting a relatively simple envelope structure for the majority of our sources (52 out of 99). The slopes of the radial distributions are systematically steeper for the most evolved group of sources (that host HII regions), which likely results from enhancements in density and/or temperature at the central parts of the warm envelopes. As for the ^{13}CO (6–5) kinematics, linear velocity gradients are common among the single-core sources (44 out of 52), and the measured mean velocity gradients are on average 3 km s^{-1} pc^{-1}. Our comparison of the ^{13}CO (6–5), ^{12}CO (6–5), and ^{13}CO (2–1) kinematics suggests that the origin of the linear velocity gradients in the warm envelopes is complex and unclear for many sources.

Conclusions. ^{13}CO (6–5) emission is ubiquitous in a wide variety of massive clumps, ranging from young sources where protostars have not yet been formed to evolved sources with fully developed HII regions. The excitation of ^{13}CO (6–5) emission in warm envelopes is likely impacted by different processes at different epochs of high-mass star formation, while the origin of the ^{13}CO (6–5) kinematics remains elusive and needs further investigation.

Key words. stars: formation – stars: massive – stars: protostars – ISM: kinematics and dynamics – ISM: molecules – ISM: structure

1. Introduction

High-mass stars ($M > 8\ M_\odot$) play an essential role in the evolution of galaxies (e.g. Kennicutt 2005). They provide a substantial amount of radiative and mechanical feedback to the surrounding interstellar medium (ISM) through ultraviolet (UV) radiation fields, stellar outflows, stellar winds, and supernova explosions, regulating star formation in galaxies (Hopkins et al. 2014). In addition, they produce and release heavy elements throughout their lifetime, driving the chemical enrichment of galaxies (Matteucci 2021).

Despite their importance for the evolution of galaxies, how high-mass stars form and interact with their surroundings remains poorly understood (e.g. Zinnecker & Yorke 2007; Motte et al. 2018). Current competing theoretical concepts of high-mass star formation include collapsing turbulent cores (McKee & Tan 2003), competitive accretion in stellar clusters (Bonnell et al. 2001; Bonnell & Bate 2006), global hierarchical collapse

⋆ Member of the International Max Planck Research School (IMPRS) for Astronomy and Astrophysics at the Universities of Bonn and Cologne.
⋆⋆ Corresponding author; tdhoang@mpifr-bonn.mpg.de

(Vázquez-Semadeni et al. 2019), and converging inertial flows (Padoan et al. 2020). Evaluating these different theories rigorously requires a statistically significant sample of high-mass star-forming regions, covering a wide range of evolutionary stages. Such a sample has been provided by the APEX Telescope Large Area Survey of the Galaxy (ATLASGAL; Schuller et al. 2009). ATLASGAL is a survey of 870 μm emission in the inner Galaxy (covering $|l| < 60°$ at $|b| < 1.5°$ and $280° < l < 300°$ at $-2° < b < 1°$) conducted with the Atacama Pathfinder EXperiment (APEX[1]; Güsten et al. 2006) 12 m submillimetre telescope in Chile. With an excellent sensitivity of 50–70 mJy beam^{-1} and a large coverage of ∼420 deg^2, ATLASGAL provides a comprehensive census of high-mass star-forming regions in the inner Galaxy.

Within high-mass star-forming regions, dense envelopes are of particular interest as they provide mass reservoirs that feed the mass build-up of newly formed protostellar objects at their centres through accretion (Shu et al. 1987; Wyrowski et al. 2016; Beltrán & de Wit 2016; Pillai et al. 2023). Once young stellar objects (YSOs) have formed, stellar feedback significantly changes the properties of the surrounding envelopes, so much so that they can be entirely dispersed at the end of the evolution, stopping the accretion process (e.g. Arce & Sargent 2006, for low-mass star-forming regions). Among other tracers, mid-J ($5 < J < 10$) rotational transitions of isotopologues of carbon monoxide (CO) are especially suitable for probing the warm ($T \gtrsim 50$ K) inner parts of the envelopes. Previous studies have suggested that the warm envelopes surrounding low- and high-mass YSOs can be heated by various physical processes that are related to star formation activities. For example, passive heating and UV radiation from outflow cavity walls have been proposed to explain ^{13}CO (6–5) emission in low-mass star-forming regions (van Kempen et al. 2009b; Yıldız et al. 2012). Similarly, UV photons from photodissociation regions (PDRs) have been shown to play an important role in the excitation of ^{13}CO (6–5) emission in several high-mass star-forming clumps with strong HII regions (Graf et al. 1993; Koester et al. 1994; Leurini et al. 2013).

While there have certainly been a number of dedicated studies of the warm envelopes, mid-J transitions of CO isotopologues still remain difficult to access observationally due to the required dry atmospheric conditions. In particular, there is a lack of studies that cross a wide range of high-mass star-forming regions (including those in the early stages before the development of HII regions). In this paper, we examine the properties of ^{13}CO (6–5)-traced warm envelopes for a sample of 99 ATLASGAL-selected high-mass star-forming regions based on APEX observations with high spatial and spectral resolutions. In particular, we focus on probing the morphology and kinematics of ^{13}CO (6–5) emission and how they change throughout different evolutionary stages, with the aim of providing an insight into how high-mass stars form and their impact on their environments.

This paper is organised as follows. In Sect. 2, we describe our sample, the APEX ^{13}CO (6–5) observations, and the derivation of moment maps. In Sect. 3, we present ^{13}CO (6–5) line properties and our classification of the sources based on the integrated intensity maps. Subsequently, we investigate the morphology and kinematics of the warm envelopes traced by ^{13}CO (6–5) emission (Sect. 4) and discuss our results in the context of previous studies (Sect. 5). Finally, we finish this paper by presenting a summary of our main results (Sect. 6).

2. Observations and data reduction

2.1. Top100 sample

The ATLASGAL survey has identified a collection of ∼10^4 candidates for high-mass star-forming regions in the inner part of the Milky Way (Schuller et al. 2009; Urquhart et al. 2022). Among these sources, a sample of the ∼110 brightest objects (Top100 sample hereafter) was selected by Giannetti et al. (2014) for follow-up studies using various dust and gas tracers, namely dust continuum emission: König et al. 2017; shocked gas traced by SiO Csengeri et al. 2016; outflows traced by mid-J CO lines Navarete et al. 2019; neutral carbon ([C I])-traced gas Lee et al. 2022. The 99 sources selected for this study are part of the Top100 sample and can be categorised into four evolutionary groups based on their infrared (IR) and radio continuum emission (König et al. 2017):

- 14 in the starless (far-IR 70 μm weak group, 70w): these comprise sources in the earliest phase, in which collapse might have already started, but no protostellar object has yet been formed, according to the lack of compact 70 μm far-IR emission detected in the Hi-GAL survey (Molinari et al. 2010).
- 30 in the protostellar (near/mid IR weak group, IRw): these objects are identified by compact 70 μm emission. However, they are not yet associated with a strong and compact mid-IR emission source, implying that they are dominated by cool gas.
- 35 in the high-mass protostellar (mid IR bright group, IRb): the gas around protostellar objects becomes hotter as the sources appear luminous at 8 μm and 24 μm.
- 20 in the compact HII region group (HII): these can be considered to be in the most evolved phase, in which stellar objects start to disperse their natal envelopes. Intense stellar radiation ionises hydrogen atoms and forms ultra- and, later, compact HII regions which are associated with compact radio continuum emission.

The physical properties of our 99 objects were determined by fitting dust spectral energy distributions from mid-IR to sub-mm wavelengths (König et al. 2017). The results show that the dust temperature ($T_{\rm dust}$) varies from 11 to 41 K from the coldest to the warmest objects. In addition, the range of bolometric luminosity, $L_{\rm bol}$, spans five orders of magnitude from 57 $L_\odot$ to 3.7×10^6 $L_\odot$, and the clump mass, $M_{\rm clump}$, ranges from 17 to 4.3×10^4 $M_\odot$. Most of our sources can form at least one massive star (König et al. 2017) according to the mass-size limit proposed by Kauffmann et al. (2010), indicating that they constitute a statistically significant sample of massive star-forming regions. Finally, we note that the distance distribution (∼1–13 kpc) is comparable amongst the different evolutionary groups (König et al. 2017), implying that there is no distance-related bias in our comparison of the groups (Sects. 3 and 4).

2.2. CHAMP$^+$ observations and data reduction

The observations of ^{13}CO (6–5) emission towards our sample were carried out using the Carbon Heterodyne Array of the MPIfR (CHAMP$^+$; Kasemann et al. 2006; Güsten et al. 2008) on the APEX telescope in 2013 and 2014. The data were obtained under the project 'Probing the warm and dense envelopes through the evolution of massive protostars' (project

[1] This publication is based on data acquired with the Atacama Pathfinder Experiment (APEX). APEX is a collaboration between the Max-Planck-Institut fur Radioastronomie, the European Southern Observatory, and the Onsala Space Observatory.

Table 1. Parameters of the CHAMP$^+$ observations.

Molecule	Transition [(a)] $J_u - J_l$	Frequency [(a)] (GHz)	E_u/k_B [(a)] (K)	A_u [(a)] (10^{-5} s^{-1})	g_u [(a)]	Beam [(b)] ($''$)	ΔV [(b)] (km s^{-1})
^{13}CO	6–5	661.067277	111.05	1.9	13	9	0.33

Notes. [(a)]Molecular data adopted from the Cologne Database for Molecular Spectroscopy (https://cdms.astro.uni-koeln.de) (CDMS, Müller et al. 2001, 2005). The frequency has been determined by (Klapper et al. 2000). E_u is the energy of the upper level, k_B is the Boltzmann constant, A_u is the Einstein A coefficient, and g_u is the statistical weight of the upper level. [(b)]Original angular resolution (FWHM beam width) and spectral resolution.

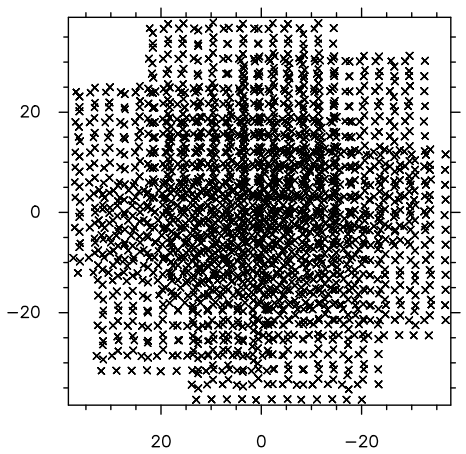

Fig. 1. Example of pointing positions for a single source in our OTF observations. The image is centred on the source and is in the units of arcsecond.

IDs: M0035-91 from June to August 2013, M0010-92 in October 2013, and M0027-93 in May 2014).

CHAMP$^+$ is a 2×7 element dual-colour heterodyne receiver array that can simultaneously observe tunings in the frequency ranges of 620–720 GHz in the low (LFA) and 780–950 GHz in the high frequency array (HFA). The Array Fast Fourier Transform Spectrometer (A-FFTS) (Güsten et al. 2008) serves as the backend for CHAMP$^+$, and the CHAMP$^+$/A-FFTS IF system is set up to process 2.8 GHz of instantaneous bandwidth over 16.4 k channels that are 212 kHz each (Güsten et al. 2008). The LFA was tuned to cover both the ^{13}CO (6–5) and C^{18}O (6–5) transitions, while the HFA was tuned to cover the ^{13}CO (8–7) line. The excellent weather with low precipitable water vapour content (0.24–1.07 mm) allowed us to observe these high frequency lines. The sources were scanned in the on-the-fly (OTF) mode, resulting in data cubes with spatial dimensions of $80'' \times 80''$ with an original angular resolution of $9''$ at 661 GHz. The 7-pixel hexagonal array enables fast mapping and improves the signal-to-noise ratio towards the map centre where the pixels' coverages overlap (Fig. 1). The parameters of our observations are presented in Table 1.

For the present study, we focused on the ^{13}CO (6–5) observations and analysed the ^{13}CO (6–5) data using the CLASS package of the GILDAS[2] software. Specifically, the obtained spectra were converted into the main-beam temperature, T_{MB}, scale via $T_{MB} = (F_{eff}/B_{eff})/T_A^*$, where F_{eff} is the forward efficiency of 0.95, B_{eff} is the main-beam efficiency of 0.43[3] obtained from a Mars observation, and T_A^* is the corrected antenna temperature. The spectra were smoothed to a velocity resolution of 0.35 km s^{-1}. Data cubes were then created by the CLASS gridding routine `XY_Map` with a pixel size of $4.8''$, where a Gaussian profile of one-third of the beam size is convolved with the gridded data to yield a final angular resolution of $10''$.

The ^{13}CO (6–5) spectra of five sources exhibit narrow negative features in velocity channels close to the peaks at sources' velocities, which indicates the presence of emission in the reference positions. To correct for this contamination, we estimated average spectra within $20''$of outer parts of the maps where only those negative features were observed and added their reversed profiles to the original spectra. This approach of utilising the average spectrum, as opposed to a single spectrum, minimises the noise one would add to the data during the correction process. The five sources affected by the contaminated reference positions are as follows: G305.21+0.2, G320.88−0.4, G337.17−0.0, G338.78+0.4, and G351.13+0.7.

2.3. Moment maps

We produced zeroth and first moment maps from the ^{13}CO (6–5) data cubes, which show the distributions of the integrated intensity and velocity centroid on the sky. These maps are valuable tools for examining the morphology and kinematics of warm gas in the inner envelopes. For each pixel, zeroth and first moment values were calculated as follows:

$$M_0 = \int T_i \, dv, \tag{1}$$

$$M_1 = \frac{\int T_i v_i \, dv}{\int T_i \, dv}, \tag{2}$$

where T_i and v_i are the main-beam brightness temperature and velocity at each channel, respectively. To determine the velocity range for the integration of M_0 and M_1, an average spectrum was estimated from the whole data cube for each source using CLASS (individual spectra were weighted by observing times), and the range of velocity channels over which emission is clearly detected above 3σ (σ is the spectral noise) was determined based on visual inspection. During the integration for M_0 and M_1, velocity channels below 3σ were not included. Similarly, pixels whose peak-to-noise ratios are lower than three were considered as non-detections and were masked in our final maps.

3. Results

3.1. Detection statistics

In this section, we analyse the detection of ^{13}CO (6–5) emission in our sources. For our analysis, we derived an average spectrum over the central region with a size of $20''$ (close to one ATLASGAL beam and noise level is improved (Fig. 1)) for each source

[2] https://www.iram.fr/IRAMFR/GILDAS/
[3] https://www.mpifr-bonn.mpg.de/4480868/efficiencies

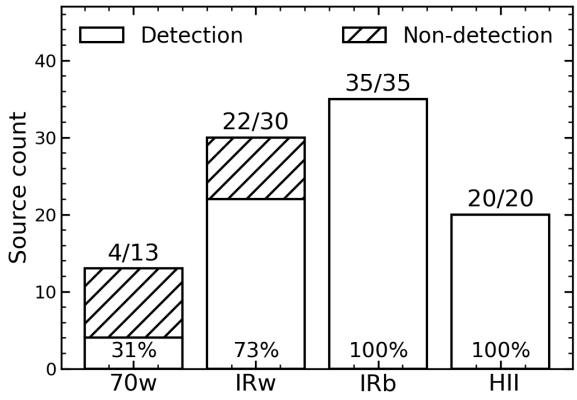

Fig. 2. Detection statistics of ^{13}CO (6–5) emission for the evolutionary groups. The exact number of the detected sources for the observed clumps is presented at the top of each bar, and the corresponding detection rates are shown in percentage terms.

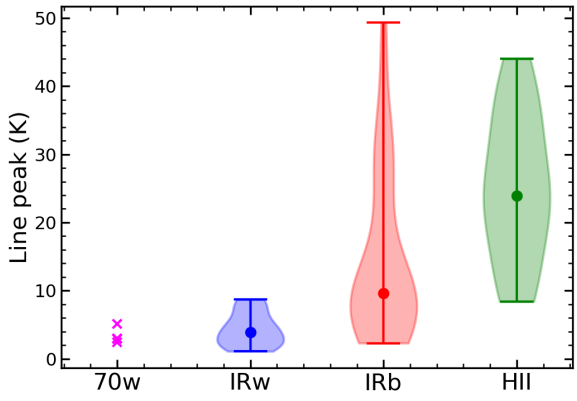

Fig. 3. Distributions of the peak brightness temperatures. These temperatures were obtained from the average spectra within the 20″-size central regions. For each evolutionary group, the minimum and maximum are shown as bars, while the median values are indicated as filled circles. For the 70w group that has only a few entries, the values for the individual sources are presented as crosses.

and considered a line to be detected if the peak main-beam brightness temperature was higher than 3σ.

We found that ^{13}CO (6–5) emission is detected towards 81 clumps with varying detection rates among the evolutionary groups (Fig. 2). Specifically, the detection rate increases from 31%[4] for the youngest group (70w) to 70–100% for more evolved groups (IRw, IRb, and HII) and is 83% for the whole sample. Similarly, the peak main-beam brightness temperature tends to increase towards the evolved source groups (Fig. 3). This increase in the detection rate and peak main-beam brightness temperature could indicate increasing density and/or temperature along the evolutionary sequence of high-mass star formation, considering that the enhancement in density and/or temperature is conducive to more easily exciting ^{13}CO molecules to mid-J rotational levels. At the same time, the warmer environment could allow more frozen ^{13}CO on dust grains to sublimate, enhancing the abundance of ^{13}CO molecules in the gas and the chance to detect mid-J ^{13}CO emission. Indeed, Giannetti et al. (2017) noted a difference between the IRw and IRb groups, finding CO to be mainly locked on dust grains in the former stage, while in the latter it exists mostly in the gas phase.

[4] G353.42−0.0 (70w) shows ^{13}CO (6–5) emission at −17.2 km s^{-1}, which is different from the source velocity of −54.4 km s^{-1}, and was excluded from our analyses.

3.2. Line profiles

In this section, we examine the general shape of ^{13}CO (6–5) line profiles based on the representative spectra of the different evolutionary groups. To produce these representative spectra, we shifted the average spectra of the central 20″ regions to 0 km s^{-1} according to C^{17}O (3−2)-based source velocities (Giannetti et al. 2014) and calculated the average of all sources in each evolutionary group. Four clumps without C^{17}O (3−2) data (two IRw, one IRb, and one HII) and one 70w source whose ^{12}CO (6–5) spectra heavily affected by a contaminated reference position were excluded from our calculation. For comparison, we also produced representative ^{12}CO (6–5) spectra in the same manner by using APEX ^{12}CO (6–5) observations from Navarete et al. (2019).

Figure 4 shows that the ^{13}CO (6–5) and ^{12}CO (6–5) spectra have systematically different shapes. In general, the ^{13}CO (6–5) spectra are much narrower and are not severely affected by self-absorption, indicating that ^{13}CO (6–5) and ^{12}CO (6–5) emission likely traces different regions of (or different conditions within) the envelopes. For 81 sources with ^{13}CO (6–5) detection in our sample, Navarete et al. (2019) indeed estimated that only 15 sources are not affected by self-absorption in their ^{12}CO (6–5) spectra. We fitted a single Gaussian function to each of the ^{13}CO (6–5) representative spectra (Fig. 4) to quantify the line width and found full width at half maximum (FWHM) values of 2.4, 4.4, 5.8, and 8.3 km s^{-1} for the 70w, IRw, IRb, and HII spectra, respectively. The increase in the FWHM is less likely to be affected by the opacity broadening effect as ^{13}CO (6–5) emission is mostly optically thin (Appendix B). Instead, it is closely linked to the increase in the source size (Sect. 4.1; Larson's size–line width relation) and suggests that non-thermal motions become stronger in evolved sources.

While a single Gaussian represents the overall shape of the ^{13}CO (6–5) spectra reasonably well, residuals are visible at velocities of ∼5–10 km s^{-1} for the IRw, IRb, and HII groups, hinting at the existence of a secondary component. In the case of low-mass YSOs, ^{13}CO (6–5) emission is considered to trace quiescent envelopes with an additional contribution from outflow cavity walls that are heated by UV photons, and/or from bow shocks or accretion discs (e.g. Spaans et al. 1995; van Kempen et al. 2009a,b). Our finding is consistent with the low-mass YSO results in that it indicates a complex origin of ^{13}CO (6–5) emission; we will further discuss possible heating mechanisms for ^{13}CO (6–5) emission in Sect. 5.1.

3.3. Line luminosities

To investigate further how the properties of ^{13}CO (6–5) emission change with the evolution of high-mass star formation, we computed the line luminosity, $L_{\rm CO}$, and examined correlations between $L_{\rm CO}$ and some of the key clump characteristics such as $L_{\rm bol}$ and $M_{\rm clump}$. The line luminosity was calculated from the average spectra of the central 20″ regions based on the following equation:

$$L_{\rm CO} = 4\pi D^2 F_\lambda, \tag{3}$$

where D is the distance to each source and F_λ is the integrated intensity in W m^{-2}. The conversion from K km s^{-1} to W m^{-2} for

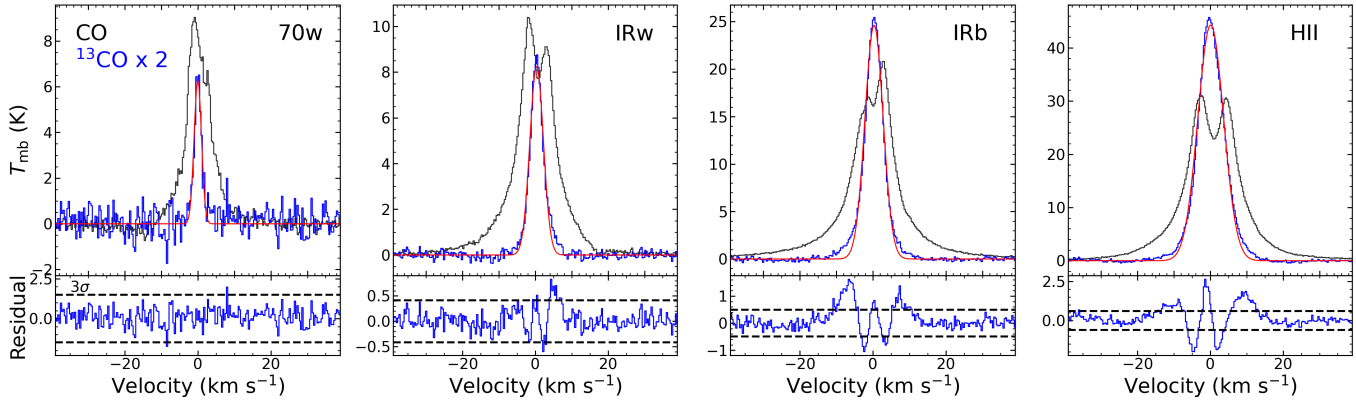

Fig. 4. Representative ^{12}CO (6–5) (black) and ^{13}CO (6–5) (blue) spectra of the four evolutionary groups. The ^{13}CO (6–5) spectra are scaled up by a factor of two for an easier comparison, and the fitted Gaussian functions are overlaid as red curves. In the bottom panels, the residuals from Gaussian fitting are shown with $\pm 3\sigma$ noise levels (dashed lines).

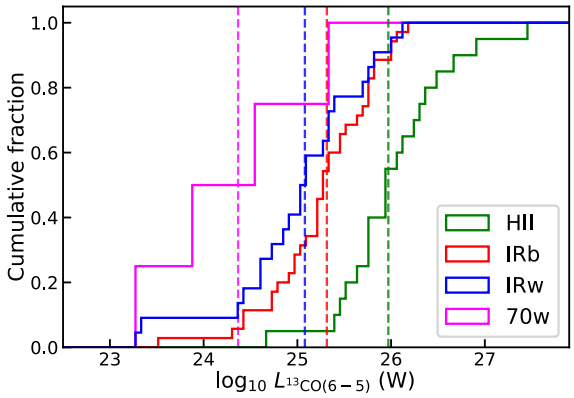

Fig. 5. Cumulative distributions of the ^{13}CO (6–5) line luminosities. These luminosities were derived from the spectra averaged over the central 20″ regions. The median values of the four evolutionary groups are shown as dashed lines in different colours.

F_λ was done following Eq. (2) in Indriolo et al. (2017):

$$\frac{F_\lambda}{(\mathrm{W\,m^{-2}})} = 1.0248 \times 10^{-18} \left(\frac{\Omega}{\mathrm{sr}}\right)\left(\frac{\nu}{\mathrm{GHz}}\right)^3 \left(\frac{M_0}{\mathrm{K\,km\,s^{-1}}}\right), \quad (4)$$

where ν is the line frequency and $\Omega = \pi\theta^2/4\ln(2)$ is the solid angle occupied by a Gaussian beam with a size $\theta = 20''$. For the sources with detections, M_0 values were calculated over the same velocity ranges used in Sect. 2.3. On the other hand, for the sources without detections, upper limits on $L_{\rm CO}$ were estimated based on the 3σ values and the median velocity range for the sources with detections (27 km s^{-1}).

Figure 5 presents the cumulative distributions of $L_{\rm CO}$ for the detected sources. From these distributions, we found that the median $L_{\rm CO}$ increases from the youngest to the most evolved group: 2.3×10^{24} W, 1.2×10^{25} W, 2.1×10^{25} W, and 9.3×10^{25} W for the 70w, IRw, IRb, and HII group, respectively. When k-sample Anderson-Darling tests were performed on each pair of the groups with sufficient numbers of sources (i.e. IRw, IRb, and HII) with a significance level of 0.05, all combinations except for the IRw-IRb pair were found to be drawn from different populations. These results suggest that the ^{13}CO (6–5) luminosities are closely related to the evolutionary state of a source. As such, $L_{\rm CO}$ is also correlated with two of the other evolutionary sequence indicators, $L_{\rm bol}$ and $M_{\rm clump}$ (König et al. 2017) (Fig. 6) with Spearman's rank correlation coefficients of 0.93 and 0.86, respectively.

In addition, we found that our ^{13}CO (6–5) luminosities are strongly correlated with the ^{12}CO (6–5) luminosities from Navarete et al. (2019) (Fig. 7; Spearman's rank correlation coefficient of 0.90). The correlation spans several orders of magnitude and remain continuous out to the high luminosity regime, which is surprising as one may expect it to flatten once the ^{12}CO (6–5) emission becomes saturated due to its high opacity[5] while the ^{13}CO (6–5) emission is still optically thin (Appendix B). One plausible explanation for the continuous increase in the ^{12}CO (6–5) luminosity could be a non-trivial contribution of optically thin high-velocity emission arising from outflows to the total emission. If this were the case, the strong correlation between the ^{13}CO (6–5) and ^{12}CO (6–5) luminosities would suggest that similar mechanisms would partly power the emission in both transitions (Sect. 5.1).

In summary, we found that ^{13}CO (6–5) emission is ubiquitous in massive clumps, including in the youngest sources that do not yet harbour protostars. The increases in the detection rate, peak brightness temperature, and line width determined for evolved sources indicate systematic changes in physical conditions, such as density, temperature, CO column density, and non-thermal motions, along the sequence of high-mass star formation. Furthermore, the tight correlation of the ^{13}CO (6–5) luminosity with the ^{12}CO (6–5) luminosity, bolometric luminosity, and clump mass implies that the origin of ^{13}CO (6–5) emission is likely linked to star formation processes.

3.4. Classification of our sources

Before probing the distribution and kinematics of warm molecular gas in detail (Sect. 4), we classified our sources based on their morphologies in the ^{13}CO (6–5) integrated intensity maps. The block diagram for our classification is shown in Fig. 8, and examples of the such classified sources are presented in Fig. 9.

In essence, our classification is based on the extent and morphology of ^{13}CO (6–5) emission. First, we considered sources with fewer than 16 detected pixels (corresponding to four telescope beams) as 'poorly resolved' and the rest as 'well resolved'. An exception is G351.51+0.7, which is categorised as a poorly resolved clump in spite of its significant number of detected pixels as the pixels are scattered across the map. Among the

[5] The ^{12}CO (6–5) profiles often suffer from self-absorption (Fig. 4).

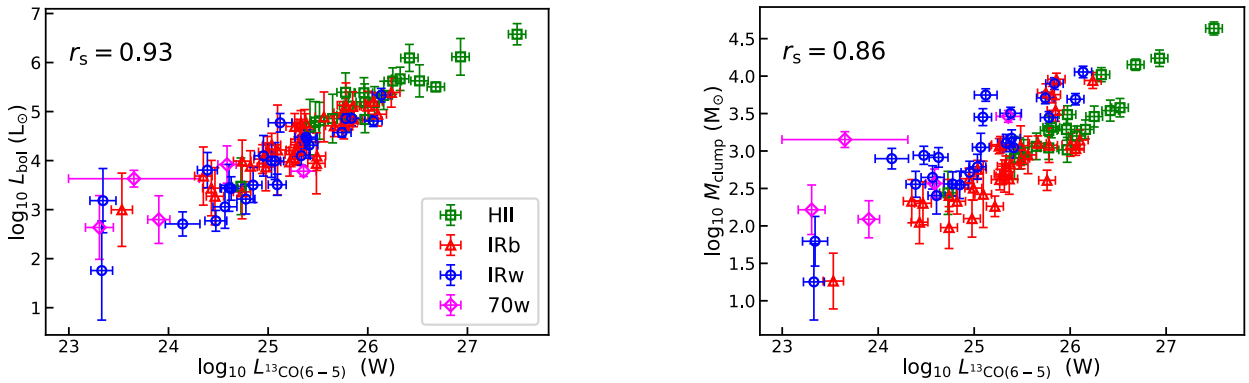

Fig. 6. ^{13}CO (6–5) line luminosity as a function of bolometric luminosity (left) and clump mass (right). The sources in the HII, IRb, IRw, and 70w groups are shown as green squares, red triangles, blue circles, and magenta diamonds, respectively. The Spearman's rank correlation coefficient, r_s, between the two quantities is presented on each plot.

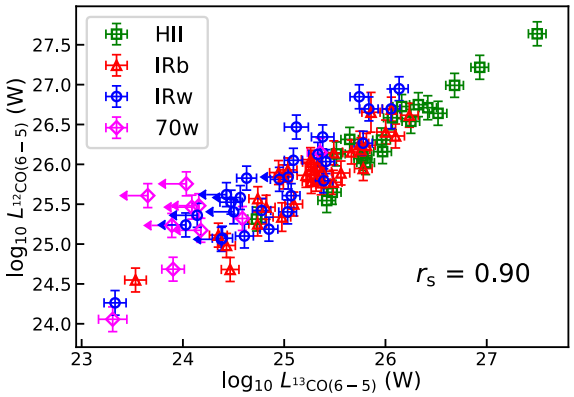

Fig. 7. Relation between the ^{13}CO (6–5) and ^{12}CO (6–5) line luminosities. The sources without ^{13}CO (6–5) detections are indicated as leftward arrows whose locations represent 3σ values. The colours and markers are the same as in Fig. 6.

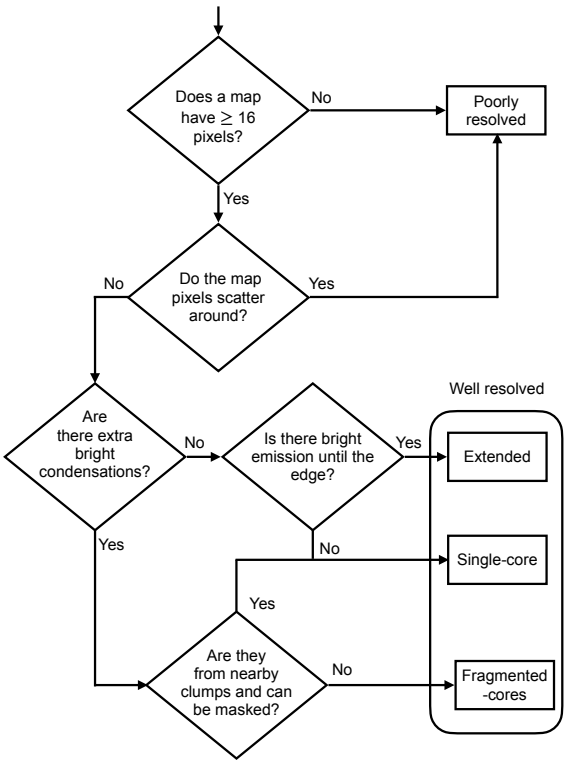

Fig. 8. Block diagram for our classification of sources based on our ^{13}CO (6–5) integrated intensity maps.

well-resolved sources, we classified those with a single bright core in the map centre as 'single-core' or 'extended'. Single-core clumps have bright emission well confined in the map centre, while extended clumps show emission extending from the centre to the edge of the maps, implying that our maps capture only a part of larger structures. ATLASGAL 870 µm maps of these regions indeed reveal large complexes of dust condensations, whose structures are generally consistent with the observed ^{13}CO (6–5) distributions (Appendix C). In addition to the simple single-core case described above, we also considered sources that have central cores along with additional peaks at the map outskirts as single-core, as the peripheral spots arise from neighbouring objects and can be masked out (Appendix D). Finally, we classified sources that have multiple central cores without extended emission as 'fragmented-cores'.

Table 2 presents the number of sources in each category and evolutionary stage. In total, 59 sources are considered as well-resolved. The majority of them (52) are single-core sources, while the rest (7) show extended emission or signs of fragmentation. Interestingly, 50 out of the 59 well-resolved clumps (85%) have evolved to IRb and HII phases, while 17 out of the 22 poorly resolved clumps (77%) are in younger stages (70w and IRw). This result suggests that the four evolutionary groups are distinctive in terms of the spatial distribution of their ^{13}CO (6–5) emission, as well as their peak brightness temperature.

Table 2. Number of sources in each category determined by the ^{13}CO (6–5) integrated intensity maps.

Category		70w	IRw	IRb	HII
Poorly resolved		3	14	5	0
Well resolved	Single-core	1	8	26	17
	Fragmented-cores	0	0	2	2
	Extended	0	0	2	1

4. Analyses

In this section, we investigate the distribution and kinematics of ^{13}CO (6–5) emission in the envelopes of massive clumps

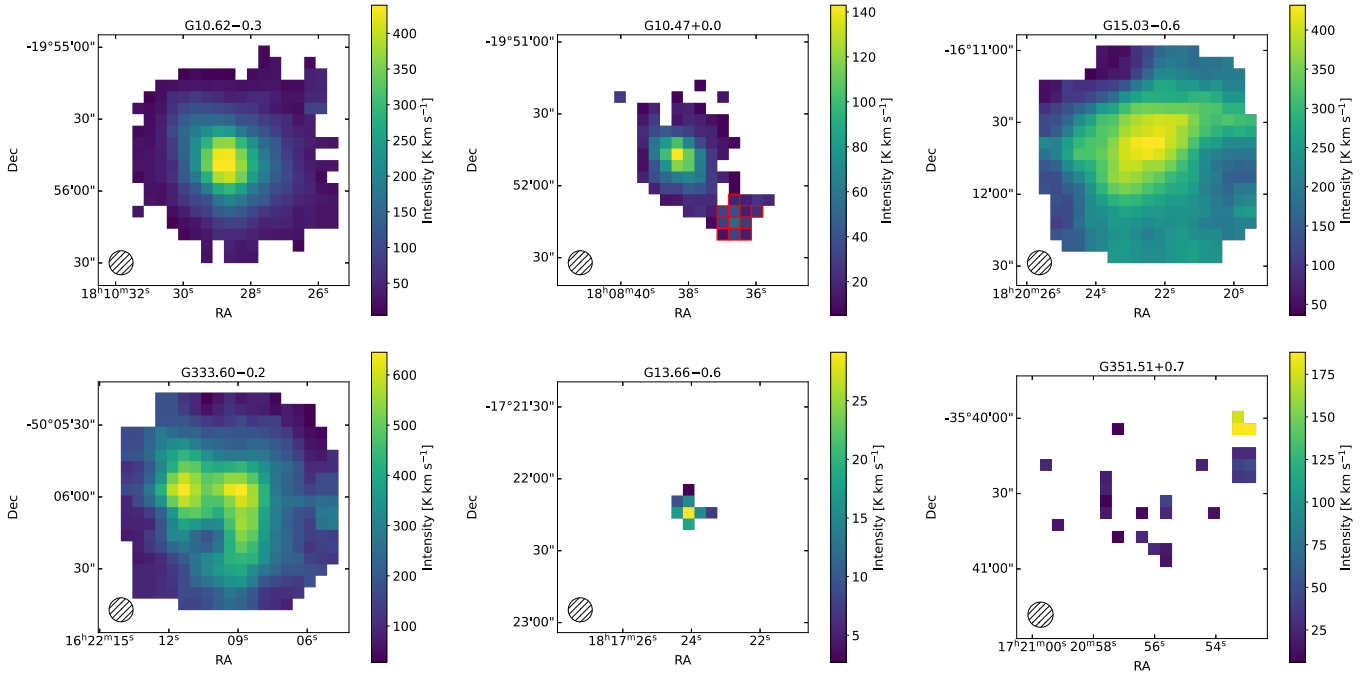

Fig. 9. Examples of the different morphological types in our sample. Top row: The first two panels show two single-core sources: the left one is an isolated source, while the right one has a neighbouring clump whose pixels outlined in red were masked to exclude them from further analyses. The most-right panel presents an extended source. Second row: The first panel showcases fragmented cores. The two remaining panels illustrate two poorly resolved clumps characterised by compact emission in neighbouring pixels (left) and distributed pixels (right). The hatched circle at the bottom left corner of each panel indicates the FWHM of telescope beam.

by considering 52 single-core sources (Sect. 2.3). While the simplest morphology of these sources makes our analyses straightforward, we note that we are biased in favour of evolved envelopes as the majority of the single-core sources are in the IRb or HII group. As such, we do not put too much emphasis on the information on evolutionary trends derived here.

4.1. Size and aspect ratio

We started our analyses by measuring the size of each source based on the total number of detected pixels. Specifically, we calculated the effective size, $S_{\rm eff}$, as the square root of the total emitting area and considered it as a representative size. The resultant cumulative distribution functions (Fig. 10) suggest that the ^{13}CO emission regions associated with HII sources are generally larger than those found for IRw and IRb sources. For example, the median sizes of the three groups (IRw, IRb, and HII) are 0.59, 0.63, and 0.99 pc, respectively, while the $S_{\rm eff}$ of the only 70w source is 0.37 pc. When a k-sample Anderson-Darling test was performed on the IRb and HII groups for which we have sufficient numbers of sources, the sizes of the HII envelopes were indeed found to be systematically larger at a significance level of 0.05.

In addition, we estimated the aspect ratio (APR) of each source by fitting a two-dimensional Gaussian function to the detected pixels in the integrated intensity image and found a range of 1.0–2.6 with a median of 1.3 and a standard deviation of 0.4. Considering that APRs vary with inclination angles and the members of our statistically significant sample of single-core sources likely have a wide range of inclination angles, the measured small range of the APR implies that the envelopes are less likely to be filamentary structures whose minimum APR is defined as three (Mattern et al. 2018).

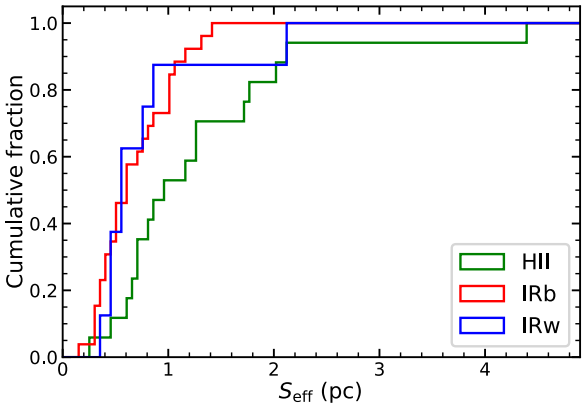

Fig. 10. Cumulative distribution functions of the effective size. The 70w group is not presented here, since it comprises only a single source.

4.2. Radial intensity profiles

Next, we examined the spatial distribution of ^{13}CO (6–5) emission by constructing the radial intensity profiles of our single-core sources. To do so, we divided each M_0 map into 5″-wide individual annuli centred on the peak location of ^{13}CO (6–5) emission and calculated median and standard deviation values. Example radial profiles are presented in Fig. 11.

The constructed radial profiles were analysed with power-law functions following Beuther et al. (2002):

$$F(r) \propto \begin{cases} r^{-m} & \text{if} \quad r > r_{\rm b} \\ r_{\rm b}^{-m} & \text{if} \quad r \leq r_{\rm b}, \end{cases} \tag{5}$$

where $F(r)$ is the integrated intensity at a given radius r, m is the power-law index, and $r_{\rm b}$ is the break radius within which

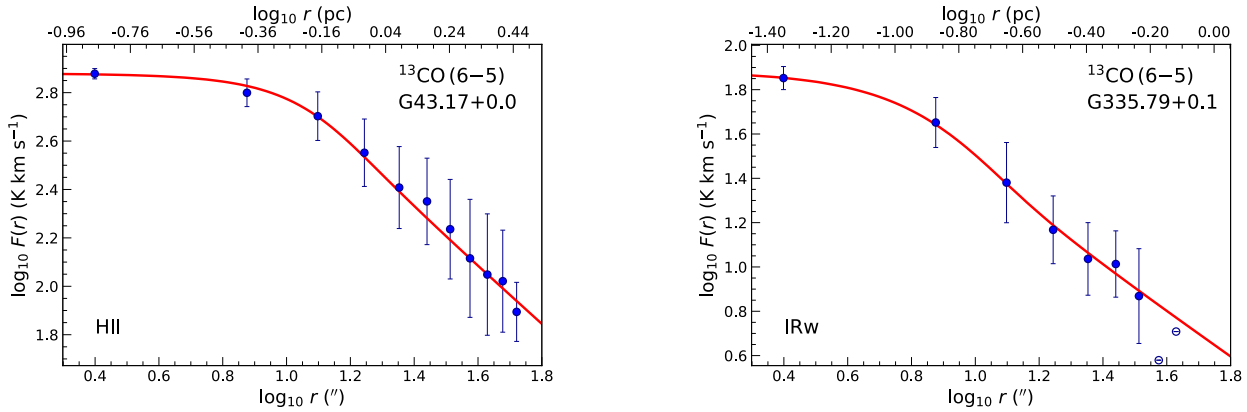

Fig. 11. Example ^{13}CO (6–5) radial profiles for an HII source (G43.17+0.0) (left) and an IRw source (G335.79+0.1) (right). At 5″-wide individual annuli, the median and standard deviation values are presented as filled blue circles and associated 'error' bars. Annuli with an insufficient number of detected pixels are indicated as open blue circles and were excluded from the determination of best-fit curves (red).

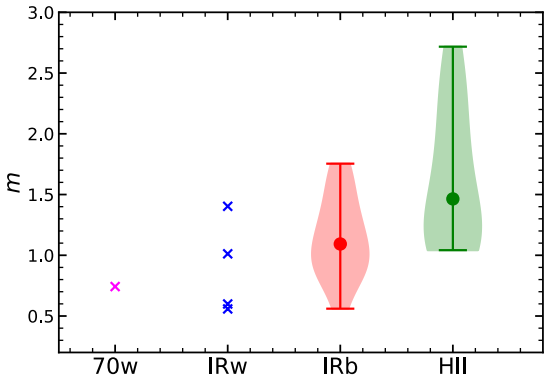

Fig. 12. Distributions of the power-law index, m, for the different evolutionary groups: 70w, IRw, IRb, and HII in magenta, blue, red, and green, respectively. The colours and symbol schemes are the same as in Fig. 3.

the integrated intensity becomes constant (introduced to prevent $F(r)$ from going to infinity as r approaches zero). This power-law function was devised based on the theoretical expectations for the structures of collapsing cores (e.g. Shu et al. 1987; McLaughlin & Pudritz 1996; Motte & André 2001) and was convolved with a 10″-size Gaussian beam (comparable to our ^{13}CO (6–5) angular resolution) to be fitted to our radial profiles.

To constrain the power-law index and break radius, we performed non-linear least squares fitting using the Python function `scipy.optimize.curve_fit` on the model and observed radial profiles. We excluded data points at large radii for which the number of detected pixels is less than 5% of the total pixels (e.g. open blue circles in Fig. 11) from fitting, as they are less likely to be statistically representative. The best-fit curves were found to reproduce the observed radial profiles reasonably well within 1σ uncertainties (hence obviating the need for a second power-law function), and their parameters are presented in Appendix A.

We examined the constrained power-law indices and break radii in detail by focusing on 36 sources (one 70w, four IRw, 17 IRb, and 14 HII sources) whose the best-fit parameters are statistically significant (i.e. higher than their 1σ uncertainties). The distributions of the power-law index for these sources are presented in Fig. 12. We find that the power-law index ranges from 0.5 to 2.7 across the entire sample and varies by less than a factor of three within each group, indicating relatively comparable slopes between the sources in the same evolutionary stage. Interestingly, there is a slight tendency for the power-law index to increase towards more evolved sources: median m values are 0.8, 1.1, and 1.5 for the IRw, IRb, and HII group, respectively. A k-sample Anderson-Darling test on the IRb and HII groups indeed suggests that the HII sources have distinctly steeper slopes than the IRb sources. These steeper slopes could result from a significant increase in the brightness of ^{13}CO (6–5) emission in the central parts of the most evolved sources (e.g. Fig. 3), which is in turn most likely due to the strong enhancement in density and/or temperature.

In addition, we probed the constrained break radii and found that r_b changes from 0.02 pc to 0.44 pc across the entire sample (Fig. 13). The variations in r_b (e.g. a factor of 22 for the whole sample and a factor of 13 for the IRb sources) are much more significant than those in m, which partly reflects the sources' wide range of distances. As in the case of m, r_b tends to increase towards the most evolved sources (e.g. median r_b of 0.05, 0.05, and 0.14 pc for the IRw, IRb, and HII group, respectively), and a k-sample Anderson-Darling test on the IRb and HII groups confirms this tendency.

While the break radius was introduced for a mathematical reason, it could manifest underlying physical conditions in the central parts of our sources, such as fragmentation on small scales and high opacity of the ^{13}CO (6–5) emission. As for the fragmentation scenario, interferometric observations of massive star-forming clumps, including several of our sources, have indeed identified fragmented cores with sizes smaller than or comparable to our spatial resolution ($\lesssim$0.1 pc) (Cesaroni et al. 2017; Beltrán et al. 2021). The convolution of these fragmented cores with our single-dish beam would smooth out small-scale structures and result in the uniform distribution of ^{13}CO (6–5) emission in the source centres. Interestingly, Beuther et al. (2002) argued that more massive clumps tend to produce larger fragmented cores or clusters, which implies larger r_b for more massive clumps. We indeed found such a positive correlation between r_b and M_{clump} (Fig. 13, bottom), supporting the fragmentation scenario for the break radius. However, we also note that M_{clump} is related to D as $M_{clump} \propto D^2$ (König et al. 2017), which could partially contribute to the correlation between r_b and M_{clump}.

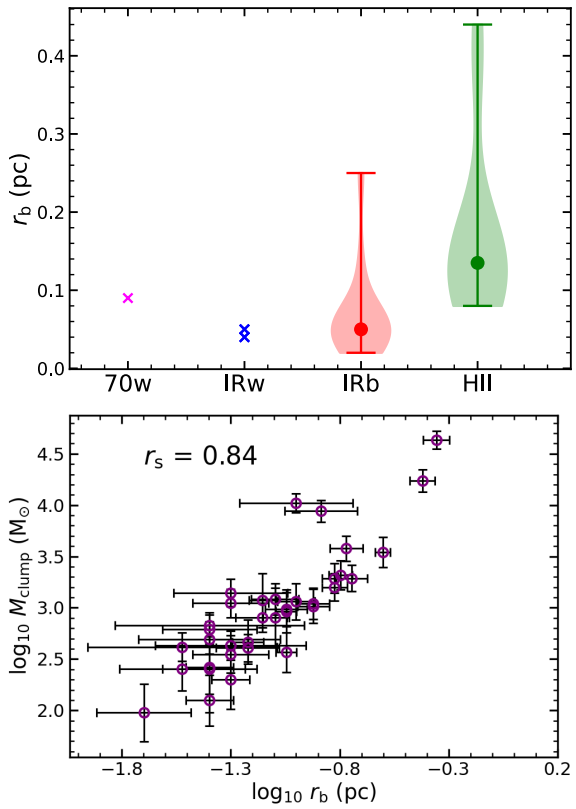

Fig. 13. Top: Distributions of the break radius, r_b, for the different evolutionary groups. The colours and symbol schemes are the same as in Fig. 3. Bottom: Scatter plot between the clump mass and the break radius. The Spearman's rank correlation coefficient is presented on the top left corner of the plot.

Another possible explanation for the break radius is high opacity of ^{13}CO (6–5) emission. When the ^{13}CO (6–5) emission is optically thick, its brightness temperature approaches the gas kinetic temperature, resulting in the saturation of the integrated intensity. Our preliminary analysis based on local thermodynamic equilibrium (LTE) suggests that most of our sources likely have optically thin ^{13}CO (6–5) emission (Appendix B). Besides, only a weak correlation exists between $\tau_{^{13}CO}$ and r_b (Spearman's rank correlation coefficient of 0.32). These results imply that the break radius is less likely to be determined by the effect of opacity.

In conclusion, we found that the radial intensity profiles of single-core clumps can be reasonably well described as power-law functions, indicating relatively simple structures of the envelopes of massive star-forming regions. The observed radial profiles retain comparable slopes within the same evolutionary group, while the most evolved sources tend to have steeper slopes that are likely related to star formation processes (higher densities and/or temperatures). In addition, fragmentation could begin in the early stage of high-mass star formation (70w) and be responsible for the uniform intensity distribution in the central parts of our sources.

4.3. Comparison between dust and warm molecular gas distributions

In this section, we examine how the distribution of warm molecular gas in high-mass star-forming regions compares to that of the colder medium by comparing ^{13}CO (6–5) and 160 μm radial intensity profiles. For our examination, we employed Hi-GAL 160 μm maps as their angular resolution (11″× 13″) is comparable to that of the ^{13}CO (6–5) data (Molinari et al. 2010).

To derive radial profiles, Hi-GAL 160 μm maps with a size of 5′ × 5′ were first converted to the equatorial coordinate system to match the ^{13}CO (6–5) data. Once the pixels with emission from nearby objects were masked (Appendix D), 160 μm radial profiles were constructed in the same manner as the ^{13}CO (6–5) radial profiles (Sect. 4.2) and were cut off at 100″ to meet the angular extent of the ^{13}CO (6–5) radial profiles. In total, we produced the 160 μm radial profiles for a sample of 36 sources for which we found reliable fitting parameters for the ^{13}CO (6–5) radial profiles (Sect. 4.2).

Visual inspections of the derived radial profiles indicated the need for more than one power law for some sources (e.g. Fig. 14, right), prompting us to fit both single (Eq. (5)) and two power-law functions to the radial profiles. The two power-law model can be written as follows:

$$F(r) \propto \begin{cases} r_{b_1}^{-m_i} & \text{if} \quad r \le r_{b_1} \\ r^{-m_i} & \text{if} \quad r_{b_1} < r \le r_{b_2} \\ r^{-m_o} & \text{if} \quad r > r_{b_2}, \end{cases} \tag{6}$$

where m_i and m_o are the indices for the inner and outer power-law functions, r_{b_1} is the break radius within which the central intensity distribution becomes constant, and r_{b_2} is the transition radius from the inner to the outer power-law function. Both the single and two power-law models were convolved with a 12″-size Gaussian beam (average of the major and minor axes of the 160 μm beam) to be fitted to our radial profiles.

We performed the same non-linear least squares fitting as in Sect. 4.2 and found that the two power-law model significantly improves fitting results for 27 sources by lowering the reduced χ^2 by more than a factor of two compared to the single power-law model. The radial profiles of the remaining nine sources were better described with the single power-law model, considering that the reduced χ^2 was improved by less than a factor of two or the width of the inner power-law distribution was smaller than the 160 μm beam; in other words, the inner power-law distribution is not well constrained. The fitting results for all 36 sources were deemed reliable (i.e. fitting parameters above their 1σ uncertainties) and are summarised in Appendix A.

For 26 out of the 27 sources for which the two power-law model is favoured, we found $m_i > m_o$, which suggests that central compact cores are surrounded by extended diffuse structures. Interestingly, Beuther et al. (2002) found the opposite result (shallower inner gradients) from their analysis of 1.2 mm dust continuum emission in a number of massive star-forming regions. It is difficult to make a one-to-one comparison with our result, however, since the sources in Beuther et al. (2002) suffer from distance ambiguities and we cannot make sure if the 1.2 mm and 160 μm profiles probe comparable spatial extents.

The inner power-law distributions of the 160 μm radial profiles have on average similar extents as the ^{13}CO (6–5) radial profiles (~40″), indicating that they probe comparable physical scales. Considering this, we directly compared the properties of the inner power-law distributions of the 160 μm radial profiles (power-law index and break radius) to those of the ^{13}CO (6–5) radial profiles. To increase the sample size, we also considered the nine sources whose 160 μm radial profiles were fitted with the single power-law function. Figure 15 shows a positive correlation between the power-law indices of the 160 μm and ^{13}CO (6–5) radial profiles. On closer inspection, the 160 μm profiles generally have steeper slopes, implying that 160 μm and

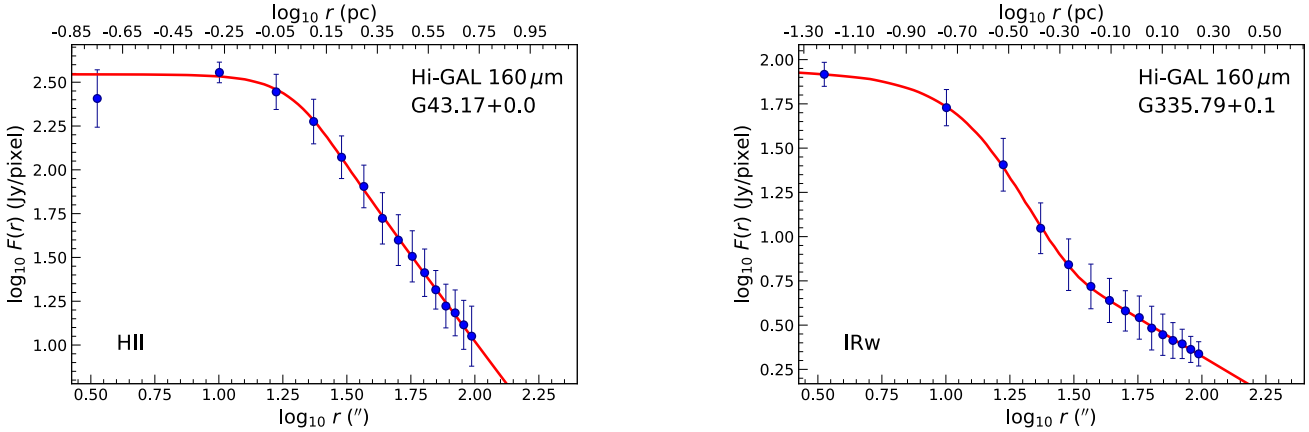

Fig. 14. Example 160 μm radial profiles of G43.17+0.0 (left) and G335.79+0.1 (right). As in Fig. 11, the median and standard deviation values at 5″-wide individual annuli are shown as blue circles and associated 'error' bars. Best-fit curves (singular and two power-law model for G43.17+0.0 and G335.79+0.1, respectively) are overlaid in red.

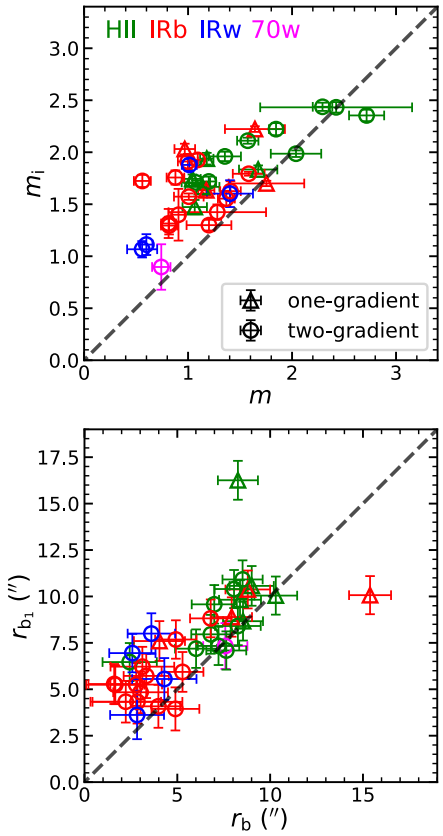

Fig. 15. Comparison of the 160 μm and ^{13}CO (6–5) radial profiles in terms of the power-law index (top) and break radius (bottom). The 27 sources whose 160 μm radial profiles were fitted with the two power-law model are shown as circles, and their inner power-law distributions are used for the comparison. The remaining nine sources with the single power-law distributions in 160 μm emission are indicated as triangles. Both circles and triangles are colour coded based on evolutionary stage: 70w, IRw, IRb, and HII in magenta, blue, red, and green, respectively. One-to-one relations are overlaid as dashed lines.

^{13}CO (6–5) emission could trace different physical conditions or processes (e.g. 160 μm emission likely traces colder structures than ^{13}CO (6–5) emission). Alternatively, the discrepancy in the power-law indices could result from the different dependencies of the two tracers on the gas temperature and density. Interestingly, the 160 μm radial profiles tend to be steeper towards more evolved sources, which is in line with what we found from the ^{13}CO (6–5) radial profiles (Sect. 4.2). On the other hand, the break radii of the 160 μm and ^{13}CO (6–5) radial profiles seem to be consistent in most cases, suggesting that the same mechanism (i.e. fragmentation) is likely responsible for the uniform distribution of 160 μm and ^{13}CO (6–5) emission in the central parts of our sources.

In conclusion, we found that the 160 μm emission from our sources typically shows two distinct structures: compact cores and their surrounding diffuse halos. Compared to 160 μm emission, ^{13}CO (6–5) emission from warm gas is more compact and probes mostly the core structures with its radial distribution decreasing less steeply. The emission from both tracers shows uniform intensity distributions in the centre of our sources, which likely originates from fragmentation on small scales.

4.4. Mean velocity gradients

In addition to the spatial distribution, we examined the kinematics of warm molecular gas for the sources of our sample of high-mass star-forming regions by analysing the ^{13}CO (6–5) first moment maps of our 52 single-core sources. Visual inspections of the ^{13}CO (6–5) M_1 maps reveal a variety of velocity fields, including linear gradients or more complex trends such as radial, hourglass-like, and outflow-like gradients (Fig. 16). Among these various velocity fields, the linear gradients are the most common (44 sources), while the other types occur much less often (eight sources).

To quantify the observed ^{13}CO (6–5) velocity fields, we estimated the mean velocity gradients (MVGs) by fitting the following equation from Goodman et al. (1993) to our M_1 maps using the Python function `scipy.optimize.curve_fit`:

$$v_{\rm LSR} = v_0 + a\Delta\alpha + b\Delta\beta, \quad (7)$$

where $v_{\rm LSR}$ is the velocity at a given pixel, v_0 is the velocity at a reference position, $\Delta\alpha$ and $\Delta\beta$ are the right ascension (RA) and declination (Dec) offsets from the reference position measured in radians, and a and b are the projections of the velocity gradient per radian onto the RA and Dec axes. For this fitting, we fixed the reference position at the centre of each source, since the MVGs

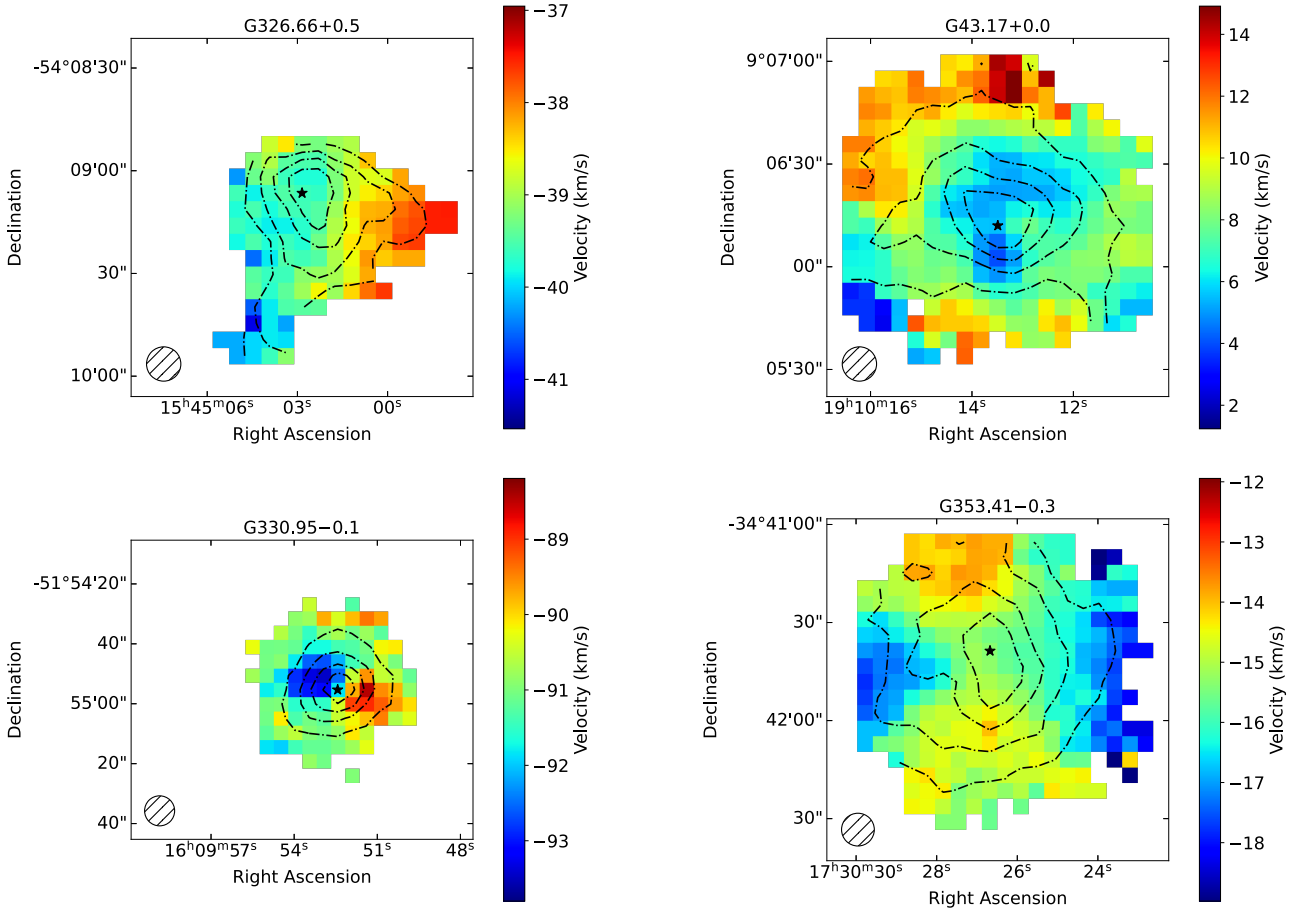

Fig. 16. Examples of various velocity fields in our sample. The ^{13}CO (6–5) M_1 maps from the top left corner in the clockwise direction demonstrate linear, radial, hourglass-like, and outflow-like gradients, respectively. For each source, the integrated intensities are overlaid as contours with levels ranging from 20% to 80% of the peak value in steps of 20%, and the peak position is marked by a star. Finally, the FWHM of the telescope beam is shown by a hatched circle.

measure the general direction of gas motions and hence the fitted a and b do not depend on the reference position.

Once a and b were constrained, the magnitude of the MVG, $\mathcal{G}$ (km s^{-1} pc^{-1}), was computed as follows:

$$\mathcal{G} = \frac{\sqrt{a^2 + b^2}}{D}, \tag{8}$$

where D is the distance to the source. In addition, the position angle (PA) of the MVG, $\theta_{\mathcal{G}}$ (degree), was measured counterclockwise from the north to the red-shifted gradient (i.e. red arrows in Fig. 18). Specifically, $\theta_{\mathcal{G}}$ was calculated from $\alpha = \left|\tan^{-1}(a/b)\right|$ as follows:

$$\theta_{\mathcal{G}} = \begin{cases} \alpha & \text{if} \quad a > 0 \quad \text{and} \quad b > 0 \\ 180^\circ - \alpha & \text{if} \quad a > 0 \quad \text{and} \quad b < 0 \\ 180^\circ + \alpha & \text{if} \quad a < 0 \quad \text{and} \quad b < 0 \\ 360^\circ - \alpha & \text{if} \quad a < 0 \quad \text{and} \quad b > 0. \end{cases} \tag{9}$$

We examined the constrained $\mathcal{G}$ for 41 sources (one 70w, 5 IRw, 21 IRb, and 14 HII sources) that have statistically significant gradients $\mathcal{G} \geq 3\sigma_{\mathcal{G}}$ (Goodman et al. 1993) and found that $\mathcal{G}$ generally ranges from 1 km s^{-1} pc^{-1} to 8 km s^{-1} pc^{-1} independent of the evolutionary group (Fig. 17). An outlier is G351.77−0.5, whose large gradient of 20 km s^{-1} pc^{-1} likely originates from the strong outflow of the source. Interestingly,

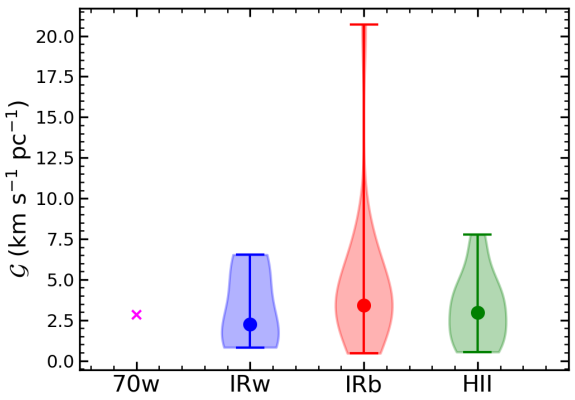

Fig. 17. Distributions of the MVG magnitude, $\mathcal{G}$, for the different evolutionary groups. The colours and symbol schemes are the same as in Fig. 3.

our median $\mathcal{G}$ (~3 km s^{-1} pc^{-1}) is comparable to that estimated by Tobin et al. (2011) for a sample of low-mass protostar envelopes (2 km s^{-1} pc^{-1}). A one-to-one comparison of these results, however, is not straightforward, considering that the angular resolution of the study by Tobin et al. (2011) is three times larger than that of our data. On the other hand, the sources in that study are, at distances of 125–460 pc, much closer than

Table 3. Possible interpretations of the observed gas kinematics.

Criteria	Interpretations [(a)]	
$\Delta PA_1 \leq 45°$ & $\Delta PA_2 \leq 45°$	The outflows affect the envelopes, as well as the clumps.	(5)
$\Delta PA_1 \leq 45°$ & $\Delta PA_2 > 45°$	The envelopes are impacted by the outflows and are decoupled from the clumps.	(2)
$45° < \Delta PA_1 \leq 135°$ & $\Delta PA_2 \leq 45°$	The envelopes and clumps rotate along the outflow axes.	(4)
$45° < \Delta PA_1 \leq 135°$ & $\Delta PA_2 > 45°$	The envelopes rotate along the outflow axes and are decoupled from the clumps.	(3)
$\Delta PA_1 > 135°$ & $\Delta PA_2 \leq 45°$	The envelopes are dominated by the clump kinematics.	(0)
$\Delta PA_1 > 135°$ & $\Delta PA_2 > 45°$	The outflows, envelopes, and clumps have different kinematics.	(1)

Notes. [(a)]Numbers in brackets present quantities of clumps in each category.

the sources in our sample. As we demonstrate in Appendix E, the measurement of the MVGs depends on the physical resolution.

4.5. Comparison of gas kinematics on different spatial scales

Section 4.4 shows that ^{13}CO (6–5) emission in our single-core sources frequently shows linear velocity gradients. To provide insights into the origin of these velocity gradients, we compared gas kinematics on three different spatial scales, including outflows from small-scale YSO cores that are traced by high velocity ^{12}CO (6–5) emission, intermediate-scale envelopes traced by ^{13}CO (6–5) emission, and large-scale clumps traced by ^{13}CO (2–1) emission. For sources in the early stage of star formation, we can expect that the intermediate-scale envelopes retain the kinematics of their parental clumps, inducing an alignment between the envelope and clump kinematics (e.g. Smith et al. 2011). As star formation progresses, strong outflows may be launched and entrain dense gas from the envelopes, resulting in an alignment between the outflow and envelope kinematics, similar to envelopes of Class 0 low-mass protostars (Arce & Sargent 2006). Once the outflows significantly erode into the envelopes, the remaining envelope material could be concentrated near the protostellar discs and be rotating together, leading to a perpendicular alignment between the outflow and envelope kinematics, similar to what is found in envelopes of low-mass Class I protostars by Arce & Sargent (2006). These possible scenarios demonstrate that the comparison of gas kinematics on different spatial scales can be valuable for understanding the processes of high-mass star formation.

We started our comparison of gas kinematics by evaluating how velocity fields of the outflows and the envelopes are linked to each other. To do so, we utilised ^{12}CO (6–5) outflow data from Navarete et al. (in preparation) and examined the absolute angular difference ΔPA_1 = | PA of the ^{13}CO (6–5) MVGs − PA of the ^{12}CO (6–5) outflows | (Fig. 18 and Appendix F). Navarete et al. identified outflow sources in the Top100 sample by integrating ^{12}CO (6–5) emission in high-velocity wings and divided them into several categories, such as single, multiple, unresolved, and resolved (defined as clearly separated blue and red lobes) outflows. For our examination, we computed ΔPA_1 for 22 sources (one 70w, three IRw, twelve IRb, and six HII sources) that have single resolved outflows along with significant ^{13}CO (6–5) MVGs and compared the resultant distributions for the different evolutionary groups. Figure 19 shows that the ΔPA_1 distributions support neither the envelope entrainment ($\Delta PA_1 \sim 0°$) nor the envelope-disc co-rotation ($\Delta PA_1 \sim 90°$) and are not significantly different between the evolutionary groups.

In addition, we probed a relation between the envelope and clump kinematics by comparing the ^{13}CO (6–5) and ^{13}CO (2–1) MVGs. To derive ^{13}CO (2–1) MVGs for our single-core sources, we used data from the SEDIGISM survey (Schuller et al. 2021) and produced $2' \times 2'$ sized M_0 and M_1 maps (Fig. 20). The $2' \times 2'$ maps, which are ∼1.5 times larger than our ^{13}CO (6–5) maps, were chosen as they include a majority of the regions in which the ^{13}CO (2–1) line's intensity is higher than 40% of the peak value. With the resultant M_0 and M_1 maps, we then estimated MVGs by applying Eqs. (8) and (9) and found that 23 sources (two IRw, twelve IRb, and nine HII sources) have statistically significant MVGs in both ^{13}CO (2–1) and ^{13}CO (6–5) emission. The estimated ^{13}CO (2–1) MVGs are presented in Appendix A.

In Fig. 21, we compared the magnitudes of the ^{13}CO (6–5) and ^{13}CO (2–1) MVGs and found that $\mathcal{G}$ is generally higher in ^{13}CO (6–5) emission. For example, the median magnitudes of the ^{13}CO (6–5) and ^{13}CO (2–1) MVGs are 2.8 km s^{-1} pc^{-1} and 0.7 km s^{-1} pc^{-1}, respectively. The smaller $\mathcal{G}$ for ^{13}CO (2–1) could partially result from the coarser angular resolution of the SEDIGISM data compared to our ^{13}CO (6–5) beam (30″ versus 10″; see Appendix E for further discussion). In addition, we examined the absolute angular difference ΔPA_2 = | PA of the ^{13}CO (6–5) MVGs − PA of the ^{13}CO (2–1) MVGs | (Fig. 22) and found that 13 sources have relatively comparable PAs in both transitions ($\Delta PA_2 \lesssim 45°$), while the remaining 10 sources show a wide range of the angular difference. Interestingly, both the magnitude and PA comparisons show no dependence on the evolutionary groups.

Finally, we examined the relationship between the outflow, envelope, and clump kinematics more comprehensively by comparing the ^{12}CO (6–5), ^{13}CO (6–5), and ^{13}CO (2–1) velocity information for a smaller sample of 15 sources. For our comparison, we considered six possibilities based on the measured ΔPA_1 and ΔPA_2 (Table 3) and examined them along with the M_1 maps. This detailed view on the individual sources revealed that the origin of the ^{13}CO (6–5) kinematics is relatively clear for seven sources only. For example, the ^{13}CO (6–5) kinematics is likely decoupled from the surrounding clumps for four sources. Three of them (G330.95−0.1, G332.09−0.3, and G337.92−0.4; two IRb and one HII sources) show a hint of the envelope entrainment, while G305.21+0.2 (IRb) has co-rotating envelope and disc. In addition, two sources (G335.79+0.1 and G345.00−0.2; that is, one IRw and one HII source) show coherent rotations of the envelopes and clumps along the outflow axes. The ^{13}CO (6–5) kinematics of the remaining source G337.41−0.4 (HII) seems to be dominated by the surrounding clump with no obvious impact from outflows.

In summary, we found that our single-core sources have significant linear velocity gradients in ^{13}CO (6–5) emission. The origin of these velocity gradients is currently unclear, although it is less likely to be systematically linked to internal star formation processes (that is, $\mathcal{G}$ does not vary much between the different evolutionary groups). The envelope kinematics traced by

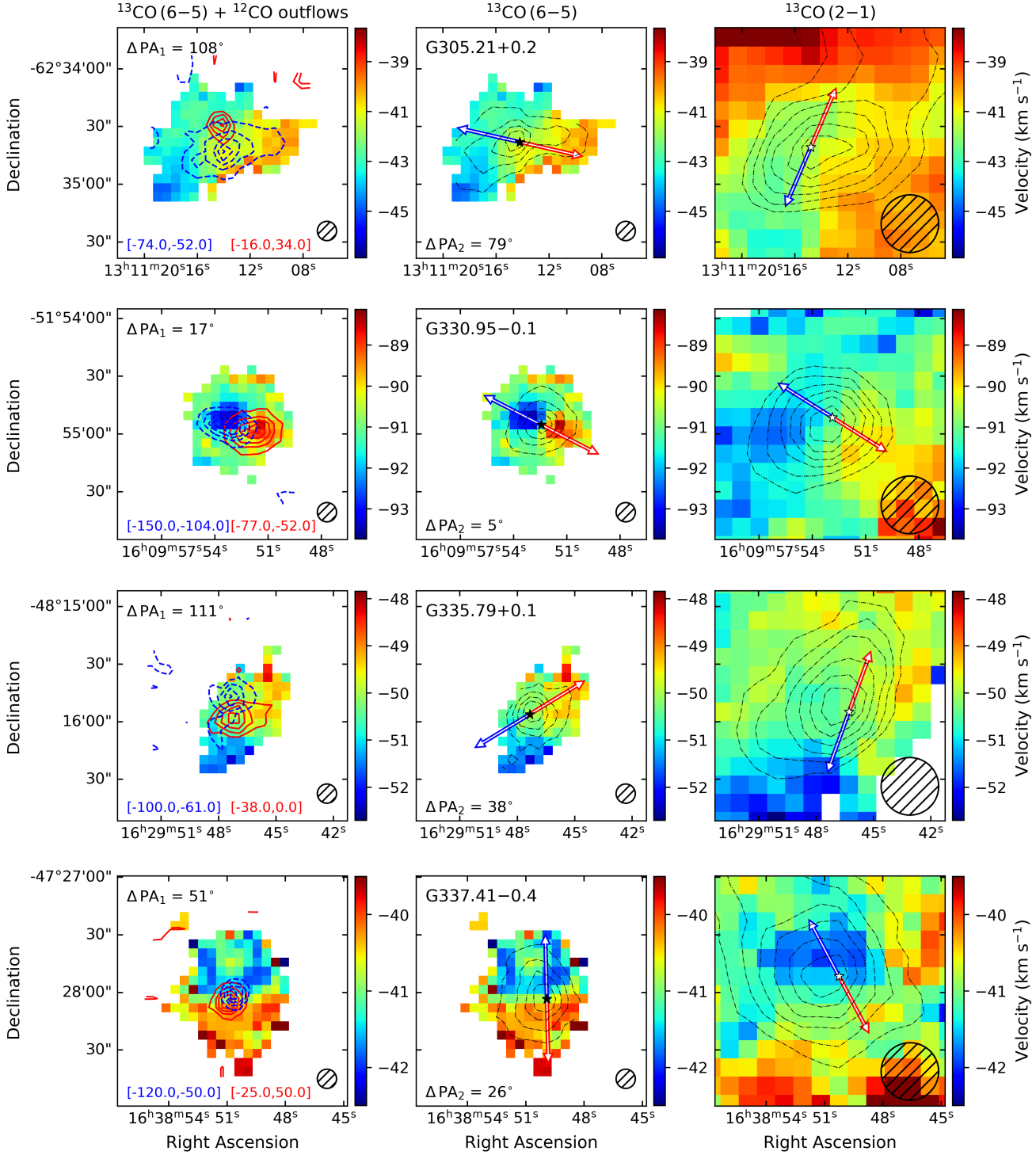

Fig. 18. Comparison of ^{13}CO (6–5), ^{12}CO (6–5), and ^{13}CO (2–1) gas kinematics for four example sources. Left column: M_1 maps of ^{13}CO (6–5) emission. For each source, the blue and red lobes of ^{12}CO (6–5) outflows are overlaid as contours with decreasing levels ranging from 95% of the peak integrated intensities down to the first level above 3σ, in steps of 20% peak values. For G309.38−0.1 and G343.76−0.1 (Appendix F), a threshold of 2σ was used instead. The velocity ranges over which the blue and red lobes were integrated are presented at the bottom left, while the absolute angular difference between the PAs of the ^{13}CO (6–5) and ^{12}CO (6–5) MVGs (ΔPA$_1$) is shown at the top left. Middle column: Same M_1 maps as in the left panel, but with the ^{13}CO (6–5) integrated intensities as contours (20% to 80% of the peak values in steps of 20%). The centre of each source with the maximum integrated intensity is indicated as a black star, while the direction of the ^{13}CO (6–5) MVG is shown as blue and red arrows. The absolute angular difference between the PAs of the ^{13}CO (6–5) and ^{13}CO (2–1) MVGs (ΔPA$_2$) is summarised at the bottom left. Right column: M_1 maps of ^{13}CO (2–1) emission. The ^{13}CO (2–1) integrated intensities are shown as contours with levels ranging from 40% to 90% of the peak values in steps of 10%, while the directions of the ^{13}CO (2–1) MVGs are indicated as blue and red arrows. The centres of the sources with the peak integrated intensities are marked as white stars. Finally, for each plot, the FWHM of corresponding telescope beam is displayed by a hatched circle.

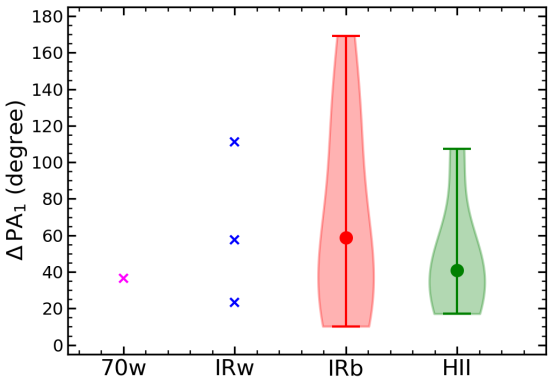

Fig. 19. Distributions of the absolute angular difference ΔPA_1 for the different evolutionary groups. The colours and symbol schemes are the same as in Fig. 3.

^{13}CO (6–5) emission appears to be highly complex, and probing its origin would benefit from higher sensitivity, higher resolution observations of a bigger sample of high-mass star-forming regions.

5. Discussion

Our observations of ^{13}CO (6–5) emission towards a statistically significant sample of massive star-forming regions have allowed us to characterise the warm envelopes surrounding high-mass YSOs. In this section, we discuss potential origins of the emission and examine ^{13}CO (6–5) kinematics in detail for several of our sources.

5.1. Excitation of ^{13}CO (6–5) emission in massive star-forming regions

Key characteristics of the Top100 sources, such as gas temperature and column density, have been examined by various authors based on multi-transition observations of molecular species. For example, Giannetti et al. (2017) derived temperature by analysing emission from CH_3CN, CH_3CCH, and CH_3OH and found a progressive warm-up of the molecular gas with evolution that likely results from stellar feedback. In addition, Giannetti et al. (2014) showed that the abundance of CO molecules in the gas phase increases with evolution, as warmer dust grains enable frozen CO molecules to sublimate efficiently. A combination of the increased temperature and CO column density in the Top100 sources would excite more CO molecules to mid-J levels, resulting in the observed increase in the ^{13}CO (6–5) brightness temperature (Sect. 3.1) and line luminosity (Sect. 3.3). This suggests that ^{13}CO (6–5) emission can be used efficiently to probe the processes of high-mass star formation.

The warm molecular gas traced by mid-J ^{13}CO emission can be heated by a range of radiative and mechanical feedback processes. For nearby low-mass star-forming regions, these processes can be probed in detail and observational and theoretical studies have suggested that mid-J ^{13}CO emission originates from passively heated envelopes, UV-heated outflow cavity walls, and outflows themselves (van Kempen et al. 2009a,b; Yıldız et al. 2012). Considering that envelopes and outflows are also prevalent in regions of high-mass star formation, the observed ^{13}CO (6–5) emission in the Top100 sources could have similar origins.

In the scenario of passively heated envelopes, dust grains are warmed up by absorbing radiation from central protostars and subsequently heat up the surrounding molecular gas via gas-dust collisions (Jørgensen et al. 2002; Kristensen et al. 2012). This mechanism has been shown to be responsible for part of the observed ^{13}CO (6–5) emission in a large sample of low-mass YSOs (Yıldız et al. 2015). While the same mechanism could certainly work for high-mass star-forming regions, dedicated modelling of gas and dust in massive envelopes is required to assess the exact role of passive heating on the excitation of ^{13}CO (6–5) emission in such complex systems.

In addition to the passively heated envelopes, ^{13}CO (6–5) emission could partly arise from UV-heated outflow cavity walls. For low-mass YSOs, UV photons can be created from disc-protostar accretion boundary layers or shocked spots along outflows. These UV photons escape through outflow cavities and are scattered by dust grains on their way, producing PDRs along the cavity walls (Spaans et al. 1995; Yıldız et al. 2015). While the efficacy of the same mechanism for high-mass star-forming regions has not been confirmed, PDRs have been observed towards many massive YSOs, in particular evolved ones whose intense UV radiation can ionise hydrogen atoms in significant volumes around them. For example, Leurini et al. (2013) analysed a number of mid-J CO maps for G327.3−0.6 and found that the emission lines, including ^{13}CO (6–5), are dominated by the PDR around a local HII region. In addition, multiple PDR layers have been proposed to reproduce the ^{13}CO (6–5) observations of several high-mass star-forming regions, such as Cepheus A, DR21, and W49 (Graf et al. 1993; Koester et al. 1994). Interestingly, our HII sources have ^{13}CO (6–5) brightness temperatures that are comparable to those measured by Graf et al. (1993), implying a non-negligible impact of UV photons on the excitation of ^{13}CO (6–5) emission in our most evolved sources.

Finally, mechanical processes such as outflows could contribute to the excitation of ^{13}CO (6–5) emission. For example, Yıldız et al. (2012) showed that ^{13}CO (6–5) spectra towards the low-mass protostar NGC 1333 IRAS 4A and 4B have both narrow and broad components with FWHMs of $\sim$2 km s^{-1} and $\sim$10 km s^{-1}. The same type of broad component has been found in low-J (Yang et al. 2018) and mid-J ^{13}CO transitions (Sect. 3.2) for ATLASGAL sources, implying that outflows are capable of entraining and heating the ^{13}CO-traced dense gas in massive star-forming regions. Currently, there is a lack of shock modelling effort to study the excitation of mid-J ^{13}CO emission in outflows, and future studies are needed. In addition to outflows, other mechanical processes during high-mass star formation, such as accretion flows onto clumps and gravitational collapse of clumps (Heitsch et al. 2009; Vázquez-Semadeni et al. 2019), could also inject a significant amount of energy into the surrounding medium and excite ^{13}CO (6–5) emission. This mechanism could be vital in particular for early-type clumps without central heating sources where gravitational collapse has just started (Pillai et al. 2023).

All in all, our study demonstrates that ^{13}CO (6–5) emission is ubiquitous in a variety of massive clumps, ranging from young sources where protostars have not been yet formed to evolved sources with strong HII regions. This suggests that ^{13}CO (6–5) emission could be excited by different processes at different epochs of high-mass star formation.

5.2. ^{13}CO (6–5) kinematics in individual clumps

Our velocity analyses for a statistically significant sample suggest the complex nature of ^{13}CO (6–5) kinematics in high-mass star-forming regions (Sects. 4.4 and 4.5). In an attempt to shed more light on the processes that drive ^{13}CO (6–5) kinematics, we

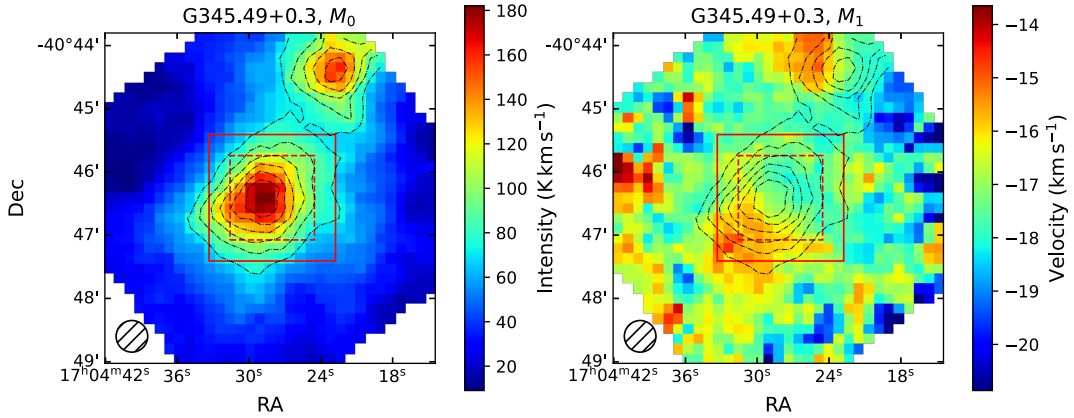

Fig. 20. ^{13}CO (2–1) M_0 (left) and M_1 (right) maps of an example source, G345.49+0.3. In both maps, the integrated intensities are overlaid as contours with levels ranging from 40% to 90% in steps of 10% of the largest integrated intensity. The 80″ × 80″ coverages of the ^{13}CO (6–5) data are outlined as dashed red boxes, while the 2′ × 2′ regions where we extracted clump-scale kinematics are indicated by solid red boxes. At the left bottom corner of each map, the FWHM of the telescope beam is shown by a hatched circle.

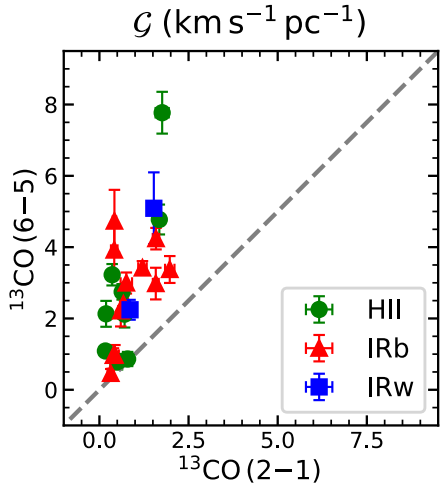

Fig. 21. Comparison between the magnitudes of the ^{13}CO (6–5) and ^{13}CO (2–1) MVGs (IRw, IRb, and HII group in blue, red, and green, respectively). A one-to-one relation is indicated by the dashed grey line.

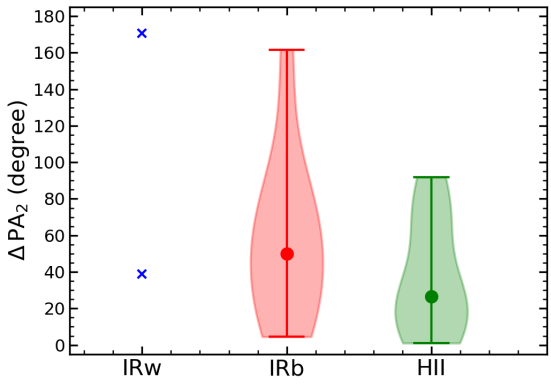

Fig. 22. Distributions of the absolute angular difference ΔPA_2 for the different evolutionary groups. The colours and symbol schemes are the same as in Fig. 12.

present here a detailed examination of several individual sources based on complementary information from literature. Our source selection was based on the availability of kinematics information from other tracers, especially those with high spatial resolutions.

G43.17+0.0 (HII)

This HII region source is a part of the well-studied Galactic mini-starburst complex W49A, whose enhanced star formation efficiency has been attributed to various processes, including gravitational collapse (Welch et al. 1987), a cloud-cloud collision (Serabyn et al. 1993), expanding shells (Peng et al. 2010), and re-collapsing shells (Rugel et al. 2019). In our observations, ^{13}CO (6–5) emission appears across a region of $S_{\rm eff}$ ∼ 4.4 pc, which is embedded within a surrounding structure that is at least 10 pc in diameter. The measured velocity centroids show a radial velocity gradient (Fig. 16) that could result from local collapse considering that the convergence of the gradient points towards the centre of our map. Another possibility is that ^{13}CO (6–5) emission traces expanding shells. For example, the observed ^{13}CO (6–5) spectra show double peaks in many places, whose velocities are consistent with those of the shells identified in C^{18}O(2–1) emission (Peng et al. 2010). However, in this case, it is not entirely clear how the expanding shells result in the radial velocity gradient.

G31.41+0.3 (HII)

This HII region source harbours a hot molecular core that has been extensively studied with multiple molecular species. For example, Cesaroni et al. (2017) performed CH_3CN observations and found a rotating and infalling toroid on ∼0.1 pc scales. In addition, Beltrán et al. (2022) identified at least six outflows with lobe sizes of ∼0.02–0.2 pc in SiO (5–4) observations. Compared to these small-scale observations, our ^{13}CO (6–5) data probe a factor of ∼10 larger region and show a linear gradient in velocity centroids (Fig. 23). Interestingly, the direction of the linear velocity gradient is perpendicular to that of the strongest SiO (5–4) outflow, implying a rotating ^{13}CO (6–5) envelope. However, the rotation axis of the envelope is not aligned with that of the small-scale toroid, hampering us from pinpointing the exact origin of ^{13}CO (6–5) kinematics.

G35.20−0.7 (IRb)

As a well-known star-forming region, G35.20−0.7 hosts an elongated dust structure that is embedded within a butterfly-shaped reflection nebula (Sánchez-Monge et al. 2013). Compared to the

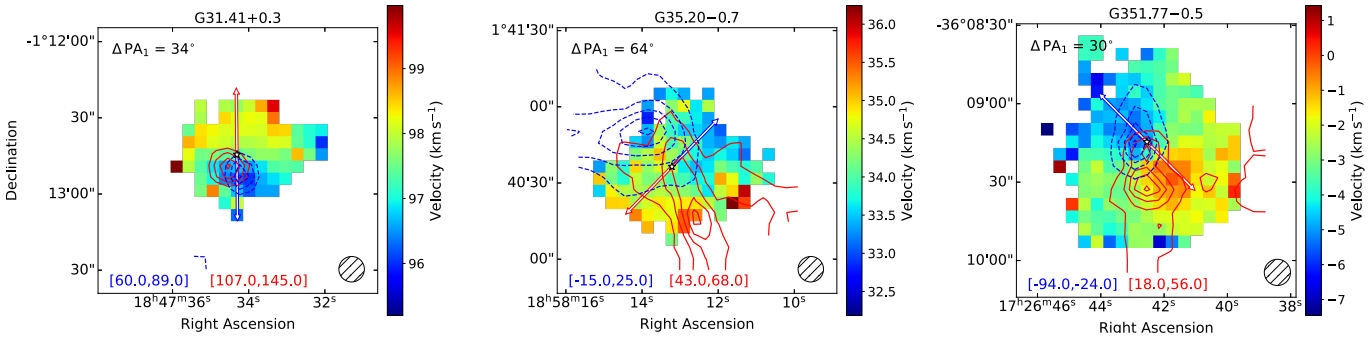

Fig. 23. ^{13}CO (6–5) M_1 maps of G31.41+0.3, G35.20−0.7, and G351.77−0.5. The descriptions for the overlaid contours, symbols, and labels are the same as in Fig. 18.

size of the observed ^{13}CO (6–5) envelope, the elongated structure is roughly one third in length, while the reflection nebula is on a similar scale. Sánchez-Monge et al. (2014) argued that the elongated structure is a filament, rather than an edge-on rotating disc, based on C^{17}O (3–2) and H^{13}CO$^+$ (4–3) observations and further suggested that G35.20−0.7 is a convergence centre of multiple filaments. Interestingly, the velocity range of 31–37 km s^{-1} along the elongated structure is comparable to the ^{13}CO (6–5) velocity gradient, implying that ^{13}CO (6–5) kinematics could trace the gas flow within the supposed converging filaments.

G351.77−0.5 (IRb)

The ^{13}CO (6–5) first moment map of G351.77−0.5 clearly shows blue-shifted and red-shifted lobes (Fig. 23), suggesting an outflow origin of ^{13}CO (6–5) kinematics. Other studies have identified outflows in this region as well. For example, Navarete et al. (in preparation) found an outflow traced by ^{12}CO (6–5) emission (blue and red contours in Fig. 23), whose PA is slightly different from that of our ^{13}CO (6–5) outflow. In addition, Leurini et al. (2009, 2011) detected three outflows in high-resolution (5.45″ × 2.08″) ^{12}CO (2−1) observations. Among the three outflows, two are relatively well-aligned with the ^{12}CO (6–5) outflow on a similar scale. The angular offset between the ^{13}CO (6–5) and ^{12}CO outflows suggests that different transitions and isotopologues of CO molecules probe different parts of the complex outflow system in G351.77−0.5.

In summary, our detailed examination of the four individual clumps supports the previous conclusion that ^{13}CO (6–5) kinematics has a complex nature. Both small-scale (e.g. outflows) and large-scale (e.g. expanding shells and gas flows along filaments) processes impact on the kinematics of warm envelopes, and understanding their impact would be essential to elucidate how ^{13}CO (6–5) emission is excited in massive star-forming regions.

6. Conclusions

In this paper, we characterised ^{13}CO (6–5) emission towards ∼100 massive star-forming clumps at different evolutionary stages. Our APEX observations with high angular and spectral resolutions allowed us to examine the morphology and kinematics of warm envelopes for a statistically significant sample. We summarise our main results and conclusions as follows:

– The ^{13}CO (6–5) emission line is detected towards sources at all stages of high-mass star formation. Key characteristics of the emission line, including the detection rate, line width, and peak brightness temperature, increase with evolutionary stages. In addition, the line luminosity is tightly correlated with the bolometric luminosity and the clump mass. These results suggest that the ^{13}CO (6–5) emission line is related to star formation processes;
– The ^{13}CO (6–5) integrated intensity images show that a majority of the warm envelopes have a simple single-core morphology and the most evolved clumps (HII) have larger envelopes. The radial intensity profiles of the single-core clumps can be reasonably well described as single power-law functions. Interestingly, the slopes of the most evolved group (HII), tend to be steeper, possibly due to enhancements in density and/or temperature at the central parts of the warm envelopes;
– The kinematics of the warm envelopes presents various forms and is likely not driven by a single physical process. While most of the single-core envelopes show significant linear velocity gradients, the origin of these gradients is unclear in many cases. A detailed examination of individual sources suggests that the gas motions in the warm envelopes could be driven by stellar feedback such as outflows and/or by inheriting the kinematics of large-scale parental clouds.

Data availability

Appendices of this paper are available on Zenodo at https://doi.org/10.5281/zenodo.14748231.

Acknowledgements. The authors thank the anonymous referee for the constructive report that helped us improve this paper. We thank MPIfR and APEX staff for operating the observatory and collecting the data. The work of FN is supported by NOIRLab, which is managed by the Association of Universities for Research in Astronomy (AURA) under a cooperative agreement with the National Science Foundation. *Herschel* was an ESA space observatory with science instruments provided by European-led Principal Investigator consortia and with important participation from NASA.

References

Arce, H. G., & Sargent, A. I. 2006, ApJ, 646, 1070
Beltrán, M. T., & de Wit, W. J. 2016, A&A Rev., 24, 6
Beltrán, M. T., Rivilla, V. M., Cesaroni, R., et al. 2021, A&A, 648, A100
Beltrán, M. T., Rivilla, V. M., Cesaroni, R., et al. 2022, A&A, 659, A81
Beuther, H., Schilke, P., Menten, K. M., et al. 2002, ApJ, 566, 945
Bonnell, I. A., & Bate, M. R. 2006, MNRAS, 370, 488
Bonnell, I. A., Bate, M. R., Clarke, C. J., & Pringle, J. E. 2001, MNRAS, 323, 785
Cesaroni, R., Sánchez-Monge, Á., Beltrán, M. T., et al. 2017, A&A, 602, A59
Csengeri, T., Leurini, S., Wyrowski, F., et al. 2016, A&A, 586, A149

Giannetti, A., Wyrowski, F., Brand, J., et al. 2014, A&A, 570, A65
Giannetti, A., Leurini, S., Wyrowski, F., et al. 2017, A&A, 603, A33
Goodman, A. A., Benson, P. J., Fuller, G. A., & Myers, P. C. 1993, ApJ, 406, 528
Graf, U. U., Eckart, A., Genzel, R., et al. 1993, ApJ, 405, 249
Güsten, R., Nyman, L. Å., Schilke, P., et al. 2006, A&A, 454, L13
Güsten, R., Baryshev, A., Bell, A., et al. 2008, SPIE Conf. Ser., 7020, 702010
Heitsch, F., Ballesteros-Paredes, J., & Hartmann, L. 2009, ApJ, 704, 1735
Hopkins, P. F., Kereš, D., Oñorbe, J., et al. 2014, MNRAS, 445, 581
Indriolo, N., Bergin, E. A., Goicoechea, J. R., et al. 2017, ApJ, 836, 117
Jørgensen, J. K., Schöier, F. L., & van Dishoeck, E. F. 2002, A&A, 389, 908
Kasemann, C., Güsten, R., Heyminck, S., et al. 2006, SPIE Conf. Ser., 6275, 62750N
Kauffmann, J., Pillai, T., Shetty, R., Myers, P. C., & Goodman, A. A. 2010, ApJ, 712, 1137
Kennicutt, R. C. 2005, in Massive Star Birth: A Crossroads of Astrophysics, 227, eds. R. Cesaroni, M. Felli, E. Churchwell, & M. Walmsley, 3
Klapper, G., Lewen, F., Gendriesch, R., Belov, S. P., & Winnewisser, G. 2000, J. Mol. Spectrosc., 201, 124
Koester, B., Stoerzer, H., Stutzki, J., & Sternberg, A. 1994, A&A, 284, 545
König, C., Urquhart, J. S., Csengeri, T., et al. 2017, A&A, 599, A139
Kristensen, L. E., van Dishoeck, E. F., Bergin, E. A., et al. 2012, A&A, 542, A8
Lee, M. Y., Wyrowski, F., Menten, K., Tiwari, M., & Güsten, R. 2022, A&A, 664, A80
Leurini, S., Codella, C., Zapata, L. A., et al. 2009, A&A, 507, 1443
Leurini, S., Codella, C., Zapata, L., et al. 2011, A&A, 530, A12
Leurini, S., Wyrowski, F., Herpin, F., et al. 2013, A&A, 550, A10
Mattern, M., Kauffmann, J., Csengeri, T., et al. 2018, A&A, 619, A166
Matteucci, F. 2021, A&A Rev., 29, 5
McKee, C. F., & Tan, J. C. 2003, ApJ, 585, 850
McLaughlin, D. E., & Pudritz, R. E. 1996, ApJ, 469, 194
Molinari, S., Swinyard, B., Bally, J., et al. 2010, PASP, 122, 314
Motte, F., & André, P. 2001, A&A, 365, 440
Motte, F., Bontemps, S., & Louvet, F. 2018, ARA&A, 56, 41
Müller, H. S. P., Thorwirth, S., Roth, D. A., & Winnewisser, G. 2001, A&A, 370, L49
Müller, H. S. P., Schlöder, F., Stutzki, J., & Winnewisser, G. 2005, J. Mol. Struct., 742, 215
Navarete, F., Leurini, S., Giannetti, A., et al. 2019, A&A, 622, A135
Padoan, P., Pan, L., Juvela, M., Haugbølle, T., & Nordlund, Å. 2020, ApJ, 900, 82
Peng, T. C., Wyrowski, F., van der Tak, F. F. S., Menten, K. M., & Walmsley, C. M. 2010, A&A, 520, A84
Pillai, T. G. S., Urquhart, J. S., Leurini, S., et al. 2023, MNRAS, 522, 3357
Rugel, M. R., Rahner, D., Beuther, H., et al. 2019, A&A, 622, A48
Sánchez-Monge, Á., Cesaroni, R., Beltrán, M. T., et al. 2013, A&A, 552, L10
Sánchez-Monge, Á., Beltrán, M. T., Cesaroni, R., et al. 2014, A&A, 569, A11
Schuller, F., Menten, K. M., Contreras, Y., et al. 2009, A&A, 504, 415
Schuller, F., Urquhart, J. S., Csengeri, T., et al. 2021, MNRAS, 500, 3064
Serabyn, E., Guesten, R., & Schulz, A. 1993, ApJ, 413, 571
Shu, F. H., Adams, F. C., & Lizano, S. 1987, ARA&A, 25, 23
Smith, R. J., Glover, S. C. O., Bonnell, I. A., Clark, P. C., & Klessen, R. S. 2011, MNRAS, 411, 1354
Spaans, M., Hogerheijde, M. R., Mundy, L. G., & van Dishoeck, E. F. 1995, ApJ, 455, L167
Tobin, J. J., Hartmann, L., Chiang, H.-F., et al. 2011, ApJ, 740, 45
Urquhart, J. S., Wells, M. R. A., Pillai, T., et al. 2022, MNRAS, 510, 3389
van Kempen, T. A., van Dishoeck, E. F., Güsten, R., et al. 2009a, A&A, 507, 1425
van Kempen, T. A., van Dishoeck, E. F., Güsten, R., et al. 2009b, A&A, 501, 633
Vázquez-Semadeni, E., Palau, A., Ballesteros-Paredes, J., Gómez, G. C., & Zamora-Avilés, M. 2019, MNRAS, 490, 3061
Welch, W. J., Dreher, J. W., Jackson, J. M., Terebey, S., & Vogel, S. N. 1987, Science, 238, 1550
Wyrowski, F., Güsten, R., Menten, K. M., et al. 2016, A&A, 585, A149
Yang, A. Y., Thompson, M. A., Urquhart, J. S., & Tian, W. W. 2018, ApJS, 235, 3
Yıldız, U. A., Kristensen, L. E., van Dishoeck, E. F., et al. 2012, A&A, 542, A86
Yıldız, U. A., Kristensen, L. E., van Dishoeck, E. F., et al. 2015, A&A, 576, A109
Zinnecker, H., & Yorke, H. W. 2007, ARA&A, 45, 481

APPENDIX B

High-J CO emission from a sample of massive star-forming clumps

A&A, 679, A121 (2023)
https://doi.org/10.1051/0004-6361/202347163

Astronomy & Astrophysics

Velocity-resolved high-*J* CO emission from massive star-forming clumps

Thanh Dat Hoang[1], Agata Karska[1,2,3], Min Young Lee[4], Friedrich Wyrowski[1], Le Ngoc Tram[1], Aiyuan Yang[5,6], and Karl M. Menten[1]

[1] Max Planck Institute for Radio Astronomy, Auf dem Hügel 69, 53121 Bonn, Germany
e-mail: tdhoang@mpifr-bonn.mpg.de
[2] Argelander-Institut für Astronomie, Universität Bonn, Auf dem Hügel 71, 53121 Bonn, Germany
[3] Institute of Astronomy, Faculty of Physics, Astronomy and Informatics, Nicolaus Copernicus University, ul. Grudziądzka 5, 87-100 Toruń, Poland
[4] Korea Astronomy and Space Science Institute, 776 Daedeok-daero, Yuseong-gu, Daejeon 34055, Republic of Korea
[5] National Astronomical Observatories, Chinese Academy of Sciences, A20 Datun Road, Chaoyang District, Beijing 100101, PR China
[6] Key Laboratory of Radio Astronomy and Technology, Chinese Academy of Sciences, A20 Datun Road, Chaoyang District, Beijing 100101, PR China

Received 12 June 2023 / Accepted 21 September 2023

ABSTRACT

Context. Massive star formation is associated with energetic processes, which result in significant gas cooling via far-infrared (IR) lines. Velocity-resolved observations can constrain the kinematics of the gas, allowing the identification of the physical mechanisms responsible for gas heating.
Aims. Our aim is to quantify far-IR CO line emission towards high-mass star-forming regions, identify the high-velocity gas component associated with outflows, and estimate the physical conditions required for the excitation of the observed lines.
Methods. Velocity-resolved SOFIA/GREAT spectra of 13 high-mass star-forming clumps of various luminosities and evolutionary stages are studied in highly excited rotational lines of CO. For most targets, the spectra are from frequency intervals covering the CO 11–10 and 16–15 lines towards two sources, also the CO 13–12 line was observed with SOFIA/4GREAT. Angular resolutions at the line frequencies range from 14″ to 20″, corresponding to spatial scales of ∼0.1–0.8 pc. Radiative transfer models were used to determine the physical conditions giving rise to the emission in the line wings.
Results. All targets in our sample show strong high-*J* CO emission in the far-IR, characterised by broad line wings associated with outflows, thereby significantly increasing the sample of high-mass objects with velocity-resolved high-*J* CO spectra. Twelve sources show emission in the line wings of the CO 11–10 line (E_u/k_B=365 K), and eight sources in the CO 16–15 line (E_u/k_B=752 K). The contribution of the emission in the line wings to the total emission ranges from ∼28% to 76%, and does not correlate with the envelope mass or evolutionary stage. Gas excitation temperatures cover a narrow range of 120–220 K for the line wings, and 110–200 K for the velocity-integrated line emission, assuming local thermodynamics equilibrium (LTE). For the two additional sources with the CO 13–12 line (E_u/k_B=503 K) data, wing emission rotational temperatures of ∼130 K and 165 K were obtained using Boltzmann diagrams. The corresponding non-LTE radiative transfer models indicate gas densities of 10^5–10^7 cm^{-3} and CO column densities of 10^{17}–10^{18} cm^{-2} in the line wings, similar to physical conditions in deeply embedded low- and high-mass protostars. The velocity-integrated CO line fluxes correlate with the bolometric luminosity over 7 orders of magnitude, including data on the low-mass protostars from the literature. This suggests that similar processes are responsible for the high-*J* CO excitation over a significant range of physical scales.
Conclusions. Velocity-resolved line profiles allow the detection of outflows towards massive star-forming clumps spanning a broad range of evolutionary stages. The lack of clear evolutionary trends suggest that mass accretion and ejection prevail during the entire lifetime of star-forming clumps.

Key words. stars: formation – stars: protostars – ISM: molecules – ISM: kinematics and dynamics – line: profiles – ISM: jets and outflows

1. Introduction

High-mass stars have a significant impact on their environments and on galaxy evolution globally through their ionising radiation, stellar winds, and their deaths in supernova explosions (Zinnecker & Yorke 2007). Already during the earliest stages of their formation, massive protostars might inject significant amounts of energy and momentum into the interstellar medium (ISM) in the form of outflows, capable of disrupting clumps and cores (Beuther et al. 2002; Bally 2016).

Outflows, a ubiquitous phenomenon in both low- and high-mass star-forming regions, play an essential role in transporting angular momentum and regulating the star-forming process across multiple spatial scales (Bally & Lada 1983; Evans 1999). Both the dissipation of the envelope material and mass loss via the outflows lower the core-to-star formation efficiency

(Krumholz et al. 2014; Offner & Chaban 2017). At cluster and clump scales, outflows drive turbulence that provides additional support against gravitational collapse (Frank et al. 2014).

Outflows are typically detected using low-J ($J \lesssim 5$) velocity-resolved rotational lines of carbon monoxide (CO), which is the second most abundant molecule in the ISM ($CO/H_2 = 1.2 \times 10^{-4}$, Frerking et al. 1982). The low-lying rotational levels of CO are easily collisionally excited even at low densities and can be observed readily at millimetre wavelengths. These lines constitute a useful diagnostic of the gas kinetic temperature of outflows (Bally & Lada 1983; Yıldız et al. 2015). An extensive search for outflows traced by such low-J CO lines towards a total of 2052 massive star-forming clumps that were identified in the APEX Telescope Large Area Survey of the Galaxy (ATLASGAL, Schuller et al. 2009), provided an overall outflow detection rate of 58% (Yang et al. 2018a, 2022).

Observations of high-J CO ($J \gtrsim 10$) lines provide an opportunity to study denser and warmer parts of star-forming clumps and the outflows that arise in them. Recent surveys with the *Herschel* Space Observatory (Pilbratt et al. 2010) found that CO lines account for the bulk far-infrared (IR) gas cooling in both low- and high-mass star-forming regions (Karska et al. 2013, 2014, 2018; van Dishoeck et al. 2021). The velocity-resolved profiles of high-J CO towards low-mass protostars revealed a significant contribution of high-velocity ($v \sim 20$–$30\,\mathrm{km\,s^{-1}}$) gas to the total far-IR line emission (San José-García et al. 2013; Yıldız et al. 2013), and a similarity to the H_2O emission likely arising from the same gas (San José-García et al. 2016; Kristensen et al. 2017). Single-pointing observations towards high-mass sources have also revealed broad, outflow wings in high-J CO line profiles, but they have been limited to just a few sources: W3 IRS5 (San José-García et al. 2013), AFGL 2591 (Kaźmierczak-Barthel et al. 2014), Orion KL, Orion S, Sgr B*, and W49N (Indriolo et al. 2017). Complementary observations have been obtained with the German REceiver for Astronomy at Terahertz frequencies[1] (GREAT, Risacher et al. 2018) on board the Stratospheric Observatory For Infrared Astronomy (SOFIA, Young et al. 2012). High-resolution spectroscopy of far-IR CO lines from an intermediate-mass protostar Cep E revealed an extremely high-velocity (EHV) gas (v up to $\sim 140\,\mathrm{km\,s^{-1}}$), tracing shocks associated with the jet and intermediate-to-high velocity gas (v from 50 to $100\,\mathrm{km\,s^{-1}}$) associated with outflow cavities and a bow shock (Gómez-Ruiz et al. 2012; Lefloch et al. 2015; Gusdorf et al. 2017). The line profiles of CO 16–15 towards two high-mass sources, however, lacked the EHV component and revealed broad line wings extending up to $v \sim 50\,\mathrm{km\,s^{-1}}$ (Leurini et al. 2015; Gusdorf et al. 2016). Other surveys, conducted with the PACS and SPIRE instruments aboard the *Herschel* Space Telescope (Pilbratt et al. 2010), lacked the high spectral resolution necessary to disentangle the envelope and outflow emission in the spectra (Karska et al. 2014; Goicoechea et al. 2013, 2015).

For this study, we used SOFIA/GREAT to quantify high-J CO emission towards 13 high-mass star-forming clumps with the aim to isolate the contribution from the outflows and estimate excitation conditions associated with the line wing emission. We also examined how the high-J CO emission varies as a function of clump properties and evolutionary stages.

The paper is organised as follows: Sect. 2 describes the source sample, observations with SOFIA, and the complementary CO observations with the APEX telescope and *Herschel*. In Sect. 3, we present line profiles of high-J CO transitions (Sect. 3.1) and decompose the emission that belongs to the line wings (Sect. 3.2). In addition, we study the correlations of velocity-integrated emission with source properties, and those of the fraction of wing emission with source evolutionary stages (Sect. 3.3). Subsequently, we analyse the excitation of high-J CO lines using LTE and non-LTE approaches (Sects. 3.4 and 3.5). Section 4 consists of the discussion of our results in the context of previous studies and Sect. 5 presents a summary and our conclusions.

2. Observations

2.1. Sample

All sources have been selected from the ATLASGAL survey covering 420 deg^2 of the inner Galactic plane in the 870 µm dust continuum (Urquhart et al. 2014; König et al. 2017). The latest version of the ATLASGAL source catalogue contains 5007 clumps spanning a wide range of masses (M_{clump}) and luminosities (L_{bol}), and it is divided into four evolutionary stages – quiescent, protostellar, young stellar objects (YSOs), and H II regions (H II). For more details, readers can refer to Urquhart et al. (2022).

For this work, we originally selected a representative sample of 20 sources grouped within four star-forming regions in the Galactic plane. Among them, 13 sources within three regions were successfully observed with SOFIA. Table 1 shows the final list of sources with the overview of their properties and evolutionary stages. The sample consists of three protostellar (24d), seven YSOs (IRb), and three H II regions (HII), with L_{bol} from 1.6×10^3 to 4.6×10^5 $L_\odot$ and M_{clump} from 1.6×10^2 to 2.3×10^3 $M_\odot$ (König et al. 2017; Urquhart et al. 2019, 2022).

2.2. SOFIA observations and data reduction

Observations of the CO 11–10 and 16–15 lines were collected using the SOFIA/GREAT (Heyminck et al. 2012; Risacher et al. 2016) and upGREAT receivers (Risacher et al. 2018). Our programme 'Probing high-J CO through the evolution of high-mass star-forming clumps' (project IDs 02_0102 and 03_0103; PI: F. Wyrowski) ran during Cycle 2 (2014 May) and Cycle 3 (2016 May).

GREAT was a high-resolution, dual-colour spectrometer ($R \geq 10^7$) initially designed for single-beam observations. In 2014, we used its L1 and L2 channels to obtain simultaneous coverage of bands in the 1.25–1.52 THz and 1.80–1.90 THz windows, respectively. In 2016, we combined GREAT's L1 channel with the upGREAT Low Frequency Array (LFA), which covered the 1.83–2.07 THz window in two polarisations. The 7-pixel hexagonal setup of the LFA provided spatial information about the line emission, whereas each pixel had a full-width at half-maximum (FWHM) beam size of 14.8″ on the sky[2]. The corresponding beam size in the L1 channel was 19.9″ in 2014 and 19.1″ in 2016. The higher frequency L2 channel provided a Field of View (FoV) of 14.1″. The adopted main beam efficiencies (η_{MB}) are 0.7 (in 2014) and 0.66 (in 2016) for the L1 channel, 0.65 for L2 channel, and 0.65 for the central spaxel of LFA. Data were processed and reduced by SOFIA/GREAT staff and released at product level 3 where first order baselines have been subtracted. Most of the data are ready to use, except

[1] GREAT is a development by the MPI für Radioastronomie and the KOSMA/Universität zu Köln, in cooperation with the MPI für Sonnensystemforschung and the DLR Institut für Planetenforschung.

[2] Observer's Handbook for Cycle 3: https://www.sofia.usra.edu/sites/default/files/ObsHandbook-Cy3.pdf

Table 1. Catalogue of source properties.

No.	Source	ATLASGAL name [a]	RA (J2000)	Dec (J2000)	V_{lsr} [b] (km s^{-1})	D [c] (kpc)	L_{bol} [d] ($L_\odot$)	M_{clump} [e] ($M_\odot$)	D_{GC} (kpc)	Type [f]
1	G351.16+0.7	AGAL351.161+00.697	17:19:56.69	–35:57:53.0	–6.0	1.3	8.8×10^3	1.2×10^3	6.7	IRb
2	G351.25+0.7	AGAL351.244+00.669	17:20:18.86	–35:54:42.5	–2.8	1.3	4.9×10^4	3.7×10^2	6.7	IRb
3	G351.44+0.7	AGAL351.444+00.659	17:20:55.20	–35:45:08.0	–3.8	1.3	2.0×10^4	1.0×10^3	6.7	24d
4	G351.58−0.4	AGAL351.581−00.352	17:25:25.03	–36:12:45.4	–95.6	8.0	4.6×10^5	2.3×10^3	2.0	IRb
5	G351.77−0.5	AGAL351.774−00.537	17:26:42.54	–36:09:20.1	–2.8	1.3	3.7×10^4	3.3×10^2	7.8	IRb
6	G12.81−0.2	AGAL012.804−00.199	18:14:13.54	–17:55:32.0	34.6	2.6	2.5×10^5	1.9×10^3	6.2	HII
7	G14.19−0.2	AGAL014.194−00.194	18:16:58.63	–16:42:16.4	39.7	3.1	3.7×10^3	5.1×10^2	4.8	24d
8	G13.66−0.6	AGAL013.658−00.599	18:17:24.09	–17:22:10.3	48.5	4.5	2.4×10^4	2.7×10^2	4.3	IRb
9	G14.63−0.6	AGAL014.632−00.577	18:19:14.65	–16:30:02.7	18.5	1.5	1.6×10^3	1.6×10^2	6.3	24d
10	G34.41+0.2	AGAL034.411+00.234	18:53:18.13	+01:25:23.7	57.9	2.9	3.1×10^3	4.4×10^2	7.2	IRb
11	G34.26+0.15	AGAL034.258+00.154	18:53:18.51	+01:14:57.6	58.0	2.9	6.1×10^4	1.7×10^3	6.9	HII
12	G34.40−0.2	AGAL034.401+00.226	18:53:18.63	+01:24:40.4	57.1	2.9	3.2×10^3	7.9×10^2	7.2	HII
13	G35.20−0.7	AGAL035.197−00.742	18:58:12.94	+01:40:40.6	33.5	2.2	2.4×10^4	4.6×10^2	6.8	IRb

Notes. [a]Source names from the ATLASGAL Compact Source Catalogue (Contreras et al. 2013; Urquhart et al. 2014). [b]Source velocities (V_{lsr}) estimated from proxy lines (see Appendix D). [c]Heliocentric distances estimated in Urquhart et al. (2022). [d]Source bolometric luminosities, L_{bol}, estimated from greybody fit to dust emission in Urquhart et al. (2018). L_{bol} of source 1, 6, and 13 were estimated in König et al. (2017). [e]Clump masses, M_{clump}, were estimated from cold dust emission at 870 µm in Urquhart et al. (2022). M_{clump} of source 1, 6, and 13 were obtained from König et al. (2017). [f]Source classification using the criteria is from König et al. (2017), and refers to IR-bright sources (IRb), IR-weak sources (24d), and HII regions (HII).

Table 2. Overview of the observations.

Molecule	Trans. $J_u - J_l$	Freq. (GHz)	E_u/k_B (K)	A_u (s^{-1})	g_u	Receiver	Beam ($''$)	Δv (km s^{-1})
CO	6–5	691.5	116.16	2.1(–5)	13	APEX/CHAMP$^+$	9	0.318
CO	11–10	1267.0	364.97	1.3(–4)	23	SOFIA/GREAT	20	(0.361, 0.578)
CO	13–12	1496.9	503.13	2.2(–4)	27	SOFIA/GREAT	20	0.978
CO	16–15	1841.4	751.72	4.1(–4)	33	SOFIA/GREAT	14	(0.248, 0.795)
^{13}CO	6–5	661.1	111.05	1.9(–5)	13	APEX/CHAMP$^+$	9	0.332
^{13}CO	10–9	1101.4	290.79	8.8(–5)	21	*Herschel*/HIFI	19	0.136
C^{18}O	6–5	658.6	110.63	1.9(–5)	13	APEX/CHAMP$^+$	9	0.334
C^{18}O	9–8	987.6	237.03	6.4(–5)	19	*Herschel*/HIFI	22	0.152

Notes. Molecular data adopted from the Leiden Atomic and Molecular Database (LAMDA, Schöier et al. 2005). Δv is the original spectral resolution of our data, before they were smoothed to a common size of 1.0 km s^{-1}. The CO 11–10 and CO 16–15 have two Δv each, which correspond to observations in 2014 and 2016, respectively.

for CO 16–15 spectra of G13.66−0.6 where an additional third order baseline was subtracted. Spectral resolutions are presented in Table 2. To perform the analyses without any spectral resolution bias, all spectra were smoothed to a common resolution of 1.0 km s^{-1}.

For G12.81−0.2 and G351.25+0.7, additional line observations were collected using the SOFIA/4GREAT receiver (Duran et al. 2021). The observations were carried out in 2019 under project 'high-J CO observations towards high-mass star-forming clumps' (project ID 83_0711; PI: H. T. Dat). 4GREAT was a single-beam system with four sub-receivers (4G-1 to 4G-4) and could observe four spectral windows simultaneously. The 4G-3 and 4G-4 modules, which cover the 1.24–1.52 THz and 2.49–2.69 THz windows, were tuned to map the CO 13–12 and 22–21 transitions. The maps were scanned in 5 × 5 grids with centres 6″ away from each other. The typical beam sizes for the 4G-3 and 4G-4 modules are 20″ and 10.5″, respectively (Duran et al. 2021). Main beam efficiencies are 0.7 for 4G-3 and 0.57 for 4G-4. Observations of the CO 22–21 line are affected by instrumental standing waves that make it difficult to confidently detect line emission. The noise levels of averaged spectra range from 0.40 K to 0.88 K at Δv of 0.6 km s^{-1}.

Data reduction for the CO 13–12 line was performed with the CLASS programme, which is part of the GILDAS[3] software developed by the Institut de Radioastronomie Millimétrique (IRAM). A second order baseline was subtracted, and the spectra were also smoothed to an adequate 1.0 km s^{-1}. For this study, we extracted averaged spectra within a beam of 20″.

[3] https://www.iram.fr/IRAMFR/GILDAS/

2.3. Additional observations and ancillary data

Additional single pointing observations of ^{13}CO 10–9 and C^{18}O 9–8 were conducted with the *Herschel*-Heterodyne Instrument for the Far-Infrared (HIFI, de Graauw et al. 2010) on board of the *Herschel* Space Telescope. Observations for ten sources (Appendix D) were obtained as part of project 'A Water survey of massive star-forming clumps in the inner Galaxy' (project ID OT2_fwyrowsk_3, PI: F. Wyrowski). In addition, archival data for G351.44+0.7 using *Herschel*/HIFI were taken from the 'Water in star-forming regions with *Herschel*' programme (San José-García et al. 2013; van Dishoeck et al. 2021). Data from the H and V polarisations of the wide-band spectrometer were averaged. Baselines lower than third order were also subtracted. The spectra were converted to a $T_{\rm MB}$ scale using a forward efficiency of 0.96 and a main beam efficiency of 0.64 for the ^{13}CO 10–9 line and 0.74 for the C^{18}O 9–8 line, respectively. Finally, the spectra were smoothed to 1.0 km s^{-1}. Angular and original spectral resolutions are listed in Table 2.

We also used high spectral resolution ^{13}CO 6–5 and C^{18}O 6–5 data from Dat et al. (in prep.) and CO 6–5 from Navarete et al. (2019). All three transitions were observed with the CHAMP^{+} receiver (Kasemann et al. 2006; Güsten et al. 2008) at the Atacama Pathfinder Experiment (APEX) 12 m submillimetre telescope (Güsten et al. 2006). The on-the-fly (OTF) scans resulted in datacubes of 80″ × 80″ with angular resolutions of ∼9″. For comparisons with the higher-J CO observations, averaged spectra with an effective beam size of 20″ around the sources were extracted and then smoothed to 1.0 km s^{-1} for all three lines.

3. Results and analysis

3.1. Line detections

In this section, we examine detection rates of high-J CO lines towards high-mass clumps from ATLASGAL. We also present their line profiles and quantify the correlations of integrated intensities with the sources' properties.

Figure 1 shows the spectra of high-J CO lines towards the central position of high-mass clumps from our sample (see also Table 1). The pattern of emission is generally compact, based on additional observations offset from the clump centres towards four sources (see Appendix A).

The CO 11–10 line is detected at 3σ or higher levels towards all sources, which span a broad range of evolutionary stages and have diverse properties. The CO 16–15 line, however, is firmly detected towards ten out of 13 clumps; G13.66−0.6 and G34.41+0.2 show only 2σ peaks and G14.19−0.2 shows a non-detection. In addition, the CO 13–12 line was successfully observed and detected towards G12.81−0.2 and G351.25+0.7. In Appendix B, the peak and integrated intensity of the detected lines are given.

The line profiles of clump central positions exhibit a broad line wing emission, suggesting the presence of outflows (Fig. 1). The median full width at zero power[4] (FWZP) of 45 km s^{-1} was measured for the CO 11–10 line and 33 km s^{-1} for the CO 16–15 line (Appendix C). The broadest profile, with FWZP of 165 km s^{-1}, is seen towards G351.77−0.5 where high-velocity gas has been detected in CO 2–1 and 6–5 lines (Leurini et al. 2009). However, multiple pointing observations show a lack of a EHV gas component towards the central source; it is only detected at offset outflow positions (Leurini et al. 2009), consistent with the analysis of the outflow emission from an intermediate mass protostar Cep E (Gómez-Ruiz et al. 2012; Lefloch et al. 2015; Gusdorf et al. 2017). The lack of clear evidence of EHV gas towards our sources may also result from the beam dilution, and could only be addressed using high angular resolution observations (e.g. Cheng et al. 2019).

The velocity ranges of high-J CO lines resemble those detected in CO 6–5 towards the same sources (Fig. 2). Self-absorption features are seen in the CO 11–10 line profiles towards G351.25+0.7 and G351.77−0.5. In addition, G12.81−0.2 and G35.20−0.7 have tilted peaks, which could be an indication of self-absorption. The latter source also shows a sign of self-absorption in the CO 16–15 line. Other profile asymmetries, in particular the triangular blue-wing shape of G351.16+0.7, resemble those of high−J CO emission from a photodissociation region in M17 SW (Pérez-Beaupuits et al. 2015).

For G34.26+0.15, an additional narrow peak is seen at ∼38 km s^{-1} in both the CO 11–10 and CO 16–15 spectra. This feature is an artefact due to over-corrected mesospheric CO, which shows the limitations of the adopted atmospheric model (see also, Gusdorf et al. 2016).

For G34.40−0.2, the line profiles of high-J CO lines seem to be shifted by ∼1 km s^{-1} from the source velocity obtained from the C^{18}O 9–8 line (Fig. 1). The uncertainty of the Gaussian fit to the C^{18}O line is smaller than 0.25 km s^{-1}, and thus cannot account for the observed shift, suggesting that it may be caused by self-absorption. Small velocity shifts are also present in the line profiles of other objects, for example G34.26+0.15 and G351.25+0.7.

We calculated CO line luminosities, $L_{\rm CO}$, as $4\pi D^2 F_{\lambda}^{\rm CO}$, where D is the distance to the source (Table 1) and $F_{\lambda}^{\rm CO}$ is the velocity integrated flux in W m^{-1}. The flux conversion from K km s^{-1} to W m^{-1} followed Eq. (1) in Indriolo et al. (2017). Figure 3 shows the correlations between $L_{\rm CO}$ and source properties (Table 1). The significance of the correlations was quantified by the Pearson correlation coefficient r, which also depends on the number of data points N (Marseille et al. 2010).

Both CO 11–10 and CO 16–15 line luminosities show weak correlations (r of 0.63–0.66) with the clump mass, $M_{\rm clump}$, primarily tracing a cold gas and dust reservoir (König et al. 2017). Stronger correlations (r of 0.85–0.95) are found for the high-J CO line luminosities and clump bolometric luminosities, $L_{\rm bol}$, in line with previous studies using CO 10–9 (see Sect. 4). It is noteworthy that clumps at different evolutionary stages do not show any clear trend in Fig. 3, suggesting that similar underlying physical processes are responsible for high-J CO emission from all sources in the sample.

In summary, high-J CO emission is detected in high-mass clumps and correlates most strongly with clump bolometric luminosity. The line shapes show that high-velocity gas is most likely associated with the outflows.

3.2. Profile decomposition

We used mid-J ($6 \lesssim J \lesssim 10$) CO rare isotopologue lines to subtract the envelope component from the line profiles of CO 11–10 and CO 16–15. This way, we isolated the high-velocity emission associated with the line wings.

The emission in the line wings is characterised using a decomposition method which is described in detail in

[4] The FWZP was calculated following a procedure described in San José-García et al. (2016). We first resampled the spectra to 3 km s^{-1}, and subsequently checked the velocity of the channel where the line emission dropped below 1σ.

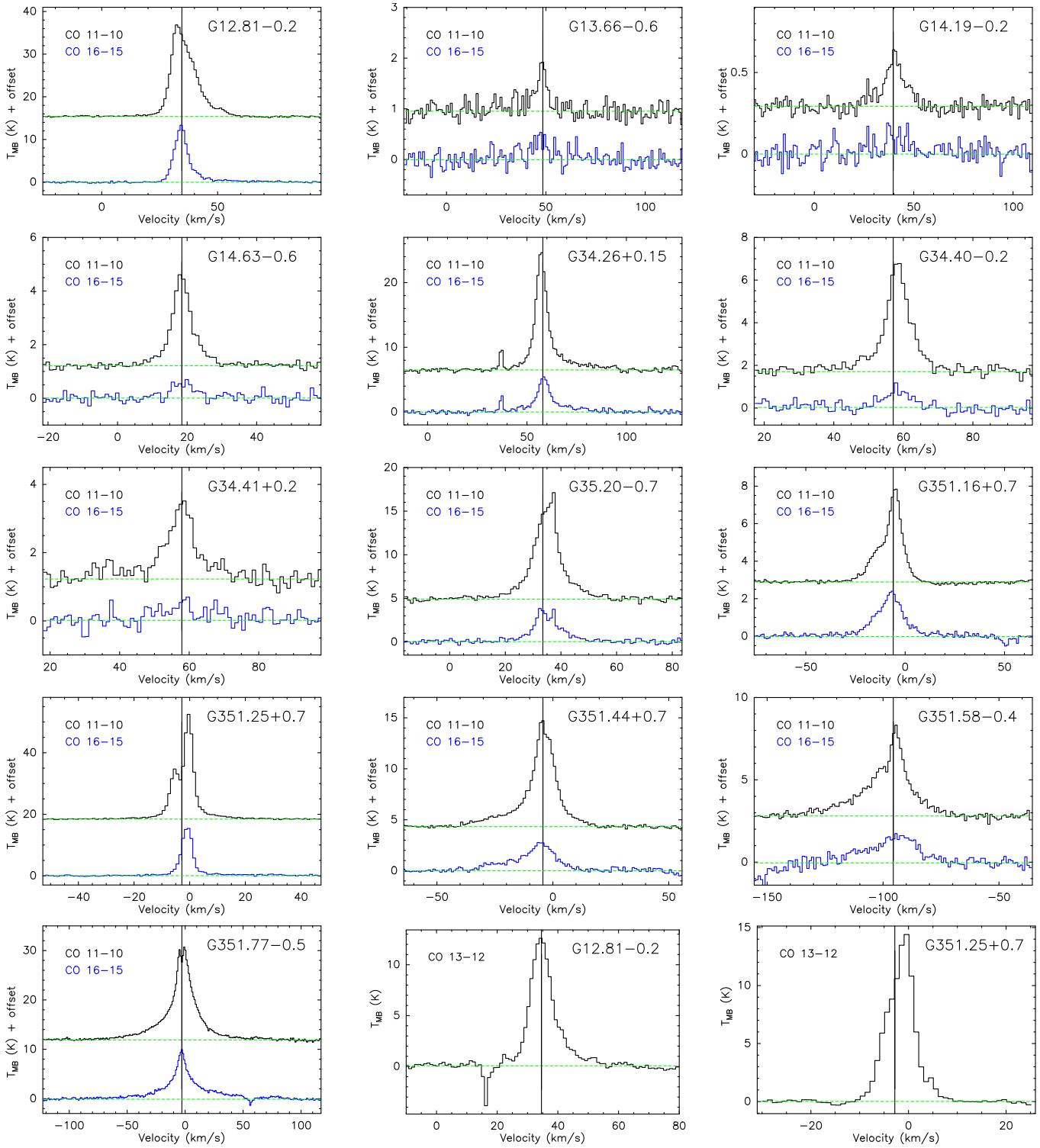

Fig. 1. SOFIA line profiles of CO J = 11–10 (black), 16–15 (blue), and 13–12 (bottom right) transitions. All spectra were resampled to a common spectral resolution of 1.0 km s^{-1}. Black vertical lines show values of $V_{\rm lsr}$ (see Table 1). Green horizontal lines show baselines.

Appendix D. Briefly, the decomposition procedure aims to subtract the contribution from the envelope, as traced by rare isotopologue emission, resulting in the residual outflow component (Codella et al. 2004; van der Walt et al. 2007; de Villiers et al. 2014; Yang et al. 2018a). This method was initially used for kinematical studies of methanol masers, and subsequently adopted for low-J CO line profiles. Here, we used the version described in Yang et al. (2018a), which does not account for the opacity broadening because the high-J CO lines are likely optically thin. Rare isotopologue lines are used as a proxy for the envelope emission; here, depending on data availability and detection, we used the emission of the C^{18}O 9–8 line for eight

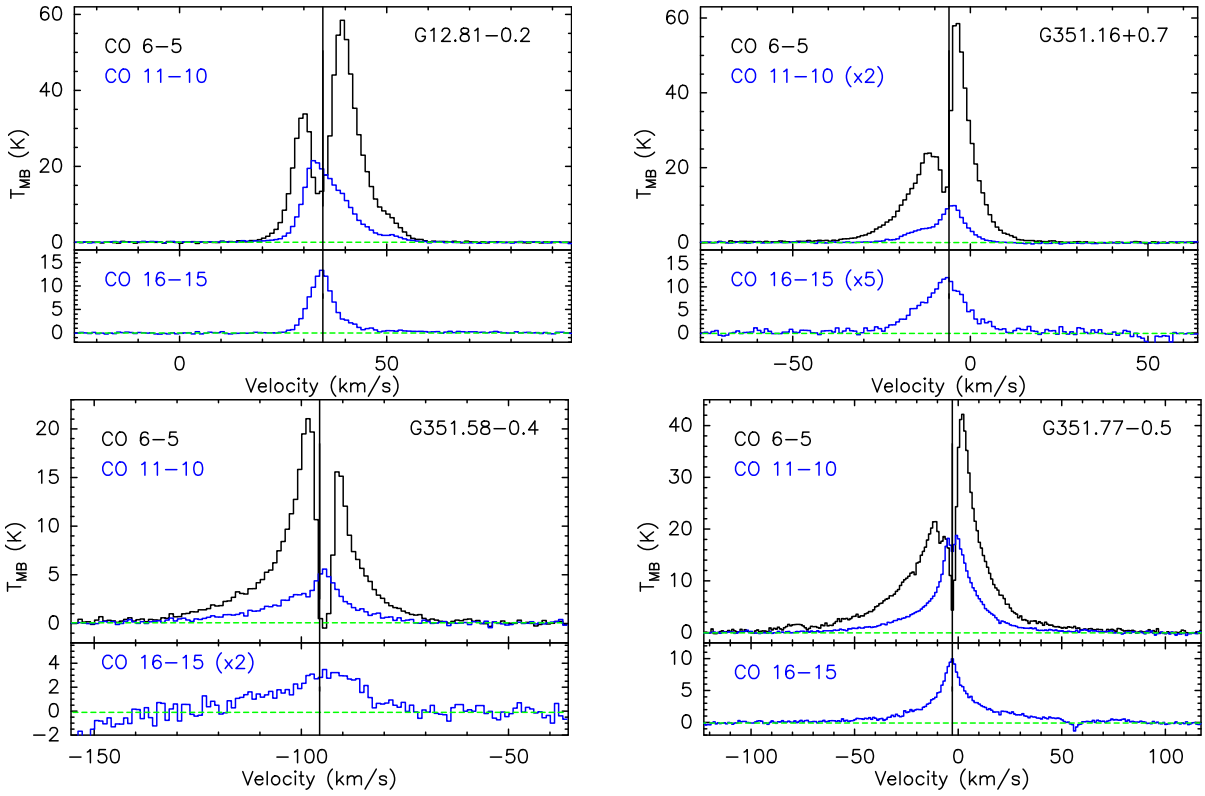

Fig. 2. SOFIA/GREAT line profiles of the CO 11–10 and 16–15 lines as well as the CO 6–5 line. Source velocities ($V_{\rm lsr}$) are shown with vertical lines. The lines were smoothed to a common bin of 1.0 km s^{-1}.

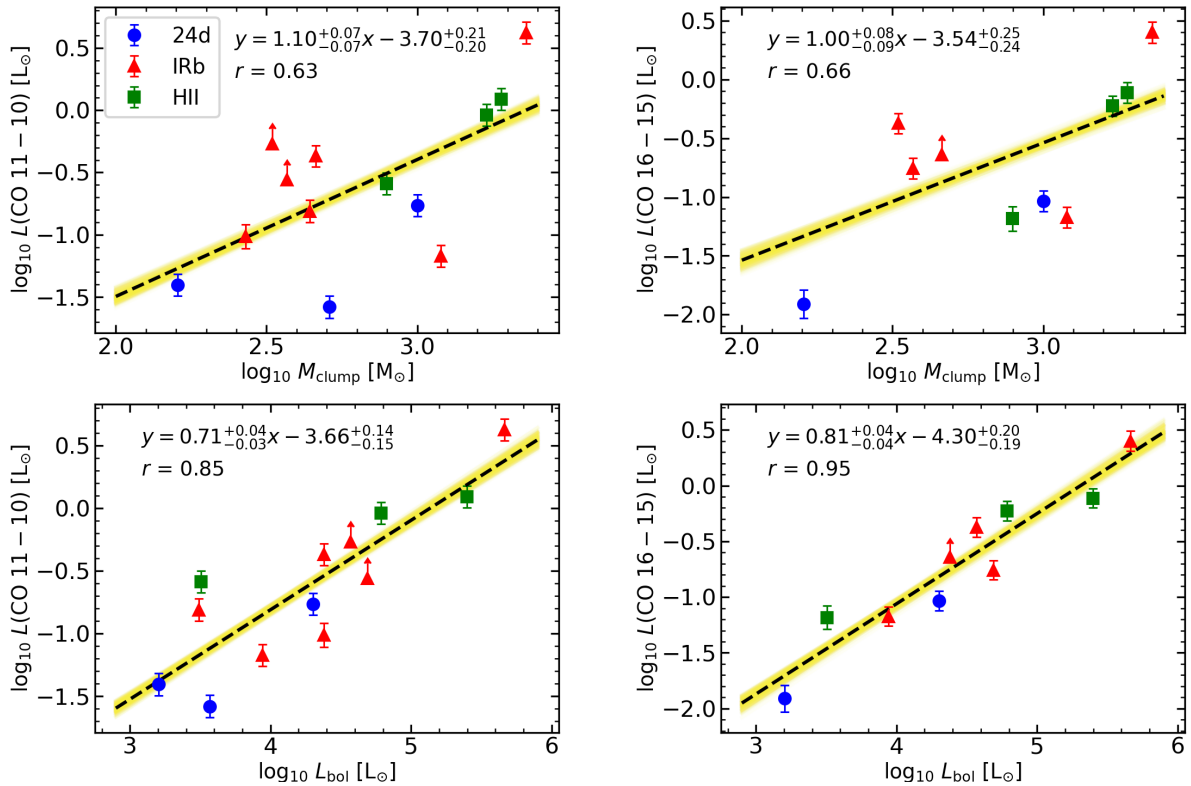

Fig. 3. Line luminosities of CO 11–10 and 16–15, as a function of $M_{\rm clump}$ and $L_{\rm bol}$. IR-weak (24d) sources are shown with blue circles, IR-bright (IRb) sources with red triangles, and HII regions (HII) with green squares. The linear regression fit with Markov chain Monte Carlo is shown with dashed black lines and yellow shades. The linear log-log and Pearson correlation coefficients, r, are presented in each plot. Objects with self-absorption are shown with an upward arrow, indicating the lower limit for calculated luminosities.

Table 3. Detection of line wing emission in high-J CO lines and their comparison to prior outflow detections.

No.	Source	CO 4–3 [(a)]	CO 6–5 [(b)]	^{13}CO 3–2 [(c)]	^{13}CO 2–1 [(d)]	SiO 2–1 [(e)]	CO 11–10 [(f)]	CO 13–12 [(f)]	CO 16–15 [(f)]
1	G351.16+0.7	✓	✓	...	–	–	✓	...	✓
2	G351.25+0.7	✓	✓	...	–	–	✓	✓	✓
3	G351.44+0.7	✓	✓	...	–	–	✓	...	✓
4	G351.58−0.4	✓	✓	...	–	–	✓	...	✓
5	G351.77−0.5	✓	✓	...	✓	–	✓	...	✓
6	G12.81−0.2	✓	✓	...	✓	–	✓	✓	✓
7	G14.19−0.2	✓	✓	...	✓	✓	✓	...	–
8	G13.66−0.6	✓	✓	...	–	✓	–	...	–
9	G14.63−0.6	✓	✓	...	–	✓	✓	...	–
10	G34.41+0.2	✓	✓	–	–	✓	✓	...	–
11	G34.26+0.15	✓	✓	✓	–	✓	✓	...	✓
12	G34.40−0.2	✓	✓	–	–	✓	✓	...	–
13	G35.20−0.7	✓	✓	–	–	–	✓	...	✓

Notes. The symbols have the following meanings: '–' non-detection, ✓ detections, and '...' lack of data or unable to detect. [(a)]Based on single pointing observations from APEX/FLASH$^+$ (Navarete et al. 2019). [(b)]Obtained from CO 6–5 maps using APEX CHAMP$^+$ (Navarete et al. 2019). [(c)]Data available only for the sources no. 10–13 in the G34 cloud (Yang et al. 2018a), due to a limited coverage of the CHIMPS survey (Rigby et al. 2016). [(d)]Based on the identification of line wings towards SEDIGISM sources (Yang et al. 2022). [(e)]Sources no. 1–5: Mopra molecular lines survey of ATLASGAL sources (Urquhart et al. 2019); and sources no. 6–13: IRAM 30m follow-up of ATLASGAL sources (Csengeri et al. 2016). [(f)]Wing detection following line decomposition in Sect. 3.2.

sources, the ^{13}CO 10–9 line for three sources, the C^{18}O 6–5 line for one source, and the ^{13}CO 6–5 line for one source (see Appendix D).

We identified line wing emission in the CO 11–10 line towards all sources except G13.66−0.6 (Table 3). The wings in the CO 16–15 line are seen only towards eight out of ten sources with the 3σ line detection. Properties and profiles of all wing emission are shown in Appendix D.

The ubiquity of line wings is consistent with previous detections of the outflows towards the same sources using lower-J lines of CO and SiO (Table 3). In particular, all sources from our sample show line wings in the CO 6–5 line (Navarete et al. 2019). The non-detection of the CO 11–10 line wing in G13.66−0.6 could be either due to a low signal-to-noise ratio (S/N; Fig. 1) or a lack of recent heating of the outflow gas due to shocks (Karska et al. 2013; Kristensen et al. 2017). The ^{13}CO 2–1 wings have only been seen towards G351.77−0.5, G12.81−0.2, and G14.19−0.2 (Yang et al. 2022) due to limited sensitivity, illustrating the difficulty in detecting line wings in rare CO isotopologues (see also, Stephens et al. 2018, 2019). Finally, SiO 2–1 have been observed towards our sources (Urquhart et al. 2019; Csengeri et al. 2016) and line wings have been detected in six of them. All the non-detections, in fact, show line wings in the high-J CO lines (Table 3), indicating that additional factors play a role in the excitation of SiO and CO lines.

Detecting outflows towards distant star-forming clumps is often hampered by confusion. Background and foreground galactic sources along the line of sight might contribute to the wing emission, which may result in false outflow detections. We note, however, that the high detection statistics (>60%) of line wings and the wings' smooth shapes in our source sample are very unlikely to be explained by source confusion. The high-J CO emission is typically well confined to the regions with active star formation.

In conclusion, our decomposition method results in the estimate of line wing emission towards 12 and eight sources in the CO 11–10 and CO 16–15 lines, respectively.

3.3. CO line wing emission

Decomposition of the line profiles allowed us to quantify the amount of high-J CO emission in the line wings, and its contribution to the entire line profiles. Furthermore, the ratio of the two CO transitions can be studied as a function of gas velocity.

The fraction of emission in the line wings of the CO 11–10 transition ranges from ~29 to 73%, whereas the mean fraction of each evolutionary stage is ~50%, suggesting that there is no dependence with the source evolution (Fig. 4). The fraction of emission in CO 16–15 line wings is similar to the CO 11–10 transition, and ranges from ~28 to 76%. These results are consistent with the fraction of line wing emission measured towards two high-mass protostellar objects: AFGL 2591 in both CO 11–10 (~37%) and CO 16–15 (~34%) from van der Wiel et al. (2013), and W3 IRS5 in CO 10–9 (~50%) from San José-García et al. (2016).

The fraction of high-J CO emission has also been estimated for several high-mass YSOs by subtracting the envelope contribution from the total, unresolved line profiles. The *Herschel*/HIFI observations of rare isotopologues of CO were used to constrain models of CO (main isotopologue) emission arising from envelopes (e.g. Herpin et al. 2012, 2016; Karska et al. 2014; Jacq et al. 2016). In the case of NGC 7538 IRS1, 70–100% of velocity-unresolved CO J = 15–14 emission and 3–22% of CO J = 22–21 was attributed to the envelope (Karska et al. 2014). Thus, the contribution of the outflow component was predicted to increase with the rotational level of the CO line.

The increase in the relative contribution of the wing emission from J_{up} = 11 to 16 was indeed measured for four out of eight sources in our sample, for which outflow wings are detected in both CO transitions. The fraction of wing emission increases from ~42% (CO 11–10) to 50% (CO 16–15) for G34.26+0.15, from 57% to 68% for G351.16+0.7, from 69% to 76% for G351.44+0.7, and from 62% to 70% for G351.58−0.4. The increase is therefore not as sharp as for the CO 15–14 and

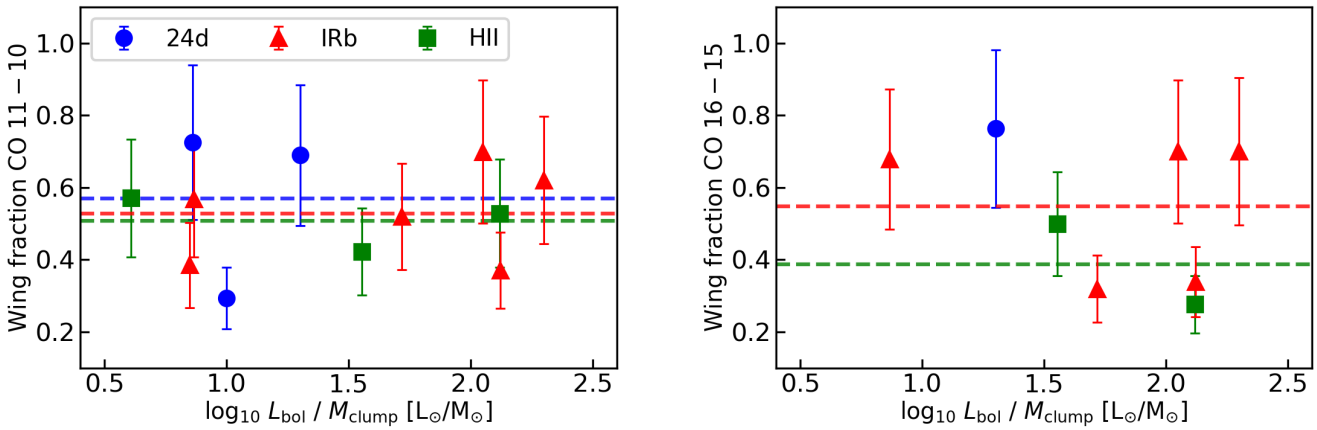

Fig. 4. Fraction of the integrated emission in the line wings of CO 11–10 (left) and CO 16–15 (right), as a function of $L_{\rm bol}/M_{\rm clump}$ (Table 1). Dashed horizontal lines show the mean wing fraction at each evolutionary stage. The colour-coding is the same as in Fig. 3.

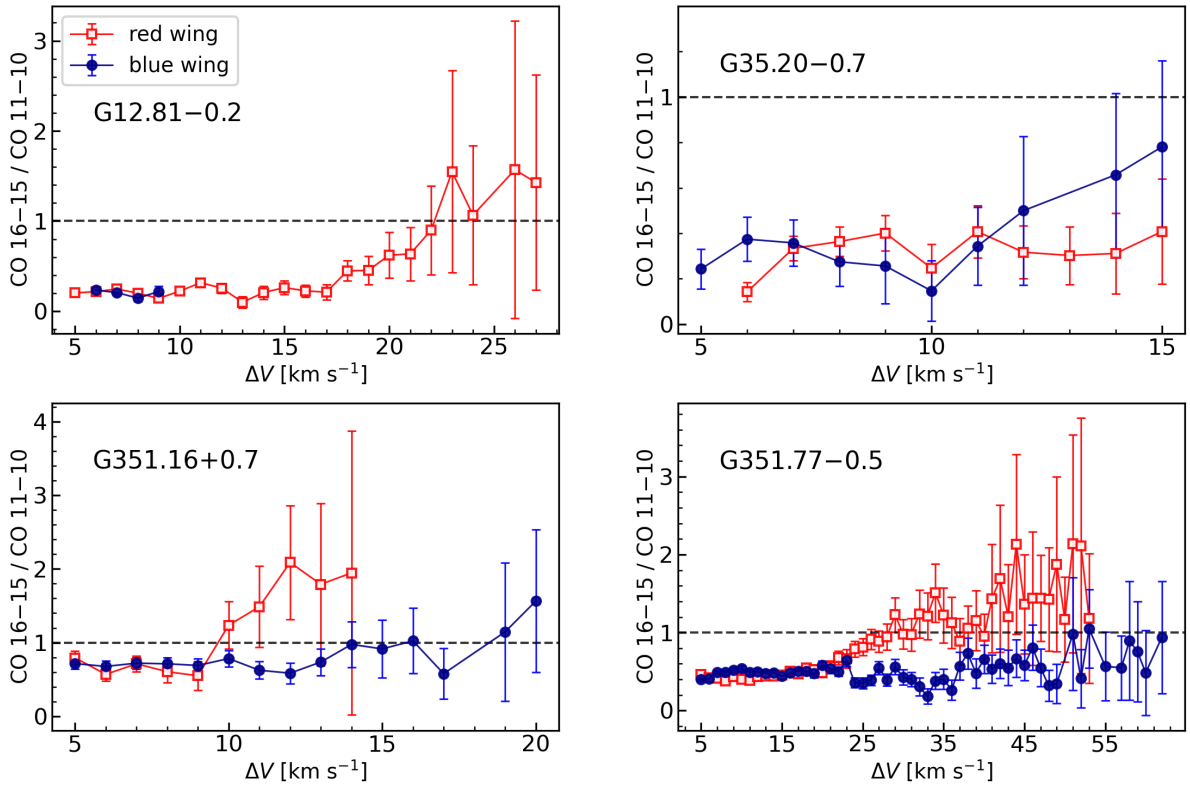

Fig. 5. Ratio of the line wing emission in CO 16–15 and 11–10 transitions as a function of the absolute velocity offset from the source velocity. The red-shifted emission is shown with red squares, and the blue-shifted emission with blue circles. The dashed horizontal line presents the level above which CO 16–15 is greater than CO 11–10.

CO 22–21 lines of NGC 7538 IRS1, but consistent with a rising contribution of wing emission in higher-J lines.

The amount of emission in the wings of higher-J CO lines allows us to study the gas excitation conditions in the outflowing gas. Assuming that emission in the line wings is optically thin and thermalised, the higher CO line ratios would correspond to higher gas kinetic temperatures, $T_{\rm kin}$ (see Sects. 3.4 and 3.5). Figure 5 shows the observed ratio of CO 16–15 and 11–10 lines in the red and blue wings as a function of the absolute offset from the source velocity. The ratio was calculated in steps of 1.0 km s^{-1}, avoiding the line centres (±5 km s^{-1}), and presented for channels where the S/N is above 2.

The ratio of CO 16–15 and CO 11–10 increases as a function of velocity for at least a few sources, for example, the red wing of G12.81−0.2, G351.16+0.7, and G351.77−0.5, and the blue wing of G35.20−0.7 (Fig. 5). In most of those cases, the highest-velocity emission is stronger in CO 16–15 than in CO 11–10. Such trends are consistent with similar studies using CO 3–2, 10–9, and 16–15 towards a sample of low- to high-mass protostars (see Sect. 4.2).

In summary, we find a lack of correlation between the fraction of high-J CO integrated emission in the line wings and the clump evolutionary stage. Even so, the fraction increases with the CO rotational level in half of the sources. The ratio of the

wing emission in the CO 16–15 and CO 11–10 lines increases with the offset velocity in several sources.

3.4. Molecular excitation in LTE (full profile + wings)

Detection of at least two CO lines allowed us to determine the rotational temperature of the outflowing gas detected in the line wings under the assumption of LTE. For comparisons with previous studies with *Herschel*/PACS, the calculations were also performed for the velocity-integrated line profiles.

Emission line fluxes of CO 11–10 and CO 16–15 were used to calculate the number of emitting molecules, $\mathcal{N}_u$, for each molecular transition as follows:

$$\mathcal{N}_u = \frac{L_{CO}\lambda}{hcA}, \quad (1)$$

where L_{CO} refers to the line luminosity of the CO line at wavelength λ, A to the Einstein coefficient, c to the speed of light, and h to Planck's constant. We note that for two sources, G12.81−0.2 and G351.25+0.7, additional observations of CO 13–12 are included. The number of emitting molecules, $\mathcal{N}_u$, was used instead of column densities, because the size of the emitting region is unresolved.

The relation between $\mathcal{N}_u$ and the total number of emitting molecules, $\mathcal{N}_{tot}$, follows the equation

$$\ln\left(\frac{\mathcal{N}_u}{g_u}\right) = -\frac{E_u}{T_{rot}k_b} + \ln\left(\frac{\mathcal{N}_{tot}}{Q(T_{rot})}\right), \quad (2)$$

where g_u is the statistical weight of the upper level, E_u the energy of the upper level, k_b the Boltzmann constant, T_{rot} the rotational temperature, and $Q(T_{rot})$ the partition function at the temperature T_{rot}.

The rotational temperature was calculated from slope b of the linear fit ($y = ax + b$) to the data in the natural logarithm units, $T_{rot} = -1/a$. The total number of emitting molecules, $\mathcal{N}_{tot}$, was determined from the fit intercept b as follows:

$$\mathcal{N}_{tot} = Q(T_{rot}) \cdot \exp(b). \quad (3)$$

Figure 6 shows example Boltzmann diagrams for G351.25+0.7 and G12.81−0.2, constructed using the velocity-integrated emission of CO (full profile). Table 4 shows T_{rot} and $\mathcal{N}_{tot}$ for all sources with at least two CO line detections separately for the integrated-profile emission and the line wings (see Sect. 3.2).

The two sources with three CO line detections are characterised by T_{rot} of ∼170 K using the integrated line emission. The remaining sources show T_{rot} in the range from ∼110 K to 200 K, with a mean of 152 K. Similar temperatures were obtained for the wing emission tracing outflow gas, with a mean T_{rot} of 167 K. While the wing emission is often responsible for the bulk of the total emission, hot core emission, with typical temperatures of ∼ 100–200 K (Fontani et al. 2007; Taniguchi et al. 2023), might also contribute to the far-IR emission at the source velocity.

For G34.26+0.15, T_{rot} of ∼150 K is significantly lower than 365 ± 15 K obtained from *Herschel*/PACS (Karska et al. 2014). We note, however, that the latter temperature was obtained using CO lines with J_u from 14 to 30, sensitive to both 'warm' and 'hot' gas components (Karska et al. 2018). If CO transitions with J_u from 14 to 16 are used instead, T_{rot} of 244 ± 45 K is obtained (adopting values from Table C.1. in Karska et al. 2014). Even lower T_{rot} is expected when the CO 11–10 line, tracing a colder gas component, is used in the calculation, in line with the results obtained for G34.26+0.15. It is noteworthy that it is essential to have many CO transitions to determine all of the underlying physical conditions.

Finally, we note that the ratio of the total number of emitting molecules ($\mathcal{N}_{tot}$) in the line wings and the total line profile ranges from 40% to 79% (Table 4), consistent with the overall fraction of wing emission (Sect. 3.2). In absolute terms, $\log_{10}\mathcal{N}_{tot}$ ranges

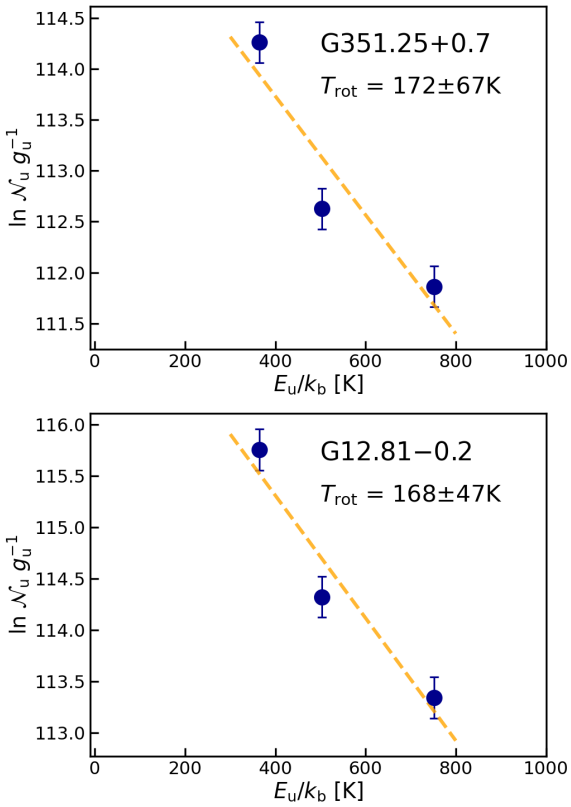

Fig. 6. Rotational diagrams of CO for G12.81−0.2 and G351.25+0.7, which are based on the observations of full profile CO transitions with J_u of 11, 13, and 16. The natural logarithm of the number of emitting molecules from a level u, $\mathcal{N}_u$ (dimensionless), divided by the degeneracy of the level, g_u, is shown as a function of the upper level energy, E_u/k_B, in Kelvins. Detections are shown as blue circles. Dashed orange lines show linear regression fits to the data; the resulting rotational temperatures are provided in the plots with the associated errors from the fit.

Table 4. CO rotational excitation for both the integrated line profiles and line wings only assuming LTE.

Source	Integrated profile		Line wings	
	T_{rot}(K)	$\log_{10}\mathcal{N}_{tot}$	T_{rot}(K)	$\log_{10}\mathcal{N}_{tot}$
G351.16+0.7	199	51.7	219	51.4
G351.25+0.7	172(67)	52.2(0.6)	165(66)	51.8(0.6)
G351.44+0.7	151	52.2	157	52
G351.58−0.4	158	53.6	166	53.3
G351.77−0.5	177	52.6	177	52.5
G12.81−0.2	168(47)	52.9(0.4)	131(31)	52.8(0.4)
G14.63−0.6	125	51.7	–	–
G34.26+0.15	152	53.0	162	52.6
G34.40−0.2	111	52.7	–	–
G35.20−0.7	141	52.7	120	52.5

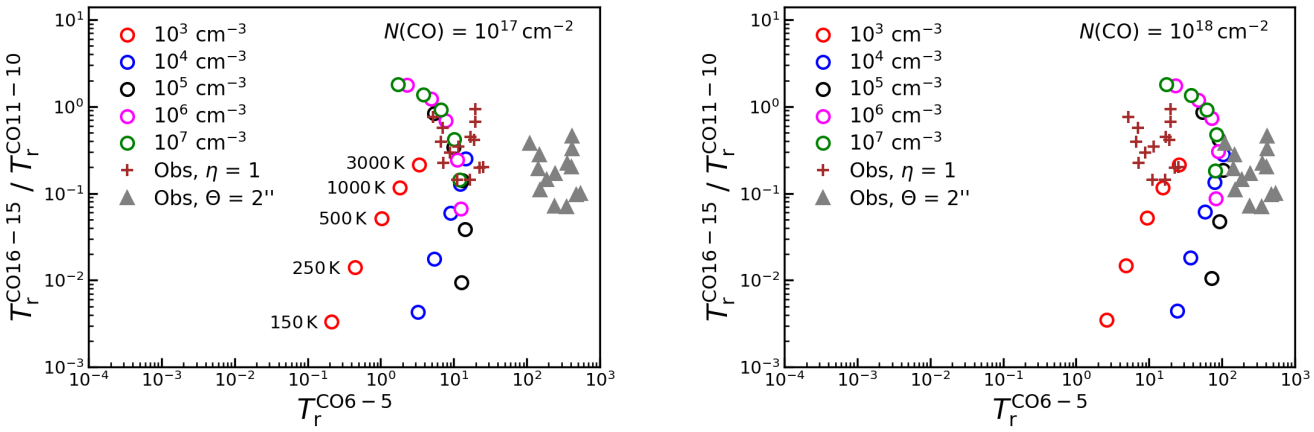

Fig. 7. CO excitation conditions from RADEX models versus observations. The plots present models at a different N(CO) of 10^{17} and 10^{18} cm^{-2}. The models are presented with empty circles, and their colours correspond to a different hydrogen volume density, n_{H_2}, between 10^3 and 10^7 cm^{-3}. At each volume density level, five temperatures – 150, 250, 500, 1000, and 3000 K – were sampled. Observations assuming a beam filling factor of 1 are shown in crosses, while observations assuming a tiny source of 2″, which correspond to an extreme case of a small beam filling factor, are shown with triangles.

from 51.7 to 53.6, consistent with the average 52.4(0.1) ± 0.5 measured for high-mass protostars with *Herschel*/PACS (Karska et al. 2014).

3.5. Molecular excitation in non-LTE (wings)

Due to relatively low densities in the regions of the ISM where outflows propagate, the LTE assumption may not hold. Non-LTE modelling is therefore necessary to determine the physical conditions responsible for the observed line emission. For this study, we used the well-established code RADEX (van der Tak et al. 2007) to estimate gas temperatures, densities, and CO column densities, which reproduce the observed line wing emission of three mid- and high-J CO lines: CO 6–5, 11–10, and 16–15.

We calculated model grids for a range of kinetic temperatures, T_{kin}, from 150 to 3000 K, H_2 number densities, n_{H_2}, from 10^3 to 10^7 cm^{-3}, and CO column densities, N(CO), of 10^{16}, 10^{17}, and 10^{18} cm^{-2}. We assumed H_2 as the only collision partner, and a background temperature of 2.73 K. The linewidths of all lines were fixed at 19 km s^{-1}, based on the observations of CO 6–5 (Appendix B and Navarete et al. 2019).

For comparisons of models with observations, we used peak intensities obtained from RADEX, since the wing emission does not follow a simple Gaussian; we also converted the observations from T_{MB} to T_r through $T_r = T_{MB}/\eta$. Because we did not spatially resolve the line emitting regions, we considered two cases during the computation of the beam filling factor: (i) the source that fills the entire beam (η = 1); and (ii) the source size of 2″ or $\eta \sim 8 \times 10^{-3} - 5 \times 10^{-2}$, consistent with the size of a source in our sample, G34.26+0.15, which was measured from the Spitzer/IRAC 3.6 μm image. The spatial extent of CO 6–5 emission is ∼4 times larger than the APEX/CHAMP$^+$ beam, according to previous observations (Navarete et al. 2019).

Figure 7 shows the comparison of non-LTE radiative transfer models with line wing observations of high-J CO lines[5] (Sect. 3.2). The ratio of CO 16–15 and CO 11–10 depends on both T_{kin} and n_{H_2}, and shows a spread of 3 orders of magnitude. On the other hand, the intensity of CO 6–5 is most sensitive to the assumed N(CO), and increases by 2–3 orders of magnitude between 10^{16} and 10^{18} cm^{-2}. The impact of the assumed beam filling factor is almost negligible to the CO 16–15 / CO 11–10 ratio.

The models match the observations best for the assumed CO column densities of 10^{17} and 10^{18} cm^{-2} (Fig. 7). The solutions for temperature and density are degenerate and can be split into two regimes: (i) a lower-density scenario with n_{H_2} of 10^3–10^4 cm^{-3} and T_{kin} of at least 1000 K, and (ii) a high-density, moderate-temperature scenario with n_{H_2} of 10^5–10^7 cm^{-3} and T_{kin} between 150 and 500 K. The ratio of high-J CO lines can be well reproduced for both considered filling factors in the scenario (ii); the best-matching source size is likely larger than 2″ but depends on the assumed column density. In scenario (i), the ratio of high-J CO lines can be reproduced for a small fraction of our sample assuming T_{kin} of 1000 K. Much higher temperatures would be required to match observations of the majority of targets. In general, the CO 6–5 peak intensity increases with gas density: for example, for n_{H_2} of 10^3 cm^{-3} and N(CO) of 10^{18} cm^{-2}, models would match the observations assuming the filling factor of 1, whereas n_{H_2} of 10^4 cm^{-3} and N(CO) of 10^{17}–10^{18} cm^{-2} point at smaller filling factors.

In conclusion, only scenario (ii) can explain the observations of all targets. The T_{kin} range in this scenario is also in better agreement with T_{rot} estimated under the LTE condition in Sect. 3.4, and it is consistent with detections of molecular species excited exclusively in high-density environments towards other high-mass clumps (e.g. van der Tak et al. 2013, 2019). On the other hand, scenario (i) requires temperatures in excess of 3000 K to explain the observed CO lines (E_{up} < 800 K) at more than half of our targets; such temperatures are too high even for the outflows from high-mass stars. Therefore, we prefer the high-density, moderate-temperature scenario to describe the physical conditions towards our source sample. We note, however, that our models constrain only the ranges of temperature and density, as we cannot fully break the degeneracy between different models.

To summarise, non-LTE radiative transfer models provide support to the LTE excitation of high-J CO emission in the high-mass clumps. The best match with observations was obtained for gas densities of 10^5–10^7 cm^{-3}, T_{kin} between 150 and 500 K, and CO column densities of 10^{17} and 10^{18} cm^{-2}. Such conditions are

[5] Observations of G351.44+0.7 are not included because we could not obtain its CO 6–5 line wing due to the lack of ^{13}CO 6–5 opacity (Appendix D).

consistent with CO excitation in outflows and this is discussed further in Sect. 4.2.

4. Discussion

High spectral resolution observations from SOFIA/GREAT allowed us to disentangle dynamical properties of high-J CO emission towards high-mass star-forming clumps. The excitation conditions have been studied in the high-velocity gas component assuming both LTE and non-LTE regimes, supporting the origin in moderate-temperature, high-density gas associated with the outflows (Sects. 3.4–3.5). Here, we discuss our results in the context of previous observations of high-mass protostars with *Herschel* and SOFIA.

4.1. High-J CO emission in high-mass clumps

The high-J ($J \gtrsim 10$) CO emission in high-mass star-forming regions has been attributed to gas cooling of several physical components, including (i) a warm, dense envelope of central protostars (Ceccarelli et al. 1996; Doty & Neufeld 1997), (ii) UV-irradiated outflow cavity walls (Bruderer et al. 2009; San José-García et al. 2016), (iii) currently shocked gas in the outflows (van der Wiel et al. 2013; Karska et al. 2014), and (iv) photodissociation regions (Lane et al. 1990; Ossenkopf et al. 2010, 2015; Stock et al. 2015). A similarity of CO to H_2O, both in spatial extent and line shapes, supported the scenario of shock excitation in similar layers composing the outflow cavity walls (see e.g. San José-García et al. 2016; Kristensen et al. 2017; van Dishoeck et al. 2021).

Broad line profiles of high-J CO lines provide a solid evidence of the outflow origin of a part of CO emission in high-mass clumps from the ATLASGAL survey (Sect. 3.1, see also San José-García et al. 2013; Indriolo et al. 2017). It is noteworthy that the fraction of CO emission in the line wings with respect to the total line emission is not sensitive to the evolutionary stage of the clumps (Sect. 3.3). In fact, a significant fraction of CO 11–10 is detected in the line wings of clumps at very early evolutionary stages (up to 76%, Sect. 3.3).

The signposts of outflow activity in the IR-weak clumps are in agreement with the ubiquitous detection of broad line wings in the SiO 2–1 line towards ATLASGAL sources spanning all evolutionary stages, including 25% of IR-quiet clumps (Csengeri et al. 2016). Molecular outflows are indeed also commonly detected towards 70 µm dark clumps using other tracers (Urquhart et al. 2022; Yang et al. 2022).

The integrated high-J CO emission shows a strong correlation with the clump bolometric luminosity (Sect. 3.1). The correlation extends even to low- and intermediate-mass protostars (Fig. 8), suggesting a similar physical mechanism operating over a few orders of magnitude different spatial scales. In deeply embedded low-mass objects, $L_{\rm bol}$ is dominated by accretion luminosity, which in turn is closely related to the amount of mass ejected in the outflows (Frank et al. 2014). Thus, the tight correlation of high-J CO emission with $L_{\rm bol}$ for ATLASGAL clumps suggests an equally high contribution of accretion luminosity in high-mass regions.

The velocity-resolved SOFIA spectra provide strong support for an origin of the bulk high-J CO emission in outflows, during all evolutionary stages of high-mass clumps. The correlation of CO line fluxes with bolometric luminosity suggest common physical conditions and processes leading to high-J CO emission from low- to high-mass star-forming regions.

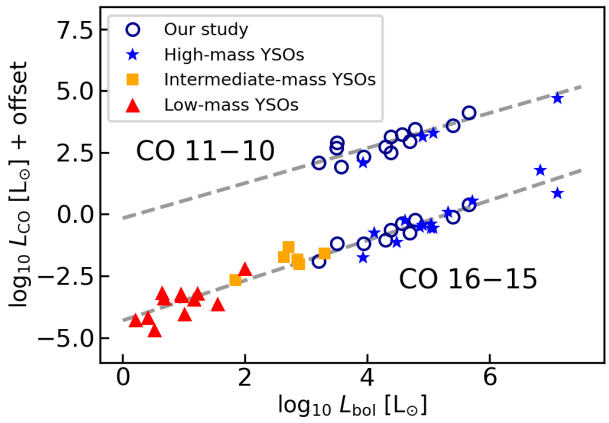

Fig. 8. Velocity-integrated CO line luminosity of 11–10 and 16–15 transitions versus source bolometric luminosity from low- to high-mass star-forming regions. The dashed lines show a linear fit obtained using only the sources from our study, which are shown in blue empty circles. Blue stars show observations of other high-mass protostars from Karska et al. (2014), Indriolo et al. (2017), and Kaźmierczak-Barthel et al. (2014); orange squares present emission from intermediate-mass objects (Matuszak et al. 2015); and red triangles show data for Class 0 protostars (Kristensen et al. 2017).

4.2. Excitation conditions

Observations of multiple CO lines allow one to study gas excitation across various source properties and evolutionary stages. In combination with other far-IR lines, they also constrain the properties of shocks responsible for the emission in broad line wings of high-J CO lines.

The rotational temperatures in the high-velocity gas in the ATLASGAL clumps range from ~120 K to 219 K, and are similar to the temperatures obtained from the full line profiles (Sect. 3.4). Five IR-bright clumps show a mean $T_{\rm rot}$ of 169 ± 30 K, whereas two H II clumps are characterised by $T_{\rm rot}$ of 147 ± 16 K. Thus, a possible decrease in the gas temperature in the outflows as the clumps evolve might be present, but for the sources in our sample the difference is not significant.

Rotational temperatures of ~200–210 K, consistent with our measurements, have been estimated in the line wings of the high-mass protostar DR21(OH) assuming LTE (Leurini et al. 2015). Non-LTE modelling of multiple CO lines indicated $T_{\rm kin}$ of 60–200 K in the outflow gas component of another high-mass source, AFGL 2591 (van der Wiel et al. 2013). In W3 IRS5, excitation temperatures of ~100–210 K were measured in a range of CO 10–9 and 3–2 lines' velocities covered by an outflow in this region (from 5 to 20 km s^{-1}), with the highest temperatures corresponding to the highest velocities (San José-García et al. 2013). A similar trend of increasing gas temperature with velocity was also clearly detected in the outflow wing emission from ATLASGAL clumps observed with SOFIA/GREAT (Sect. 3.3), and in the SiO survey of ~430 clumps observed with the IRAM 30 m telescope (Csengeri et al. 2016).

Comparisons of gas excitation using high-J CO lines can be extended to a larger number of sources once the emission in the full line profiles is considered. The velocity-integrated *Herschel*/PACS detections of CO transitions from $J_{\rm u}$ of 14 to 30 towards ten high-mass protostars provided an average $T_{\rm rot}$ of ~300(23)±60 K (Karska et al. 2014). Protostars with detections of higher-J lines were generally characterised by a higher $T_{\rm rot}$, suggesting the possible presence of an additional

Table 5. CO rotational excitation determined from integrated line profiles towards high-mass objects.

Source	$T_{\rm rot}$(K)	Reference
NGC 7538 IRS1 [(a)]	160(10)	Karska et al. (2014)
AFGL 2591	130(5)	Kaźmierczak-Barthel et al. (2014)
W49N [(b)]	220(20)	Indriolo et al. (2017)
Orion S	145(5)	Indriolo et al. (2017)
Orion KL	180(25)	Indriolo et al. (2017)
Sgr B2(M)	140(20)	Indriolo et al. (2017)
G12.81−0.2	168(47)	This work
G351.25+0.7	172(67)	This work
ATLASGAL (all) [(c)]	111–199	This work

Notes. Rotational temperatures obtained from the integrated line profiles of CO transitions with $J_{\rm u}$ of 11, 13, and 16. [(a)]Calculation using CO lines with $J_{\rm u}$ from 14 to 17. [(b)]Calculation using CO lines with $J_{\rm u}$ from 14 to 16. [(c)]Based only on CO 11–10 and CO 16–15 detections, see Sect. 3.3.

$T_{\rm rot} \gtrsim 700$ K gas component detected towards low-mass protostars that appears to be 'hidden' in their high-mass counterparts, possibly due to the a small beam filling factor of such emission and/or optically thick continuum emission (Manoj et al. 2013; Green et al. 2013; Karska et al. 2013, 2018). Clearly, any comparisons of $T_{\rm rot}$ should consider the similar J levels for their calculation (Sect. 3.4, and e.g. Neufeld 2012; Jiménez-Donaire et al. 2017; Yang et al. 2018b).

Table 5 compares $T_{\rm rot}$ measurements for several high-mass protostars with the data of the same or similar CO transitions to our SOFIA/GREAT survey (Sect. 3.4). All sources with at least three observed transitions show $T_{\rm rot}$ from 130 K to 220 K, consistent with the values determined for ATLASGAL clumps and hot cores. The relatively narrow range of $T_{\rm rot}$ is qualitatively similar to that of the universal 'warm', ~300 K gas component based on CO 14–13 to 25–24 transitions towards low-, intermediate-, and high-mass protostars (Karska et al. 2014, 2018; Matuszak et al. 2015; van Dishoeck et al. 2021). The CO 11–10 transition in low-mass protostars is typically associated with a 'cool' gas component with $T_{\rm rot}$ ~100 K (e.g. Yang et al. 2018b), and its inclusion in the fit causes the lower values of $T_{\rm rot}$ (< 300 K).

The CO rotational temperature depends on the gas density and kinetic temperature, and it can be characterised with both (i) low-density, high-temperature (Neufeld 2012; Manoj et al. 2013; Yang et al. 2018b) and (ii) high-density, low-temperature regimes (Karska et al. 2013, 2018; Green et al. 2013; Kristensen et al. 2017). The first scenario requires $n_{\rm H_2}$ ~10^3 cm^{-3} and $T_{\rm kin} \gtrsim$ 2000 K, and has the advantage of reproducing the positive curvature of the CO diagrams over a broad range of energy levels (Neufeld 2012). In contrast, the second scenario accounts for the similarity of $J \gtrsim 14$ CO and H_2O emission most evidently seen in low-mass protostars with high-densities required for H_2O excitation (Karska et al. 2013; van Dishoeck et al. 2021).

Non-LTE modelling of massive clumps provides strong support for a high-density scenario of CO excitation (Sect. 3.5). In the regime of moderate gas temperatures ($T_{\rm kin}$ from 150 to 500 K), gas densities of 10^5–10^7 cm^{-3} match the data best. Such physical conditions are fully consistent with the modelling of high-J CO and H_2O emission towards high-mass protostars (San José-García et al. 2016; van Dishoeck et al. 2021). They are also comparable to the physical conditions determined in the jet, terminal shock, and cavities of the intermediate-mass protostar Cep E (Lefloch et al. 2015).

The underlying mechanism behind the highly excited CO gas has been investigated for both Cep E and its high-mass counterpart Cep A. Detailed comparisons of CO, in combination with [O I] and OH, suggest that the origin is in dissociative or UV-irradiated shock models with pre-shock densities above 10^5 cm^{-3} (Gusdorf et al. 2016, 2017). Assuming a compression factor of ~100, typical for dissociative shocks (Karska et al. 2013), such models would also be in agreement with radiative-transfer modelling for high-mass clumps (Sect. 3.5). However, a fraction of high-J CO emission detected at source velocity could also originate from the central hot core.

5. Conclusions

We have characterised the SOFIA/GREAT line profiles observed towards 13 high-mass protostars selected from the ATLASGAL survey, which significantly increases the number of high-mass objects that have velocity-resolved high-J CO lines. The velocity information enabled us to quantify the line components and the properties of their emitting sources. We summarise and draw the following conclusions:

- CO 11–10 emission was detected towards all of the sources, as early as the 24d stage. Ten out of 13 clumps also show a clear detection of CO 16–15. Additionally, CO 13–12 was detected towards two sources. The lines exhibit broad line wing emission typical for outflows from YSOs;
- We detected wing emission in the CO 11–10 line from 12 clumps and in the CO 16–15 line from eight clumps, implying that the highly excited CO lines originate in outflows. The wing fraction is similar for all clump evolutionary stages. On the other hand, we found no signatures of high-velocity gas (i.e. bullets) in the far-IR spectra;
- Under the LTE assumption, we found $T_{\rm rot}$ of 110–200 K for the entire line profiles and 120–220 K for the wing component. Such temperatures are in agreement with gas densities of 10^5–10^7 cm^{-3}, moderate temperatures of 150 K and 500 K, and CO column densities of 10^{17} and 10^{18} cm^{-2} obtained from the non-LTE models;
- Significant correlations between high-J CO emission and bolometric luminosities suggest similar underlying physical processes and conditions across all evolutionary stages of high-mass clumps. The correlation also extends to low-mass protostars, where high-J CO emission originate in outflow shocks, consistent with our study.

High angular resolution maps of high-mass clumps would be necessary to better characterise the physical structure of the regions with strong high-J CO emission and spatially disentangle outflows and hot cores (Goicoechea et al. 2015). The MIRI instrument on board the *James Webb* Space Telescope could pinpoint the spatial extent of shocked gas in high-mass star-forming clumps.

Acknowledgements. The authors thank the anonymous referee for detailed comments that have helped us improve this paper. We thank SOFIA/GREAT staff for collecting and reducing the data. We also thank Dr. Helmut Wiesemeyer for his support in reducing data from the SOFIA/4GREAT observations. A.K. acknowledges support from the Polish National Agency for Academic Exchange grant no. BPN/BEK/2021/1/00319/DEC/1. A.Y.Y. acknowledges support from the National Natural Science Foundation of China (NSFC) grants no. 11988101 and no. 12303031. This work is based on observations made with the NASA/DLR Stratospheric Observatory for Infrared Astronomy (SOFIA). SOFIA is jointly operated by the Universities Space Research Association, Inc. (USRA), under NASA contract NNA17BF53C, and the Deutsches SOFIA Institut (DSI) under DLR contract 50 OK 2002 to the University of Stuttgart. *Herschel* was an ESA space observatory with science instruments provided by European-led Principal Investigator consortia and with important participation from NASA. This

publication is based on data acquired with the Atacama Pathfinder Experiment (APEX). APEX is a collaboration between the Max-Planck-Institut fur Radioastronomie, the European Southern Observatory, and the Onsala Space Observatory.

References

Bally, J. 2016, ARA&A, 54, 491
Bally, J., & Lada, C. J. 1983, ApJ, 265, 824
Beuther, H., Schilke, P., Sridharan, T. K., et al. 2002, A&A, 383, 892
Bruderer, S., Benz, A. O., Bourke, T. L., & Doty, S. D. 2009, A&A, 503, L13
Ceccarelli, C., Hollenbach, D. J., & Tielens, A. G. G. M. 1996, ApJ, 471, 400
Cheng, Y., Qiu, K., Zhang, Q., et al. 2019, ApJ, 877, 112
Codella, C., Lorenzani, A., Gallego, A. T., Cesaroni, R., & Moscadelli, L. 2004, A&A, 417, 615
Contreras, Y., Schuller, F., Urquhart, J. S., et al. 2013, A&A, 549, A45
Csengeri, T., Leurini, S., Wyrowski, F., et al. 2016, A&A, 586, A149
de Graauw, T., Helmich, F. P., Phillips, T. G., et al. 2010, A&A, 518, A6
de Villiers, H. M., Chrysostomou, A., Thompson, M. A., et al. 2014, MNRAS, 444, 566
Doty, S. D., & Neufeld, D. A. 1997, ApJ, 489, 122
Duran, C. A., Gusten, R., Risacher, C., et al. 2021, IEEE Trans. Terahertz Sci. Technol., 11, 194
Evans, Neal J., I. 1999, ARA&A, 37, 311
Fontani, F., Pascucci, I., Caselli, P., et al. 2007, A&A, 470, 639
Frank, A., Ray, T. P., Cabrit, S., et al. 2014, in Protostars and Planets VI, eds. H. Beuther, R. S. Klessen, C. P. Dullemond, & T. Henning, 451
Frerking, M. A., Langer, W. D., & Wilson, R. W. 1982, ApJ, 262, 590
Giannetti, A., Wyrowski, F., Brand, J., et al. 2014, A&A, 570, A65
Goicoechea, J. R., Etxaluze, M., Cernicharo, J., et al. 2013, ApJ, 769, L13
Goicoechea, J. R., Chavarría, L., Cernicharo, J., et al. 2015, ApJ, 799, 102
Gómez-Ruiz, A. I., Gusdorf, A., Leurini, S., et al. 2012, A&A, 542, L9
Green, J. D., Evans, Neal J., I., Jørgensen, J. K., et al. 2013, ApJ, 770, 123
Gusdorf, A., Güsten, R., Menten, K. M., et al. 2016, A&A, 585, A45
Gusdorf, A., Anderl, S., Lefloch, B., et al. 2017, A&A, 602, A8
Güsten, R., Nyman, L. Å., Schilke, P., et al. 2006, A&A, 454, L13
Güsten, R., Baryshev, A., Bell, A., et al. 2008, SPIE Conf. Ser., 7020, 702010
Herpin, F., Chavarría, L., van der Tak, F., et al. 2012, A&A, 542, A76
Herpin, F., Chavarría, L., Jacq, T., et al. 2016, A&A, 587, A139
Heyminck, S., Graf, U. U., Güsten, R., et al. 2012, A&A, 542, A1
Indriolo, N., Bergin, E. A., Goicoechea, J. R., et al. 2017, ApJ, 836, 117
Jacq, T., Braine, J., Herpin, F., van der Tak, F., & Wyrowski, F. 2016, A&A, 595, A66
Jiménez-Donaire, M. J., Meeus, G., Karska, A., et al. 2017, A&A, 605, A62
Karska, A., Herczeg, G. J., van Dishoeck, E. F., et al. 2013, A&A, 552, A141
Karska, A., Herpin, F., Bruderer, S., et al. 2014, A&A, 562, A45
Karska, A., Kaufman, M. J., Kristensen, L. E., et al. 2018, ApJS, 235, 30
Kasemann, C., Güsten, R., Heyminck, S., et al. 2006, SPIE Conf. Ser., 6275, 62750N
Kaźmierczak-Barthel, M., van der Tak, F. F. S., Helmich, F. P., et al. 2014, A&A, 567, A53
König, C., Urquhart, J. S., Csengeri, T., et al. 2017, A&A, 599, A139
Kristensen, L. E., van Dishoeck, E. F., Mottram, J. C., et al. 2017, A&A, 605, A93
Krumholz, M. R., Bate, M. R., Arce, H. G., et al. 2014, in Protostars and Planets VI, eds. H. Beuther, R. S. Klessen, C. P. Dullemond, & T. Henning, 243
Lane, A. P., Haas, M. R., Hollenbach, D. J., & Erickson, E. F. 1990, ApJ, 361, 132
Lefloch, B., Gusdorf, A., Codella, C., et al. 2015, A&A, 581, A4
Leurini, S., Codella, C., Zapata, L. A., et al. 2009, A&A, 507, 1443
Leurini, S., Wyrowski, F., Wiesemeyer, H., et al. 2015, A&A, 584, A70
Manoj, P., Watson, D. M., Neufeld, D. A., et al. 2013, ApJ, 763, 83
Marseille, M. G., van der Tak, F. F. S., Herpin, F., & Jacq, T. 2010, A&A, 522, A40
Matuszak, M., Karska, A., Kristensen, L. E., et al. 2015, A&A, 578, A20
Navarete, F., Leurini, S., Giannetti, A., et al. 2019, A&A, 622, A135
Neufeld, D. A. 2012, ApJ, 749, 125
Offner, S. S. R., & Chaban, J. 2017, ApJ, 847, 104
Ossenkopf, V., Röllig, M., Simon, R., et al. 2010, A&A, 518, A79
Ossenkopf, V., Koumpia, E., Okada, Y., et al. 2015, A&A, 580, A83
Pérez-Beaupuits, J. P., Güsten, R., Spaans, M., et al. 2015, A&A, 583, A107
Pilbratt, G. L., Riedinger, J. R., Passvogel, T., et al. 2010, A&A, 518, A1
Rigby, A. J., Moore, T. J. T., Plume, R., et al. 2016, MNRAS, 456, 2885
Risacher, C., Gusten, R., Stutzki, J., et al. 2016, IEEE Trans. Terahertz Sci. Technol., 6, 199
Risacher, C., Güsten, R., Stutzki, J., et al. 2018, J. Astron. Instrum., 7, 1840014
San José-García, I., Mottram, J. C., Kristensen, L. E., et al. 2013, A&A, 553, A125
San José-García, I., Mottram, J. C., van Dishoeck, E. F., et al. 2016, A&A, 585, A103
Schöier, F. L., van der Tak, F. F. S., van Dishoeck, E. F., & Black, J. H. 2005, A&A, 432, 369
Schuller, F., Menten, K. M., Contreras, Y., et al. 2009, A&A, 504, 415
Stephens, I. W., Dunham, M. M., Myers, P. C., et al. 2018, ApJS, 237, 22
Stephens, I. W., Bourke, T. L., Dunham, M. M., et al. 2019, ApJS, 245, 21
Stock, D. J., Wolfire, M. G., Peeters, E., et al. 2015, A&A, 579, A67
Taniguchi, K., Majumdar, L., Caselli, P., et al. 2023, ApJS, 267, 4
Urquhart, J. S., Csengeri, T., Wyrowski, F., et al. 2014, A&A, 568, A41
Urquhart, J. S., König, C., Giannetti, A., et al. 2018, MNRAS, 473, 1059
Urquhart, J. S., Figura, C., Wyrowski, F., et al. 2019, MNRAS, 484, 4444
Urquhart, J. S., Wells, M. R. A., Pillai, T., et al. 2022, MNRAS, 510, 3389
van der Tak, F. F. S., Black, J. H., Schöier, F. L., Jansen, D. J., & van Dishoeck, E. F. 2007, A&A, 468, 627
van der Tak, F. F. S., Chavarría, L., Herpin, F., et al. 2013, A&A, 554, A83
van der Tak, F. F. S., Shipman, R. F., Jacq, T., et al. 2019, A&A, 625, A103
van der Walt, D. J., Sobolev, A. M., & Butner, H. 2007, A&A, 464, 1015
van der Wiel, M. H. D., Pagani, L., van der Tak, F. F. S., Kaźmierczak, M., & Ceccarelli, C. 2013, A&A, 553, A11
van Dishoeck, E. F., Kristensen, L. E., Mottram, J. C., et al. 2021, A&A, 648, A24
Yang, A. Y., Thompson, M. A., Urquhart, J. S., & Tian, W. W. 2018a, ApJS, 235, 3
Yang, Y.-L., Green, J. D., Evans, Neal J., I., et al. 2018b, ApJ, 860, 174
Yang, A. Y., Urquhart, J. S., Wyrowski, F., et al. 2022, A&A, 658, A160
Yıldız, U. A., Kristensen, L. E., van Dishoeck, E. F., et al. 2013, A&A, 556, A89
Yıldız, U. A., Kristensen, L. E., van Dishoeck, E. F., et al. 2015, A&A, 576, A109
Young, E. T., Becklin, E. E., Marcum, P. M., et al. 2012, ApJ, 749, L17
Zinnecker, H., & Yorke, H. W. 2007, ARA&A, 45, 481

Appendix A: Spatial extent of line emission

For four sources, the GREAT/LFA provided additional CO 16–15 spectra towards six positions that are at 31″.8 (Risacher et al. 2018) from the source centre. We detected no extended emission towards G34.40−0.2 and G35.20−0.7. On the other hand, G34.41+0.2 and G34.26+0.15 show a weak line emission at one offset position each (Fig. A.1). For G34.41+0.2, we found similar line intensity peaks at the central and extended positions. However, G34.26+0.15 shows ∼5 times weaker emission at the offset positions than in the centre. At both objects, we observed no signs of line wing emission at the offset positions.

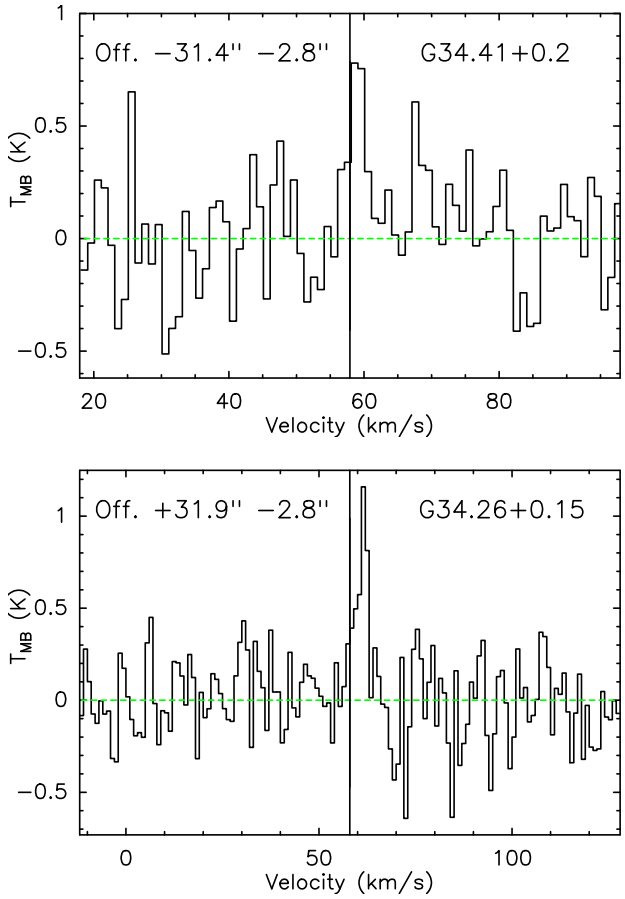

Fig. A.1: Spectra of the CO 16–15 emission arising from extended positions away from source centres. The offsets in right ascension and declination are shown in each spectrum. Black vertical lines mark the position of $V_{\rm lsr}$. Baselines are shown with green horizontal lines. The spectra were smoothed to 1.0 km s^{-1}.

Appendix B: Line parameters for emission at central position

Table B.1 presents peak and integrated intensities, and line luminosities of the high-J CO lines. Table B.2 shows results of the multiple Gaussian fit for sources with self-absorption.

Table B.1: Line properties of CO lines at different rotational transitions: J=11–10 and 16–15.

No.	Source	CO 11–10			CO 13–12			CO 16–15		
		P (K)	$S_{\rm int}$ [(a)] (K km s^{-1})	L ($L_\odot$)	P (K)	$S_{\rm int}$ [(b)] (K km s^{-1})	L ($L_\odot$)	P (K)	$S_{\rm int}$ [(c)] (K km s^{-1})	L ($L_\odot$)
1	G351.16+0.7	5.0	58.2(0.3)	6.7×10^{-2}	–	–	–	2.4	37.7(0.6)	6.7×10^{-2}
2	G351.25+0.7	34.5	238.5(1.2)	2.8×10^{-1}	14.4	92.4(0.8)	1.3×10^{-1}	15.6	98.1(1.3)	1.7×10^{-1}
3	G351.44+0.7	11.0	148.1(1.1)	1.7×10^{-1}	–	–	–	3.0	51.9(1.2)	9.2×10^{-2}
4	G351.58−0.4	5.7	95.7(1.4)	4.2×10^{0}	–	–	–	1.8	37.3(1.6)	2.5×10^{0}
5	G351.77−0.5	18.9	465.8(2.5)	5.4×10^{-1}	–	–	–	10.0	237.3(1.8)	4.2×10^{-1}
6	G12.81-02	21.6	265.8(1.1)	1.2×10^{0}	12.6	126.2(1.6)	6.8×10^{-1}	13.8	108.2(1.4)	7.7×10^{-1}
7	G14.19−0.2	0.4	4.0(0.2)	2.6×10^{-2}	–	–	–	–	–	–
8	G13.66−0.6	1.2	7.0(0.7)	9.7×10^{-2}	–	–	–	–	–	–
9	G14.63−0.6	3.6	25.5(0.6)	3.9×10^{-2}	–	–	–	0.6	5.2(1.0)	1.2×10^{-2}
10	G34.41+0.2	2.5	29.1(1.6)	1.5×10^{-1}	–	–	–	–	–	–
11	G34.26+0.15	18.6	172.1(1.9)	9.1×10^{-1}	–	–	–	5.5	60.9(1.6)	5.9×10^{-1}
12	G34.40−0.2	5.4	48.7(1.3)	2.6×10^{-1}	–	–	–	1.3	6.7(0.9)	6.5×10^{-2}
13	G35.20−0.7	13.1	140.3(1.8)	4.3×10^{-1}	–	–	–	3.9	40.7(1.1)	2.3×10^{-1}

Notes. [(a,b,c)]The numbers within brackets represent the statistical uncertainty of the integrated intensity.

Table B.2: Results of multiple Gaussian decomposition for the CO 6–5, 11–10, and 16–15 lines with self-absorption.

No.	Source	First component			Second component			Third component		
		$V_{\rm central}$ (km s^{-1})	$FWHM$ (km s^{-1})	$T_{\rm peak}$ (K)	$V_{\rm central}$ (km s^{-1})	$FWHM$ (km s^{-1})	$T_{\rm peak}$ (K)	$V_{\rm central}$ (km s^{-1})	$FWHM$ (km s^{-1})	$T_{\rm peak}$ (K)
		CO 6–5								
1	G351.16+0.7	-5.4	9.0	46.3	-8.5	22.7	18.7	–	–	–
2	G351.58−0.4	-95.4	10.2	19.2	-98.9	32.0	6.1	–	–	–
3	G351.77−0.5	-1.2	12.1	27.6	-2.8	33.6	16.1	-14.1	77.0	5.5
4	G12.81−0.2	50.0	8.6	4.9	34.6	10.8	36.7	37.0	12.8	42.6
5	G34.26+0.15	58.2	8.2	73.3	57.9	20.6	7.0	73.0	39.9	2.2
6	G34.40−0.2	58.0	6.3	19.0	55.2	12.3	7.3	60.0	12.4	10.9
7	G35.20−0.7	34.7	10.3	38.3	47.5	11.1	1.7	29.8	19.0	12.2
		CO 11–10								
1	G351.25+0.7	-6.3	3.7	5.9	-1.9	5.0	50.8	-0.5	21.5	2.4
2	G351.77−0.5	-2.6	7.9	8.6	-0.3	19.4	8.3	-6.8	56.4	3.9
		CO 16–15								
1	G35.20−0.7	34.7	4.8	5.0	35.4	17.9	1.5	–	–	–

Appendix C: Full velocity spectra at central position

Figure C.1 and C.2 present the CO 11–10 and CO 16–15 spectra from Section 3.1, but covering a velocity range of ±150 km s^{-1}. The spectra illustrate a lack of EHV emission or any other significant high-velocity gas components towards the high-mass clumps. A 2-σ feature at -125 km s^{-1} appears to be tentatively detected towards G351.77−0.5, which is known to drive multiple outflows associated with EHV gas detected in CO 2 − 1 and 6 − 5 (Leurini et al. 2009). It is noteworthy that the EHV gas component was exclusively detected towards the outflow positions of G351.77−0.5, and absent from the on-source spectra (Leurini et al. 2009), consistent with observations towards an intermediate-mass protostar Cep E (Gómez-Ruiz et al. 2012; Lefloch et al. 2015; Gusdorf et al. 2017). Thus, we do not consider this feature as real.

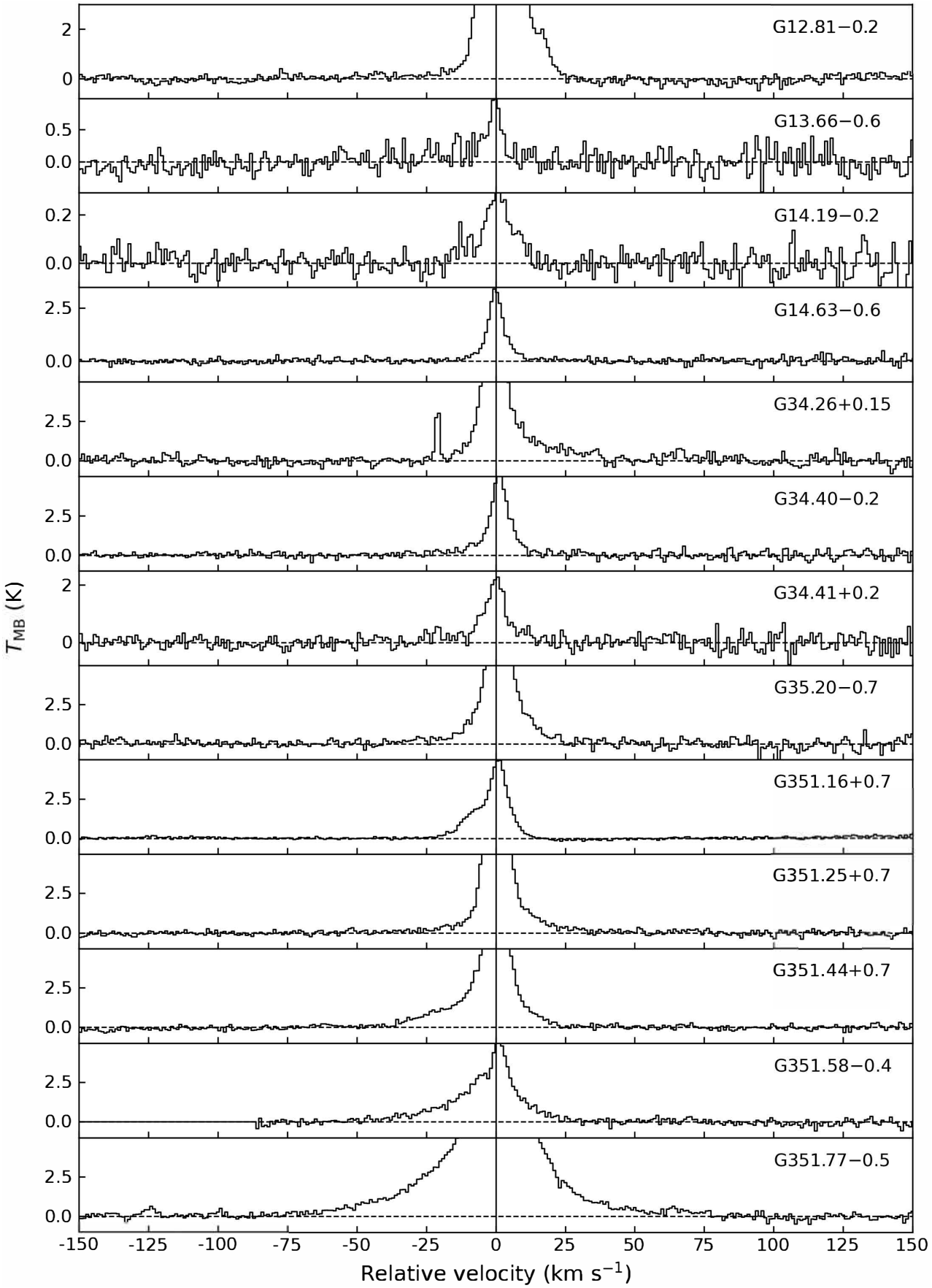

Fig. C.1: CO 11–10 spectra on a 300 km s^{-1} window, in which source velocities were shifted to 0 km s^{-1} and are marked by the solid vertical line. Horizontal dashed lines present the zero intensity level.

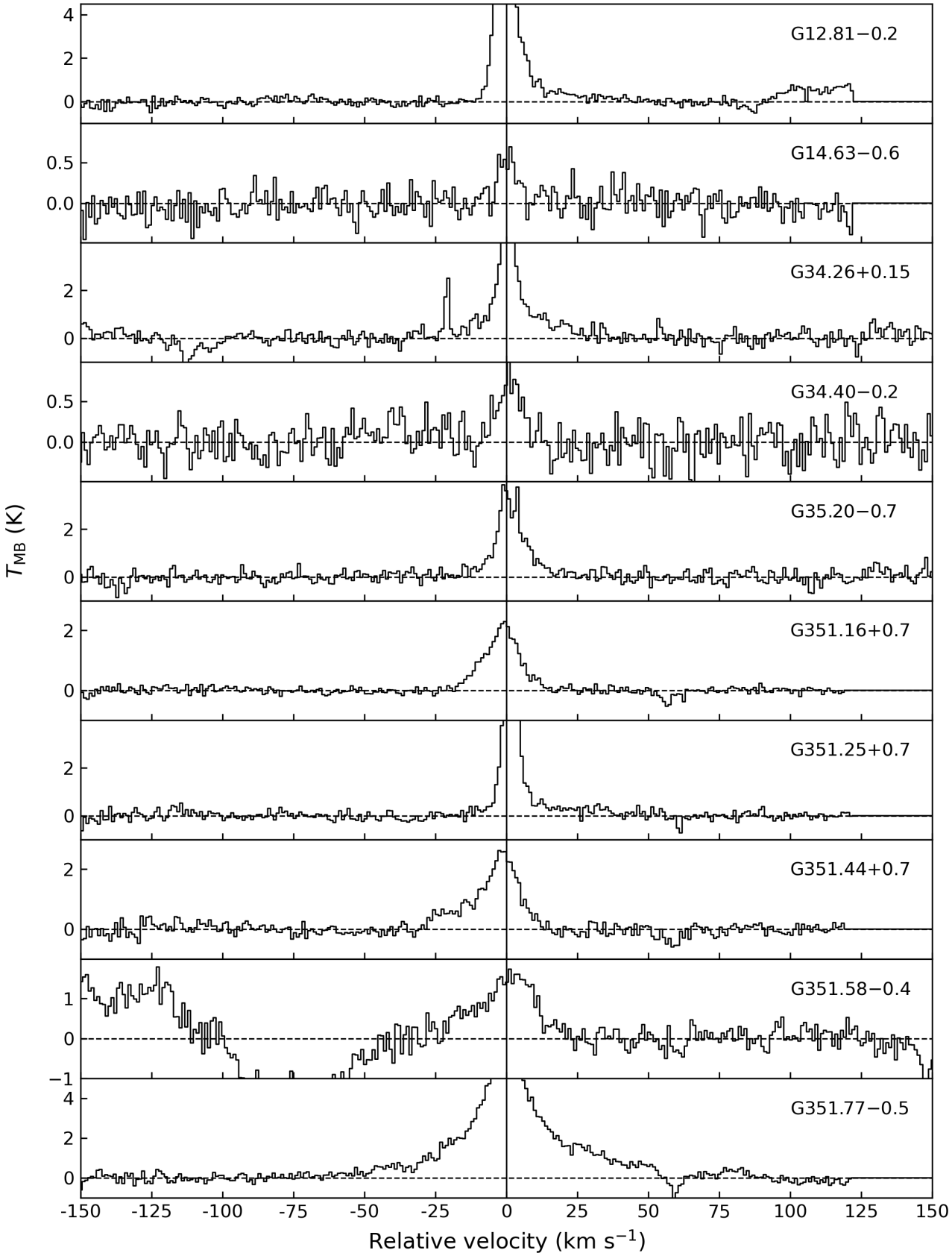

Fig. C.2: CO 16–15 spectra on a window of 300 km s^{-1}. The source velocities were shifted to 0 km s^{-1}. Vertical and horizontal lines are similar to those in Fig. C.1.

Appendix D: Details of the profile decomposition method

Appendix D.1: Line wing emission in high-J CO lines

Assuming that the high-J CO lines are optically thin, the detailed steps to identify wing emission are as follows:

(1) Scale the isotopologue line that is used as a proxy for envelope emission (called proxy line hereafter) to the height of the high-J CO profiles (see Fig. D.1, top). Table D.2 presents the envelope tracer used for each source.

(2) Fit a Gaussian to the peak of the scaled proxy line (see Fig. D.1, middle) and use it as a model for the envelope emission. In some cases, proxy lines have non-Gaussian shapes with additional wing features. The Gaussian fit helps remove contamination from the wing emission. The fit is iterated following van der Walt et al. (2007), with high velocity channels being gradually removed until a reasonable fit is obtained with a significant improvement of reduced-χ^2.

(3) Shift the envelope model to the velocity of the high-J CO peaks. This step is skipped for the CO 11–10 line of G12.81−0.2 and G035.20-0.7 as their line peaks are tilted, suggesting that a part of the line profile is attenuated.

(4) Subtract the envelope model from the high-J CO profiles (see Fig. D.1, bottom), leaving wing emission in the residual. If the residual shows significant emission above three times the spectral noise, a wing detection is confirmed.

Properties of line wing emission are presented in Table D.3. From step (2), the Gaussian fit to the scaled proxy lines provides source radial velocities, $V_{\rm lsr}$. Although $V_{\rm lsr}$ was previously determined with other tracers (e.g. $C^{17}O$ 3–2 in Giannetti et al. (2014)), low opacity proxy lines provide more reliable estimations as they probe the central gas envelope thoroughly.

The use of different envelope tracers in Table D.2 could pose a bias on the extracted outflow emission. To assess this issue, we decomposed the CO 11–10 line of G351.16+0.7 using all four envelope tracers (see Fig. D.3). Table D.1 shows that wings extracted by using the $C^{18}O$ lines and the ^{13}CO 10–9 agree well with each other with differences less than 10%. Using the ^{13}CO 6–5 line, however, returns much less wing emission. The mid-J ^{13}CO line might have a higher opacity than the others, and thus having a wider width and smaller wing component at the CO 11–10 line. For this work, we used ^{13}CO 6–5 for only one source. Therefore, the bias has been minimised. In fact, wing emission derived for that sources is a lower limit for the actual outflow emission, thereby the wing detection statistics is not affected.

Table D.1: Line wing emission of CO 11–10 towards G351.16+0.7 using various envelope tracers.

Transition	$S_{\rm int}$ [(a)] (K km s^{-1})	$T_{\rm peak}^{\rm blue}$ (K)	$T_{\rm peak}^{\rm red}$ (K)
$C^{18}O$ 9–8	33.9	1.9	2.4
$C^{18}O$ 6–5	35.4 (4%)	1.9 (0%)	2.6 (8%)
^{13}CO 10–9	32.5 (4%)	1.8 (5%)	2.2 (8%)
^{13}CO 6–5	23.5 (31%)	1.7 (11%)	1.1 (54%)

Notes. Numbers inside brackets show the difference with respect to wing parameters obtained using the $C^{18}O$ 9–8 transition (top row). [(a)]Total integrated intensity of both blue and red wings.

To extract wing emission from self-absorbed lines, we need an adjusted approach (Fig D.2). The line peak is underestimated because the emission is absorbed by cooler gas in front of the bulk emission. To recover the line peak, we fitted a multiple-Gaussian profile to the line with the absorbed parts being masked out. The fitting process was adopted from Navarete et al. (2019). At first, a single Gaussian was fit to the full profiles. A second component was added if there was significant emission above 3σ in the residual. Subsequently, a third Gaussian would be added if the residual still showed emission. The fit was set to not adding further Gaussian component after the third one. Results of the multiple-Gaussian fit are shown in Table B.2. Adopting the fit peak, we could carry out line decomposition following the four steps above. In step (3), the envelope model was shifted to the velocity of the fit peak.

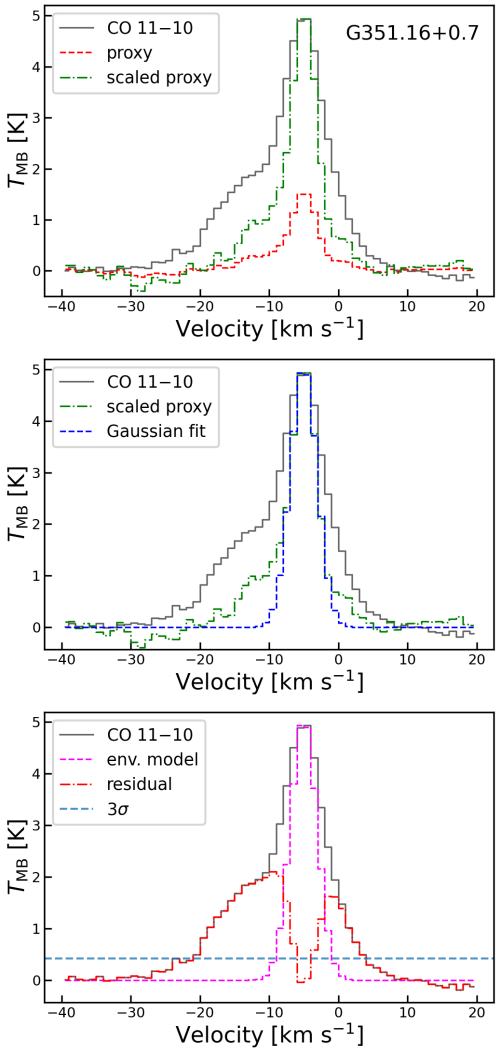

Fig. D.1: Wing extraction steps for an example high-J CO line from top to bottom.

Appendix D.2: Wing emission in CO 6–5

Navarete et al. (2019) found broad components associated with outflows on CO 6–5 lines of our sources. For this study, we attempted to extract wing emission from the CO 6–5 line of seven sources in our sample (Table D.3) by applying the decomposition method in (Yang et al. 2022) (see Fig. D.8). This method is similar to the decomposition method we used for the high-J CO lines, but an additional step was added after step (2) to account for the opacity broadening effect of the optically thick CO 6–5.

Table D.2: Tracers of dense gas envelopes at each region.

No.	Source	$C^{18}O$ 9–8	^{13}CO 10–9	$C^{18}O$ 6–5	^{13}CO 6–5
1	G351.16+0.7	✓			
2	G351.25+0.7	✓			
3	G351.44+0.7	✓			
4	G351.58−0.4	✓			
5	G351.77−0.5		✓		
6	G12.81−0.2	✓			
7	G14.19−0.2				✓
8	G13.66−0.6		✓		
9	G14.63−0.6		✓		
10	G34.41+0.2	✓			
11	G34.26+0.15			✓	
12	G34.40−0.2	✓			
13	G35.20−0.7	✓			

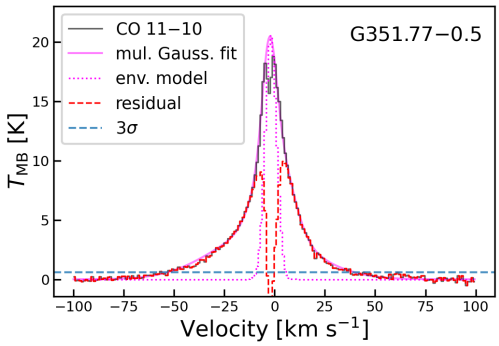

Fig. D.2: Line wing extraction for a self-absorption line in which the line peak was determined from a multiple Gaussian fit.

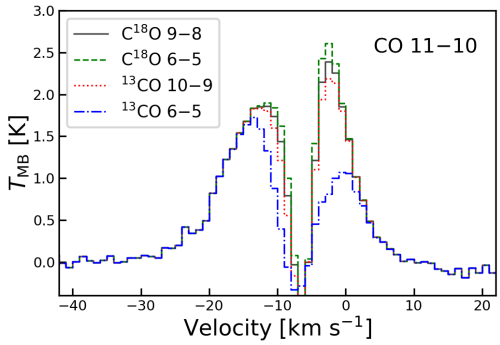

Fig. D.3: CO 11–10 wing emission of G351.16+0.7 obtained by using different envelope tracers.

To correct for the opacity broadening, one needs to derive opacity in each frequency channel:

$$\tau_\nu = \tau_0 \times \exp\left(-\frac{(\nu-\nu_0)^2}{2\sigma^2}\right), \quad \text{(D.1)}$$

where τ_0 and ν_0 are the central opacity and line frequency, and σ is the gas intrinsic velocity dispersion, namely, the FWHM of the Gaussian fit to the scaled proxy line. The CO 6–5 central opacity was estimated by multiplying the optical depth of ^{13}CO 6–5 (Dat et al., in preparation) with the abundance ratio of ^{12}CO relative to ^{13}CO, $X_{^{12}CO/^{13}CO}$, which was calculated using the galactic radius relation derived in Giannetti et al. (2014) and the galactic distance. The broaden line, which can be used as a model for the envelope emission, then, could be obtained by the radiative transfer equation:

$$T_{mb,\nu} = [F_\nu(T_{ex}) - F_\nu(T_{bg})] \times [1 - \exp(-\tau_\nu)], \quad \text{(D.2)}$$

where $F_\nu(T) = \frac{h\nu/k}{\exp(h\nu/kT)-1}$, and T_{ex} and T_{bg} are the excitation and background temperature, respectively. The term $[J_\nu(T_{ex})-J_\nu(T_{bg})]$ was directly obtained from the peak of the Gaussian fit to the scaled proxy line.

The very high optical depths of the CO 6–5 line (up to 122) result in broad lines with flat peaks (see Fig. D.8, middle). Such line profiles are not seen in observed spectra, which suggests that our envelope models are not perfect. However, the wing emission retained after subtracting such envelope models from the full line profiles can still serve as a lower limit for the outflow emission. In total, we could determine CO 6–5 wing emission for all seven sources.

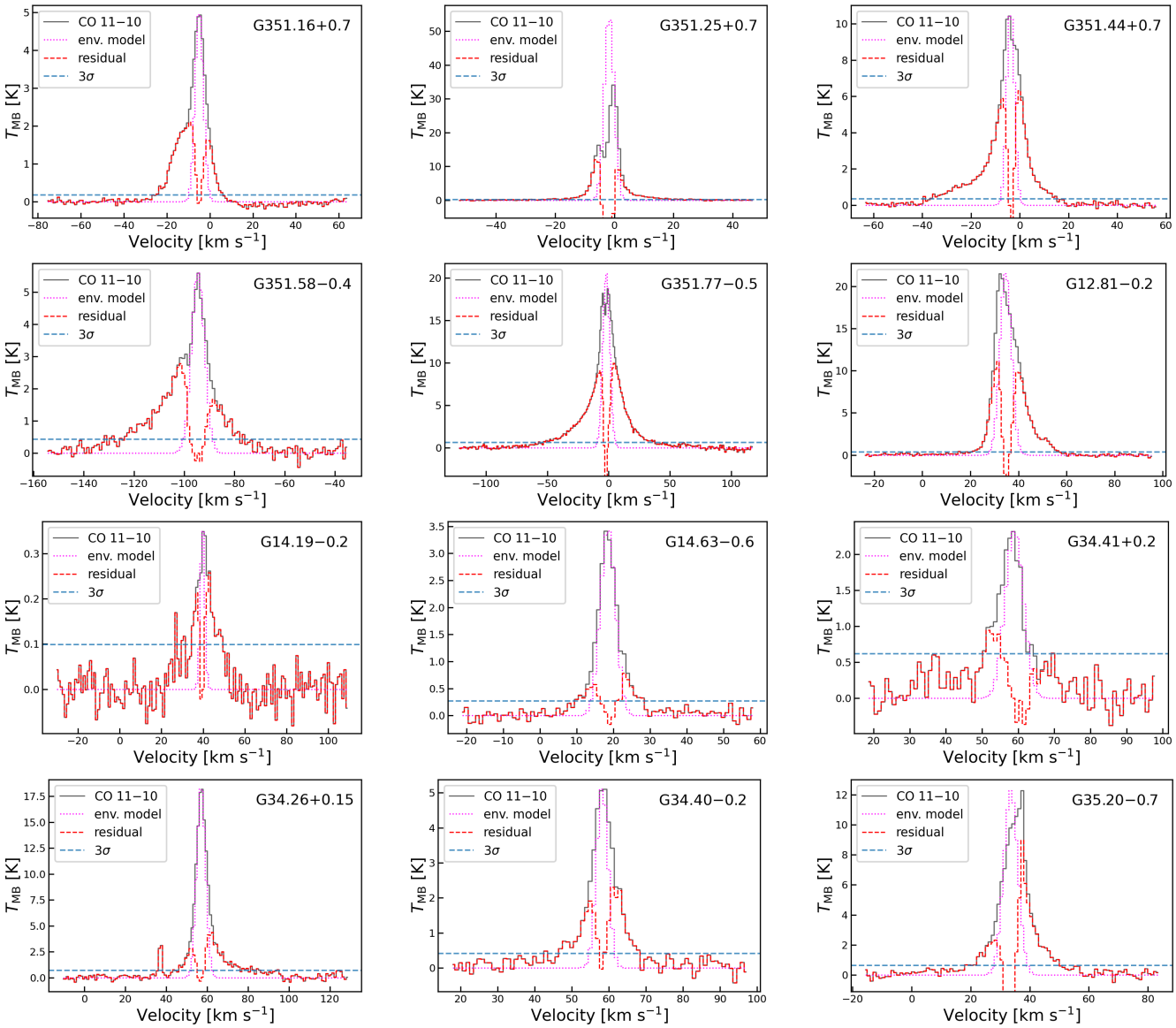

Fig. D.4: CO 11–10 wing emission (dashed red profile) extracted from the full line (solid black profile). The dotted magenta line is a model of envelope emission. The detection 3σ threshold is shown with a dashed blue line.

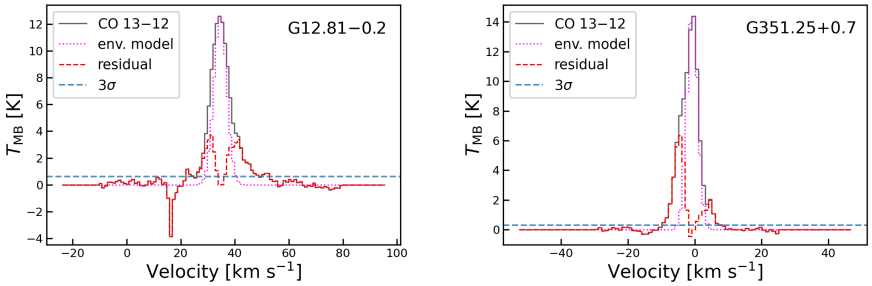

Fig. D.5: CO 13–12 wing emission (dashed red profile). The colour-coding and line styles are the same as in Fig. D.4.

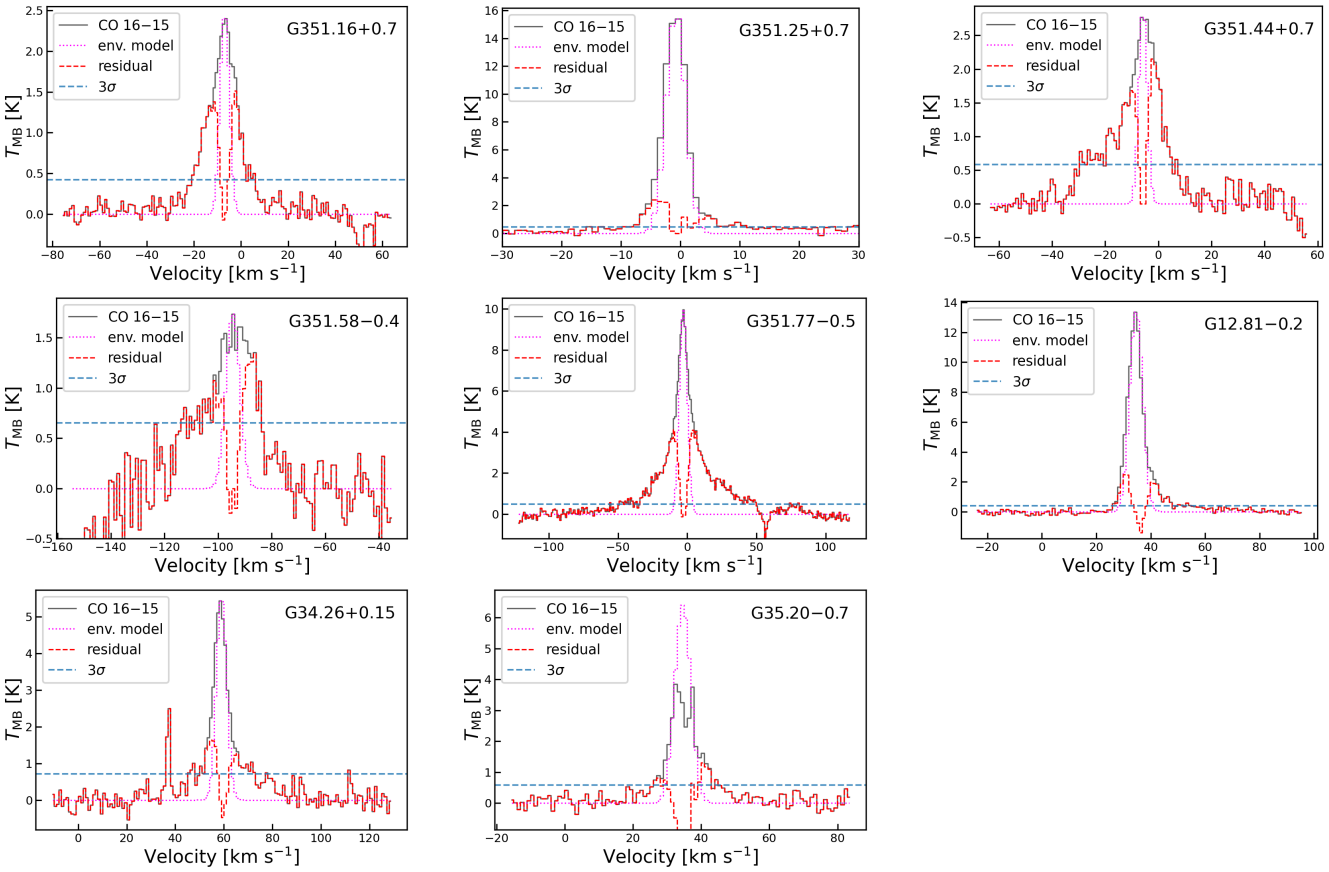

Fig. D.6: CO 16–15 wing emission (dashed red profile). The colour-coding and line styles are the same as in Fig. D.4.

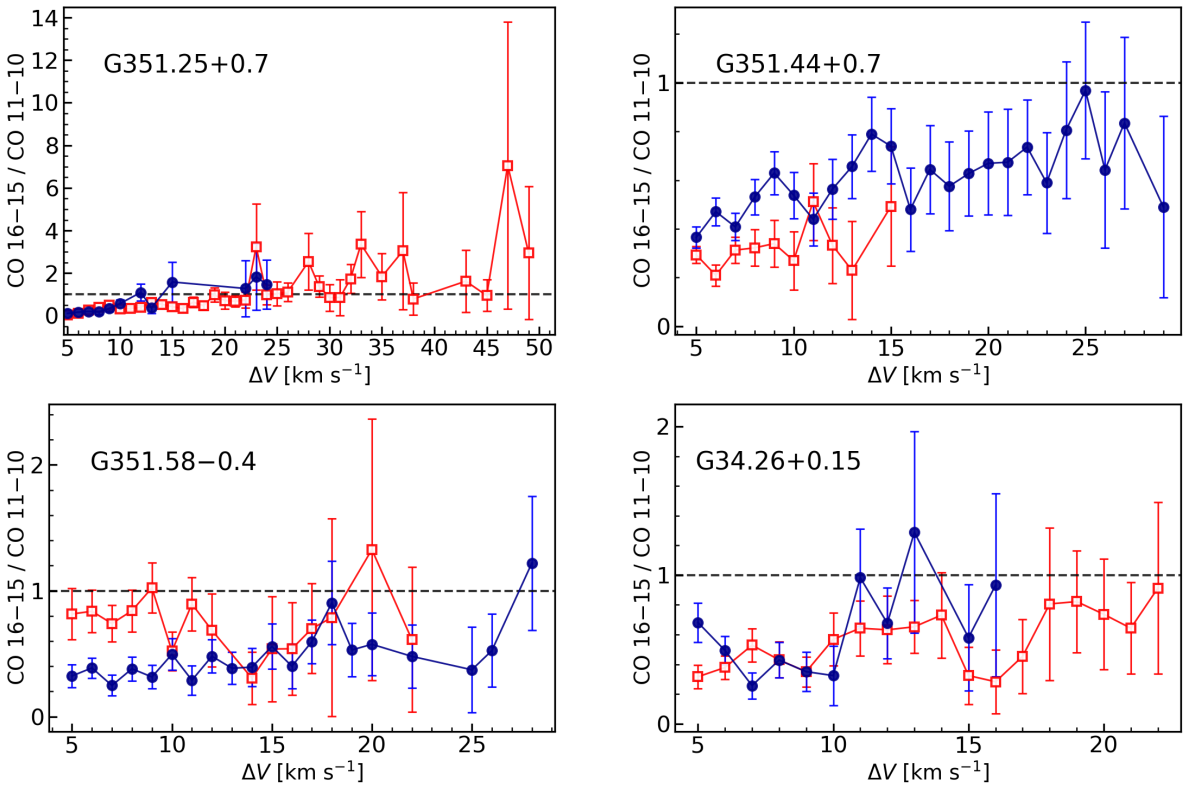

Fig. D.7: Ratio of line wing emission in the CO 16–15 and 11–10 transitions versus the absolute velocity offset from the source velocity. The red-shifted emission is shown with the red squares, while the blue-shifted emission is shown with the blue circles. The dashed horizontal line presents the level above which CO 16–15 is greater than CO 11–10.

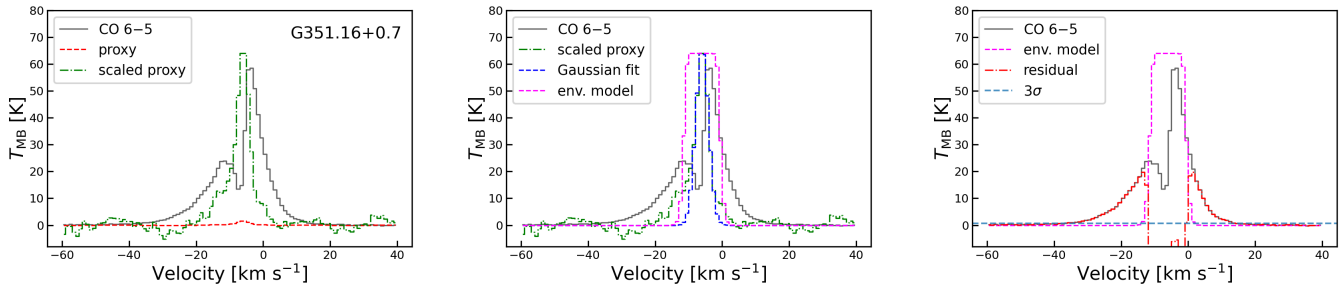

Fig. D.8: Wing extraction steps for the CO 6–5 line of G351.16+0.7 from left to right (see Appendix D).

Table D.3: Line wing emission in the CO 11–10, 16–15, 13–12, and 6–5 line.

No.	Source	Blue wing			Red wing		
		V_{range} (km s^{-1})	T_{peak} (K)	S_{int} (K km s^{-1})	V_{range} (km s^{-1})	T_{peak} (K)	S_{int} (K km s^{-1})
CO 11–10							
1	G351.16+0.7	[-32, -6]	2.1	23.7	[-5, 8]	1.6	9.4
2	G351.25+0.7	[-47, -5]	12.1	44.9	[0, 33]	9.1	43.6
3	G351.44+0.7	[-43, -5]	5.9	60.4	[-3, 21]	6.3	41.7
4	G351.58−0.4	[-137, -96]	2.8	41.4	[-93, -68]	1.7	18.0
5	G351.77−0.5	[-81, -3]	9.1	171.4	[0, 76]	9.9	154.3
6	G12.81−0.2	[-1, 34]	11.1	59.1	[36, 65]	9.9	81.4
7	G14.19−0.2	[21, 38]	0.2	1.4	[40, 54]	0.3	1.5
8	G14.63−0.6	[2, 18]	0.6	3.9	[20, 30]	0.8	3.6
9	G34.41+0.2	[28, 58]	0.9	11.2	–	–	–
10	G34.26+0.15	[41, 56]	2.8	19.6	[57, 98]	4.4	53.1
11	G34.40−0.2	[30, 57]	1.9	14.5	[58, 75]	2.3	13.3
12	G35.20−0.7	[-8, 31]	2.3	23.4	[35, 58]	9.0	49.5
CO 16–15							
1	G351.16+0.7	[-31, -8]	1.4	13.9	[-7, 20]	1.5	11.7
2	G351.25+0.7	[-28, -1]	2.4	15.2	[0, 47]	1.3	18.0
3	G351.44+0.7	[-36, -7]	1.7	23.7	[-5, 14]	2.2	15.9
4	G351.58−0.4	[-119, -97]	1.1	14.1	[-93, -72]	1.3	12.0
5	G351.77−0.5	[-89, -4]	4.1	77.1	[-1, 93]	4.1	89.0
6	G12.81−0.2	[23, 34]	2.5	10.9	[38, 81]	2.0	19.0
7	G34.26+0.15	[40, 58]	1.6	14.5	[61, 88]	1.3	15.9
8	G35.20−0.7	[20, 32]	0.8	5.2	[37, 50]	1.3	7.8
CO 13–12							
1	G351.25+0.7	[-11, -2]	6.3	23.7	[0, 12]	2.0	8.0
2	G12.81−0.2	[20, 35]	3.7	21.0	[35, 57]	3.4	29.7
CO 6–5							
1	G351.16+0.7	[-68, -12]	19.8	174.7	[-1, 26]	19.7	111.8
2	G351.25+0.7	[-53, -8]	22.6	114.9	[2, 47]	16.6	143.8
3	G351.58-0.4	[-150, -103]	6.7	85.6	[-88, -56]	5.2	45.3
4	G351.77−0.5	[-98, -12]	16.9	371.2	[6, 98]	19.1	289.8
5	G12.81−0.2	[9, 27]	7.2	27.5	[41, 68]	25.4	170.3
6	G34.26+0.15	[2, 51]	7.0	54.1	[65, 129]	8.8	108.4
7	G35.20−0.7	[-8, 27]	11.6	91.0	[40, 68]	11.2	69.1

Notes. V_{range} is the velocity range of line wing. T_{peak} and S_{int} are peak and integrated intensity of the line wing emission, respectively.

Bibliography

Andre, P., D. Ward-Thompson and M. Barsony (2000), "From Prestellar Cores to Protostars: the Initial Conditions of Star Formation", *Protostars and Planets IV*, ed. by V. Mannings, A. P. Boss and S. S. Russell 59, arXiv: astro-ph/9903284 [astro-ph].

Arce, H. G. and A. I. Sargent (2006), *The Evolution of Outflow-Envelope Interactions in Low-Mass Protostars*, **646** 1070, arXiv: astro-ph/0605139 [astro-ph].

Bachiller, R. (1996), *Bipolar Molecular Outflows from Young Stars and Protostars*, **34** 111.

Bally, J. and C. J. Lada (1983), *The high-velocity molecular flows near young stellar objects*, **265** 824.

Bally, J. (2016), *Protostellar Outflows*, **54** 491.

Beltrán, M. T. and W. J. de Wit (2016), *Accretion disks in luminous young stellar objects*, **24**, 6 6, arXiv: 1509.08335 [astro-ph.GA].

Beltrán, M. T., V. M. Rivilla, R. Cesaroni, D. Galli et al. (2022), *The sharp ALMA view of infall and outflow in the massive protocluster G31.41+0.31*, **659**, A81 A81, arXiv: 2201.10438 [astro-ph.GA].

Beltrán, M. T., V. M. Rivilla, R. Cesaroni, L. T. Maud et al. (2021), *Fragmentation in the massive G31.41+0.31 protocluster*, **648**, A100 A100, arXiv: 2103.04953 [astro-ph.GA].

Bergin, E. A. and M. Tafalla (2007), *Cold Dark Clouds: The Initial Conditions for Star Formation*, **45** 339, arXiv: 0705.3765 [astro-ph].

Bertin, E. and S. Arnouts (1996), *SExtractor: Software for source extraction.*, **117** 393.

Beuther, H., T. Henning et al. (2015), *Hierarchical fragmentation and collapse signatures in a high-mass starless region*, **581**, A119 A119, arXiv: 1508.01540 [astro-ph.GA].

Beuther, H., R. Kuiper and M. Tafalla (2025), *Star formation from low to high mass: A comparative view*, arXiv e-prints, arXiv:2501.16866 arXiv:2501.16866, arXiv: 2501.16866 [astro-ph.GA].

Beuther, H., P. Schilke, K. M. Menten et al. (2002), *High-Mass Protostellar Candidates. II. Density Structure from Dust Continuum and CS Emission*, **566** 945, arXiv: astro-ph/0110370 [astro-ph].

Beuther, H., P. Schilke, T. K. Sridharan et al. (2002), *Massive molecular outflows*, **383** 892, arXiv: astro-ph/0110372 [astro-ph].

Beuther, H. and J. Steinacker (2007), *The Protostar in the Massive Infrared Dark Cloud IRDC 18223-3*, **656** L85, arXiv: astro-ph/0701185 [astro-ph].

Bonnell, I. A., M. R. Bate, C. J. Clarke and J. E. Pringle (2001), *Competitive accretion in embedded stellar clusters*, **323** 785, arXiv: astro-ph/0102074 [astro-ph].

Bonnell, I. A. (2005), "Competitive Accretion and the IMF", *The Initial Mass Function 50 Years Later*, ed. by E. Corbelli, F. Palla and H. Zinnecker, vol. 327, Astrophysics and Space Science Library 425, arXiv: astro-ph/0501258 [astro-ph].

Bonnell, I. A. and M. R. Bate (2005), *Binary systems and stellar mergers in massive star formation*, **362** 915, arXiv: astro-ph/0506689 [astro-ph].

– (2006), *Star formation through gravitational collapse and competitive accretion*, **370** 488, arXiv: astro-ph/0604615 [astro-ph].

Bonnell, I. A., S. G. Vine and M. R. Bate (2004), *Massive star formation: nurture, not nature*, **349** 735, arXiv: astro-ph/0401059 [astro-ph].

Bruderer, S., A. O. Benz, T. L. Bourke and S. D. Doty (2009), *Evidence of warm and dense material along the outflow of a high-mass YSO*, **503** L13.

Carey, S. J. et al. (1998), *The Physical Properties of the Midcourse Space Experiment Galactic Infrared-dark Clouds*, **508** 721.

Ceccarelli, C., D. J. Hollenbach and A. G. G. M. Tielens (1996), *Far-Infrared Line Emission from Collapsing Protostellar Envelopes*, **471** 400.

Cesaroni, R. et al. (2017), *Chasing discs around O-type (proto)stars: Evidence from ALMA observations*, **602**, A59 A59.

Cheng, Y. et al. (2019), *Multiline Observations of Molecular Bullets from a High-mass Protostar*, **877**, 112 112.

Churchwell, E. (2002), *Ultra-Compact HII Regions and Massive Star Formation*, **40** 27.

Churchwell, E. et al. (2009), *The Spitzer/GLIMPSE Surveys: A New View of the Milky Way*, **121** 213.

Codella, C., A. Lorenzani, A. T. Gallego, R. Cesaroni and L. Moscadelli (2004), *The association between masers and outflows in massive star forming regions*, **417** 615.

Contreras, Y. et al. (2013), *ATLASGAL - compact source catalogue: 330° < ℓ < 21°*, **549**, A45 A45, arXiv: 1211.0741 [astro-ph.GA].

Crutcher, R. M., T. C. Mouschovias, T. H. Troland and G. E. Ciolek (1994), *Structure and Evolution of Magnetically Supported Molecular Clouds: Evidence for Ambipolar Diffusion in the Barnard 1 Cloud*, **427** 839.

Csengeri, T., S. Bontemps et al. (2017), *ALMA survey of massive cluster progenitors from ATLASGAL. Limited fragmentation at the early evolutionary stage of massive clumps*, **600**, L10 L10, arXiv: 1703.03273 [astro-ph.GA].

Csengeri, T., S. Leurini et al. (2016), *ATLASGAL-selected massive clumps in the inner Galaxy. II. Characterisation of different evolutionary stages and their SiO emission*, **586**, A149 A149, arXiv: 1511.05138 [astro-ph.GA].

Csengeri, T., J. S. Urquhart et al. (2014), *The ATLASGAL survey: a catalog of dust condensations in the Galactic plane*, **565**, A75 A75, arXiv: 1312.0937 [astro-ph.GA].

de Graauw, T. et al. (2010), *The Herschel-Heterodyne Instrument for the Far-Infrared (HIFI)*, **518**, L6 L6.

de Jong, T., W. Boland and A. Dalgarno (1980), *Hydrostatic models of molecular clouds.*, **91** 68.

de Jong, T., S. Chu and A. Dalgarno (1975), *Carbon monoxide in collapsing interstellar clouds.*, **199** 69.

de Villiers, H. M. et al. (2014), *Methanol maser associated outflows: detection statistics and properties*, **444** 566, arXiv: 1407.6042 [astro-ph.SR].

Doty, S. D. and D. A. Neufeld (1997), *Models for Dense Molecular Cloud Cores*, **489** 122, arXiv: astro-ph/9707171 [astro-ph].

Duarte-Cabral, A. et al. (2013), *CO outflows from high-mass Class 0 protostars in Cygnus-X*, **558**, A125 A125, arXiv: 1308.6490 [astro-ph.GA].

Duran, C. A. et al. (2021), *4GREAT—A Four-Color Receiver for High-Resolution Airborne Terahertz Spectroscopy*, IEEE Transactions on Terahertz Science and Technology **11** 194, arXiv: 2012.05106 [astro-ph.IM].

Evans Neal J., I. (1999), *Physical Conditions in Regions of Star Formation*, **37** 311, arXiv: astro-ph/9905050 [astro-ph].

Fischer, C. et al. (2018), *FIFI-LS: The Field-Imaging Far-Infrared Line Spectrometer on SOFIA*, Journal of Astronomical Instrumentation **7**, 1840003-556 1840003.

Fontani, F. et al. (2007), *Comparative study of complex N- and O-bearing molecules in hot molecular cores*, **470** 639, arXiv: 0705.1637 [astro-ph].

Frank, A. et al. (2014), "Jets and Outflows from Star to Cloud: Observations Confront Theory", *Protostars and Planets VI*, ed. by H. Beuther, R. S. Klessen, C. P. Dullemond and T. Henning 451, arXiv: 1402.3553 [astro-ph.SR].

Frerking, M. A., W. D. Langer and R. W. Wilson (1982), *The relationship between carbon monoxide abundance and visual extinction in interstellar clouds.*, **262** 590.

Gaczkowski, B. et al. (2013), *Herschel far-infrared observations of the Carina Nebula complex. II. The embedded young stellar and protostellar population*, **549**, A67 A67, arXiv: 1211.2995 [astro-ph.GA].

Garay, G. and S. Lizano (1999), *Massive Stars: Their Environment and Formation*, **111** 1049, arXiv: astro-ph/9907293 [astro-ph].

Giannetti, A., S. Leurini et al. (2017), *ATLASGAL-selected massive clumps in the inner Galaxy. V. Temperature structure and evolution*, **603**, A33 A33, arXiv: 1703.08485 [astro-ph.GA].

Giannetti, A., F. Wyrowski et al. (2014), *ATLASGAL-selected massive clumps in the inner Galaxy. I. CO depletion and isotopic ratios*, **570**, A65 A65, arXiv: 1407.2215 [astro-ph.GA].

Goicoechea, J. R., L. Chavarría et al. (2015), *Herschel Far-infrared Spectral-mapping of Orion BN/KL Outflows: Spatial Distribution of Excited CO, H_2O, OH, O, and C^+ in Shocked Gas*, **799**, 102 102, arXiv: 1411.2930 [astro-ph.GA].

Goicoechea, J. R., M. Etxaluze et al. (2013), *Herschel Far-infrared Spectroscopy of the Galactic Center. Hot Molecular Gas: Shocks versus Radiation near Sgr A**, **769**, L13 L13, arXiv: 1305.1119 [astro-ph.GA].

Goldreich, P. and J. Kwan (1974), *Molecular Clouds*, **189** 441.

Gómez-Ruiz, A. I. et al. (2012), *High-J CO emission in the Cepheus E protostellar outflow observed with SOFIA/GREAT*, **542**, L9 L9, arXiv: 1203.1890 [astro-ph.GA].

Gong, Y. et al. (2018), *The Serpens filament at the onset of slightly supercritical collapse*, **620**, A62 A62, arXiv: 1809.07598 [astro-ph.GA].

Goodman, A. A., P. J. Benson, G. A. Fuller and P. C. Myers (1993), *Dense Cores in Dark Clouds. VIII. Velocity Gradients*, **406** 528.

Graf, U. U. et al. (1993), *CO Lines toward NGC 2024 and Other Star-forming Regions: A Closer Look at the Warm Gas Component*, **405** 249.

Green, J. D. et al. (2013), *Embedded Protostars in the Dust, Ice, and Gas In Time (DIGIT) Herschel Key Program: Continuum SEDs, and an Inventory of Characteristic Far-infrared Lines from PACS Spectroscopy*, **770**, 123 123, arXiv: 1304.7389 [astro-ph.GA].

Griffin, M. J. et al. (2010), *The Herschel-SPIRE instrument and its in-flight performance*, **518**, L3 L3, arXiv: 1005.5123 [astro-ph.IM].

Gusdorf, A., S. Anderl et al. (2017), *Nature of shocks revealed by SOFIA OI observations in the Cepheus E protostellar outflow*, **602**, A8 A8, arXiv: 1704.03796 [astro-ph.GA].

Gusdorf, A., R. Güsten et al. (2016), *Challenging shock models with SOFIA OH observations in the high-mass star-forming region Cepheus A*, **585**, A45 A45, arXiv: 1509.08367 [astro-ph.GA].

Güsten, R., A. Baryshev et al. (2008), "Submillimeter heterodyne arrays for APEX", *Millimeter and Submillimeter Detectors and Instrumentation for Astronomy IV*, ed. by W. D. Duncan, W. S. Holland, S. Withington and J. Zmuidzinas, vol. 7020, Society of Photo-Optical Instrumentation Engineers (SPIE) Conference Series 702010 702010.

Güsten, R., L. Å. Nyman et al. (2006), *The Atacama Pathfinder EXperiment (APEX) - a new submillimeter facility for southern skies -*, **454** L13.

Harper, D. A. et al. (2018), *HAWC+, the Far-Infrared Camera and Polarimeter for SOFIA*, Journal of Astronomical Instrumentation **7**, 1840008-1025 1840008.

Heitsch, F., J. Ballesteros-Paredes and L. Hartmann (2009), *Gravitational Collapse and Filament Formation: Comparison with the Pipe Nebula*, **704** 1735, arXiv: 0909.2018 [astro-ph.GA].

Herpin, F., L. Chavarría, T. Jacq et al. (2016), *Herschel-HIFI view of mid-IR quiet massive protostellar objects*, **587**, A139 A139, arXiv: 1601.04599 [astro-ph.SR].

Herpin, F., L. Chavarría, F. van der Tak et al. (2012), *The massive protostar W43-MM1 as seen by Herschel-HIFI water spectra: high turbulence and accretion luminosity*, **542**, A76 A76, arXiv: 1204.0397 [astro-ph.GA].

Herter, T. L. et al. (2018), *FORCAST: A Mid-Infrared Camera for SOFIA*, Journal of Astronomical Instrumentation **7**, 1840005-451 1840005.

Heyer, M. et al. (2016), *The rate and latency of star formation in dense, massive clumps in the Milky Way*, **588**, A29 A29, arXiv: 1601.06875 [astro-ph.GA].

Heyminck, S. et al. (2012), *GREAT: the SOFIA high-frequency heterodyne instrument*, **542**, L1 L1, arXiv: 1203.2845 [astro-ph.IM].

Hoang, T. D., A. Karska et al. (2023), *Velocity-resolved high-J CO emission from massive star-forming clumps*, **679**, A121 A121, arXiv: 2309.14095 [astro-ph.GA].

Hoang, T. D., M.-Y. Lee et al. (2025), *ATLASGAL-selected high-mass clumps in the inner Galaxy: XI. Morphology and kinematics of warm inner envelopes*, **695**, A24 A24, arXiv: 2501.13752 [astro-ph.GA].

Hoare, M. G., S. E. Kurtz, S. Lizano, E. Keto and P. Hofner (2007), "Ultracompact Hii Regions and the Early Lives of Massive Stars", *Protostars and Planets V*, ed. by B. Reipurth, D. Jewitt and K. Keil 181, arXiv: astro-ph/0603560 [astro-ph].

Hogerheijde, M. R. and F. F. S. van der Tak (2000), *An accelerated Monte Carlo method to solve two-dimensional radiative transfer and molecular excitation. With applications to axisymmetric models of star formation*, **362** 697, arXiv: astro-ph/0008169 [astro-ph].

Hopkins, P. F. et al. (2014), *Galaxies on FIRE (Feedback In Realistic Environments): stellar feedback explains cosmologically inefficient star formation*, **445** 581, arXiv: 1311.2073 [astro-ph.CO].

Indriolo, N. et al. (2017), *CO Spectral Line Energy Distributions in Galactic Sources: Empirical Interpretation of Extragalactic Observations*, **836**, 117 117, arXiv: 1701.03789 [astro-ph.GA].

Ivezic, Z. and M. Elitzur (1997), *Self-similarity and scaling behaviour of infrared emission from radiatively heated dust - I. Theory*, **287** 799, arXiv: astro-ph/9612164 [astro-ph].

Jacob, A. M. et al. (2020), *First detection of ^{13}CH in the interstellar medium*, **640**, A125 A125, arXiv: 2007.01190 [astro-ph.GA].

Jacq, T., J. Braine, F. Herpin, F. van der Tak and F. Wyrowski (2016), *Structure and kinematics of the clouds surrounding the Galactic mini-starburst W43 MM1*, **595**, A66 A66, arXiv: 1608.08776 [astro-ph.GA].

Jiménez-Donaire, M. J. et al. (2017), *Herschel observations of the circumstellar environments of the Herbig Be stars R Mon and PDS 27*, **605**, A62 A62, arXiv: 1705.05860 [astro-ph.SR].

Jørgensen, J. K., F. L. Schöier and E. F. van Dishoeck (2002), *Physical structure and CO abundance of low-mass protostellar envelopes*, **389** 908, arXiv: astro-ph/0205068 [astro-ph].

Kahn, F. D. (1974), *Cocoons around early-type stars.*, **37** 149.

Karska, A., G. J. Herczeg et al. (2013), *Water in star-forming regions with Herschel (WISH). III. Far-infrared cooling lines in low-mass young stellar objects*, **552**, A141 A141, arXiv: 1301.4821 [astro-ph.SR].

Karska, A., F. Herpin et al. (2014), *Far-infrared molecular lines from low- to high-mass star forming regions observed with Herschel*, **562**, A45 A45, arXiv: 1311.6644 [astro-ph.SR].

Karska, A., M. J. Kaufman et al. (2018), *The Herschel-PACS Legacy of Low-mass Protostars: The Properties of Warm and Hot Gas Components and Their Origin in Far-UV Illuminated Shocks*, **235**, 30 30, arXiv: 1802.03379 [astro-ph.SR].

Kasemann, C. et al. (2006), "CHAMP $^+$: a powerful array receiver for APEX", *Millimeter and Submillimeter Detectors and Instrumentation for Astronomy III*, ed. by J. Zmuidzinas, W. S. Holland, S. Withington and W. D. Duncan, vol. 6275, Society of Photo-Optical Instrumentation Engineers (SPIE) Conference Series 62750N 62750N.

Kauffmann, J., T. Pillai, R. Shetty, P. C. Myers and A. A. Goodman (2010a), *The Mass-Size Relation from Clouds to Cores. I. A New Probe of Structure in Molecular Clouds*, **712** 1137, arXiv: 1002.0608 [astro-ph.GA].

– (2010b), *The Mass-size Relation from Clouds to Cores. II. Solar Neighborhood Clouds*, **716** 433, arXiv: 1004.1170 [astro-ph.GA].

Kaźmierczak-Barthel, M. et al. (2014), *The HIFI spectral survey of AFGL 2591 (CHESS). II. Summary of the survey*, **567**, A53 A53, arXiv: 1405.4761 [astro-ph.GA].

Kennicutt, R. C. (2005), "The role of massive stars in astrophysics", *Massive Star Birth: A Crossroads of Astrophysics*, ed. by R. Cesaroni, M. Felli, E. Churchwell and M. Walmsley, vol. 227 3.

Keto, E. (2003), *The Formation of Massive Stars by Accretion through Trapped Hypercompact H II Regions*, **599** 1196, arXiv: astro-ph/0309131 [astro-ph].

Klapper, G., F. Lewen, R. Gendriesch, S. P. Belov and G. Winnewisser (2000), *Sub-Doppler Measurements of the Rotational Spectrum of $^{13}C\,^{16}O$*, Journal of Molecular Spectroscopy **201** 124.

Koester, B., H. Stoerzer, J. Stutzki and A. Sternberg (1994), *Carbon monoxide line emission from photon dominated regions.*, **284** 545.

König, C. et al. (2017), *ATLASGAL-selected massive clumps in the inner Galaxy. III. Dust continuum characterization of an evolutionary sample*, **599**, A139 A139, arXiv: 1610.09055 [astro-ph.GA].

Kristensen, L. E., E. F. van Dishoeck, E. A. Bergin et al. (2012), *Water in star-forming regions with Herschel (WISH). II. Evolution of 557 GHz 1_{10}-1_{01} emission in low-mass protostars*, **542**, A8 A8, arXiv: 1204.0009 [astro-ph.SR].

Kristensen, L. E., E. F. van Dishoeck, J. C. Mottram et al. (2017), *Origin of warm and hot gas emission from low-mass protostars: Herschel-HIFI observations of CO J = 16-15. I. Line profiles, physical conditions, and H_2O abundance*, **605**, A93 A93, arXiv: 1705.10269 [astro-ph.GA].

Krumholz, M. R. et al. (2014), "Star Cluster Formation and Feedback", *Protostars and Planets VI*, ed. by H. Beuther, R. S. Klessen, C. P. Dullemond and T. Henning 243, arXiv: 1401.2473 [astro-ph.GA].

Kurtz, S., R. Cesaroni, E. Churchwell, P. Hofner and C. M. Walmsley (2000), "Hot Molecular Cores and the Earliest Phases of High-Mass Star Formation", *Protostars and Planets IV*, ed. by V. Mannings, A. P. Boss and S. S. Russell 299.

Lane, A. P., M. R. Haas, D. J. Hollenbach and E. F. Erickson (1990), *Far-Infrared Spectroscopy of the DR 21 Star Formation Region*, **361** 132.

Lee, M. .-., F. Wyrowski, K. Menten, M. Tiwari and R. Güsten (2022), *ATLASGAL-selected massive clumps in the inner Galaxy. X. Observations of atomic carbon at 492 GHz*, **664**, A80 A80, arXiv: 2204.11414 [astro-ph.GA].

Lefloch, B. et al. (2015), *The structure of the Cepheus E protostellar outflow: The jet, the bowshock, and the cavity*, **581**, A4 A4.

Leurini, S., C. Codella, L. Zapata et al. (2011), *On the kinematics of massive star forming regions: the case of IRAS 17233-3606*, **530**, A12 A12, arXiv: 1104.0857 [astro-ph.SR].

Leurini, S., C. Codella, L. A. Zapata et al. (2009), *Extremely high velocity gas from the massive young stellar objects in IRAS 17233-3606*, **507** 1443, arXiv: 0909.0525 [astro-ph.SR].

Leurini, S., F. Wyrowski, F. Herpin et al. (2013), *The distribution of warm gas in the G327.3-0.6 massive star-forming region*, **550**, A10 A10, arXiv: 1211.3554 [astro-ph.GA].

Leurini, S., F. Wyrowski, H. Wiesemeyer et al. (2015), *Spectroscopically resolved far-IR observations of the massive star-forming region G5.89-0.39*, **584**, A70 A70, arXiv: 1510.00366 [astro-ph.GA].

Manoj, P. et al. (2013), *Herschel/PACS Spectroscopic Survey of Protostars in Orion: The Origin of Far-infrared CO Emission*, **763**, 83 83, arXiv: 1211.2234 [astro-ph.GA].

Marseille, M. G., F. F. S. van der Tak, F. Herpin and T. Jacq (2010), *Tracing early evolutionary stages of high-mass star formation with molecular lines*, **522**, A40 A40, arXiv: 1006.3236 [astro-ph.GA].

Mattern, M. et al. (2018), *SEDIGISM: the kinematics of ATLASGAL filaments*, **619**, A166 A166, arXiv: 1808.07499 [astro-ph.GA].

Matteucci, F. (2021), *Modelling the chemical evolution of the Milky Way*, **29**, 5 5, arXiv: 2106.13145 [astro-ph.GA].

Matuszak, M. et al. (2015), *Far-infrared CO and H_2O emission in intermediate-mass protostars*, **578**, A20 A20, arXiv: 1504.03347 [astro-ph.SR].

McKee, C. F. and E. C. Ostriker (2007), *Theory of Star Formation*, **45** 565, arXiv: 0707.3514 [astro-ph].

McKee, C. F. and J. C. Tan (2003), *The Formation of Massive Stars from Turbulent Cores*, **585** 850, arXiv: astro-ph/0206037 [astro-ph].

McLaughlin, D. E. and R. E. Pudritz (1996), *A Model for the Internal Structure of Molecular Cloud Cores*, **469** 194, arXiv: astro-ph/9605018 [astro-ph].

Mihalas, D. (1978), *Stellar atmospheres*.

Molinari, S., J. Brand, R. Cesaroni and F. Palla (2000), *A search for precursors of Ultracompact Hii regions in a sample of luminous IRAS sources. III. Circumstellar dust properties*, **355** 617, arXiv: astro-ph/0001231 [astro-ph].

Molinari, S., B. Swinyard, J. Bally, M. Barlow, J. .-. Bernard, P. Martin, T. Moore, A. Noriega-Crespo, R. Plume, L. Testi, A. Zavagno, A. Abergel, B. Ali, L. Anderson et al. (2010), *Clouds, filaments, and protostars: The Herschel Hi-GAL Milky Way*, **518**, L100 L100, arXiv: 1005.3317 [astro-ph.GA].

Molinari, S., B. Swinyard, J. Bally, M. Barlow, J. .-. Bernard, P. Martin, T. Moore, A. Noriega-Crespo, R. Plume, L. Testi, A. Zavagno, A. Abergel, B. Ali, P. André et al. (2010), *Hi-GAL: The Herschel Infrared Galactic Plane Survey*, **122** 314, arXiv: 1001.2106 [astro-ph.GA].

Motte, F. and P. André (2001), *The circumstellar environment of low-mass protostars: A millimeter continuum mapping survey*, **365** 440.

Motte, F., S. Bontemps, P. Schilke et al. (2007), *The earliest phases of high-mass star formation: a 3 square degree millimeter continuum mapping of Cygnus X*, **476** 1243, arXiv: 0708.2774 [astro-ph].

Motte, F., A. Zavagno et al. (2010), *Initial highlights of the HOBYS key program, the Herschel imaging survey of OB young stellar objects*, **518**, L77 L77.

Motte, F., S. Bontemps and F. Louvet (2018), *High-Mass Star and Massive Cluster Formation in the Milky Way*, **56** 41, arXiv: 1706.00118 [astro-ph.GA].

Müller, H. S. P., S. Thorwirth, D. A. Roth and G. Winnewisser (2001), *The Cologne Database for Molecular Spectroscopy, CDMS*, **370** L49.

Müller, H. S. P., F. Schlöder, J. Stutzki and G. Winnewisser (2005), *The Cologne Database for Molecular Spectroscopy, CDMS: a useful tool for astronomers and spectroscopists*, Journal of Molecular Structure **742** 215.

Myers, P. C. and E. F. Ladd (1993), *Bolometric Temperatures of Young Stellar Objects*, **413** L47.

Myers, P. C. and A. Lazarian (1998), *Turbulent Cooling Flows in Molecular Clouds*, **507** L157, arXiv: astro-ph/9811044 [astro-ph].

Nakano, T. (1989), *Conditions for the Formation of Massive Stars through Nonspherical Accretion*, **345** 464.

Navarete, F. et al. (2019), *ATLASGAL-selected massive clumps in the inner Galaxy. VII. Characterisation of mid-J CO emission*, **622**, A135 A135, arXiv: 1812.08327 [astro-ph.GA].

Neufeld, D. A. (2012), *Collisional Excitation of Far-infrared Line Emissions from Warm Interstellar Carbon Monoxide (CO)*, **749**, 125 125, arXiv: 1202.2850 [astro-ph.GA].

Offner, S. S. R. and J. Chaban (2017), *Impact of Protostellar Outflows on Turbulence and Star Formation Efficiency in Magnetized Dense Cores*, **847**, 104 104, arXiv: 1709.01086 [astro-ph.GA].

Osorio, M., S. Lizano and P. D'Alessio (1999), *Hot Molecular Cores and the Formation of Massive Stars*, **525** 808.

Ossenkopf, V., E. Koumpia et al. (2015), *Fine-structure line deficit in S 140*, **580**, A83 A83, arXiv: 1506.01991 [astro-ph.GA].

Ossenkopf, V., M. Röllig et al. (2010), *HIFI observations of warm gas in DR21: Shock versus radiative heating*, **518**, L79 L79, arXiv: 1005.2517 [astro-ph.GA].

Osterbrock, D. E. and G. J. Ferland (2006), *Astrophysics of gaseous nebulae and active galactic nuclei*.

Padoan, P., L. Pan, M. Juvela, T. Haugbølle and Å. Nordlund (2020), *The Origin of Massive Stars: The Inertial-inflow Model*, **900**, 82 82, arXiv: 1911.04465 [astro-ph.GA].

Peng, T. .-., F. Wyrowski, F. F. S. van der Tak, K. M. Menten and C. M. Walmsley (2010), *W49A: a starburst triggered by expanding shells*, **520**, A84 A84, arXiv: 1011.1166 [astro-ph.GA].

Peng, T. .-., F. Wyrowski, L. A. Zapata, R. Güsten and K. M. Menten (2012), *The APEX-CHAMP$^+$ view of the Orion Molecular Cloud 1 core. Constraining the excitation with submillimeter CO multi-line observations*, **538**, A12 A12, arXiv: 1112.1009 [astro-ph.GA].

Peretto, N. and G. A. Fuller (2010), *A Statistical Study of the Mass and Density Structure of Infrared Dark Clouds*, **723** 555, arXiv: 1009.0716 [astro-ph.GA].

Pérez-Beaupuits, J. P. et al. (2015), *Disentangling the excitation conditions of the dense gas in M17 SW*, **583**, A107 A107, arXiv: 1508.06699 [astro-ph.GA].

Peters, T., R. S. Klessen, M.-M. Mac Low and R. Banerjee (2010), *Limiting Accretion onto Massive Stars by Fragmentation-induced Starvation*, **725** 134, arXiv: 1005.3271 [astro-ph.GA].

Pickett, H. M. et al. (1998), *Submillimeter, millimeter and microwave spectral line catalog.*, **60** 883.

Pilbratt, G. L. et al. (2010), *Herschel Space Observatory. An ESA facility for far-infrared and submillimetre astronomy*, **518**, L1 L1, arXiv: 1005.5331 [astro-ph.IM].

Pillai, T. G. S. et al. (2023), *Infall and outflow towards high-mass starless clump candidates*, **522** 3357, arXiv: 2305.04256 [astro-ph.GA].

Plume, R., D. T. Jaffe, N. J. Evans II, J. Martín-Pintado and J. Gómez-González (1997), *Dense Gas and Star Formation: Characteristics of Cloud Cores Associated with Water Masers*, **476** 730, arXiv: astro-ph/9609061 [astro-ph].

Poglitsch, A. et al. (2010), *The Photodetector Array Camera and Spectrometer (PACS) on the Herschel Space Observatory*, **518**, L2 L2, arXiv: 1005.1487 [astro-ph.IM].

Rathborne, J. M., J. M. Jackson and R. Simon (2006), *Infrared Dark Clouds: Precursors to Star Clusters*, **641** 389, arXiv: astro-ph/0602246 [astro-ph].

Reber, G. (1944), *Cosmic Static.*, **100** 279.

Rigby, A. J. et al. (2016), *CHIMPS: the $^{13}CO/C^{18}O$ ($J = 3 \rightarrow 2$) Heterodyne Inner Milky Way Plane Survey*, **456** 2885, arXiv: 1512.08235 [astro-ph.GA].

Risacher, C., R. Güsten et al. (2018), *The upGREAT Dual Frequency Heterodyne Arrays for SOFIA*, Journal of Astronomical Instrumentation **7**, 1840014 1840014, arXiv: 1812.07403 [astro-ph.IM].

Risacher, C., R. Gusten et al. (2016), *First Supra-THz Heterodyne Array Receivers for Astronomy With the SOFIA Observatory*, IEEE Transactions on Terahertz Science and Technology **6** 199, arXiv: 1512.02908 [astro-ph.IM].

Rugel, M. R. et al. (2019), *Feedback in W49A diagnosed with radio recombination lines and models*, **622**, A48 A48, arXiv: 1812.00758 [astro-ph.GA].

Sakai, T. et al. (2008), *A Molecular Line Observation toward Massive Clumps Associated with Infrared Dark Clouds*, **678** 1049, arXiv: 0802.3030 [astro-ph].

San José-García, I., J. C. Mottram, L. E. Kristensen et al. (2013), *Herschel-HIFI observations of high-J CO and isotopologues in star-forming regions: from low to high mass*, **553**, A125 A125, arXiv: 1301.4658 [astro-ph.GA].

San José-García, I., J. C. Mottram, E. F. van Dishoeck et al. (2016), *Linking low- to high-mass young stellar objects with Herschel-HIFI observations of water*, **585**, A103 A103, arXiv: 1511.00357 [astro-ph.SR].

Sánchez-Monge, Á., M. T. Beltrán et al. (2014), *A necklace of dense cores in the high-mass star forming region G35.20-0.74 N: ALMA observations*, **569**, A11 A11, arXiv: 1406.4081 [astro-ph.GA].

Sánchez-Monge, Á., R. Cesaroni et al. (2013), *A candidate circumbinary Keplerian disk in G35.20-0.74 N: A study with ALMA*, **552**, L10 L10, arXiv: 1303.4242 [astro-ph.GA].

Schöier, F. L., F. F. S. van der Tak, E. F. van Dishoeck and J. H. Black (2005), *An atomic and molecular database for analysis of submillimetre line observations*, **432** 369, eprint: arXiv:astro-ph/0411110.

Schuller, F., K. M. Menten et al. (2009), *ATLASGAL - The APEX telescope large area survey of the galaxy at 870 μm*, **504** 415, arXiv: 0903.1369 [astro-ph.GA].

Schuller, F., J. S. Urquhart et al. (2021), *The SEDIGISM survey: First Data Release and overview of the Galactic structure*, **500** 3064, arXiv: 2012.01527 [astro-ph.GA].
Serabyn, E., R. Guesten and A. Schulz (1993), *Fragmentation and Kinematics of the W49N Cloud Core*, **413** 571.
Shu, F. H., F. C. Adams and S. Lizano (1987), *Star formation in molecular clouds: observation and theory.*, **25** 23.
Siringo, G. et al. (2009), *The Large APEX BOlometer CAmera LABOCA*, **497** 945, arXiv: 0903.1354 [astro-ph.IM].
Smith, R. J., S. C. O. Glover, I. A. Bonnell, P. C. Clark and R. S. Klessen (2011), *A quantification of the non-spherical geometry and accretion of collapsing cores*, **411** 1354, arXiv: 1009.5395 [astro-ph.GA].
Spaans, M., M. R. Hogerheijde, L. G. Mundy and E. F. van Dishoeck (1995), *Photon Heating of Envelopes around Young Stellar Objects: an Explanation for CO J= 6–5*, **455** L167.
Sridharan, T. K., H. Beuther, M. Saito, F. Wyrowski and P. Schilke (2005), *High-Mass Starless Cores*, **634** L57, arXiv: astro-ph/0508421 [astro-ph].
Sridharan, T. K., H. Beuther, P. Schilke, K. M. Menten and F. Wyrowski (2002), *High-Mass Protostellar Candidates. I. The Sample and Initial Results*, **566** 931, arXiv: astro-ph/0110363 [astro-ph].
Stephens, I. W., T. L. Bourke et al. (2019), *Mass Assembly of Stellar Systems and Their Evolution with the SMA (MASSES)—Full Data Release*, **245**, 21 21, arXiv: 1911.08496 [astro-ph.GA].
Stephens, I. W., M. M. Dunham et al. (2018), *Mass Assembly of Stellar Systems and Their Evolution with the SMA (MASSES)—1.3 mm Subcompact Data Release*, **237**, 22 22, arXiv: 1806.07397 [astro-ph.GA].
Stock, D. J. et al. (2015), *Herschel PACS and SPIRE spectroscopy of the photodissociation regions associated with S 106 and IRAS 23133+6050*, **579**, A67 A67, arXiv: 1504.06627 [astro-ph.GA].
Tang, X. D. et al. (2018), *ATLASGAL-selected massive clumps in the inner Galaxy. VI. Kinetic temperature and spatial density measured with formaldehyde*, **611**, A6 A6, arXiv: 1711.10012 [astro-ph.GA].
Taniguchi, K. et al. (2023), *Chemical Differentiation around Five Massive Protostars Revealed by ALMA -Carbon-Chain Species, Oxygen-/Nitrogen-Bearing Complex Organic Molecules-*, arXiv e-prints, arXiv:2304.13873 arXiv:2304.13873, arXiv: 2304.13873 [astro-ph.GA].
Tigé, J. et al. (2017), *The earliest phases of high-mass star formation, as seen in NGC 6334 by Herschel-HOBYS*, **602**, A77 A77, arXiv: 1703.09839 [astro-ph.GA].
Tobin, J. J. et al. (2011), *Complex Structure in Class 0 Protostellar Envelopes. II. Kinematic Structure from Single-dish and Interferometric Molecular Line Mapping*, **740**, 45 45, arXiv: 1107.4361 [astro-ph.SR].
Urquhart, J. S., T. Csengeri et al. (2014), *ATLASGAL - Complete compact source catalogue: 280°<ℓ< 60°*, **568**, A41 A41, arXiv: 1406.5741 [astro-ph.GA].
Urquhart, J. S., C. Figura et al. (2019), *ATLASGAL - molecular fingerprints of a sample of massive star-forming clumps*, **484** 4444, arXiv: 1901.03759 [astro-ph.GA].
Urquhart, J. S., C. König, D. Colombo et al. (2024), *OGHReS: star formation in the outer galaxy (ℓ = 250°-280°)*, **528** 4746, arXiv: 2401.00808 [astro-ph.GA].
Urquhart, J. S., C. König, A. Giannetti et al. (2018), *ATLASGAL - properties of a complete sample of Galactic clumps*, **473** 1059, arXiv: 1709.00392 [astro-ph.GA].
Urquhart, J. S., T. J. T. Moore, T. Csengeri et al. (2014), *ATLASGAL - towards a complete sample of massive star forming clumps*, **443** 1555, arXiv: 1406.5078 [astro-ph.GA].

Urquhart, J. S., T. J. T. Moore, F. Schuller et al. (2013), *ATLASGAL - environments of 6.7 GHz methanol masers*, **431** 1752, arXiv: 1302.2538 [astro-ph.GA].

Urquhart, J. S., M. A. Thompson et al. (2013), *ATLASGAL - properties of compact H II regions and their natal clumps*, **435** 400, arXiv: 1307.4105 [astro-ph.GA].

Urquhart, J. S., M. R. A. Wells et al. (2022), *ATLASGAL - evolutionary trends in high-mass star formation*, **510** 3389, arXiv: 2111.12816 [astro-ph.GA].

Valeille-Manet, M. et al. (2025), *ALMA-IMF: XVII. Census and lifetime of high-mass prestellar cores in 14 massive protoclusters*, **696**, A11 A11, arXiv: 2502.09426 [astro-ph.GA].

van der Tak, F. F. S., J. H. Black, F. L. Schöier, D. J. Jansen and E. F. van Dishoeck (2007), *A computer program for fast non-LTE analysis of interstellar line spectra. With diagnostic plots to interpret observed line intensity ratios*, **468** 627, arXiv: 0704.0155 [astro-ph].

van der Tak, F. F. S., L. Chavarría et al. (2013), *Water in star-forming regions with Herschel (WISH). IV. A survey of low-J H_2O line profiles toward high-mass protostars*, **554**, A83 A83, arXiv: 1304.2949 [astro-ph.GA].

van der Tak, F. F. S., R. F. Shipman et al. (2019), *Multi-line Herschel/HIFI observations of water reveal infall motions and chemical segregation around high-mass protostars*, **625**, A103 A103, arXiv: 1903.11305 [astro-ph.GA].

van der Walt, D. J., A. M. Sobolev and H. Butner (2007), *Inferences from the kinematic properties of 6.7 GHz methanol masers*, **464** 1015.

van der Wiel, M. H. D., L. Pagani, F. F. S. van der Tak, M. Kaźmierczak and C. Ceccarelli (2013), *The HIFI spectral survey of AFGL 2591 (CHESS). I. Highly excited linear rotor molecules in the high-mass protostellar envelope*, **553**, A11 A11, arXiv: 1303.3339 [astro-ph.GA].

van Dishoeck, E. F. et al. (2021), *Water in star-forming regions: physics and chemistry from clouds to disks as probed by Herschel spectroscopy*, **648**, A24 A24, arXiv: 2102.02225 [astro-ph.GA].

van Kempen, T. A., L. E. Kristensen et al. (2010), *Origin of the hot gas in low-mass protostars. Herschel-PACS spectroscopy of HH 46*, **518**, L121 L121, arXiv: 1005.2031 [astro-ph.SR].

van Kempen, T. A., E. F. van Dishoeck, R. Güsten, L. E. Kristensen, P. Schilke, M. R. Hogerheijde, W. Boland, K. M. Menten et al. (2009), *APEX-CHAMP$^+$ high-J CO observations of low-mass young stellar objects. II. Distribution and origin of warm molecular gas*, **507** 1425, arXiv: 0908.3446 [astro-ph.SR].

van Kempen, T. A., E. F. van Dishoeck, R. Güsten, L. E. Kristensen, P. Schilke, M. R. Hogerheijde, W. Boland, B. Nefs et al. (2009), *APEX-CHAMP$^+$ high-J CO observations of low-mass young stellar objects. I. The HH 46 envelope and outflow*, **501** 633, arXiv: 0905.2878 [astro-ph.SR].

Vázquez-Semadeni, E., A. Palau, J. Ballesteros-Paredes, G. C. Gómez and M. Zamora-Avilés (2019), *Global hierarchical collapse in molecular clouds. Towards a comprehensive scenario*, **490** 3061, arXiv: 1903.11247 [astro-ph.GA].

Walmsley, M. (1995), "Dense Cores in Molecular Clouds", *Revista Mexicana de Astronomia y Astrofisica Conference Series*, ed. by S. Lizano and J. M. Torrelles, vol. 1, Revista Mexicana de Astronomia y Astrofisica Conference Series 137.

Ward-Thompson, D., P. F. Scott, R. E. Hills and P. Andre (1994), *A Submillimetre Continuum Survey of Pre Protostellar Cores*, **268** 276.

Welch, W. J., J. W. Dreher, J. M. Jackson, S. Terebey and S. N. Vogel (1987), *Star Formation in W49A: Gravitational Collapse of the Molecular Cloud Core toward a Ring of Massive Stars*, Science **238** 1550.

Wilson, R. W., K. B. Jefferts and A. A. Penzias (1970), *Carbon Monoxide in the Orion Nebula*, **161** L43.
Wilson, T. L., K. Rohlfs and S. Huttemeister (2012), *Tools of Radio Astronomy, 5th edition*.
Wolfire, M. G. and J. P. Cassinelli (1987), *Conditions for the Formation of Massive Stars*, **319** 850.
Wolstencroft, R. D. and W. B. Burton, eds. (1988), *Millimetre and submillimetre astronomy*, vol. 147, Astrophysics and Space Science Library.
Wood, D. O. S. and E. Churchwell (1989), *Massive Stars Embedded in Molecular Clouds: Their Population and Distribution in the Galaxy*, **340** 265.
Wyrowski, F. et al. (2016), *Infall through the evolution of high-mass star-forming clumps*, **585**, A149 A149, arXiv: 1510.08374 [astro-ph.SR].
Yang, A. Y., M. A. Thompson, J. S. Urquhart and W. W. Tian (2018), *Massive Outflows Associated with ATLASGAL Clumps*, **235**, 3 3, arXiv: 1712.04599 [astro-ph.GA].
Yang, A. Y., J. S. Urquhart et al. (2022), *The SEDIGISM survey: A search for molecular outflows*, **658**, A160 A160, arXiv: 2111.10850 [astro-ph.GA].
Yang, Y.-L. et al. (2018), *CO in Protostars (COPS): Herschel-SPIRE Spectroscopy of Embedded Protostars*, **860**, 174 174, arXiv: 1805.00957 [astro-ph.GA].
Yıldız, U. A., L. E. Kristensen, E. F. van Dishoeck, M. R. Hogerheijde et al. (2015), *APEX-CHAMP$^+$ high-J CO observations of low-mass young stellar objects. IV. Mechanical and radiative feedback*, **576**, A109 A109, arXiv: 1501.03259 [astro-ph.SR].
Yıldız, U. A., L. E. Kristensen, E. F. van Dishoeck, I. San José-García et al. (2013), *High-J CO survey of low-mass protostars observed with Herschel-HIFI*, **556**, A89 A89, arXiv: 1306.3981 [astro-ph.SR].
Yıldız, U. A., L. E. Kristensen, E. F. van Dishoeck, A. Belloche et al. (2012), *APEX-CHAMP$^+$ high-J CO observations of low-mass young stellar objects. III. NGC 1333 IRAS 4A/4B envelope, outflow, and ultraviolet heating*, **542**, A86 A86, arXiv: 1203.2965 [astro-ph.SR].
Young, E. T. et al. (2012), *Early Science with SOFIA, the Stratospheric Observatory For Infrared Astronomy*, **749**, L17 L17, arXiv: 1205.0791 [astro-ph.IM].
Zhang, C.-P. and G.-X. Li (2017), *Mass-size scaling $M \sim r1.67$ of massive star-forming clumps - evidences of turbulence-regulated gravitational collapse*, **469** 2286, arXiv: 1704.02067 [astro-ph.GA].
Zinnecker, H. and H. W. Yorke (2007), *Toward Understanding Massive Star Formation*, **45** 481, arXiv: 0707.1279 [astro-ph].

List of Figures

List of Tables

Acronyms

CSC Compact Source Catalogue. 14

FWHM full width at half maximum. 25

GCSC GaussClump Source Catalogue. 13, 14

GHC global hierarchical collapse. 7, 8, 10, 11

HCHII hyper-compact HII. 9, 11

HMC hot molecular core. 9

HMPO high-mass protostellar object. 10

HMSF high-mass star formation. 6, 9–11, 13–16, 61, 121

IMF initial mass function. 8

IR infrared. 5, 9–11, 13–15, 19, 23, 61, 121

IRDC infrared dark cloud. 10

ISM interstellar medium. 1, 12, 19, 23, 24, 27, 38, 43, 65

LTE local thermodynamic equilibrium. iii, x, 27, 28, 38, 40, 41, 43, 44, 46–48, 50, 52, 54, 56, 58, 63

MDC massive dense core. 9–11

mm millimetre. ix, 19, 20, 61

MVG mean velocity gradient. 30, 31, 33, 34, 62, 122

PDR photon-dominated region. 64

SED spectral energy distribution. 5, 10, 12, 13, 121

SLED spectral line energy distribution. 48, 49, 53, 55–57, 123

sub-mm sub-millimetre. ix, 4, 5, 10, 13, 17, 19, 20, 125

UCHII ultra-compact HII. 9

UV ultra-violet. 9, 11, 12, 121

YSO young stellar object. 9, 14, 29, 30, 33, 34, 38, 43

ZAMS zero-age-main-sequence. 2, 9

Acknowledgements

This incredible journey brought me all the way from Vietnam to Germany, taking step by step through all the ups and downs. Now, finally, at the end of my doctoral thesis, I look back and realise how fortunate I am to have met wonderful colleagues and friends, without whom this thesis would not have been completed. I want to express my gratitude to all of them here.

The beginning of this whole journey dates back to the time when I joined the Ho Chi Minh City Amateur Astronomy Club (HAAC). I want to thank the members of the club who share my love of astronomy and gave me the courage to pursue Astronomy studies. I thank Dr. Quang Nguyen-Luong for his guidance from those early days. I thank Tan Vu Nguyen for his countless advice.

I want to thank Prof. Karl M. Menten for letting me join his Millimetre and Sub-millimetre group at the Max Planck Institute for Radio Astronomy. I have learned a great deal about radio astronomy in the group and had numerous unique experiences; visiting the Atacama Desert to observe with the APEX telescope is definitely a highlight. It is our loss that Karl passed away suddenly. We will miss him. I express my gratitude to Prof. Frank Bigiel for agreeing to step in and succeed Karl as my primary supervisor. I also extend my sincerest thanks to Prof. Pavel Kroupa, Prof. Jochen Dingfelder, and Prof. Ulrike Endesfelder for agreeing to serve as the members of my thesis committee.

I am grateful to Dr. Friedrich Wyrowski and Dr. Min-Young Lee for their continuous support and guidance throughout my doctoral years. Thank you, Friedrich, for your help with the scientific ideas and discussions that shape this thesis. I am fascinated by your brilliant mind in every one of our discussions. Thank you for teaching me how to conduct observations with a radio telescope and sharing interesting stories over a galactic map in the APEX control room in San Pedro. To Min-Young, my long-distance advisor, no words can express my gratitude. Despite an over 8000 km distance and a seven/eight-hour difference between Bonn and Deajeon, you are still one of the biggest helps, pushing me forward to complete my thesis. Thank you for being strict with me over my scientific work and writing. I will miss our weekly online meeting. I owe a great deal to Dr. Agata Karska for her support and guidance during parts of my thesis. I am very grateful that Agata joined our group and helped many students, including me. I also thank Dr. Ngoc Tram Le, Dr. Aiyuan Yang, and Dr. Felipe Navarete, the co-authors of my publications, for carefully reviewing our manuscripts in great detail and providing valuable feedback. I extend my thanks to Dr. Helmut Wiesemeyer and Dr. Dario Colombo for answering my scientific and technical questions, whether silly or not. I would like to thank Dr. Dirk Muders for helping me with IT-related issues. It is incomplete without mentioning chi Lê, Barbara Menten, and Eva Schmelmer for their tremendous support with the administrative work. My thanks also go to the International Max Planck Research School (IMPRS) for Astronomy and Astrophysics at the Universities of Bonn and Cologne for partially supporting me financially with travel to conferences.

It goes without saying that this work would not have come to fruition without the support of my

dear friends, whom I am so fortunate to have met. To Hans and Arshia, my family in Bonn, thank you for your companionship, for our sushi dates with the wasabi challenge, and for sharing stories and endless gossip with me. Hans, I have fond memories of our time as housemates. I hope we did not wreck the apartment a little too much. To Franzi, my 'housemate' during the pandemic, thank you for sharing a quality quarantine with Hans and me. I truly enjoyed our LoL games. To Ben, the legendary party thrower, who would have guessed that meeting in Belgium led to you sleeping on our couch, and then came many interesting trips together. Thank you for bringing many new colours into my life. Zuong, when we started playing PUBG together, I did not think we would end up as friends, but I am happy that we do. Thank you for being there not only for me but also for my family. Linh P., thank you for the time we shared; it gave me so much strength to reach the end of this PhD journey.

I owe a big thank you to Rohit, Henning, Sarwar, Ivalu, Manali, and Ivana (aka Potato). I look forward to having more hangouts with you guys, playing board games and video games. I also extend my thanks to my fellow MPIfR friends, Iason, Efi, Anahat, Kartik, Laure, Maitrayee, Nina, Carsten, and Parichay, for the fun and interesting conversations, discussions, and moments we have shared. They indeed helped keep me sane during difficult times.

To Jasmin and Dennis, my housemates, thank you for our delicious dinners together: pho, Thai curry, schnitzel, and hotpot - you name it. Dennis, thank you for the wonderful cake you made for my 30th birthday. The WG parties we had were also a lot of fun. I will miss both of you when you leave for your world trip. I extend my thanks to Li, Lau, Ben, Nico, Natalie, Marco, and Achaiah. Thank you for our small gatherings at my WG's kitchen, from making cookies to drinking beers.

To my Vietnamese friends in the Bonn-Cologne area, Tung, Giang, Linh, anh Liem, chi Chau, anh Dung, anh Tram, chi Nhu, be Gao, anh Vu, chi Trang, Hai lon, Hai nho, chi Duong, anh Loc, thank you for our warm gatherings. Although many of you have moved away, I truly hope we can meet up again soon. To my other Vietnamese friends in Germany, chi Huong, chi Thuy, Mia, Thao, anh Quan, chau Jolie, anh Thanh, anh Phong, anh Tam, chi Dung, Tung Anh, thank you for our memorable raves and visits, for taking care of me during our trips. Thank you also to chu Thang and co Hang, every time I come to visit, you make me feel like I am at home.

To Khanh Linh, thank you for your unexpected but pleasant company during the final stages of this PhD journey. It means a lot to me.

Mom and Dad, I love you deeply, and I know you also love me no matter what. I am sorry for being away from home for so long. Thank you for always believing in me, supporting me, and letting me live the life I choose. Without your love and support, I would not have been able to make it this far. To my younger brother, Phat, thank you for being my brother, for being with Mom and Dad while I study abroad. To my bigger brother, anh Hai, you are not with us anymore, but I hope you are in a better place.

Cover page background image: a resampled version of the image of The Pillars of Creation taken by the Near-Infrared Camera (NIRCam) onboard the NASA's James Webb Space Telescope (*JWST*). Credits: NASA, ESA, CSA, STScI; Image Processing: Joseph DePasquale (STScI), Anton Koekemoer (STScI), Alyssa Pagan (STScI).